Crystal growth and characterization of 4d and 5d transition metal compounds

INAUGURAL-DISSERTATION

zur

Erlangung des Doktorgrades

der Mathematisch-Naturwissenschaftlichen Fakultät

der Universität zu Köln

vorgelegt von

Henrik Schilling

aus Leverkusen

Abstract

In this work, both the flux method for growing single crystals from the melt and the chemical transport reaction method for growing crystals from the gas phase were employed.

The flux method was applied to the crystal growth of quaternary perovskite compounds of the types $Ba_3MM'_2O_9$ and $Ba_4MM'_3O_{12}$. In these structure types, the metal atoms *M* and *M′* occupy distinct crystallographic sites, both in octahedral coordination. The *M′* atoms form face-sharing octahedral units: $[M'_2O_9]$-dimers in $Ba_3MM'_2O_9$ and $[M'_3O_{12}]$-trimers in $Ba_4MM'_3O_{12}$. These structural units are corner-connected via $[MO_6]$-octahedra, resulting in isolated cluster motifs.

Due to the short metal–metal distances within the $[M'_2O_9]$-dimers and $[M'_3O_{12}]$-trimers, the formation of molecular orbitals is possible [1; 2; 3]. Therefore, these compounds are classified as "cluster materials" [4]. In this study, the clusters were occupied by either ruthenium or iridium, since these 4d and 5d transition metals exhibit strong spin–orbit coupling due to their high atomic numbers, leading to pronounced splitting of the valence electron levels. The interaction between molecular orbitals and spin–orbit coupling can give rise to novel electronic configurations, making these materials highly promising candidates in the field of quantum materials.
The oxidation states of Ir and Ru are derived from the charge neutrality condition of the compound and are predominantly dictated by the valence of the *M*-site cation, with Ba^{2+} and O^{2-} acting as constant components. This enables for targeted tuning of the electron count per dimer or trimer cluster, by selective substitution of differently valent elements on the *M*-site, as demonstrated in [5; 6].

Due to the limited understanding of the phase diagrams of such complex systems, experimental data were collected to identify suitable synthesis conditions. The effect of the $BaCl_2$ flux on the crystal growth process was investigated, and parameters such as temperature, crucible material and chemical composition were optimized. As a result, several iridium- and ruthenium-based single crystals of $Ba_3MM'_2O_9$ and $Ba_4MM'_3O_{12}$ types were synthesized.

Following optimization of the growth parameters, thermal, chemical and structural characterization of the synthesized crystals was carried out. It was found that the ruthenates exhibit greater thermal stability at elevated temperatures compared to their iridium analogues. Chemically, all compounds matched the target stoichiometry, with the exception of systems containing *M* = Nb and Ta, where partial substitution by Ir and Ru, respectively, was observed.

Structural investigations using single-crystal X-ray diffraction were carried out on $Ba_3MRu_2O_9$ (with *M* = Ce, Eu, Tb, Yb and Y), $Ba_4MRu_3O_{12}$ (with *M* = Ce and Ta) and $Ba_4TaIr_3O_{12}$.
For $Ba_3MRu_2O_9$ with *M* = Eu and Tb, potential structural distortions and symmetry reductions from $P6_3/mmc$ to $P6_3mc$ were observed. For all other compounds of this structure type, the hexagonal symmetry $P6_3/mmc$ could be confirmed.
$Ba_4TaRu_3O_{12}$ crystallizes in space group $R\bar{3}m$, is isostructural with $Ba_4NbRu_3O_{12}$, and exhibits Ru–Ta substitution. In contrast, the iridium analogue $Ba_4TaIr_3O_{12}$ shows no such substitution. $Ba_4CeRu_3O_{12}$ is monoclinically distorted and crystallizes in space group $C2/m$. Other synthesized trimer-type compounds with *M* = rare-earth elements showed severe structural disorder along the *c*-axis. These stacking faults hindered the indexing of the single-crystal data.

In the final part of this work, the crystal growth of Ni_2InSbO_6 was investigated using the CTR method in combination with a transport balance to measure transport rates. The experimentally determined rates were compared with theoretically calculated values in order to enable controlled crystal growth. The results revealed that the chemical composition of the grown crystals depends on the transport rate and the partial vapor pressures of the starting materials.

Kurzzusammenfassung

In dieser Arbeit kamen zwei Methoden zur Einkristallzüchtung komplexer Oxide zum Einsatz: die Flux-Methode zur Kristallisation aus der Schmelze sowie die chemische Transportreaktion (CTR) zur Züchtung aus der Gasphase.

Die Flux-Methode wurde für die Kristallzüchtung quaternärer Perowskitverbindungen vom Typ $Ba_3MM'_2O_9$ und $Ba_4MM'_3O_{12}$ angewendet. In diesen Strukturtypen besetzen die Metallatome *M* und *M*‘ unterschiedliche kristallographische Gitterpositionen in oktaedrischer Koordination. Die *M*‘-Atome bilden flächenverknüpfte Oktaedereinheiten: $[M'_2O_9]$-Dimere in $Ba_3MM'_2O_9$ sowie $[M'_3O_{12}]$-Trimere in $Ba_4MM'_3O_{12}$. Diese strukturellen Einheiten sind über Eck mit $[MO_6]$-Oktaedern verknüpft und dadurch voneinander isoliert.

Aufgrund kurzer Metall–Metall-Abstände innerhalb der $[M'_2O_9]$-Dimere und $[M'_3O_{12}]$-Trimere ist die Ausbildung von Molekülorbitalen möglich [1; 2; 3]. Daher werden diese Verbindungen als „Cluster-Materialien” klassifiziert [4]. In dieser Arbeit wurden die Cluster gezielt mit Ruthenium oder Iridium besetzt, da diese 4d- bzw. 5d-Übergangsmetalle aufgrund ihrer hohen Ordnungszahlen eine starke Spin-Bahn-Kopplung aufweisen, was zu einer deutlichen Aufspaltung der Valenzelektronenniveaus führt. Die Wechselwirkung zwischen Molekülorbitalen und Spin-Bahn-Kopplung kann zu neuartigen elektronischen Konfigurationen führen und macht diese Materialien zu einem vielversprechenden Forschungsfeld im Bereich der Quantenmaterialien.
Die Oxidationsstufen von Ir und Ru ergeben sich aus der Ladungsbilanz der Verbindung und werden dabei im Wesentlichen durch die Valenz des *M*-Kations bestimmt, da Ba als Ba^{2+} und O als O^{2-} vorliegen. Dies ermöglicht es, die Elektronenzahl pro Dimer- oder Trimer-Cluster gezielt zu variieren, indem die *M*-Position mit Elementen verschiedener Valenz besetzt wird [5; 6].

Da die Phasendiagramme derart komplexer Systeme meist nur unzureichend erforscht sind, wurden experimentelle Daten erhoben, um geeignete Synthesebedingungen zu identifizieren. Der Einfluss des Flussmittels $BaCl_2$ wurde systematisch untersucht und Parameter wie Temperatur, Tiegelmaterialien und chemische Zusammensetzung wurden

optimiert. Dadurch gelang es verschiedene Iridium- und Ruthenium-basierte Einkristalle vom Typ $Ba_3MM'_2O_9$ und $Ba_4MM'_3O_{12}$ zu synthetisieren.

Die gezüchteten Kristalle wurden thermisch, chemisch und strukturell charakterisiert. Dabei zeigte sich, dass die Ruthenate im Vergleich zu ihren Iridium-Analoga bei höheren Temperaturen stabiler sind. Chemisch stimmten alle Verbindungen, mit Ausnahme der Systeme mit *M* = Nb und Ta, bei denen eine partielle Substitution durch Ir bzw. Ru beobachtet wurde, mit der Zielstöchiometrie überein.

Strukturelle Untersuchungen mittels Einkristallröntgenbeugung wurden an $Ba_3MRu_2O_9$ (mit *M* = Ce, Eu, Tb, Yb und Y), $Ba_4MRu_3O_{12}$ (mit *M* = Ce und Ta) und $Ba_4TaIr_3O_{12}$ durchgeführt. Für *M* = Eu und Tb wurden mögliche Verzerrungen und eine Symmetriereduktion von $P6_3/mmc$ zu $P6_3mc$ festgestellt. Die Verbindung $Ba_4TaRu_3O_{12}$ kristallisiert in der Raumgruppe $R\bar{3}m$, ist isostrukturell zu $Ba_4NbRu_3O_{12}$ und zeigt eine Substitution zwischen Ru und Ta. Das Iridium-basierte Analog $Ba_4TaIr_3O_{12}$ zeigt hingegen keine Substitution zwischen Ta und Ir. $Ba_4CeRu_3O_{12}$ ist monoklin verzerrt und kristallisiert in der Raumgruppe $C2/m$. Alle weiteren synthetisierten Trimer-Verbindungen mit *M* = seltene Erden zeigten starke strukturelle Störungen entlang der *c*-Achse. Diese Störungen, verursacht durch Stapelfehler, verhinderten eine Indizierung der Einkristalldaten.

Im letzten Teil dieser Arbeit wurde die Kristallzüchtung von Ni_2InSbO_6 untersucht. Hierfür wurde die CTR-Methode in Kombination mit einer Transportwaage eingesetzt, um die Transportraten zu messen. Die experimentell bestimmten Raten wurden mit theoretisch berechneten Werten verglichen, um eine kontrollierte Kristallzüchtung zu ermöglichen. Dabei zeigte sich, dass die chemische Zusammensetzung der Kristalle von der Transportrate bzw. von den unterschiedlichen Dampfdruckverhältnissen der Ausgangsstoffe abhängt.

Contents

List of Figures

Introduction

Perovskite type structures

Principle techniques of single crystal growth

Crystal growth investigations

Characterization Iridates

Characterization Ruthenates

Crystal growth of Ni_2InSbO_6

List of Tables

Crystal growth investigations

Characterization Iridates

Characterization Ruthenates

Crystal growth of Ni_2InSbO_6

1 Introduction

The study of single crystals and the increasing understanding of quantum states are fundamental to modern technological progress. This thesis aims to deepen the understanding of quasi-ternary systems containing the 4d and 5d transition metals ruthenium and iridium, with a particular focus on the synthesis of high-quality crystalline cluster materials. By achieving a deeper understanding of these complex systems through targeted crystal growth, this work establishes a solid foundation for future investigations into the physics of cluster materials. The successful synthesis of single crystals is crucial for accurately characterizing the structural and electronic properties of these materials, which are particularly intriguing due to their complex electronic interactions, strong spin-orbit coupling, and potential to exhibit exotic quantum states.

The thesis is structured into eight main chapters that cover the theoretical background, a detailed description of crystal growth and the characterization of grown crystals.

Chapter 1 outlines the fundamental physical principles that govern the behavior of the studied materials. This includes an overview of electronic correlations, crystal field effects, spin-orbit interactions, and molecular orbital formation, all of which play a crucial role in defining the behavior of these materials. Following this, the concept of cluster materials is introduced, providing a broader context within the field of condensed matter physics. The discussion then narrows to perovskite cluster materials, highlighting their significance and the necessity of synthesizing high-quality single crystals to analyze their physical properties.

Chapter 2 provides an in-depth discussion of the perovskite structure and its variations, including distortions, stacking sequences, and changes in the oxidation states of iridium and ruthenium. These structural changes can have a profound impact on electronic and physical properties.

Chapter 3 outlines the methodological framework used to assess the quality and phase purity of the synthesized crystals. It describes the analytical techniques applied, including X-ray diffraction, electron microscopy, and thermal analysis.

Chapter 4 addresses the theoretical background of crystal growth, and outlines the experimental growth method which is used in the present work.

Chapter 5 offers a systematic investigation of selected quasi-ternary systems, exploring on their phase formation and structural stability. A systematic approach to optimizing synthesis conditions is presented, considering key factors such as phase stability and evaporation effects.

Chapters 6 and 7 focus on the structural and chemical characterization of the grown perovskite cluster crystals. The primary analytical techniques include precise structure determination using both powder X-ray diffraction and single-crystal X-ray diffraction, complemented by elemental analysis via energy-dispersive X-ray spectroscopy and thermal analysis using simultaneous thermal analysis. These methods provide critical insights into the crystallographic quality, phase purity, and thermodynamic stability of the synthesized materials.

Finally, chapter 8 focuses on the synthesis and characterization of Ni_2InSbO_6. The synthesis was carried out using chemical transport reaction and monitored with a transport balance. By comparing the measured transport rates with theoretical calculations, conclusions can be drawn about the partial pressures and the transport-active species in the system.

1.1 Spin-orbit coupling

Crystalline solids can be characterized by their band structure, which results from various factors such as atomic states, crystal structure, and interactions between atoms and electrons [7]. The band structure is also influenced by relativistic effects, including spin-orbit coupling (SOC), which becomes particularly relevant for heavy elements [8; 9]. SOC is a relativistic phenomenon that arises due to the interaction between an electron's spin and its orbital motion around the nucleus [9]. As the electron moves through the electric field generated by the positively charged nucleus, it experiences this field as a magnetic field in its own rest frame [9]. This effective magnetic field interacts with the electron’s intrinsic magnetic moment, leading to the coupling of the spin $\vec{S}$ and the orbital angular momentum $\vec{L}$ [9] .

In light elements, SOC is often negligible because the Coulomb interactions are significantly stronger. However, for heavier elements, SOC can substantially modify the band structure, particularly near the Fermi level. This strong effect arises because the magnitude of SOC, denoted by λ, scales approximately with the atomic number Z as $\lambda \propto Z^4$ [10; 11].

For a single-site 4d or 5d transition metal in an octahedral coordination, the five degenerate d orbitals experience an initial splitting primarily due to electrostatic interactions with the surrounding ligands, although additional effects such as covalent bonding, relativistic interactions, and structural distortions may also contribute. This results in the well-known division into two higher-energy e_g orbitals (d_{z2}, d_{x2-y2}) and three lower-energy t_{2g} orbitals (d_{xy}, d_{xz}, d_{yz}) [12; 13]. This crystal field splitting arises from the spatial distribution of electron density relative to the ligand positions. The e_g orbitals point toward the ligands and are subject to a stronger electrostatic repulsion than the t_{2g} orbitals.
Trigonal distortions in a local crystal field break the cubic symmetry of the octahedral ligand field, causing additional splitting of the t_{2g} orbitals [13]. Specifically, the three t_{2g} orbitals transform into a singlet a_{1g} orbital and a pair of degenerate e_g^{π} orbitals, reflecting the lower D_{3d} point-group symmetry of the distorted environment [13].

Similar to the crystal field splitting due to structural distortion, splitting occurs when the intrinsic effect of SOC is strong. For transition metal compounds with up to a d^6 electron configuration, the higher-energy e_g orbitals typically remain unoccupied, and only the t_{2g} orbitals contribute to the description of the electronic structure. Therefore, the t_{2g} orbitals can be described by an effective orbital angular momentum $L_{eff} = 1$**,** reducing the system to a simpler form that behaves similarly to a *p*-orbital system where $L = 1$ (see Figure 1.2) [14].

The interaction between L_{eff} and the spin angular momentum $S = 1/2$ lead to the formation of new quantum states described by the total angular momentum J, which is given by:

$$\vec{J} = \vec{L}_{eff} + \vec{S} \tag{1.1}$$

The coupling of $L_{eff} = 1$ with $S = 1/2$ results in two distinct sets of states, $J = 3/2$ and $J = 1/2$ [7]. The higher energy $J = 3/2$ state consists of four levels with $m_j = \pm 3/2$ and $\pm 1/2$, while the lower energy $J = 1/2$ state contains two levels with $m_j = \pm 1/2$ [7].

The energy gap between the $J = 3/2$ and $J = 1/2$ states is proportional to λ and typically ranges from 0.1 to 1 eV for 5d elements [15]. In real systems, a combination of crystal field splitting and SOC can lead to a splitting to discrete energy levels in the fine structure of the band model. This allows for new occupancies and excitation states, which directly influence the physical properties of the material.

1.2 Molecule orbital

The concept of molecular orbitals is a fundamental phenomenon that was first described by Mulliken and Hund in 1928 and is explained in numerous textbooks [16].

The valence bond theory assumes that electron pairs belong either to two atoms **(**bonding electron pairs) or to a single atom (lone pairs). In contrast, molecular orbital (MO) theory considers the entire molecule as a unified electronic system. Rather than being confined to atomic orbitals associated with specific nuclei, electrons occupy molecular orbitals that extend over the entire molecule [16]. This leads to delocalized electronic states across the molecule. According to the linear combination of atomic orbitals (LCAO) theory, MOs form through the constructive or destructive interference of atomic wavefunctions, resulting in bonding (σ, π) and antibonding (σ^*, π^*) states [4]. The occupation of these bonding and antibonding MOs plays a crucial role in determining the stability and electronic structure of a system [16].

While originally developed for discrete molecules, this concept also applies to crystalline materials where metal atoms are sufficiently close to allow orbital overlap and MO formations [4]. In contrast to real molecules, the electrons in these materials, called cluster materials, are delocalized only within a specific structural unit of the crystal lattice. For this reason, this state is referred to as a quasimolecular state.

1.3 Cluster materials

Cluster materials are characterized by electronically delocalized structural motifs within an extended lattice. Before defining cluster materials, the term “cluster” must be clarified. Without focusing on cluster chemistry, the term ”cluster” frequently is used to describe an intermediate-sized aggregate of atoms or molecules, bridging the gap between discrete molecules and bulk solids. Clusters exhibit unique properties that can significantly deviate from those of their bulk counterparts [17]. Moreover, even minimal variations in cluster size or composition can induce drastic changes in their physical and chemical properties [17]. However, this definition must be distinguished from the usage of the term “cluster” in the present study.

In the context of cluster materials, a cluster refers to a structural unit within a crystalline lattice in which metal atoms are close enough to enable orbital overlap and the formation of MOs [4]. In transition metal (TM) clusters, the formation of MOs leads to the emergence of delocalized electronic states that extend across the cluster. This electronic delocalization is particularly pronounced in 4d- and 5d-metal systems, where the spatially extended d-orbitals promote strong hybridization, giving rise to quasimolecular electronic structures [2; 18; 3; 12].

Clusters can be formed in various structures and differ in geometry and size. Moreover, the formation of clusters and MOs within a crystal structure has a significant impact on its physical properties. For instance, in CsW_2O_6 with β-pyrochlore-type structure, a phase transition occurs below 215 K, driven by the trimerization of three tungsten atoms arranged in a small triangle [19; 20; 21]. This structural rearrangement and formation of MOs, results in a non-magnetic insulating state [20]. Similarly, in Ti-based pyroxenes, a dimerization process occurs at low temperatures, altering the magnetic ordering from antiferromagnetic to ferromagnetic [22]. A further example is found in $[Mo_3O_8]$ cluster magnets, such as $LiZn_2Mo_3O_8$, where Mo atoms are arranged in an anisotropic kagomé lattice [23; 24]. In these systems, $[Mo_3O_{13}]^{15-}$ clusters form triangular units, which dictate the material's electronic and magnetic behavior [24]. In the lacunar spinel $GaTa_4Se_8$ the tantalum atoms are arranged in a tetrahedral ordering [25; 26; 18]. The Ta_4 tetrahedra host quasimolecular J_{tet} = 3/2 moments for which the actual wavefunction is governed by SOC and the competition of different intra-tetrahedral hopping channels [18]. A more complex cluster formation is observed in AlV_2O_4. In this distorted spinel structure, both, trimer and tetramer units occur [27]. Beyond pyrochlore-, spinel- or triangular 2D-structures the perovskites represent another significant platform for cluster physics.

This work is focused on cluster materials of the type $Ba_3MM'_3O_9$ and $Ba_4MM'_3O_{12}$ (see Figure 1.1). Here, *M′* is either Ir or Ru, while *M* refers to a second transition metal or a 4f-element. These structures, as reported in [28; 6; 29], typically consist of face-sharing

[*M*'O_6] octahedra which organize into [*M*'$_2O_9$] "dimers" and [*M*'$_3O_{12}$] "trimers", with short metal-metal distances of approximately 2.5–2.7 Å.

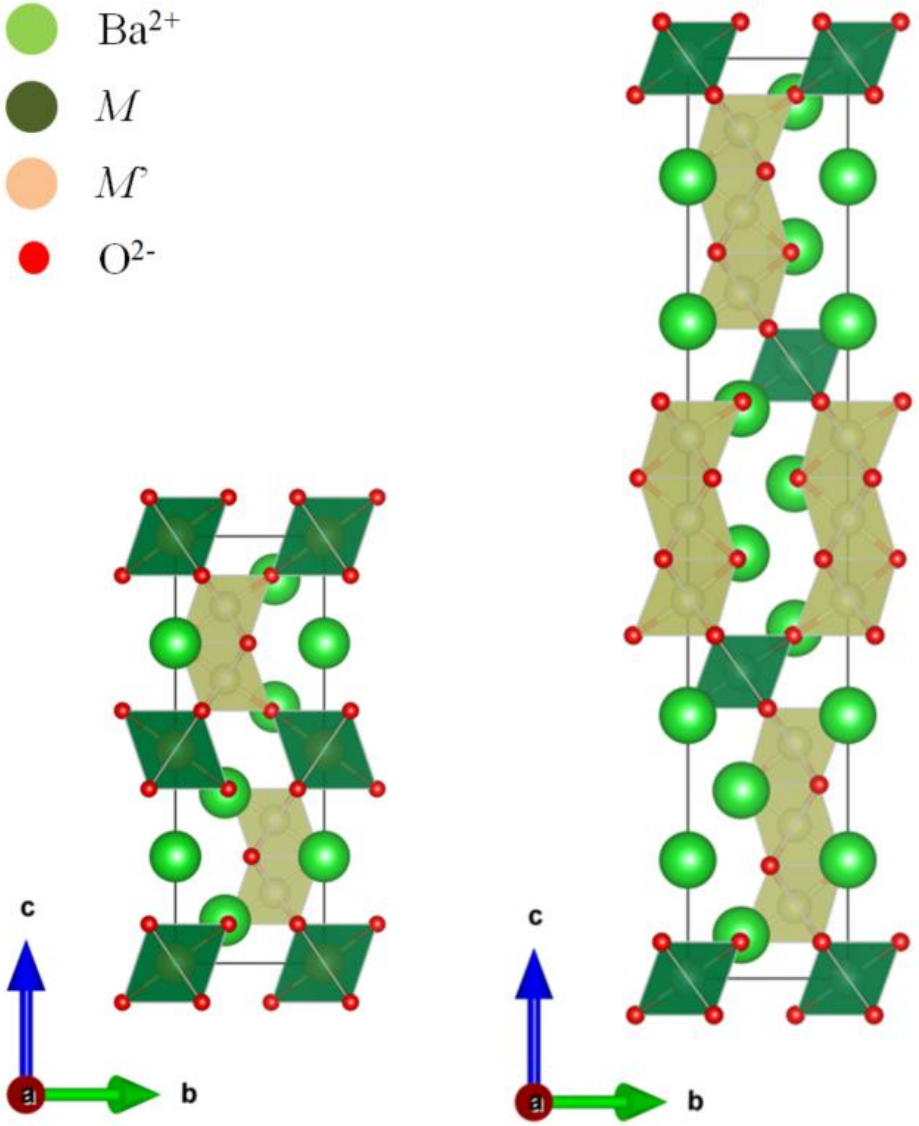

Figure 1.1: Crystal structures of a hexagonal $Ba_3MM'_2O_9$ compound (left) and a trigonal $Ba_4MM'_3O_{12}$ compound (right), the structure models were taken from [30; 29].

A better understanding of the structure and properties of "dimer" and "trimer" compounds containing 4d and 5d elements can be gained by applying an orbital model that considers the effects of spin–orbit coupling (SOC) and molecular orbital (MO) formation.

As explained previously, for a single-site 4d or 5d TM in an octahedral coordination, the interplay between crystal field splitting, spin-orbit coupling (SOC) and SO exciton can result in the formation of three discrete energy levels derived from the t_{2g} orbitals [13]. In cluster materials, the formation of MO occurs due to the overlap of t_{2g} orbitals from adjacent metal atoms, as observed in the case of [M'_2O_9] dimer clusters. According to the LCAO approach, this overlap generates 6 discrete MO states resulting from the interaction of t_{2g} orbitals from two metal atoms [13]. The formation of these MO states alters the effective energy levels, modifying the energy gap between states and enhancing the hopping rate between metal sites. This high hopping rate is a key characteristic of cluster materials and plays a crucial role in their electronic properties (see Figure 1.2) [31].

The $Ba_3MIr_2O_9$ and $Ba_3MRu_2O_9$ families mentioned above comprise a wide range of compounds, where M can be occupied by a variety of TM, alkaline earth metals, and elements from the boron group, such as indium. The valence of iridium or ruthenium depends on the choice of the metal M and can be specifically tuned. Despite the vast diversity of these compounds, only a few of them have been thoroughly investigated regarding their electronic state. Studies on $Ba_3MIr_2O_9$ with M = Ti^{4+}, In^{3+}, Ce^{4+}, Mg^{2+}, Zn^{2+}, Ca^{2+}, Sr^{2+} reveal a strong delocalization of electrons across the dimer [13; 2; 32; 1]**.** Due to weaker spin-orbit coupling (SOC) in ruthenium compared to iridium, [Ru_2O_9] dimers exhibit less pronounced molecular orbital formation [1].
In $Ba_3MRu_2O_9$, the orbital energy levels exhibit a heightened sensitivity to even minor structural distortions. For M = Y^{3+}, In^{3+}, La^{3+}, only small variations in bond lengths occur, yet they lead to significant energetic differences [1].

Similar to the [M'_2O_9] dimer we can describe the orbital hierachy of [M'_3O_{12}] trimers with the interplay of crystal field splitting, SOC and MO formation. In an ideal D_{3h} symmetry, the electronic configuration of an [Ir_3O_{12}] or [Ru_3O_{12}] trimer follows a molecular orbital hierarchy, $(a_{1g})(e_g)(a_{2u})(e_u)(e_g^*)(a_{1g}^*)$ for example in $Ba_4NbM'_3O_{12}$ with M' = Ir, Ru [28; 6; 30]. However, in most $Ba_4MIr_3O_{12}$ and $Ba_4MRu_3O_{12}$ compounds with M = REE, monoclinic distortion lowers the symmetry, lifting degeneracies and further splitting energy levels [28; 6]. Additionally, the SOC of 5d electrons in Ir introduces an additional nontrivial splitting of molecular orbitals, modifying the effective electronic structure of the trimer.
The occupation of these orbitals determines the physical properties, with the valence state of the metal playing a crucial role in the magnetic and electronic behavior, similar to the [M'_2O_9] dimers. In an [$Ir_3^{4.33+}O_{12}$] trimer, the highest occupied molecular orbital (HOMO) is fully occupied, leading to a S = 0 ground state. This configuration explains the

diamagnetic behavior observed in $Ba_4M^{3+}Ir_3^{4.33+}O_{12}$ compounds. In contrast, in $Ba_4M^{4+}Ir_3^{4+}O_{12}$ compounds, an additional electron occupies a higher-energy split state, resulting in a $S = 1/2$ configuration [28].

For $[Ru_3^{4.33+}O_{12}]$ trimers in $Ba_4M^{3+}Ru_3^{4.33+}O_{12}$, the weaker SOC in 4d electrons leads to a different molecular orbital configuration [6; 33]. In this case, the highest occupied e_u orbital retains an unpaired electron ($S = 1/2$), allowing $[Ru_3^{4.33+}O_{12}]$ trimers to contribute to magnetism. Consequently, $[Ru_3^{4+}O_{12}]$ trimers, with a fully filled HOMO, result in an $S = 0$ ground state [6; 33]. Further investigations of $Ba_4Nb_{1-x}Ru_{3+x}O_{12}$ reveal a tunable heavy spinon Fermi surface, governing both heavy-fermion strange-metal behavior and quantum spin-liquid states, with the Nb concentration acting as a key control parameter [34].

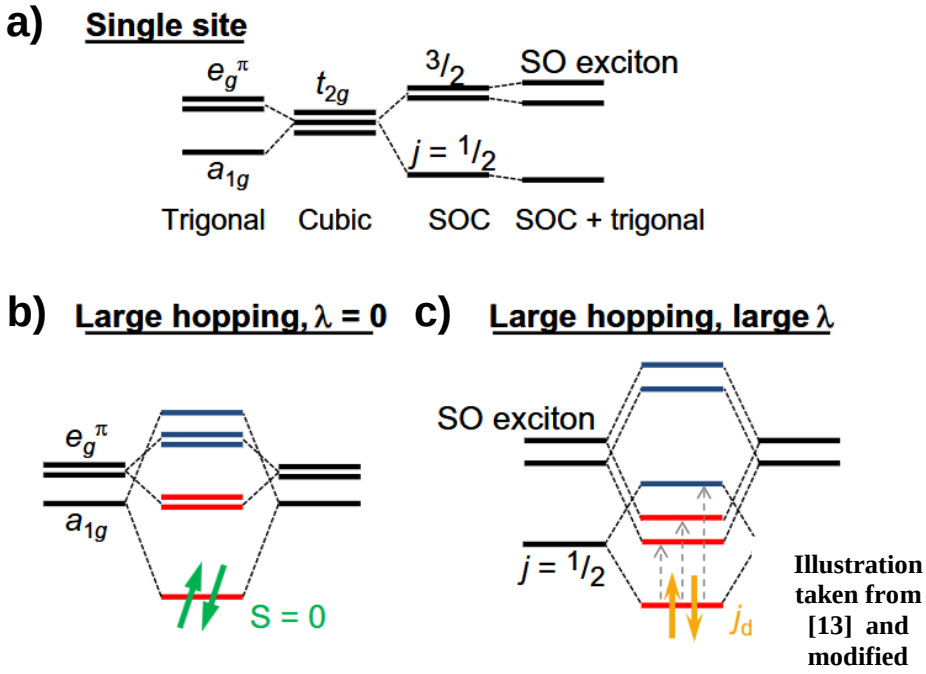

Figure 1.2: (a) For a single site Ir^{4+}, the t_{2g} level is split by a trigonal crystal field into a_{1g} and e_g^π orbitals or by spin-orbit coupling into $J = 1/2$ and 3/2 states. Real materials show both SOC and crystal field splitting, which yields three distinct orbitals. (b) For an Ir_2O_9 dimer cluster quasi-molecular orbitals form. Without SOC the ground state is the a_{1g}^2 spin singlet with total $S = 0$. In (c), the effect of the spin-orbit is illustrated. The band gap becomes shorter so the hopping of the electrons to higher energy levels is forced [13].

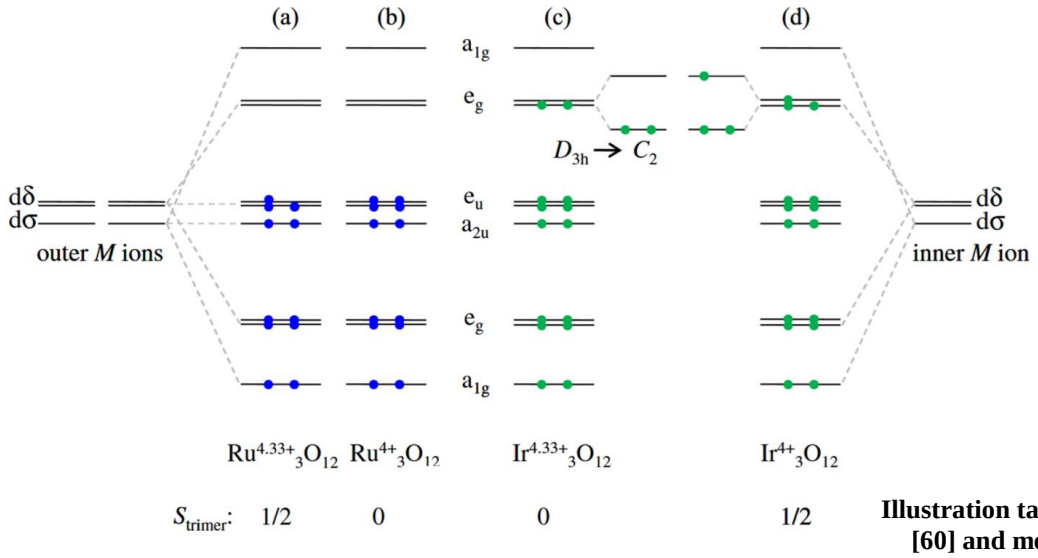

Figure 1.3: Schematic energy level diagrams for (a) $[Ru_3^{4.33+}O_{12}]$ trimer, (b) $[Ru_3^{4+}O_{12}]$ trimer and (c) $[Ir_3^{4.33+}O_{12}]$ timer, (d) $[Ir_3^{4+}O_{12}]$ trimer with spin-orbit exciton and monoclinic distortions of the e_g molecule orbital.

2 Perovskite type structures

2.1 Perovskite structures

Perovskite is the name of a mineral with the sum formula $CaTiO_3$ and was described for the first time by Gustav Rose in 1839 [35]. First descriptions of the $CaTiO_3$ crystal structure suggested a cubic symmetry and date back to 1925 [36]. This was revised, as orthorhombic distortions in the structure were detected breaking the cubic symmetry. However, the cubic space group still represents the idealized perovskite structure with the space group $Pm\bar{3}m$. Most perovskite type compounds with the general formula AMX_3 consist of an alkaline earth metal at the *A* position, a transition metal at the *M* position, and oxygen at the *X* position, such as the cubic holotype $SrTiO_3$ [37].

The perovskite holotype structure can be described as a face-centered cubic (*fcc*) lattice composed of *A* and *X* atoms. The *A* atoms occupy the origin positions, while the *X* atoms center the faces of the unit cell. The *M* atom is positioned at the center of the *fcc* lattice, occupying one-quarter of the available octahedral sites**.** Consequently, the *M* atom is coordinated by six *X* atoms, forming a network of corner-sharing $[MX_6]$ octahedra (Figure 2.1). The *A* atoms at the origin are situated in a $[AX_{12}]$ cuboctahedral coordination, surrounded by twelve *X* atoms (see Figure 2.1 [37]).
As previously mentioned, many perovskite structures deviate from the idealized cubic aristotype. A well-documented phenomenon in this context is structural distortions, which commonly arise when the *A*-site cation is slightly too small to fully stabilize the cubic framework [38]. This size mismatch induces rotations of the $[MX_6]$ octahedra and alterations in the *A*–*X* bond lengths. Due to the corner-sharing connectivity of the octahedral network, these distortions are inherently correlated. A tilt around the cubic *a*-axis must occur in opposite directions for octahedra connected along the *b*- or *c*-axis, whereas octahedra aligned along the *a*-axis can rotate either in-phase (same direction) or out-of-phase (opposite direction). Many structural distortions can thus be systematically described by defining the tilt angles of octahedra along the *a*, *b*, and *c* crystallographic axes. A widely adopted notation for categorizing octahedral tilting in perovskite type structures

was introduced by Glazer (1972) [39]. In this formalism, the undistorted perovskite structure is designated as $a^0a^0a^0$, indicating the absence of octahedral tilting. Identical labels for different axes signify equal tilt magnitudes, while the superscript notation conveys the relative tilt direction between adjacent layers. A "+" superscript denotes that the octahedra in successive layers rotate in the same direction (in-phase), whereas a "−" superscript indicates that neighboring octahedra rotate in opposite directions (out-of-phase) [39].

However, this study focuses on the hexagonal perovskite type. Hexagonal perovskites are particularly prevalent in systems where the *A*-site cation is too large to stabilize the cubic structure, resulting in a Goldschmidt tolerance factor greater than one [38]. The hexagonal structure can be derived from the cubic perovskite structure by examining the cubic close-packed (*ccp*) AX_3 layers within the *abc* stacking sequence. In the cubic unit cell, this stacking sequence is oriented along to the [111] direction. The *abc* stacking of AX_3 layers becomes visible when the ccp structure is viewed along the space diagonal, or by transforming the unit cell according to equation 2.1 (see Figure 2.2).

$$\begin{pmatrix} a' \\ b' \\ c' \end{pmatrix} = \begin{pmatrix} \bar{1} & \bar{1} & 2 \\ 1 & \bar{1} & 0 \\ 1 & 1 & 1 \end{pmatrix} \begin{pmatrix} a \\ b \\ c \end{pmatrix} \tag{2.1}$$

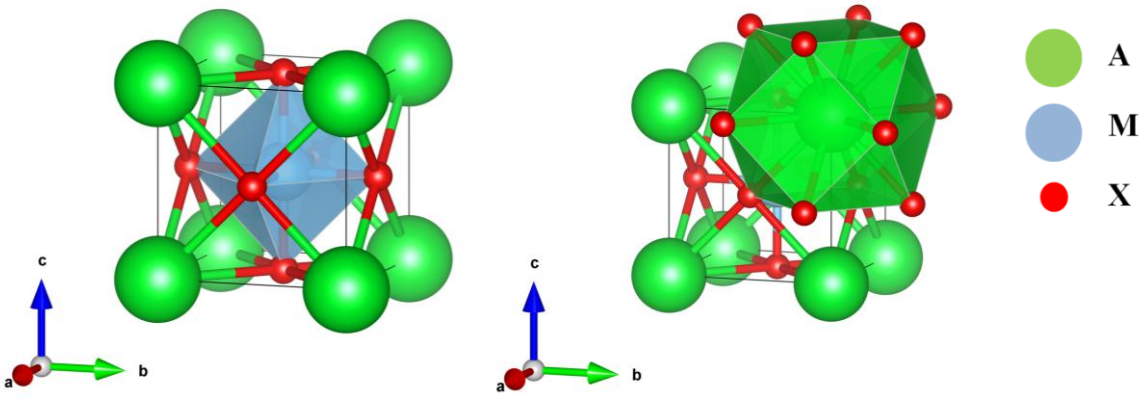

Figure 2.1: Crystal structure of the idealized cubic perovskite structure $Pm\bar{3}m$. The [MX_6] octahedra are highlighted on left hand side. The [AX_{12}] cuboctahedra are highlighted on the right hand side. The structural model was taken from [37]. (Visualization created using VESTA)

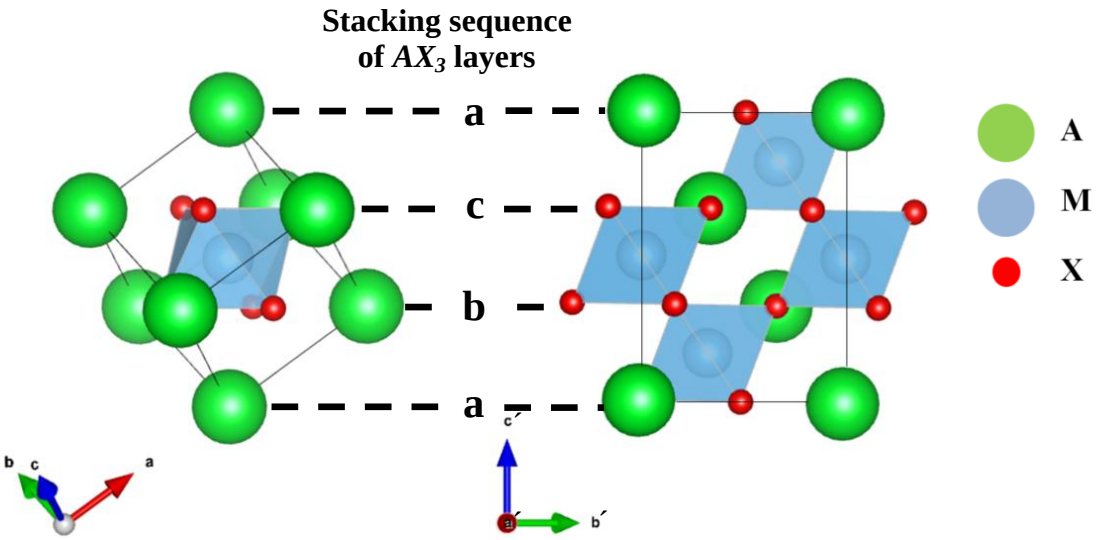

Figure 2.2: Cubix AMX_3 perovskite crystal structure with *ccp* AX_3 layers in the standard cubic setting (left) and in the transformed setting with the *c*-axis perpendicular to the [111] (right). (Visualization created using VESTA)

The simplest hexagonal perovskite, known as the 2H-perovskite, is constructed from AX_3 layers arranged in a hexagonal close-packed (*hcp*) stacking sequence *ab*, resulting in a one-dimensional chain of face-sharing octahedra. This structure represents the holotype of the 2H-perovskite and can be found, for example, in $BaNiO_3$ [40].

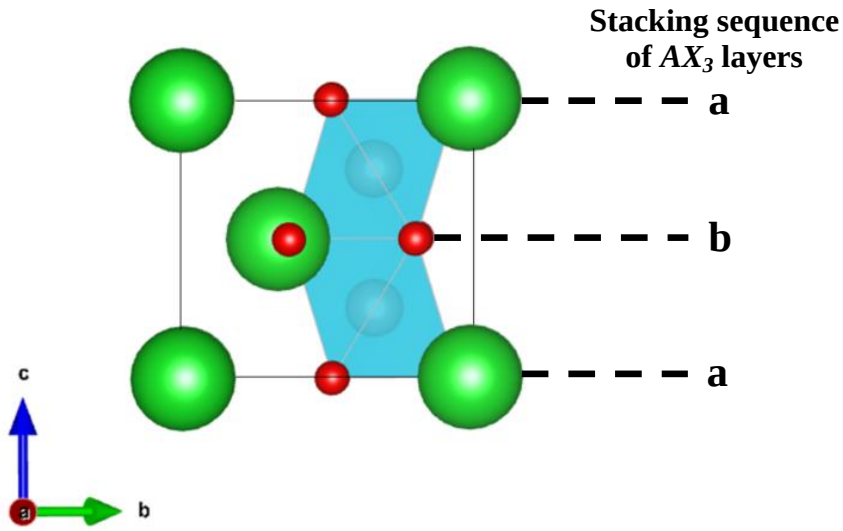

Figure 2.3: Holotype of the hexagonal 2H-perovskite structure of the AMX_3 type. The model is based on the crystal structure of $BaNiO_3$ [40]. *A*-type atoms are shown in green, *X* atoms in red, and MX_6 octahedra in blue. (Visualization created using VESTA)

According to Pauling's third rule, face-sharing octahedra are generally less stable than corner-sharing octahedral units, but bonding metal-metal interactions can overcome the $M - M$ repulsion and stabilize the hexagonal structure [31].
Starting from the 2H-perovskite structure, the stacking sequence within the hexagonal perovskite family can vary significantly, leading to the formation of complex structures. The hexagonal modification of $BaTiO_3$ crystallizes in the so called 6H-perovskite structure [41], characterized by an *abacbc* stacking sequence of BaO_3 layers with a periodicity of six (Figure 2.4). The symmetry is described with the $P6_3/mmc$ (196) space group.

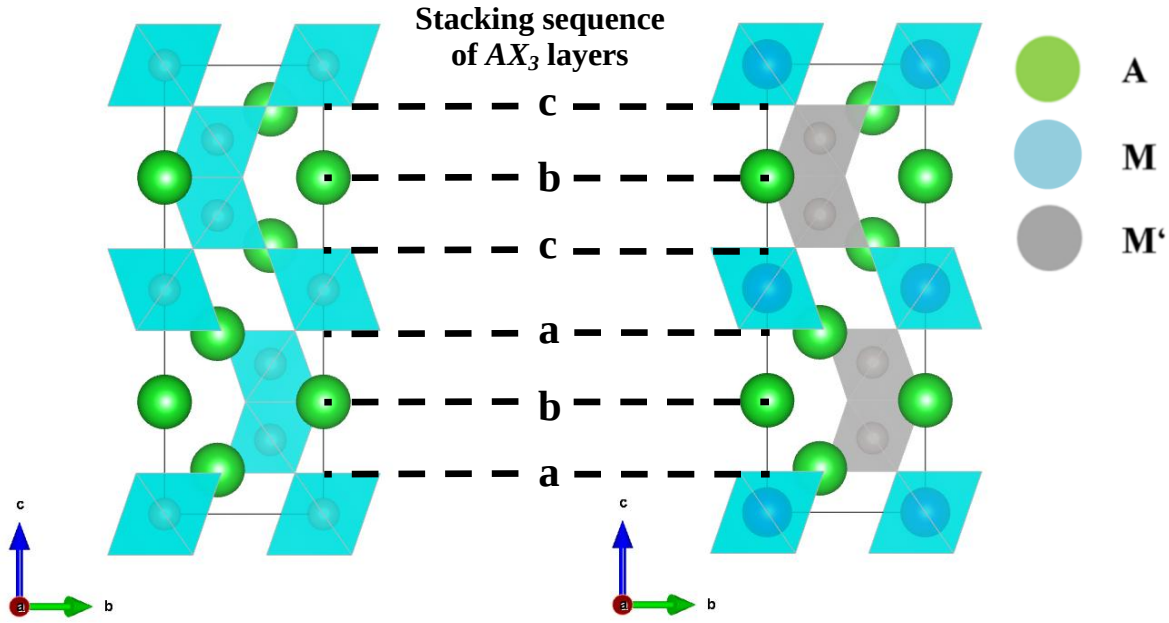

Figure 2.4: Illustration of the AMX_3 (left) and $A_3MM'_2X_9$ (right) 6H-perovskite structure. In $A_3MM'_2X_9$, a separation of the octahedral positions occurs. The dimers are fully occupied by *M*', while the monolayers of octahedra contain *M*. For better visualization of the structure, the *X* atoms have not been depicted. The structural model was taken from [41] and modified. (Visualization created using VESTA)

In this structure, the metal atoms *M* occupy the two Wyckoff positions 2a and 4f. The 2a position is situated in the site symmetry $\bar{3}m$, forming the layer of corner-sharing octahedra between the *ac* sequence. In contrast, the 4f position is located in the site symmetry $3m$, hosting the face-sharing octahedral units between the *aba* and *cbc* sequences. The atoms *A* occupy the two Wyckoff positions 2b and 4f while the *X* atoms occupy the positions 6h and 12k.
When 6H-perovskite structures incorporate two different metals (*M* and *M'*) in a 1 : 1 ratio, they adopt the hexagonal double perovskite structure, with the general formula $A_2MM'X_6$. Due to the 1 : 2 multiplicity ratio of the 2a and 4f sites, the 4f position exhibits a mixed

occupancy of 1/4 *M* and 3/4 *M'* which is realized for example in Ba_2EuIrO_6 [42].
Compounds with an *M* : *M'* ratio of 1 : 2 allow for the full occupation of the Wyckoff positions, leading to structures with the general formula $A_3MM'_2X_9$. In these systems, the face-sharing $[M'_2X_9]$ dimers form characteristic structural units. These units are arranged in a triangular lattice within the (*a*,*b*)-plane and are separated along the *c*-axis by a monolayer of corner-sharing $[MX_6]$ octahedra, which are also arranged in a triangular lattice. As described in [13], the fundamental building blocks $[M'_2X_9]$ are referred to as dimer clusters and, due to the short *M' - M'* distance, can exhibit quasimolecular behavior.

Extending the $[M'_2X_9]$ dimer cluster to a $[M'_3X_{12}]$ trimer cluster alters the *M : M'* ratio to 1 : 3, driving a transition from the 6H-perovskite structure to the rhombohedral 12R-perovskite structure. The 12R-perovskite structure is distinguished by its *ababcacabcbc* stacking sequence of AX_3 layers (Figure 2.5) [28]. The symmetry is described with the $R\bar{3}m$ (164) space group. As in the 6H-perovskite, both the monolayers of corner-sharing $[MX_6]$ octahedra and the $[M'_3X_{12}]$ trimer clusters are arranged in a triangular lattice within the (*a*,*b*)-plane. The positions of the $[MX_6]$ octahedra correspond to the Wyckoff position 3a with site symmetry $\bar{3}m$. The trimer units are formed by the Wyckoff positions 3b and 6c, located in the symmetry sites $\bar{3}m$ and 3*m*. The *A* atoms occupy two 6c positions within the symmetry site 3*m*, while the *X* atoms are located at two 18h positions with *m* symmetry.

There is a wide variety of hexagonal perovskites with different stacking sequences. An overview of the numerous compounds can be found in [43].

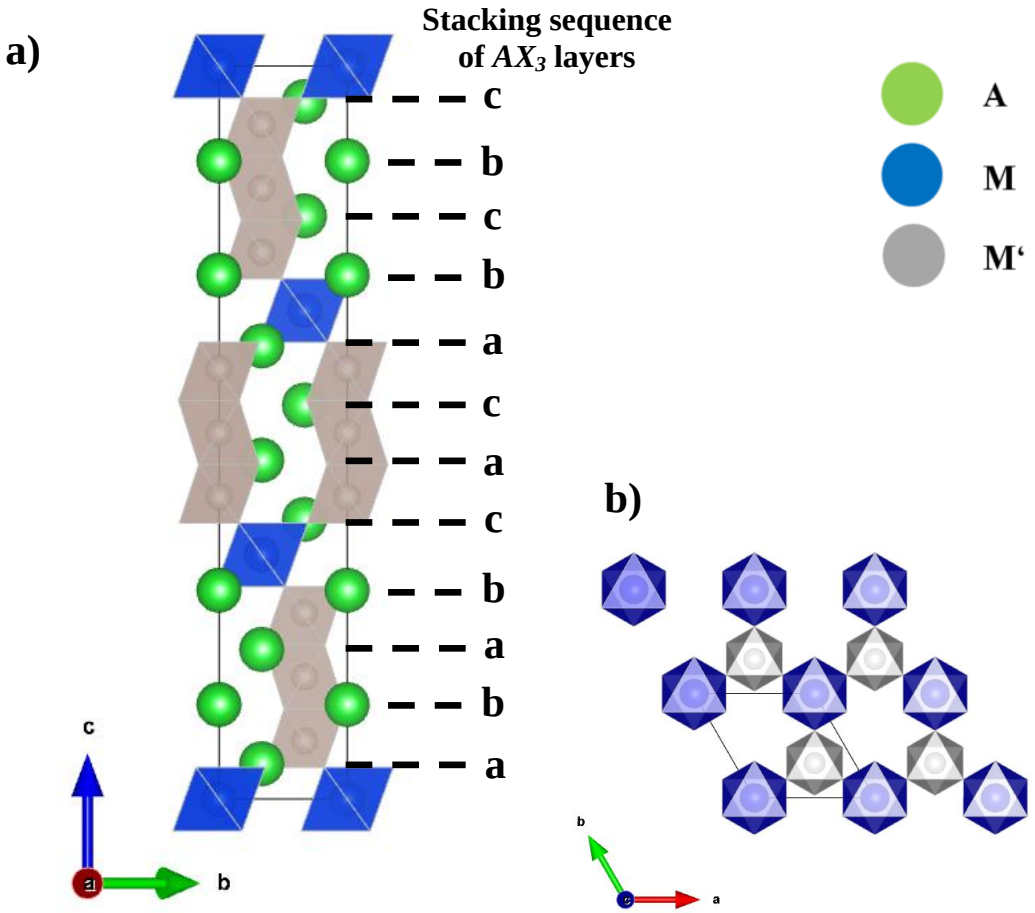

Figure 2.5: a) Illustration of the rhombohedral 12R-perovskite structure with *ababcacabcbc* stacking sequence along the *c*-axis. b) View along the *c*-axis showing [MX_6] and [M'_3X_{12}] units arranged in a triangular lattice within the *ab*-plane. The structural model was taken from [30]. For better visualization of the structure, the *X* atoms have not been depicted; they correspond to the corners of the octahedral units. (Visualization created using VESTA)

2.1.1 6H-Perovskite of the type $Ba_3MM_2'O_9$

The family of 6H-perovskite-type compounds, characterized by a TM ratio of $M : M' = 1 : 2$ is extensive. Therefore, this work focuses on selected representatives containing Ru and Ir. Representative compounds include $Ba_3MRu_2O_9$ with M = Y, La-Lu [44; 45; 29], Ni, Co, Zn [46], and Cu, In, Co, Ni, Fe [47], as well as $Ba_3MIr_2O_9$ with M = Y, La-Lu [48], Mg, Ca, Sc, Ti, Zn, Sr, Zr, Cd, In [49] and Nb [50].
Most of these compounds crystallize in the high-symmetric hexagonal space group $P6_3/mmc$, maintaining the ideal 6H-perovskite crystal structure. However, a subset of $Ba_3MIr_2O_9$ compounds with M = La, Nd, Ca, Sr, Cd, In, Nb, and Ce undergoes a monoclinic distortion, lowering the symmetry to the $C2/c$ space group [48; 49; 50].

The transition from $P6_3/mmc$ to $C2/c$ leads to an increase in the number of unique Wyckoff positions from six to nine, reflecting the symmetry reduction and structural reconfiguration:

- The 2b and 4f Wyckoff positions, corresponding to the two A-site atoms and M'-site atom, change to the 4e (site symmetry 2) and 8f (site symmetry 1).
- The 2a Wyckoff position of the second M atom changes to the 4a position (site symmetry $\bar{1}$).
- The 6h and 12k Wyckoff positions, associated with the two X (here, oxygen) sites, split into one 4e and one 8f position, while the 12k position further splits into three 8f positions.

The monoclinic distortion in these perovskite-derived structures occurs when the radius of the transition metal (TM) cation is incompatible with hexagonal symmetry. As a result, the crystal structure undergoes a small shearing deformation perpendicular to the c-axis. This distortion breaks the sixfold rotational symmetry of the hexagonal structure, resulting in a C-centered Bravais lattice**.** One possible transformation matrix is given in equation 2.2.

$$\begin{pmatrix} a' \\ b' \\ c' \end{pmatrix} = \begin{pmatrix} 1 & 1 & 0 \\ \bar{1} & 1 & 0 \\ 0 & 1 & 1 \end{pmatrix} \begin{pmatrix} a \\ b \\ c \end{pmatrix} \tag{2.2}$$

Additionally, this symmetry breaking is accompanied by a rotation of the octahedra around the monoclinic b-axis and an elongation along the same axis. Due to the connectivity between adjacent octahedral units and dimer clusters, the rotation direction alternates systematically, further stabilizing the monoclinic structure.
This interplay of ionic radius, octahedral tilting, and symmetry reduction highlights the

intricate structural adaptability of 6H-perovskites, making them a compelling system for studying structure-property relationships in transition metal oxides.

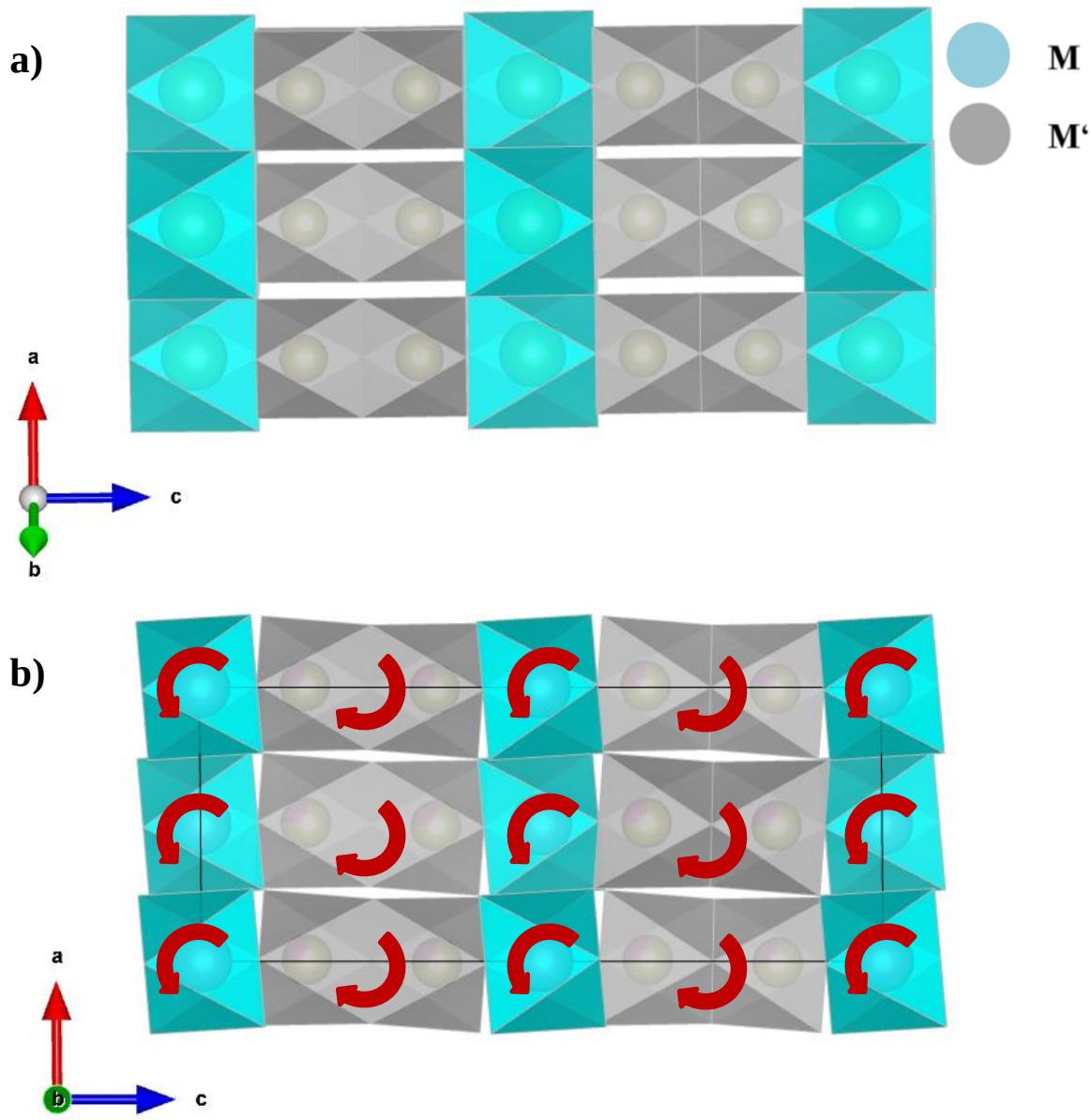

Figure 2.6: a) Shown is the undistorted structure of a 6H-perovskite with the general formula $A_3MM'_2X_9$ in the high-symmetry space group $P6_3/mmc$, exemplified by $Ba_3CeRu_2O_9$ [51]. b) Monoclinic distortions are illustrated resulting in the space group $C2/c$ on the example of $Ba_3InIr_2O_9$ [50]. For better visualization of the distortion, only the MX_6 (blue) and M_2X_9 (gray) units are shown, where the X atoms correspond to the corners of the polyhedra. (Visualization created using VESTA)

2.1.2 12L-Perovskites of the type $Ba_4MM_3'O_{12}$

First mentions in literature of a 12-layered perovskite type structure (12L-perovskite) were placed in 1965 by John M. Longo and Lewis Katzand Roland [52]. They initially described quaternary compounds of the type $A_4^{2+}Re_2^{7+}M^{2+}O_{12}^{2-}$, with A = Ba (M = Mg, Ca, Co, Zn, Cd, In) and A = Sr (M = Mg, Co, Ni, Zn), all exhibiting a transition metal ratio of 2 : 1. These compounds were distinguished by a characteristic structural vacancy at the Wyckoff position 3b, corresponding to the central octahedral position within the trimer units [49]. The first reported 12L-perovskite structure featuring a fully occupied trimer was $Ba_4NbIr_3O_{12}$, synthesized and characterized in 1991 [53]. A major advancement followed in 2008 with the publication of $Ba_4LnRu_3O_{12}$ (Ln = Lanthanide), which exhibited distinct [Ru_3O_{12}] trimers [51]. Shortly after, in 2009, structural data on $Ba_4LnIr_3O_{12}$ (Ln = Lanthanide) were reported, demonstrating analogous structural motifs between the ruthenate and iridate compounds [21]. In 2016, $Ba_4BiIr_3O_{12}$ was successfully synthesized, further expanding the class of known 12L-perovskites [54; 55]. While some perovskite-type materials incorporating Rh, such as $Ba_4NbRh_3O_{12}$, have been synthesized, their number remains limited [56; 57]. Additionally, manganese-based 12L-perovskites, such as $Ba_4MMn_3O_{12}$ (M = Nb, Ta), have been identified, highlighting the structural versatility of this perovskite subclass [58; 59]. A striking feature of these compounds is the prevalence of 4d and 5d transition metals, particularly Ru and Ir, in the trimer units.

$Ba_4NbIr_3O_{12}$ crystallizes in the rhombohedral space group $R\bar{3}m$ (Nr. 166) which is the highest symmetry observed for this type of compounds [53]. As already mentioned, the structure can be understood as a twelve-layer perovskite type structure with trimer units [Ir_3O_{12}] which are separated by a monolayer of corner-charring [NbO_6] octahedra. Further investigation shows, that the trimers are completely occupied by iridium, while the monolayers are occupied by 1/4 iridium and 3/4 niobium [53; 30].
Besides $Ba_4NbIr_3O_{12}$, the ruthenates $Ba_4MRu_3O_{12}$ with M = Tb – Lu also crystallize in the rhombohedral space group $R\bar{3}m$ and are isostructural with $Ba_4NbIr_3O_{12}$ [33; 6]. For $Ba_4M'Ru_3O_{12}$ compounds with M' = La – Gd, the larger ionic radii of the rare-earth elements (REEs) induce a distortion, leading to a crystallization in the monoclinic space group $C2/m$ [51]. The monoclinic distortion leads to the loss of the threefold symmetry axis, a key characteristic of the high-symmetry trigonal phase. As a result, the structure adopts a C-centered Bravais lattice, resulting in a doubling of the unit cell volume. A key consequence of this symmetry reduction is the splitting of Wyckoff positions, which increases the number of occupied sites in the monoclinic phase to 25 distinct Wyckoff positions [6]:

- The 6c Wyckoff positions, corresponding to the two *A*-site atoms and one *M*' atom, split into three 4i positions, each with site symmetry *m*.
- The 3b Wyckoff position of the second *M*' site splits into one 4i and one 2c positions with site symmetry m and 2/*m*.
- The 3a Wyckoff position of the *M* atom splits into one 4i and one 2a position with site symmetry *m* and 2/*m*.
- The 18h Wyckoff positions associated with the two *X* sites each split into three 8j positions and three 4i positions with site symmetry 1 and *m*.

For iridium based compounds $Ba_4MIr_3O_{12}$ with *M* = La – Lu and Bi a similar monoclinic distortion is pronounced, resulting in the same space group symmetry *C*2/*m* [6].
A comparison of both structures reveals the following description of the monoclinic distortion similar to the 6H-perovskite type structure. The monoclinic distortion in these perovskite-derived structures arises when the radius of the transition metal cation is incompatible with trigonal symmetry. In response, the crystal lattice undergoes a shearing deformation perpendicular to the *c*-axis. This distortion breaks the threefold rotational symmetry inherent to the trigonal structure, leading to a C-centered Bravais lattice and an effective doubling of the unit cell. This shearing deformation is further accompanied by a rotation of the octahedra around the monoclinic *b*-axis and an elongation along the monoclinic *a*-axis, particularly affecting the octahedra occupying the 2a Wyckoff position. Due to the structural connectivity between octahedral units and [M_3O_{12}] trimers, the outer trimer units within the *abab* and *bcbc* layers are strongly distorted.

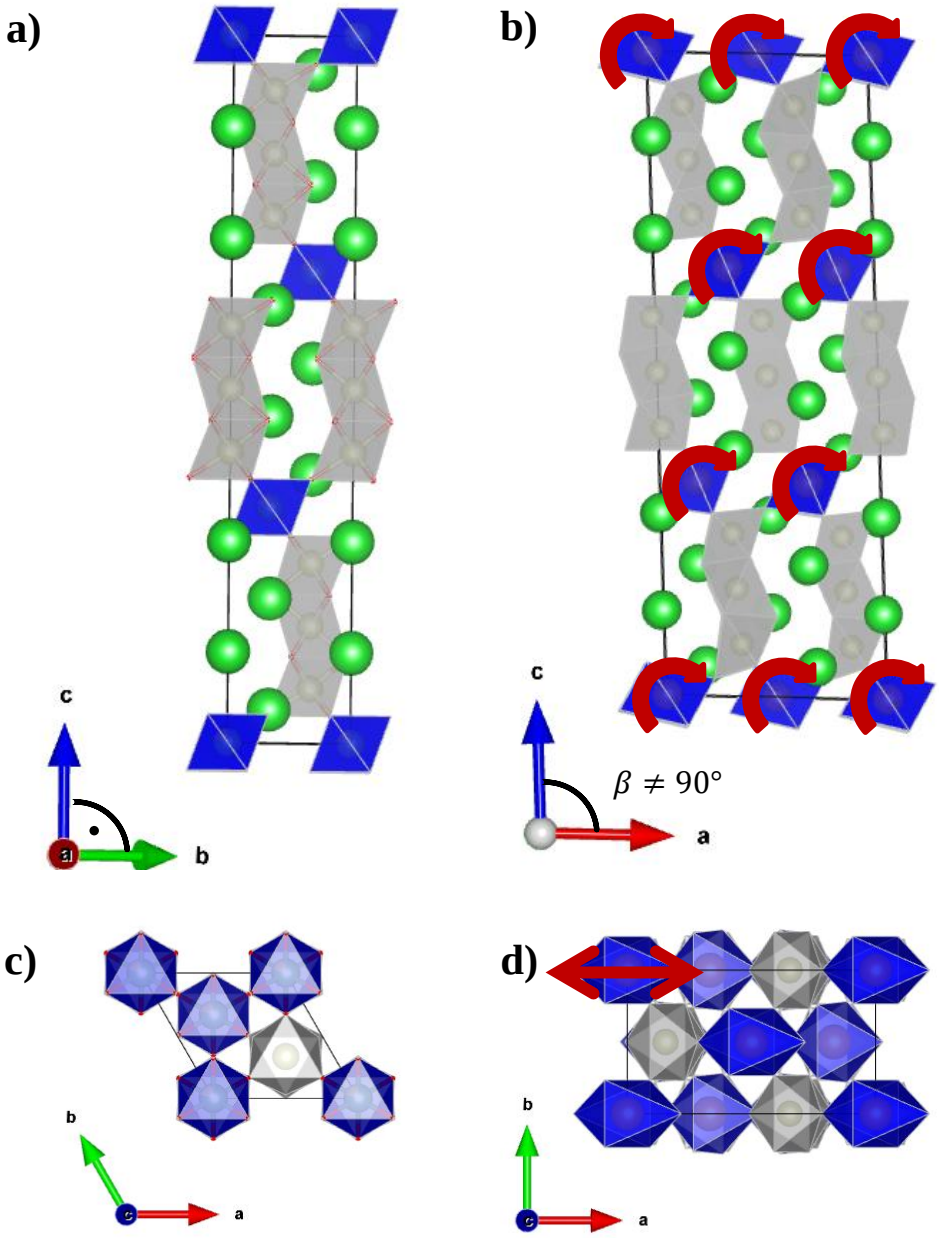

Figure 2.7: a) and c) illustrate the undistorted rhombohedral structure of an $A_4MM'_3X_{12}$ compound, based on the $Ba_4NbIr_3O_{12}$ crystal structure [56]. b) and d) depict the monoclinic distorted structure on the example of $Ba_4EuIr_3O_{12}$ [60]. The rhombohedral structure displays undistorted octahedral units, whereas the monoclinic structure exhibits pronounced distortions, which are highlighted by red arrows. These monoclinic distortions result in an angle $\beta > 90°$. *A* atoms are shown in green, *M* atoms in blue, and *M'* atoms in gray; *X* atoms are not depicted. (Visualization created using VESTA)

3 Methods of characterization

3.1 Structural analysis

Structural analyses were performed using X-ray diffraction experiments. Both powder diffraction (P-XRD) and single-crystal diffraction (SC-XRD) data were collected. Powder diffraction is particularly well-suited for qualitatively identifying crystalline phases and phase mixtures. In addition, the Rietveld refinement method allows for precise determination of lattice parameters and refinement of structural models. Single-crystal data provide significantly more reflections and data points for a crystal, enabling the determination of complete structures. The fundamental principles of crystal structure determination as well as the application of Rietveld refinement are comprehensively described in the literature, for example by W. Massa [61].

Diffraction is based on the fact that crystalline materials can diffract light or particle waves as long as the wavelength is on the same order of magnitude as the unit cell of the crystal. This phenomenon was discovered in 1912 by Max von Laue, Paul Friedrich, and Walter Knipping and described by William Henry Bragg and William Lawrence Bragg by the Bragg equation in 1913 [62].

$$n * \lambda = 2d * sin(\theta) \tag{3.1}$$

- n: the diffraction order (an integer)
- λ: the wavelength of the X-rays
- d: the distance between the lattice planes in the crystal
- θ: the diffraction angle

This equation defines the geometric conditions under which X-rays are scattered by the crystal lattice planes, resulting in constructive interference of the waves. In all other geometries, the X-rays are destructively scattered, with wave crests canceling each other out. The scattering power of a lattice plane is described by the structure amplitude $F(\vec{h})$ [63]:

$$F_{hkl} = \sum_j f_j e^{2\pi i(hxj+kyj+lzj)} * e^{-B_j sin^2 \frac{\theta}{\lambda^2}} \quad (3.2)$$

- f_j: Atomic scattering factor of atom j, dependent on the atom type and X-ray wavelength.
- (x_j,y_j,z_j): Coordinates of atom j in the unit cell.
- B_j: Thermal Debye-Waller factor, which accounts for the thermal vibrations of atom j.
- θ: Scattering angle.
- λ: Wavelength of the X-rays

Through X-ray diffraction, the direct crystal lattice is transformed into reciprocal space, where the reciprocal lattice corresponds to the Fourier transform of the real lattice [61]. The structure amplitude $F(\vec{h})$ is directly related to the electron density distribution within the crystal. Diffraction experiments provide access to the magnitude of the structure amplitude $|F(\vec{h})|$, resulting in the loss of phase information and leading to the well-known phase problem ($|F(\vec{h})|^2 \sim I$) [61]. To address this issue, various approaches exist, with the direct method being the most widely used for inorganic compounds. The direct method relies on mathematical relationships between the measured diffraction intensities and phases to derive the electron density distribution. By leveraging probability theories and phase relationships, it enables the reconstruction of a crystal's atomic structure without prior phase information.

3.1.1 Powder diffraction

P-XRD experiments were carried out on a Bruker D8 Discover diffractometer equipped with an one-dimensional energy dispersive strip detector (LynxEye XE, Bruker) in Bragg-Brentano geometry. The characteristic Kα_1/Kα_2 X-ray radiation from a Cu X-ray tube was used as the source, with a subsequent nickel filter to eliminate the Kβ radiation. Primary and secondary soller slits were fixed to 2.5 ° and the divergence slit was fixed to 0.3 °. The acceleration voltage was set to 40 kV and the heating electricity was set to 40 mA. For low-temperature measurements, a closed-cycle helium cryostat (Oxford PheniX) was employed, enabling measurements under vacuum conditions in a temperature range 300 to 12 K.
To measure small sample quantities, the powder was dispersed in propanol and applied to a zero-background silicon sample holder. This method allows for the straightforward

preparation of flat samples using minimal amounts of material.
For structure refinements, data were collected up to at least 120° in 2θ and refined using the software package DIFFRAC.TOPAS [64]. For phase identification, data were collected up to at least 60° in 2θ, and the peak positions were compared with the ICSD database (version 2024).

Rietveld refinement:

The Rietveld method is a widely used tool for obtaining detailed structural information about a compound. In the following, the theoretical principles of this method are explained in more detail. The Rietveld method involves the refinement of a theoretical diffraction pattern to best match the experimental data by minimizing the difference between the observed and calculated intensities. This is achieved by iteratively adjusting structural parameters such as atomic positions, atomic displacement parameters (ADPs), unit cell dimensions, and site occupancies, as well as instrumental factors like peak shape and background [61]. At its core, the Rietveld method uses a least-squares approach to optimize the agreement between the calculated pattern, derived from a structural model, and the experimental diffraction data [61]. The calculated intensity $y_{calc,i}$ at a point i in the diffraction pattern is derived from the sum of the diffraction intensities of all Bragg reflections at this position [61]. For a reflection hkl, the intensity is determined by the following equation:

$$y_{calc,i} = s \sum_{hkl} L_{hkl} \; | \, F_{hkl} \, |^2 \, \Phi(2\theta_i - 2\theta_{hkl}) \tag{3.3}$$

- s: Scale factor, which sets the proportionality between the measured and calculated intensities, accounting for the experimental conditions.
- L_{hkl}: Lorentz-polarization correction factor, which describes the effect of sample geometry and radiation polarization on the intensity of each reflection.
- $|F_{hkl}|^2$: The square of the structure factor F_{hkl}, which describes the strength of the diffraction signal for the reflection hkl.
- $\Phi(2\theta_i - 2\theta_{hkl})$: Profile function, which describes how the Bragg reflection hkl contributes at a specific angle $2\theta_i$. This function models the intensity distribution around the Bragg angle $2\theta_{hkl}$, often using Gaussian or

pseudo-Voigt functions to account for effects such as instrument broadening and crystal defects.

$$\Phi(x) = \eta L(x) + (1 - \eta)G(x) \tag{3.4}$$

where:

- η: Mixing parameter that indicates the ratio of Lorentzian to Gaussian components.
- L(x): Lorentzian profile.
- G(x): Gaussian profile.

The quality of a refinement is indicated by various values such as R_{Bragg} and the Goodness of Fit (*GOF*). Both values compare the model with the measured data and indicate the agreement.

$$R_{Bragg} = \frac{| I_{obs}(hkl) - I_{calc}(hkl) |}{\sum I_{obs}(hkl)} \tag{3.5}$$

- $I_{\text{obs}}(hkl)$: The observed intensity of the diffraction peak for a given reflection with Miller indices *hkl*.
- $I_{\text{calc}}(hkl)$: The calculated intensity based on the model for the reflection with Miller indices *hkl*.

$$GOF = \frac{R_{wp}}{\sqrt{N_{data} - N_{param}}} \tag{3.6}$$

- R_{wp}: Weighted profile *R*-factor, which is a measure of the difference between the observed and calculated intensities, weighted by their respective uncertainties.
- N_{data}: Number of measured reflections
- N_{param}: Number of parameters refined during the process

3.1.2 Single crystal diffraction

For SC-XRD experiments a single crystal diffractometer Bruker D8 Venture with MoKα radiation with a wavelength of 0.71073 Å was used. To minimize errors, a tunable graphite crystal acts as a monochromator, and the beam is collimated before it reaches the sample. The X-ray tube was operated with an acceleration voltage of 50 kV and a current of 30 mA. The diffractometer is equipped with an Oxford Cryosystem, allowing measurements down to 80 K.

The samples were mounted on a goniometer, which consists of three axes ω, κ, and φ that allow precise orientation of the crystal. The measurement programs were designed to achieve a minimum redundancy of 4 and a completeness of 99.9 %. This ensures that almost all theoretically possible reflections calculated from the unit cell were collected, providing a nearly complete dataset. A redundancy of 4 was chosen to improve the accuracy and reliability of the measured intensities by minimizing the impact of random errors and radiation damage. Furthermore, the resolution was set to 0.44 Å, and the measurements were performed in an angle-dependent manner. This approach was chosen to ensure sufficient intensities and high data quality at higher diffraction angles by allowing for longer exposure times. The Bruker APEX3 suite was used to process the measured dataset [65]. During the integration of the measured reflections, the unit cell was refined. Subsequently, the intensities were scaled according to the corresponding space group, and an absorption correction was applied.

The absorption correction was performed using the Multi-scan method, where multiple measurements of the single crystal are taken from different orientations and angles. This method accounts for the anisotropy of absorption of the crystal, which can change depending on its alignment with the X-ray beam. The intensities of the reflections are corrected based on these different measurements to minimize the impact of absorption on the results. Due to the flat, anisotropic morphology of the crystals, an additional spherical absorption correction was applied. This correction is derived from the product of the absorption coefficient and the smallest measured dimension of the crystal.

The data were scaled in the Laue group $\bar{1}$ to examine all possible distortions in the structure. The structural calculations and further scaling was carried out using the Jana2020 software package [66; 67]. The data quality was assessed by the R_{int} value, which quantifies the internal consistency of symmetry-equivalent reflections:

$$R_{int} = \frac{\sum |F_{obs}^2 - F_{obs}^2(mean)|}{\sum F_{obs}^2} \tag{3.7}$$

where F_{obs}^2 is the measured intensity of an independent reflection (*hkl*), and $F_{obs}^2(mean)$ is the average intensity of all symmetry-equivalent reflections ⟨*hkl*⟩ related by the chosen Laue or point group.

Further important quality indicators to describe the structural model are the R_1 and wR_2 values. A distinction is made between "all data" and "observed data" with $I > 3$ sigma(I). The calculation is equivalent in both cases:

$$R_1 = \frac{\sum\left||F_{obs}^2| - |F_{calc}^2|\right|}{\sum|F_{obs}^2|} \tag{3.8}$$

$$wR_2 = \sqrt{\frac{\sum w(F_{obs}^2 - F_{calc}^2)^2}{\sum w(F_{obs}^2)^2}} \tag{3.9}$$

Distortions and potential symmetry reductions were investigated as follows: An initial structure model was refined in the highest possible symmetry. The ADPs were refined isotropically to keep the number of refined parameters small. After refinement, the structure was transformed into a lower symmetry, and the additional degrees of freedom in the structure were constrained in such a way that the number of degrees of freedom is equal to the higher symmetry. Subsequently, the *R*-values of the refinement from both models were compared to see if the lower symmetry better described the measured data. After that all degrees of freedom of the structure were released, and the ADPs were refined anisotropically.

3.2 Simultaneous thermal analysis

The NETZSCH STA 449 F3 was used to investigate the thermal stability of the materials. This instrument combines thermogravimetric analysis (TGA) and differential scanning calorimetry (DSC), enabling simultaneous measurement of mass change and heat flow. These techniques are essential for determining phase stability and detecting phase transitions, as both mass and enthalpy changes (ΔH) are tracked as a function of temperature.

One of the key advantages of STA lies in its ability to measure multiple physical properties simultaneously. This can provide a more comprehensive understanding of the thermal behavior of the material, and can help to identify correlations between different properties. For example, it may be possible to identify a relationship between the melting point of a material and its heat capacity, or between its enthalpy of transformation and its boiling point.

For the analytic, Al_2O_3 crucibles with lid were used. An empty crucible was used as reference. The sample and the reference crucible were heated in a nitrogen flow as both a flushing and protective gas, with heating a rate of 20 K/min up to 1623 K.
The theoretical principles and practical aspects of STA, including TGA and DSC techniques, are comprehensively discussed in many standard references, such as Gabbott [68].

Differential Scanning Calorimetry (DSC) is a method used to quantify the amount of heat released or absorbed by a substance. The device features two crucible positions, each with a heat sensor underneath. One crucible is filled with the sample material, while the other is used as a reference. Both crucibles are heated at identical heating rates. Due to differences in heat capacity between the sample and the reference, the sample crucible requires a different amount of energy to achieve the same temperature increase as the reference crucible. This energy difference is measured and forms the basis of the signal.
The core of a DSC experiment is the measurement of heat flow into or out of the sample. This flow is governed by the thermal resistance of the system and depends on whether an endothermic or exothermic process occurs. This measured heat flow corresponds to the first derivative of the Gibbs free energy with respect to temperature, i.e., the enthalpy change ΔH. Considering the second derivative of Gibbs energy, $\frac{\partial^2 G}{\partial T^2} = -C_P/T$, yields the heat capacity C_P. Therefore, the slope of the DSC curve provides information about the specific heat capacity C ($\approx C_P \approx C_V$ in solids).

Heat capacity C is a physical quantity that describes the change in temperature of a substance relative to the amount of energy added or removed:

$$C = \frac{\Delta T}{\Delta Q} \tag{3.10}$$

The heat capacity per unit weight or unit amount is referred to as specific heat capacity C. A distinction is made between heat capacities C_P and C_V. C_P describes heat capacity at constant pressure, while C_V applies at constant volume. At C_P, mechanical work is done against the external pressure (thermal expansion), which does not occur at constant volume. Both quantities define the energy required to raise the temperature of 1 kg of a substance by 1 K. The distinction between C_P and C_V is particularly relevant for gases and liquids. In solid phases, the difference between C_P and C_V is negligible, and the approximation $C_P = C_V = C$ can be assumed.

In crystalline substances, heat capacity is largely determined by quantized lattice vibrations, known as phonons. The phonon contribution to heat capacity can be calculated using the Debye model, which will not be further discussed here.

Thermogravimetric analysis (TGA) signal displays the sample's weight with an accuracy of up to 10^{-4} g. This allows decomposition reactions in which a species becomes volatile to be directly observed. The temperature at which a structure begins to decompose is referred to as T_{Onset}.

3.3 Scanning electron microscope / Electron beam microprope

For the chemical analysis, both an electron beam microprobe (EPMA) JEOL JXA-8900RL equipped with a Wavelength-Dispersive X-ray spectroscopy system (WDX) and a Zeiss Sigma 300-VP scanning electron microscope (SEM) equipped with Energy-Dispersive X-ray spectroscopy (EDX) and EBSD detectors were used.
Large crystals were embedded in epoxy resin and polished to create a perfectly planar surface. Crystals that could not be embedded due to their size were mounted on carbon conductive tabs with their well-developed (001) face oriented upwards to ensure the measurement of the flattest possible crystal surface. Due to the lower accuracy of EDX compared to WDX, only the WDX data can reliably provide information about possible substitutions or vacancies.

The fundamental principle is based on the interaction of a sample with a focused electron beam. Electrons are thermally generated at a cathode and accelerated toward the sample by applying an accelerating voltage in a high vacuum. Electromagnetic coils focus the electron beam, allowing for precise measurements with an accuracy of up to 1 µm.
The interaction between the electron beam and the sample varies with sample depth, resulting in a shell-shaped interaction volume, the depth of which correlates with the accelerating voltage. The emitted electrons possess different energies depending on their formation process, and each can be individually detected. The electron energy increases from the Auger process, to secondary electrons, and up to backscattered electrons. Additionally, the atoms in the sample are excited, leading to the emission of element-specific characteristic X-ray radiation, which allows for a quantitative analysis of the composition. Each of these effects is briefly explained below. A detailed describtion of REM and EPMA is given in [69; 70].

Auger Electrons:

Auger electron spectroscopy is a surface-specific analysis technique based on the release of energy during quantum transitions from higher to lower energy levels. The electron beam excites core-level electrons, creating vacancies that are filled by electrons from higher energy levels. The energy difference is emitted as a photon, which can then eject an electron from a lower energy shell. This ejected electron, known as an Auger electron, can be detected.

Secondary Electrons:

Secondary electrons are those ejected from the sample's atomic shells by direct bombardment with the electron beam. This effect mainly occurs near the surface, enabling high-resolution imaging of the sample. Secondary electrons from deeper layers cannot escape the sample and are not detected.

Backscattered Electrons (BSE):

Backscattered electrons (BSE) are generated when electrons from the electron beam interact with the electrostatic field of the atomic nucleus. The positively charged nucleus deflects the negatively charged electrons, causing them to scatter back toward the detector. The extent of deflection is influenced by the atomic number of the nucleus; higher atomic numbers have stronger electrostatic fields, resulting in a greater probability of backscattering. This increased interaction with heavier elements produces a higher intensity of backscattered electrons, making heavier regions appear brighter in the resulting image. BSE imaging is particularly useful for identifying regions with differences in average atomic mass and visualizing compositional heterogeneity or chemical gradients. It is important to note that BSE detection provides qualitative or semi-quantitative information rather than absolute chemical compositions.

Characteristic X-rays:

Characteristic X-ray radiation is element-specific and results from discrete electron transitions from higher to lower energy shells. The electron beam promotes inner-shell electrons, vacancies are created, which are subsequently filled by electrons from higher energy levels. The energy difference between the shells is then emitted in the form of a photon. This radiation can be analyzed either based on its energy (using EDX) or based on its wavelength (using WDX). A detailed description of the methodology as well as a comprehensive discussion of potential error sources can be found in the review article [71]. For both techniques, a perfectly planar surface oriented perpendicular to the electron beam is essential, as the intensity depends on both the surface roughness and the orientation

relative to the electron beam. On rough or inclined surfaces, the penetration depth of the electron beam varies, which directly affects the emitted X-ray radiation. Further effects that are usually accounted for with a ZAF matrix correction include corrections for the atomic number (Z) in the sample, absorption effects (A), and fluorescence effects (F).

- In WDX (Wavelength-Dispersive X-ray Spectroscopy), X-rays emitted from the sample are diffracted by an analyzing crystal according to Bragg's law, allowing for selective detection of specific wavelengths with high spectral resolution (~10 eV). For quantitative analysis, a reference with known concentration must be measured alongside the sample. After matrix correction, the concentration is calculated using the following equation:

$$C_S = \frac{C_R}{I_R} * I_S \tag{3.11}$$

  - C_S = concentration sample
  - C_R = concentration reference
  - I_S = intensity sample
  - I_R = intensity standard

  This method enables quantitative analysis of major elements with a typical relative error of around 1 to 3 wt%.

- In contrast, EDX (Energy-Dispersive X-ray Spectroscopy) uses a semiconductor detector to measure the energy of incoming X-ray photons. No matrix correction is applied here, and the concentration is calculated directly from the measured intensity spectrum of the sample. This method is faster and allows for simultaneous multi-element detection, but has a lower energy resolution and a relative error for major elements of approximately 5–15 wt%.

As already mentioned, it was only possible to prepare WDX samples with polished, flat surfaces from large crystals. Smaller crystals were oriented as best as possible, using smooth growth surfaces perpendicular to the electron beam, and analyzed with EDX. This preparation for EDX analysis is prone to errors, so the lower measurement accuracy is insufficient to draw conclusions regarding substitution effects. Therefore, the EDX analyses in this work were used only to confirm the phase and to examine the homogeneity of the crystal. Due to the lower accuracy of EDX compared to WDX, only the WDX data can reliably provide information about possible substitutions or vacancies.

4 Principles and techniques of single crystal growth

The knowledge of crystal growth and the underlying physical principles is extensive, and cannot be covered in this work. Instead, some fundamental principles will be presented to provide a solid foundation. For a more detailed understanding, reference should be made to literature such as [72; 73; 74].

Crystal growth is a fundamental method in materials science that enables the controlled crystallization of materials with specific physical properties. Crystal growth generally refers to a phase transition resulting in a solid state with a well-defined crystalline structure. This transition can occur between solid-solid, liquid-solid, as well as gas-solid phases. Depending on the phase system and targeted compound, it is the responsibility of the crystal grower to select the best growth method and to determine the optimal growth conditions. In this section, the advantages and disadvantages of solid-state reactions, the flux method and chemical transport reaction method (CVT) are discussed in detail.

4.1 Solid-state reaction method

A solid-state reaction is a chemical process in which the reactants are in the solid state. This means that all atoms are initially arranged within a crystal structure, and activation energy is required to initiate a chemical reaction. As a result, solid-state reactions are typically exothermic, and high temperatures are necessary to enable ion diffusion through the crystal lattices [75].

Volume diffusion of ions occurs primarily via structural defects, such as vacancies or interstitial sites. The reaction usually begins at the grain boundaries of the reactants, where a product phase initially forms as a thin interfacial layer [75]:

$$A_s + B_s \rightleftarrows AB_s \tag{4.1}$$

This reaction layer subsequently grows by volume diffusion of additional ions. The growth rate for volume diffusion follows a parabolic rate law, commonly expressed as [75]:

$$\frac{dx}{dt} = k * x - 1 \tag{4.2}$$

Where x is the thickness of the reaction layer, k is the diffusion coefficient, and t is the reaction time. This indicates that the growth rate is directly dependent on the thickness of the reaction layer. To minimize the thickness of this interfacial layer and to enhance reaction kinetics, solid-state reactions are typically carried out using compacted powders, which maximize the interfacial area between the reactants [75].
In real systems, in addition to volume diffusion, grain boundary diffusion, transport along linear defects and surface diffusion also occur, all of which exhibit significantly higher diffusion coefficients [72]. Furthermore, partial melting and the formation of a gas phase are often observed, both of which can strongly influence the growth rate of the reaction layer [72].

In this study, well-homogenized reactant mixtures were compacted into 10 mL conical Al_2O_3 crucibles closed with an Al_2O_3 lid and sealed with high temperature ceramic glue, Ceramabond 503. In the glue joint between crucible and lid, a 0.1 mm thick capillary of SiO_2 glass was inserted to maintain pressure equilibrium, following a method similar to that described in [76]. The crucibles were heated in a muffle furnace under controlled conditions. Over a period of 24 hours (~45 K/h), the samples were gradually heated to facilitate the decarbonization of $BaCO_3$ and the release of CO_2. Once the target temperature was reached, the reaction proceeded for 40 hours, followed by a gradual cooling to room temperature over an additional 24 hours. The phase composition of the synthesized samples was analyzed via X-ray diffraction to confirm phase and purity.

4.2 Crystal growth from high temperature solution

A detailed description of crystal growth from high-temperature solutions and the underlying theoretical principles can be found in key references such as D. Elwell and H. J. Scheel [73]. In general, a high-temperature solution is defined as a system operating above 574 K [73]. This section focuses on the key fundamentals of crystallization and experimental considerations relevant to the growth of oxide perovskite compounds containing 4d and 5d transition metals.
Crystallization from a melt involves a phase transition from the liquid to the solid state.

This process occurs when the crystallization lowers the Gibbs free energy (G) of the system. Under isobaric conditions, the Gibbs free energy of a phase is described by its enthalpy (H) and entropy (S) and is a function of temperature (T) [74]:

$$G = H - TS \tag{4.3}$$

The temperature at which the Gibbs free energy of the solid phase G_S equals that of the liquid phase $G_S = G_L$, defines the point where both phases coexist in equilibrium and corresponds to the melting point T_m. If the melt is supercooled below T_m, the solid phase becomes energetically favorable, leading to crystallization. The change in free energy ΔG is determined by the energy difference between the two phases:

$$\Delta G = \Delta H - T\Delta S \tag{4.4}$$

Nucleation:

When a high temperature solution or melt becomes supersaturated, for example, due to a change in temperature, the equilibrium phase shifts from a liquid phase L to a solid phase $A + L$. Crystallization occurs spontaneously. Crystallization begins with the spontaneous formation of crystal nuclei. There are many different concepts that describe the process of nucleation. Here, the classical nucleation theory first introduced by J.W. Gibbs [77; 78] is briefly explained.

When a solution is brought out of equilibrium towards the solid state, atoms come together statistically and form bonds. This leads to the formation of clusters of atoms or smaller building blocks, which in turn statistically combine to form larger units. These units can be approximately considered as spheres, whose stability depends on the surface-to-volume ratio, neglecting elastic effects [72].

The formation of a new phase creates a phase boundary, which contributes a positive interfacial term to the Gibbs free energy, denoted as ΔG_S. The surface contribution is proportional to the surface tension σ and the surface area of the nucleus i.e. r^2. Opposing this is the volume contribution ΔG_V which becomes negative under supersaturated conditions. ΔG_V is proportional to the volume of the nucleus r^3 and the molar change in Gibbs free energy Δg_V [72].

$$\Delta G_S = 4\pi r^2 \sigma \tag{4.5}$$

$$\Delta G_V = \frac{4}{3}\pi r^3 |\Delta g_V| \tag{4.6}$$

From this, the total Gibbs free energy change of the nucleation process ΔG_K is given by the sum of the surface and volume contributions [72]:

$$\Delta G_K = \Delta G_S + \Delta G_V \tag{4.7}$$

In Figure 4.1, ΔG_S, ΔG_V, and ΔG_K are shown as functions of the nucleus radius r. It can be seen that, up to a critical nucleus radius r_K^*, the surface energy predominates, making the nuclei unstable. Consequently, nucleation work ΔG_K^* must be applied for spontaneous nucleation to occur [72]. This nucleation work can be regarded as the activation energy for nucleation and is the reason why melts can remain in a metastable, supercooled state. Both r_K^* and ΔG_K^* depend on the degree of supersaturation and decrease with increasing supersaturation [72].

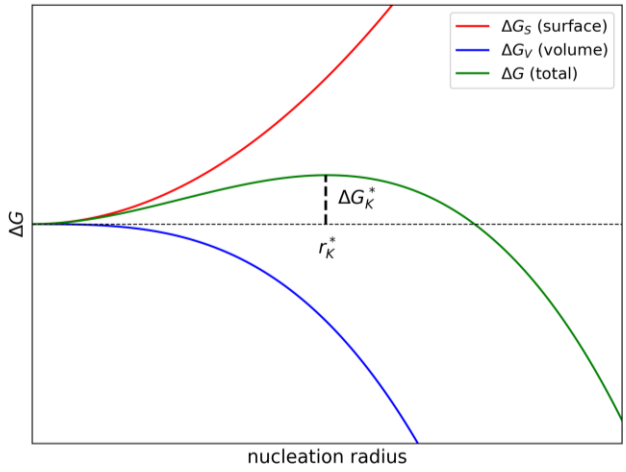

Figure 4.1: Plot of the free Gibbs energy, ΔG, as a function of nuclei radius, r. ΔG_K^* corresponds to the radius of the critical nucleus r_K*. For $r < r_K^*$, the positive free interfacial enthalpy ΔG_S dominates, resulting in an increase of the free energy. Consequently, nuclei are unstable and tend to dissolve. Only nuclei with $r > r_K^*$, where the free volumetric enthalpy ΔG_V overcomes the free interfacial enthalpy, are stable.

Nucleation occurs as a result of statistical thermal fluctuations within the system and is therefore a statistical process. Accordingly, it is useful to consider the nucleation rate J, with A representing the kinetic prefactor [74].

$$J = A * e^{-\Delta G_K^*/K_B T} \tag{4.8}$$

The temperature range in which the nucleation rate is negligibly low, but the supersaturation is already sufficiently high for existing nuclei to grow, is known as the Oswald–Miers range [79]. The solution is in a metastable supersaturation state where

spontaneous nucleation does not occur but crystal growth is possible. This region is used to introduce seed crystals, enabling controlled growth, ideally without the formation of additional nuclei.

A distinction is made between homogeneous and heterogeneous nucleation. When a crystal forms freely in a solution, ΔG_K^* is maximal, and this is referred to as homogeneous nucleation. When a nucleus forms on a secondary phase, such as crucible walls, the crucible bottom or, in the application of epitaxy, on a crystalline substrate, it is termed heterogeneous nucleation [72].
Heterogeneous nucleation can also be described thermodynamically by the contributions of ΔG_S and ΔG_V. In contrast to homogeneous nucleation, where the nucleus is idealized as a complete sphere, the geometry in the heterogeneous case is modified due to contact with a substrate. The nucleus typically forms as a spherical cap on the surface. This altered geometry is taken into account in the calculation of the nucleation work through a geometrical factor *f(θ)*, which depends on the contact angle θ and thus directly on the wettability of the substrate [72]. As a result, the contribution of ΔG_S is reduced by the area in contact with the substrate, significantly lowering the total nucleation barrier for the critical nucleus [72]. Heterogeneous nucleation therefore exhibits a lower energy barrier and is thermodynamically favored. In the context of crystal growth, this implies that efforts are made to reduce the wettability of surfaces in order to suppress heterogeneous nucleation. Wettability is primarily influenced by the choice of crucible material, the surface roughness, and, where feasible, by mechanical stirring to hinder the attachment of nuclei to the crucible walls [72].

Crystal growth:
Crystal growth describes the process of shifting the phase boundary in favor of the crystal, which proceeds continuously once the equilibrium is exceeded and an appropriate potential difference $\Delta\mu$ is given.
The energetic favorability of an atom's incorporation into the crystal structure increases with the number of bonds it can form. Therefore, incorporation on an atomically flat surface is the least favorable process. The most favorable instead is a kink site position, in which the atom has half of the number of neighbors that it would have in the crystal bulk [80]. For this reason, a distinction is made between crystal growth on atomically rough and atomically smooth surfaces.
The concept of crystal growth on rough surfaces was described by Wilson and Frenkel in 1900. On an atomically rough surface, building units can be directly incorporated into a half-crystal layer. This is often described as isotropic growth within the considered plane. It

should be emphasized that due to structural anisotropy, only symmetry-equivalent faces exhibit the same growth rate ν. Consequently, the crystal morphology is dominated by the faces with the lowest growth rates. The growth rate ν of a given crystal plane results from the competing processes of attachment and detachment of building units at the crystal surface. Thermodynamically, this process can be described using the vibrational frequency of the crystal ν^-, that of the nutrient solution ν^+, and the activation energies for incorporation into the crystal Q^+ and for detachment from the crystal Q^- [72].

$$\nu = a\left[\left(\nu^+ e^{-\frac{Q^+}{kT}}\right) - \left(\nu^- e^{-\frac{Q^-}{kT}}\right)\right] \tag{4.9}$$

This implies that, at low undercooling near the equilibrium temperature, the growth rate is proportional to the degree of undercooling. The activation energy Q^+ can, to a first approximation, be considered as the energy required for the bulk diffusion of a building unit from the solution to the crystal. If $Q^- > Q^+$, the difference between these energies approximates the latent heat Φ of crystallization.

The concept of crystal growth of atomic smooth surface was described by W. Kossel in 1927 [80]. Growth on an atomically smooth surface is a complex process that proceeds in a layer-by-layer fashion. Initially, a surface nucleus forms, which then serves as a site for the attachment of additional building units. The energetic consideration of surface nucleus formation is similar to that of homogeneous crystal nucleation [72]. The continued growth occurs in a sequence of intermediate steps, with each step characterized by its own energy barrier and relaxation time. The individual steps were summarized by Elwell and Scheel as follows [73].

1) Transport of solute to the phase boundary via convection and diffusion.
2) Adsorption on the crystal surface (desolvation 1).
3) Diffusion over the surface (surface diffusion).
4) Attachment to a step (desolvation 2).
5) Diffusion along the step (step diffusion).
6) Integration into the crystal at a kink (desolvation 3).

Considering the coupled volume and surface diffusion, the growth rate can be expressed as follows [72]:

$$\nu = \frac{C^{L\infty} - C_e^L}{C^S} * \left(\frac{\bar{\delta}}{D^L} + \frac{1}{K_F}\right)^{-1} \tag{4.10}$$

- C_e^L: saturation concentration in the liquid phase
- $C^{L\infty}$: concentration far from the phase boundary
- C^S: concentration in the crystal phase

Through the incorporation of atoms from the solution into the crystal structure, a concentration gradient develops at the phase boundary. As a result, a diffusion boundary layer forms around the crystal, which must be traversed by further building units via volume diffusion. The thickness of this diffusion boundary layer, denoted as $\bar{\delta}$, depends on the degree of supersaturation, the viscosity of the solution, and convective conditions:

- D^L is the diffusion coefficient in the liquid phase.
- The coefficient K_F represents the overall kinetics of interfacial processes that influence the crystal growth rate.

As follows from equation 4.10, for a high growth rate ν, the thickness $\bar{\delta}$ of the diffusion boundary must be kept as small as possible. This can be achieved by stirring the solution or moving the seed crystal through the solution. It should be noted that in real systems, additional factors such as crystal defects or spiral growth can play a significant role in the crystal growth process [72]. However, these aspects will not be discussed further in this work.

Thermodynamic considerations:

To achieve crystallization of a specific phase, the knowledge of its stability field as a function of thermodynamic parameters such as temperature and chemical composition is essential. Once these conditions are established, the equilibrium can be shifted toward the desired phase, thereby enabling targeted crystallization.

In high-temperature solutions, ions are constantly in motion due to thermal energy and interact with one another through various exchange processes. At equilibrium, a statistical distribution of atomic states is established, where the occupancies of microstates, such as molecular species, bonding states, or quantum states remain constant on average over time [72]. Under these conditions, the macroscopic properties of the equilibrium solution no longer change. The equilibrium state of a system can be described by state variables such as pressure (p), temperature (T), and chemical composition (n) [74].

Graphical representations of state equations produce phase diagrams, which illustrate equilibrium phases typically as a function of T and n [74]. The point at which the melt and

a crystalline phase coexist in equilibrium is referred to as the liquidus line. For successful crystal growth, it is necessary to slightly depress below the liquidus in order to shift the equilibrium toward the crystalline phase. This understanding allows one to select a temperature and chemical profile that minimizes the Gibbs free energy, thereby facilitating the targeted crystallization of a specific phase.

Flux-method:

The so-called flux method (or "high temperature solution growth method") belongs to the group of solution growth methods, where the desired compound is dissolved in a solvent with a chemical composition other than the crystal to be growth. The fundamental principle of the flux method involves transferring a substance into a liquid phase or melt by using a high temperature solvent known as flux. For substances with prograde solubility, a targeted lowering of the temperature can generate supersaturation of the melt with dissolved ions, from which the desired phase subsequently crystallizes. Since the flux component generally has a lower melting point, it crystallizes at a later stage. This enables the selective formation of the target compound from the supersaturated solution.

During the growth of a crystal phase from the melt, heat transport plays a crucial role. As the crystal forms, crystallization heat is released, resulting in a temperature gradient within the crystal. This gradient becomes steeper with increasing thermal conductivity of the solid. A temperature gradient also forms in the melt, particularly at the phase boundary, analogous to the diffusion boundary layer. Since the growth rate is proportional to the degree of undercooling, it reaches its maximum when the temperature gradient within the crystal is high, and the gradient within the melt is low. Under these conditions, the crystallization heat can be efficiently dissipated through the melt or, in the case of the top-seeding method, through the crystal. This maintains a stable undercooled state at the phase boundary, which continuously drives further crystal growth. In contrast, local undercooling can occur when insoluble or weakly soluble species concentrate at the growth front, leading to constitutional undercooling. This promotes morphological instability and results in the formation of an atomically rough surface or even dendritic growth.

The use of a flux can significantly lower the melting point of the educts. Therefore, this method is particularly suitable for phases that melt incongruently, have high vapor pressures, or consist of highly refractory elements. Crystallization is induced by supersaturating the solution, either through cooling or flux evaporation.

The selection of a suitable flux is challenging and requires thorough research as well as a solid understanding of the chemical behavior of the involved components. Some fundamental selection criteria are summarized in [73] as follows:

1. High solubility for the crystal constituents
2. The crystal phase required should be the only stable solid phase
3. Appreciable change of solubility with temperature
4. Viscosity in the range of 1 to 10 centipoises
5. Low melting point
6. Low volatility at the highest applied temperature
7. Low reactivity with the container material
8. Absence of elements which are incorporated into the crystal
9. Ready availability in high purity at low cost
10. Density appropriate for the mode of growth
11. Ease of separation from the grown crystal by chemical or physical means
12. Low tendency of the solvent to "creep" out of the crucible
13. Low toxicity

When selecting a suitable flux, it is essential to ensure that the flux does not act as a reactant and crystallize with the dissolved starting materials into an undesired phase. To avoid such issues, the self-flux method is often preferred. In this approach, a low-melting component of the target system is added in excess and serves as the flux itself. This approach is commonly used for example in metallic systems, such as bismuth-containing compounds, where elemental bismuth (Bi) functions simultaneously as reactant and flux [81]. In addition to flux selection, the crystal growth conditions, especially the temperature profile, must be carefully considered. The flux should be thermally stable and not highly volatile. If volatility is high, appropriate safety measures must be taken, such as using sealed setups or controlled atmospheres. If the self-flux technique is not possible, an external flux must be employed. This is commonly the case for oxide compounds containing refractory elements. If the compound contains an alkali or alkaline earth element, the corresponding halide salt is often used as a flux [73].

After the experiment, the flux must be separated from the crystals in order to isolate them. The key techniques to mention here are dissolution, evaporation, centrifugation or by mechanically isolating the crystals from the melt.

4.3 Crystal growth via chemical transport reactions

Chemical transport reaction (CTR) is a widely employed method for synthesizing high-quality single crystals. One of the primary advantages of this technique is its ability to precisely control the redox state, enabling the synthesis of compounds that may not be attainable through other methods. A detailed description of the technique can be found, for example, in Binnewies et al. [82].

The fundamental principle of the CTR method is based on a chemical reaction of the reactants with a transport agent, forming volatile species. The reaction equilibrium must be slightly shiftable with temperature so that the equilibrium position is not strongly fixed on one side. This makes it possible to transfer a solid phase into the gas phase, transport it along a temperature gradient, and subsequently enable recrystallization [82]. In this process, crystallization occurs directly from the gas phase. The location where the solid phase is dissolved is referred to as the source. The location where the solid phase recrystallizes is referred to as the sink. For an exotherm reaction, the temperature on the source side (T_1) is higher than the temperature on the sink side (T_2), meaning $T_1 > T_2$. In contrast, for an endotherm reaction, the transport direction is inverse, from the lower temperature regime to the higher temperature regime.

For a phase to be effectively transported and crystallized at the sink, the partial pressure *p(i)* of the phase must be sufficiently high, $>10^{-5}$ atm [82]. Most solid compounds exhibit such low partial pressures, even at high temperatures, that the transport rate is insufficient for crystal growth. For this reason, a gaseous reactant, known as a transport agent, is introduced to react with the solid phase, forming a volatile species at manageable temperatures. Typically, halogens or halogen compounds are used as transport agents. A simple transport experiment in a closed system with a solid phase A_s and a transport agent B_g can be described as follows [82]:

$$A_{(s)} + B_{(g)} \rightleftharpoons AB_{(g)} \tag{4.11}$$

The transport agent B_g reacts with the solid phase A_s at the source side to form a volatile species AB_g, which diffuses along a temperature gradient ΔT towards the sink. At the sink, the reaction reverses, resulting in the phase A_s and B_g. The species B_g diffuses back to the source side and reacts again with the solid phase A_s. In this way, the transport agent is essentially recycled, creating a cycle that transports continuously phase A_s from the source to the sink. A schematic illustration of a chemical transport reaction is shown in Figure 4.2.

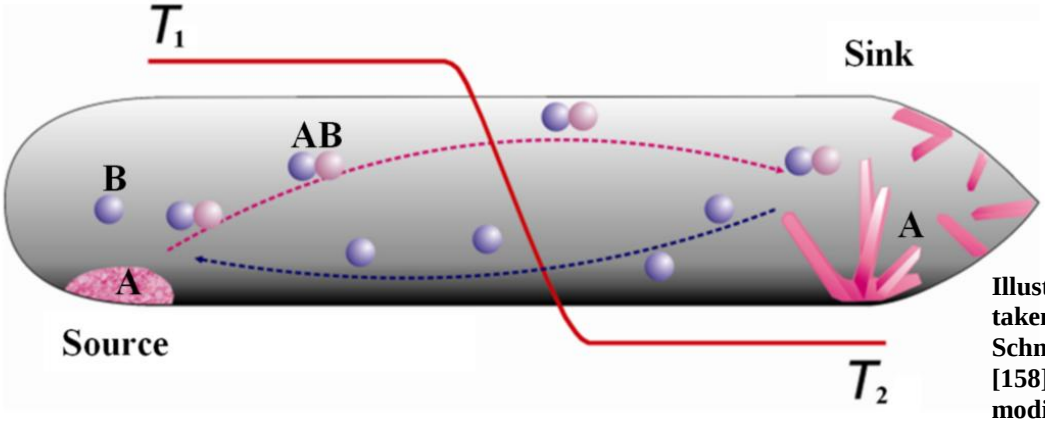

Illustration taken from Schmitt et al. [158] and modified

Figure 4.2: Schematic illustration of a growth experiment using chemical transport in a closed system. The educt *A* at the source side (pink) reacts with the transport gas *B* (blue) at temperature T_1 to form a volatile phase *AB*. This volatile phase diffuses along the temperature gradient (red) to the sink at lower temperature T_2. The reaction reverses and the educt crystallize. The transport gas then diffuses back to the source side, completing the cycle.

In this example, the source and sink solid phases have the same composition, the process is referred to as stationary transport. In a more complex system, the solid phases in the source and sink can differ. In such cases, the process is referred to as non-stationary transport, during which the composition of the source phase inevitably changes over the course of the experiment. For the further description, the focus will be on stationary systems.

In order for a transport reaction to be suitable for crystal growth, two main criteria must be fulfilled. First, all reaction products formed during the forward transport reaction must be gaseous under the given reaction conditions, as illustrated by the reaction equation 4.12:

$$AC_{(s)} + 2B_{(g)} \rightleftharpoons AB_{(g)} + CB_{(g)} \tag{4.12}$$

Second, the equilibrium position of the transport reaction should not be extremely on one side [82]. This specifically means that the free reaction enthalpy $\Delta_r G_0$ should lay between approximately -100 and +100 kJ/mol^{-1} [82]. Otherwise, the equilibrium is too heavily skewed to one side, preventing the back reaction/resublimation into the solid phase ($\Delta_r G_0 <$ -100 kJ/mol^{-1}), or the dissolution of the solid phase is not favored, and the partial pressure is too low ($\Delta_r G_0 >$ 100 kJ/mol^{-1}).

The transport of the gas phase can be described by two mechanisms. If the total pressure exceeds 3 atm, convection is the dominant mechanism. For total pressures below 3 atm, as is commonly applied in transport experiments, diffusion is the prevailing mechanism. To describe a diffusion-controlled transport process, Schäfer presented a model in 1962 [83].

The core assumption of this model is that the diffusion of gaseous species constitutes the slowest step in the overall transport reaction [84]. As a result, the source and sink can be considered independently [84]. At both the source and the sink, a chemical equilibrium is established between the solid phase and the gas phase. The resulting partial pressure difference of the volatile species drives its diffusion through the gas phase, enabling the transport of material.

The transport rate is proportional to the partial pressure gradient $\frac{dp}{ds}$ and the diffusion coefficient D. The diffusion coefficient, in turn, is inversely proportional to the total pressure $\sum p$, resulting in the transport rate being proportional to the ratio $\frac{\Delta p}{\sum p}$. All other influencing factors, such as cross-sectional area, diffusion length, and temperature, can be directly defined through the setup of the transport experiment. A quantitative expression for the transport rate is provided by the Schäfer equation [83]:

$$n'(A) = \frac{n(A)}{t'} = \frac{i}{j} * \frac{\Delta p(C)}{\sum p} * \frac{T^{0.75} * q}{s} * 0.6 * 10^{-4}\ (mol * h^{-1}) \tag{4.13}$$

n'(A) - Transport rate (mol*h^{-1})
i, j - Stoichiometric coefficients in the transport equation
Δp(C) - Partial pressure difference of the transport effective species C (bar)
T - Mean temperature along the diffusion path (K)
q - Cross section of the diffusion path (cm^2)
s - Length of the diffusion path (cm)
t - Duration of the transport experiment (h)

This means, that the equation can be solved if the partial pressures and diffusion coefficient *D* is known. To calculate the equilibrium state at the source and sink, and thus determine the partial pressures, it is necessary to know the standard enthalpy of formation ΔH_f^0, entropy S^0, and heat capacity as function of the temperature Cp^0 of all compounds present in the system.

The thermodynamic data of most binary oxides and halides are well-documented in databases and literature, see e.g. [85]. However, for more complex compounds the thermodynamic data are unknown. These data must be measured experimentally, calculated, or estimated. Estimating the data is the least precise method but is often possible with sufficient accuracy. Estimation can be performed in several ways, as described in detail in the 'Estimation of Thermodynamic Data' section of [82].

The estimation of heat capacity *Cp* follows the Dulong-Petit law and the Neumann-Kopp rule. The Dulong-Petit law states that the molar heat capacity of solid elements at room temperature (298 K) is approximately constant at around 25 J/mol·K per atom. This law primarily applies to simple crystalline solids, particularly metals. The Neumann-Kopp rule extends the Dulong-Petit law to compounds. It states that the reaction entropy $\Delta_R S$ and the change of $C_{p,T}^0$ are close to zero, which allows the calculation of the molar heat capacity and entropy of a solid compound as the sum of the molar heat capacities and entropies of the individual elements that make up the compound. In other words, the heat capacity and entropy of a compound is derived from the sum of the contributions of its constituent elements. These estimated values typically derived in a range of ±8 J mol^{-1} K^{-1} to the experimental determined values. By applying this approach, the calculated values for Cp^0 are more accurate than those obtained using the Dulong-Petit law. Additionally, the Neumann-Kopp rule allows for a temperature-dependent description of heat capacity by following the polynomial expression, with the numerical constants *a*, *b*, *c*, and *d*.

$$C_{p,T}^0 = a + b \cdot T + c \cdot T^{-2} + d \cdot T^2 \tag{4.14}$$

There is no standardized method for estimating enthalpy. One approach is based on the assumption that homologous compounds exhibit similar properties and that these properties, such as enthalpy, follow a trend. If related compounds are known, the enthalpy of the target compound can be estimated based on the behavior of the known related compounds. However, if such data are not available, an alternative approach must be applied. In such cases, the compound can be considered as being composed of simple binary oxides. The mathematical foundation for this approach is provided by Hess's Law:

$$\Delta_R H = \sum \Delta H_{products}^0 - \sum \Delta H_{educts}^0 \tag{4.15}$$

The reaction enthalpy for such a reaction can be approximated as 20 kJ per metal atom. If the thermodynamic data of the binary oxides are known, the formation enthalpy of the targeted compound can be estimated. Based on this, the enthalpy can be calculated as the sum of the enthalpies of the oxide components plus the reaction enthalpy, which is approximately 20 kJ per metal atom in the compound.

CVTRANS

CVTRANS is a computer program developed to numerically solve the Schäfer equation [65], which models diffusion-controlled chemical transport reactions. The core of its functionality lies in an iterative procedure that minimizes the Gibbs free energy of the system to determine chemical equilibrium. According to thermodynamic principles, a system at equilibrium exhibits a minimum in its Gibbs free energy.
The mathematical description presented here follows Lindner 2006 [84]. To calculate the equilibrium state, CVTRANS requires the standard enthalpy of formation, ΔH_f^0, the standard entropy, S^0, and the temperature-dependent heat capacity, Cp^0, for all species involved in the system. Based on these thermodynamic data, the program computes the chemical potentials (μ_i) and evaluates the total Gibbs free energy, which is given by:

$$G = \sum_{i=1}^{N} n_i \mu_i = \min \qquad (\Delta G = 0) \tag{4.16}$$

The Gibbs free energy is minimized under the constraint of mass conservation, which is expressed as:

$$b_j = \sum_{i=1}^{N} a_{ji} n_i = const. \tag{4.17}$$

Here, n_i denotes the molar quantity of species i, μ_i is the chemical potential, b_j the total molar amount of element j, and L is the number of different elements in the system. The number of atoms of element j in species i is given by a_{ji}.

The chemical potential μ_i of each species is calculated as:

$$\mu_i = \mu° RT \ ln \ a_i \tag{4.18}$$

where $\mu°$ is the standard chemical potential, R the universal gas constant, T the absolute temperature, and a_i the activity of species i. For ideal gases, the activity a_i corresponds to the partial pressure $a_i = p_i$, whereas for pure solids and condensed phases, the activity is assumed to be unity ($a_i = 1$).

Since the number of independent variables is typically large and the mass balance constraints impose linear dependencies among them, the minimization is carried out under

equality constraints. These constraints are derived from the elemental balance equation (4.17), which ensures that the total amount of each element remains conserved throughout the reaction. In matrix notation, the mass balance can be expressed as:

$$b = A * n \tag{4.19}$$

where b is the vector of total elemental abundances, A is the stoichiometric matrix whose entries a_{ji} indicate the number of atoms of element j in species i, and n is the vector of unknown molar amounts of all N species.

The constrained minimization problem is then formulated as:

$$\min_{n} \left(G_n = \sum_{i=1}^{N} n_i \mu_i \right) \quad \text{subject to} \quad b = A * n \tag{4.20}$$

This system of equations is typically solved numerically using methods such as the method of Lagrange multipliers or other gradient-based constrained optimization algorithms. These approaches ensure that, at every iteration, the Gibbs free energy is minimized while strictly satisfying the elemental mass balance constraints.

Once the equilibrium state is reached, the partial pressures of the gaseous species are determined via the ideal gas law.

$$p_i = \frac{n_i RT}{V} \tag{4.21}$$

The resulting equilibrium composition and partial pressures serve as input for the Schäfer transport equation. The calculated partial pressure difference Δp determines the transport rate of the solid material. As a practical guideline, a minimum transport rate of 0.1 mg/d is considered necessary for chemical transport to be detectable. For the synthesis of polycrystalline materials, a transport rate exceeding 0.1 mg/h is typically sufficient. However, for single crystal growth, a significantly higher transport rate, usually above 1 mg/hour is desirable [72].

Experimental Setup:

All transport experiments conducted in this work were performed in closed systems. Therefore, silica glass tubes were sealed at one end, while the open end was welded to a glass flange. This is necessary in order to evacuate the ampoule. To facilitate the sealing of the ampoule, the diameter of the glass was narrowed at the desired ampoule length. The ampoules were then dried at approximately 1073 K under high vacuum for several hours to remove water and hydroxyl groups from the SiO_2 glass. The outgassed ampoule was filled in a glovebox with dry argon atmosphere, using a well-homogenized mixture of the pre-synthesized compound (obtained via solid-state reaction) and $PtCl_4$. In the final step, the ampoule was evacuated again and sealed under dynamic vacuum at the narrowed section.

The transport experiment was carried out using a two-zone furnace combined with a transport balance, as described for example by V. Plies et al. 1989 [86] . The setup is shown in Figure 4.3. Two temperature controllers were used to set the temperatures T_1 and T_2, allowing the temperature gradient to be determined. A rail was placed in the furnace opening, balanced by a joint and counterweights. The rail was adjusted so that it rested on a balance, with the length between the balance and the pivot point corresponding to L. When mass transport occurred along the ampoule ΔS, the rail was displaced from its equilibrium position, leading to a change in measured mass m_2. The balance was connected to a computer interface, allowing the weight to be recorded automatically every five minutes. Using the principle of leverage (see equation 4.13), the measured mass could be converted into the actual transported mass m_1:

$$m_1 = m_2 * \frac{\Delta S}{L} \tag{4.22}$$

Due to the presence of the transport balance, the furnace remains open on one side, causing a temperature gradient along the furnace tube axis. To select a suitable position for the growth ampoule within this gradient the furnace temperature was measured at 40 points along the furnace. The measurements were taken at 1 cm intervals in the range between 15 and 55 cm, see Figure 4.3. The recorded temperature profile showed a linear trend between 33 cm and 48 cm, and therefore, the ampoules were placed within this region for synthesis.

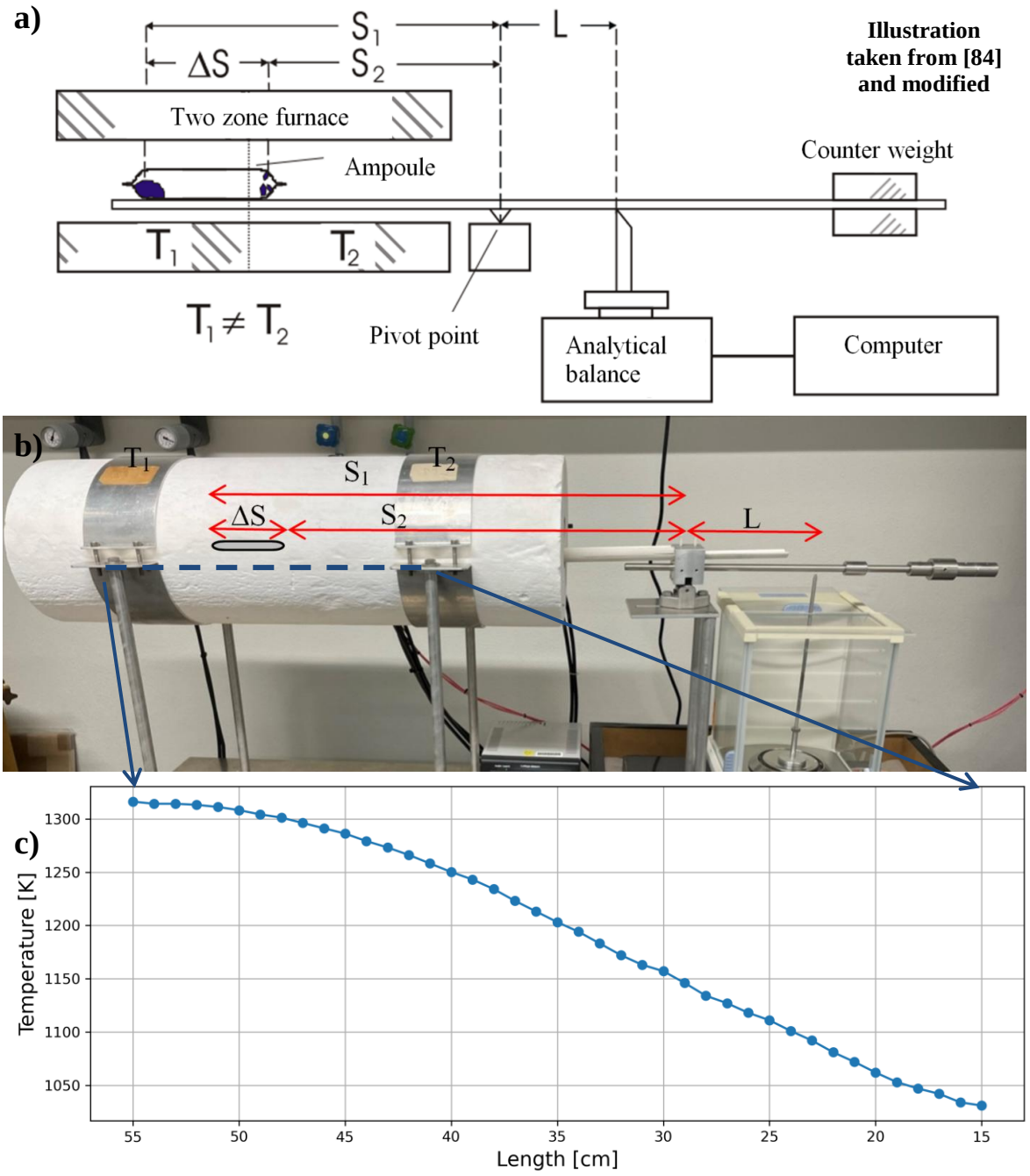

Figure 4.3: a) Schematic setup of a growth experiment using chemical transport in combination with a transport balance. The transport distance ΔS is given by $S_1 - S_2$ and corresponds to the length of the ampoule. L denotes the distance between the joint and the transport balance. b) A photograph of the setup used for crystal growth experiments using CTR, with the characteristic distances indicated as in (a). The blue dashed line marks the region measured at set temperatures of T_1 = 1273 K and T_2 = 1173 K. The temperature profile is shown in (c).

4.4 Crystal growth of 4d and 5d oxides:

Selection of chemical compositions and growth method:

Most hexagonal perovskite cluster compounds reported in the literature are predominantly based on barium occupying the *A*-site, with iridium or ruthenium positioned at the *M*'-site [6; 48; 29]. The large ionic radius of barium appears to stabilize the hexagonal perovskite structure, promoting the formation of [M'_2O_9] dimers or [M'_3O_{12}] trimers by iridium and ruthenium.

Iridium and ruthenium are both transition metals (d-block elements) with Ru being member of group 8 and Ir of group 9 of the periodic table. Their ionic radii, 63 pm for Ir^{4+} and 62 pm for Ru^{4+} in a six-fold coordination environment, are similar, allowing for frequent substitution between the two elements and the formation of isotypic compounds [6]. However, iridium (atomic number Z = 77) is significantly heavier and possesses more electrons than ruthenium (atomic number Z = 44), reflecting its nature as a 5d element compared to ruthenium's 4d classification. The 5d orbitals of iridium are more spatially extended and are subject to stronger relativistic effects, resulting in enhanced covalency in chemical bonding [87]. Additionally, the greater atomic mass leads to markedly SOC compared to the lighter ruthenium [10; 11]. These factors significantly influence the electronic structures and chemical reactivities of both metals as described in Section 1.3.

Both iridium and ruthenium exhibit a broad range of accessible oxidation states. Iridium most commonly adopts the +3 and +4 oxidation states. However, higher oxidation states can also be stabilized in solid compounds, such as +5 in Ba_2YIrO_6 [88]. Under special conditions, even higher oxidation states are attainable, such as +6 in Sr_2NiIrO_6 [89]. Nevertheless, high-valent species are usually unstable under ambient conditions and tend to occur only in molecular or volatile forms [90]. Ruthenium, exhibits oxidation states of +2, +3, and +4, with +3 and 4+ being the most stable under ambient conditions. Compounds with higher oxidation states, such as +5 in Ba_2YRuO_6 [91] are also known for ruthenium, analogous to the corresponding iridium compounds. Higher oxidations states are only realized in in molecular or volatile species.

The oxides IrO_2 and RuO_2 are practically insoluble in water. Although their corresponding chlorides (e.g., $IrCl_3$ or $RuCl_3$) are highly soluble, they cannot be used to access high oxidation states (e.g., Ir^{4+} or Ir^{5+}) that are characteristic for perovskite-type oxides. Such higher oxidation states are only thermodynamically stable under oxidizing conditions at elevated temperatures [92]. This implies that the crystal growth of oxidic perovskite-type structures from aqueous solution is not feasible, as the necessary thermodynamic conditions cannot be fulfilled under such conditions.

At elevated temperatures, both elements can react with oxygen to form volatile IrO_3 and

RuO_3 species. IrO_3 reaches a vapor pressure of approximately 10^{-5} atm at around 1473 K, making it highly effective for transport processes [76]. In comparison, RuO_3 achieves the same vapor pressure at about 1573 K, indicating that ruthenium is less volatile under similar conditions [76]. The volatility at elevated temperatures has been exploited to synthesize ternary compounds, such as Li_2IrO_3 and Li_2RuO_3, via chemical transport reaction [76].

In perovskite-type compounds such as those discussed here, the *A*-site is occupied by barium, as its large ionic radius 135 pm contributes to the stabilization of the hexagonal perovskite crystal structure [38]. Unlike the more volatile alkali metals, alkaline earth metals exhibit significantly lower volatility, which further decreases with increasing atomic number. Barium and barium oxide are thus characterized by a highly refractory nature, making them unsuitable for CTR under standard synthesis conditions.
BaO is highly hygroscopic and readily reacts with atmospheric moisture, forming $Ba(OH)_2$. Therefore, $BaCO_3$ is typically used as a more stable starting material. $BaCO_3$ undergoes thermal decomposition at approximately 1200 K according to the following reaction [93]:

$$BaCO_{3(s)} \rightleftarrows BaO_{(s)} + CO_{2(g)} \tag{4.23}$$

For the reasons outlined above, the flux method represents the most suitable method for the crystal growth of perovskite compounds.

After addressing the selection of elements for the *A*-site and *M'*-site, attention must now be given to the *M*-site as well as the choice of flux.

Elements of particular interest for the *M*-site include trivalent, tetravalent and pentavalent metals, such as In, Sc, the rare earth elements, as well as the transition metals Nb and Ta.
The rare earth elements (REEs) include the 15 lanthanides from lanthanum (La) to lutetium (Lu). They are characterized by similar chemical behavior across the series and a most common +3 oxidation state. Other oxidation states such as +4 are mainly known for cerium, terbium, and praseodymium, while +2 is typical for europium, ytterbium and samarium. Their preferred coordination environment is octahedral, which ensures good compatibility with perovskite-type structures. In a six fold coordination ionic radii range from 103 pm for La^{3+} to 86 pm for Lu^{3+}. This gradual decrease in ionic size across the series is a result of the well-known lanthanide contraction. The contraction results from the increasing nuclear charge across the lanthanide series, coupled with the poor shielding efficiency of the 4f electrons. As a result, the effective nuclear attraction experienced by the outer electrons increases, which leads to a continuous reduction in both atomic and ionic

radii from lanthanum to lutetium.
The transition metals niobium (Nb) and tantalum (Ta) are characterized by a preferred +5 oxidation state. Although both exhibit relatively small ionic radii (~68 pm), niobium in particular is well-established in the literature as being compatible with the hexagonal perovskite framework [56; 50]. In contrast to the highly refractory REEs, Nb and Ta form volatile chloride and oxochloride species, such as $NbCl_5$ and $NbOCl_3$ [94; 95]. By introducing elements with different valence states at the *M* position, the oxidation state of Ru and Ir at the *M'* position and thus the number of electrons per dimer or trimer can be selectively modified. This tuning of structures is currently of great interest in the field of materials science and has already been described for similar compounds [1; 34].

Selection of the flux:
As outlined in the Section 4.2, the choice of a suitable flux is important and a critical aspect of crystal growth. In the present case, the self-flux method is not applicable, as all relevant starting materials exist in oxidic form and either exhibit melting points exceeding 1773 K or undergo thermal decomposition before melting. Moreover, no low-lying eutectics are known in the corresponding phase diagrams. Consequently, the use of a flux of composition which deviates from the educts is required.
The solubility of the reactants in fluxes poses a significant limitation in the selection of suitable fluxes. Since the educts exhibit prograde solubility behavior, only fluxes that remain thermally stable at high temperatures are suitable. This criterion is met primarily by halide-based melts, which, although offering only limited solubility for oxides (typically around 1%) [72], remain the only viable option for such systems, as no better alternative has been found to date.

Among the available fluxes, barium chloride ($BaCl_2$) has proven particularly effective and is frequently employed in the synthesis of perovskite-type single crystals containing Ba on the *A* site [30; 2; 96]. $BaCl_2$ offers several advantages: apart from chlorine, it introduces no foreign elements into the system, thereby minimizing the risk of contamination. Its melting point of approximately 1233 K provides sufficient thermal stability for the dissolution and crystallization of refractory oxide phases. In addition, the low viscosity of halide melts (typically 1–5 cP) [72] promotes efficient convection and diffusion, both of which are essential for controlled crystal growth.

However, in addition to its limited solubility for oxides, $BaCl_2$ also presents certain drawbacks. Above its melting point, $BaCl_2$ exhibits an increased tendency to volatilize [97]. Furthermore, literature sources report that $BaCl_2$ undergoes partial decomposition at high

temperatures, during which BaO is formed and molecular chlorine (Cl_2) can be released. Therefore, appropriate safety measures must be implemented to ensure that significant amounts of volatile species do not escape uncontrollably during the synthesis process. Although $BaCl_2$ is not an ideal flux due to its limitations, no superior alternative is currently available for the synthesis of oxide-based perovskite compounds.

The flux $BaCl_2$ is hygroscopic under ambient conditions and typically exists as $BaCl_2 \cdot 2H_2O$. The structural water is released in two steps with a mass loss of ~7.89 % at 423 K and further 7.12 % at 453 K [97]. Upon further heating, $BaCl_2$ undergoes a phase transition to β-$BaCl_2$ at approximately 1193 K [98] and subsequently melts at around 1233 K [74]. Above its melting point, $BaCl_2$ increasingly decomposes and volatilizes, resulting in a mass loss of approximately 50 % at 1552 K at a heating rate of 10 K/min, followed by an additional volatilization step of around 10 % [97]. At 1673 K, only about 24 % of the original mass of $BaCl_2 \cdot 2H_2O$ remains [97]. $BaCl_2$ is highly soluble in water, with a solubility of 357 g/L, which allows the flux to be dissolved after crystallization in order to isolate the poorly soluble perovskite oxide crystals, which are not attached by H_2O.

Experimental Setup:

Different setups were used for the crystal growth experiments. For safety reasons, it was crucial to minimize the release of volatile species such as $BaCl_2$ into the atmosphere. The reactants were thoroughly mixed with the flux and placed into Al_2O_3 crucibles. Depending on the sample amount, mainly cylindrical Al_2O_3 crucibles with dimensions of 60 mm in height and 39 mm in diameter, as well as conical crucibles with dimensions of 30 mm by 25 mm, were used. Furthermore, the furnace volume was purged with argon gas to create an inert atmosphere. However, this had no observable effect on the crystallization process or the volatility of different species.

In the simplest approach, the Al_2O_3 crucibles were sealed with a ceramic glue Ceramabond 503 (Kager GmbH), into which a 0.1 mm glass capillary was embedded to allow for pressure equalization.

In an alternative setup, the sealed crucibles were placed inside a second protective crucible, which was also sealed. This could influence the crystal growth, as the double sealing may establish a different atmosphere within the crucibles. To further vary the atmospheric conditions, the volume of the protective environment was increased by enclosing the crucibles within a sealed Al_2O_3 box that occupied the entire furnace volume. This containment box consisted of two Al_2O_3 trays (15 × 15 × 8 cm), separated by a 1.5 mm thick layer of silica ceramic paper. The use of silica ceramic paper was essential to facilitate

the separation of the box halves after the experiment. The box was securely sealed using Ceramabond 503 to ensure a controlled environment.

To verify the uniformity of the temperature distribution within the furnace, a temperature profile was established, see Figure 4.4. The furnace chamber was measured at 1373 K through 16 individual measurements. The results revealed a temperature deviation of less than 12 K with measured temperatures 30 K above the set point temperature, confirming a highly uniform temperature profile suitable for reliable crystal growth.

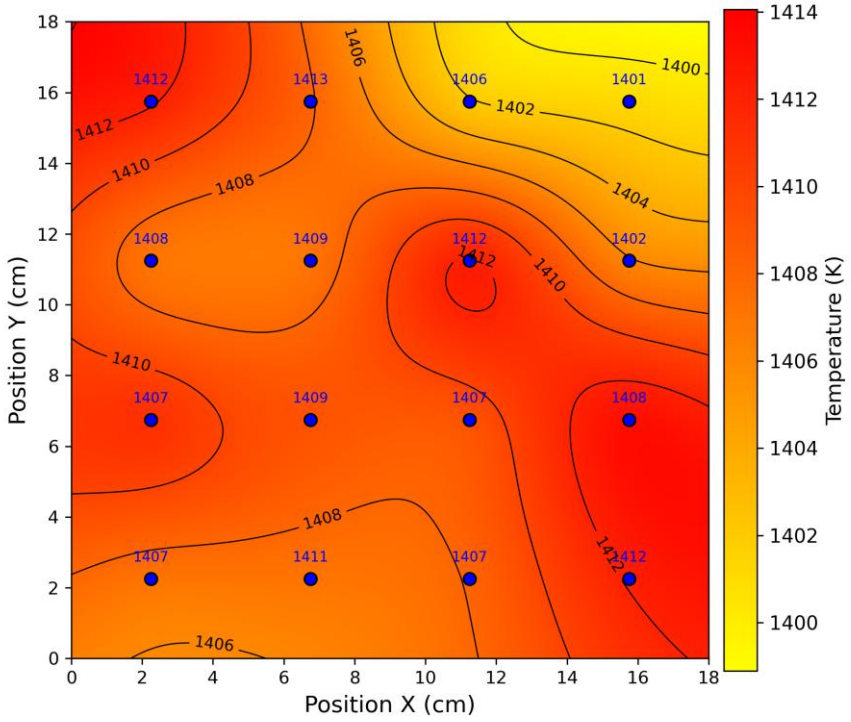

Figure 4.4: Temperature distribution of the muffle furnace at a set-point of 1373 K. The measured temperatures are shown in blue and have been interpolated across the entire plot area, representing the muffle zone, for better illustration.

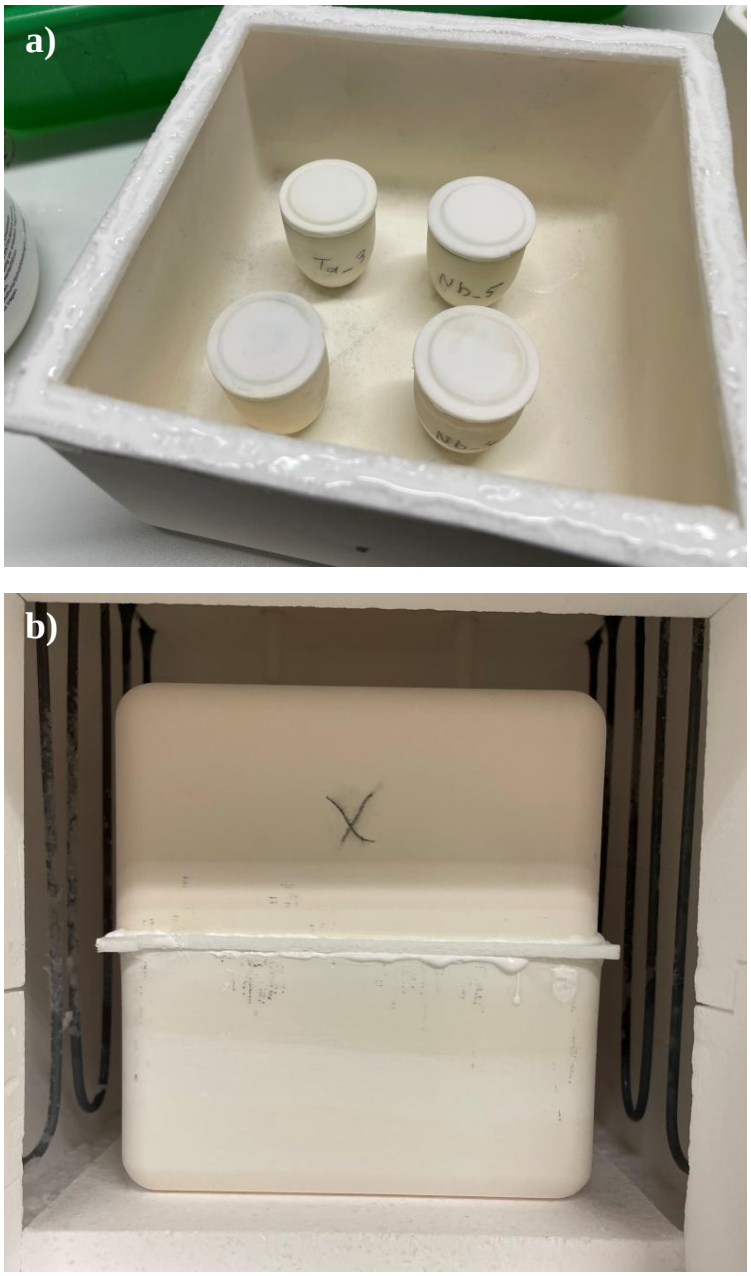

Figure 4.5: a) Four 10 mL Al_2O_3 crucibles covered with a loose fitting lid are placed in an Al_2O_3 tray, with the edges covered by high-temperature paper and ceramic glue. b) Closed and sealed Al_2O_3 box inside the muffle furnace.

Chemicals:

The laboratory chemicals utilized for the crystal growth experiments conducted in this work.

chemicals	Producer	Specifications	Batch number
$BaCO_3$	ChemPur	99.99 %	190504
CeO_2	AUER-REMY K.-G.	99.9 %	-
RuO_2	Alfa Aesar	99.95 %	-
	Sigma-Aldrich	99.9 %	MKCT3525
Lu_2O_3	chemPUR	99.99 %	221298
IrO_2	chemPUR	99.9 %	004513
	chemPUR	99.9 %	110123
	Alfa Aesar	99.99 %	Y13G079
Nb_2O_5	Heraeus Feinchemikalien und Forschungsbedarf GmbH	99.9 %	-
Ta_2O_5	H. C. Starck GmbH	99.9 %	20010864
Eu_2O_3	Alfa Aesar	99.99 %	B21N37
Pr_6O_{11}	chemPUR	99.9 %	310105
$BaCl_2$-*$2H_2O$	VWR chemicals	>99 %	20D214110
Tb_4O_7	chemPUR	99.99 %	191203
Yb_2O_3	chemPUR	99.999 %	70703
Sc_2O_3	-	99.99 %	-
Y_2O_3	CERAC	99.9 %	X8760
NiO	Alfa Aesar	99,998 %	24025
In_2O_3	chemPUR	99.99 %	250806
Sb_2O_5	Alfa Aesar	99.998 %	W05E043
PtCl4	Alfa Aesar	99.99%	M30E065

5 Crystal growth investigations

In this section, the investigation of oxidic ternary systems containing either Ir or Ru as platinum group elements is presented. The focus is on the crystal growth of perovskite-type compounds with the general formulas $Ba_3MM'_2O_9$ and $Ba_4MM'_3O_{12}$, which serve as model systems for studying the interplay between strong spin–orbit coupling (SOC) and molecular orbital formation, as discussed in the Sections 1 and 2. In addition, the presence of magnetic ions such as Ir^{4+} and Ru^{3+} with $S = 1/2$ enables magnetic ordering phenomena at low temperatures. These systems are currently of significant scientific interest, as they serve as key model materials for exploring the interaction between localized physical phenomena and itinerant electronic behavior [1].

High-quality single crystals are essential for precise structural characterization and for enabling subsequent measurements of physical properties.

The methodology and information on the chemicals used are described in Section 4. Phase analysis was carried out using P-XRD, with experimental data compared to reference structures from the ICSD database (2024). The measured diffraction patterns, along with calculated reference patterns, are provided in Appendix A. Minor discrepancies between measured and calculated reflections arise from slight differences in lattice parameters. For compounds not included in the database, reference structures of isotypic and chemically related compounds were used, or powder patterns were simulated based on single-crystal structure data determined in the present study.

5.1 Iridium based systems

5.1.1 $BaO – Eu_2O_3 – IrO_2$

In the $BaO–Eu_2O_3–IrO_2$ system, the perovskite compounds Ba_2EuIrO_6 [42], $Ba_3EuIr_2O_9$ [48], and $Ba_4EuIr_3O_{12}$ [28] are documented in literature and have been successfully synthesized via solid-state reaction. Ba_2EuIrO_6 and $Ba_3EuIr_2O_9$ were obtained using $BaCO_3$, Eu_2O_3, and IrO_2 as starting materials [42; 48]. For Ba_2EuIrO_6, the synthesis conditions are not fully reported, but the addition of $BaCl_2$ has been shown to promote the growth of single crystals [42]. The formation of $Ba_3EuIr_2O_9$ is reported to occur at temperatures between 1373 and 1573 K [48]. The compound $Ba_4EuIr_3O_{12}$ was synthesized from a stoichiometric mixture of $BaIrO_3$, Eu_2O_3, BaO, and BaO_2. The reaction was carried out in a platinum crucible, sealed within a vacuum-closed glass ampoule, and held at 1523 K for 36 hours [28]. Due to the detection of $Ba_3EuIr_2O_9$ impurities in the product, which suggests volatilization of Ir and Ba during the reaction, a 30 % excess of $BaIrO_3$ was added in order to suppress the formation of this secondary phase [28].

Solid state reaction experiments and thermal analysis:

Since no phase diagram of the $BaO–Eu_2O_3–IrO_2$ system is known, this system was experimentally investigated using solid-state reaction experiments as described in Section 4.1.

A stoichiometric composition for the trimer phase $Ba_4EuIr_3O_{12}$ i.e. $BaCO_3 : Eu_2O_3 : IrO_2 = 4 : 0.5 : 3$, reacted at 1573 K to resulted in the formation of $Ba_3EuIr_2O_9$, while the same composition reacted at 1373 K formed $Ba_4EuIr_3O_{12}$. This indicates that the trimer phase is unstable at high temperatures and that the stability of the dimer phase prevails. To verify this observation, approximately 50 mg of $Ba_4EuIr_3O_{12}$ was examined with STA analysis in an Al_2O_3 crucible, closed with a loosely fitting lid. The DSC data revealed the onset of decomposition at approximately 1453 K, marked by distinct changes in heat capacity and a weight loss shown in the TGA signal (see Figure 5.1). Subsequent P-XRD analysis of the sample heated to 1473 K confirmed the partial decomposition of $Ba_4EuIr_3O_{12}$ to the dimer phase $Ba_3EuIr_2O_9$ (see Figure 5.2). The dimer phase $Ba_3EuIr_2O_9$ decomposes at even higher temperatures, but no melting was observed up to 1673 K.

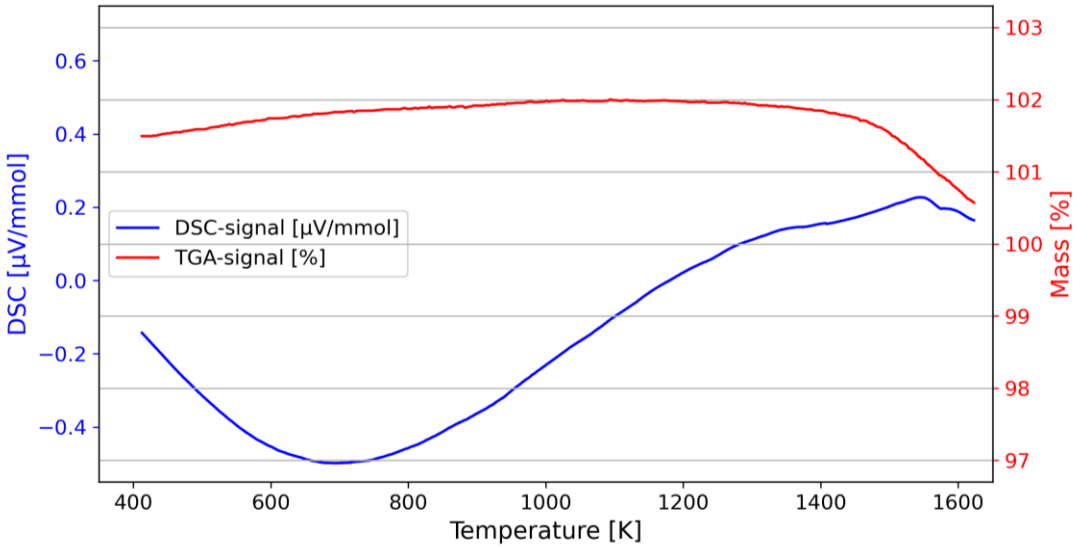

Figure 5.1: TGA signal in red and DSC signal in blue of a $Ba_4EuIr_3O_{12}$ sample measured up to 1673 K at a heating rate of 20 K/min. It can be observed that at a T_{onset} temperature of approximately 1453 K, a reaction occurs in both the TGA and DSV signals.

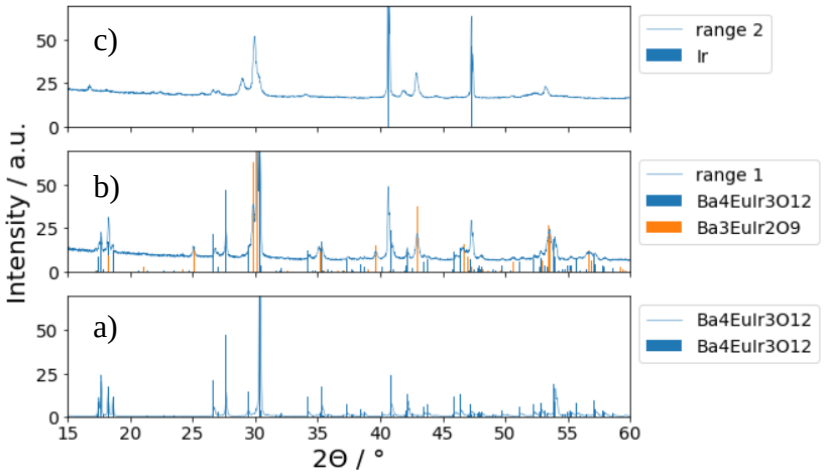

Figure 5.2: XRD data of a $Ba_4EuIr_3O_{12}$ sample before heating (a), after heating to 1473 K (b), and after heating to 1673 K (c). The crystal structure data used for reference powder patterns (vertical lines) taken from [60; 48].

Based on these findings, all subsequent solid state experiments were conducted at 1373 K to ensure the stability of the trimer phase. The samples were heated to 1373 K over a 20-hour period, followed by a 40-hour dwell period at the same temperature. Subsequently, the furnace was turned off and the samples were cooled to room temperature. The specific compositions used for these experiments are listed in Table 5.1, and the results are summarized in Figure 5.3.

The compositional phase diagram derived from these experiments is characterized by four stability fields:

1. Single-Phase $Ba_4EuIr_3O_{12}$ (Figure 5.3: Yellow range):
   This field corresponds to the stoichiometric composition of the trimer phase, indicating its stability within a narrow compositional range.
2. Single-Phase $Ba_3EuIr_2O_9$ (Figure 5.3: Red range):
   Extending from the stoichiometric composition toward a barium and iridium excess with an approximate ratio of 2:1.
3. $BaIrO_3$ + $Ba_4EuIr_3O_{12}$ (Figure 5.3: Blue range):
   This stability field appears when the barium-to-iridium ratio is around 1.6, resulting in a phase mixture of $BaIrO_3$ and $Ba_4EuIr_3O_{12}$.
4. $Ba_4Ir_3O_{10}$ + $Ba_4EuIr_3O_{12}$ (Figure 5.3: Green range):
   When the barium-to-iridium ratio is reduced to approximately 1.3, the simultaneous occurrence of $Ba_4Ir_3O_{10}$ and $Ba_4EuIr_3O_{12}$ is observed.

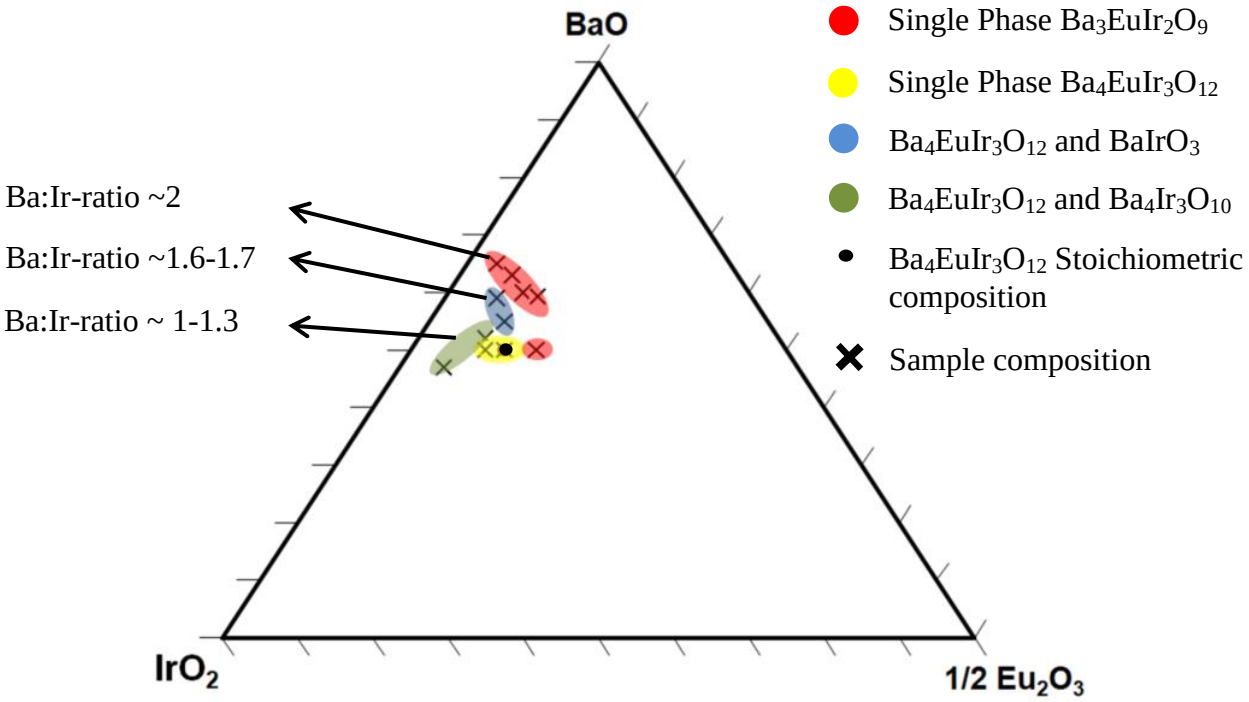

Figure 5.3: Ternary plot of all solid state experiments of the system BaO – IrO_2 – Eu_2O_3. Four distinct regions can be identified, each representing different phase fields characterized by their Ba to Ir ratio.

Sample Nr.	Educts (molar ratio)			T_{max} [K]	Products
	$BaCO_3$	Eu_2O_3	IrO_2		
IREU0	4	0.5	3	1573	$Ba_3EuIr_2O_9$
IREU1	7.833	0.5	7.833	1373	$Ba_4Ir_3O_{10}$ + $Ba_4EuIr_3O_{12}$
IREU2	16.25	0.5	7.75	1373	$Ba_3EuIr_2O_9$
IREU3	9	0.5	4.28	1373	$Ba_3EuIr_2O_9$
IREU4	8.43	0.5	4.86	1373	$BaIrO_3$ + $Ba_4EuIr_3O_{12}$
IREU5	5.778	0.5	4.33	1373	$Ba_4Ir_3O_{10}$ + $Ba_4EuIr_3O_{12}$
IREU6	4	0.5	3	1373	$Ba_4EuIr_3O_{12}$
IREU7	5.5	0.5	3.5	1373	$BaIrO_3$ + $Ba_4EuIr_3O_{12}$
IREU8	6	0.5	3	1373	$Ba_3EuIr_2O_9$
IREU9	4.8	0.5	2.3	1373	$Ba_3EuIr_2O_9$
IREU10	5	0.5	4	1373	$Ba_4EuIr_3O_{12}$
IREU11	3	0.5	2	1373	$Ba_3EuIr_2O_9$

Table 5.1: Chemical composition of all solid state experiments in the $BaO–Eu_2O_3–IrO_2$ system.

Flux invetsigations:

Before proceeding with the crystal growth experiments, the flux behavior of the system was analyzed. For this purpose, a sample with the molar composition 4 $BaCO_3$: 0.5 Eu_2O_3 : 3 $BaIrO_3$: 7 $BaCl_2{\cdot}2H_2O$ was heated to 1473 K. During this experiment, three distinct reaction steps were observed at elevated temperatures of approximately 1003 K, 1043 K, and 1073 K (see Figure 5.4). To further investigate these reactions, the experiment was repeated with new samples, which were heated to 1023 K, 1063 K, and 1093 K, respectively. After each heating, the samples were analyzed using P-XRD to determine their phase composition.

Initially, $BaCl_2{\cdot}2H_2O$ was observed to release its water content in two distinct steps at approximately 423 K and 453 K [97]. These dehydration events were clearly resolved in both the DSC and TG signals. The observed mass loss closely matched the calculated H_2O mass content of 6.62 %.

The next reaction step occurred around 653 K, which aligns with the decomposition of $Ba(ClO_3)_2$, a species likely formed during heating and dehydration. This decomposition is represented by the following reaction, and it accounts for the minor mass loss detected in the TGA signal [99]:

$$Ba(ClO_3)_2 \rightleftarrows BaCl_2 + 3O_2 \tag{5.1}$$

At approximately 1003 K, the first prominent endothermic peak at elevated temperatures

appeared in the DSC signal. This peak is attributed to the reaction of $BaCl_2$ with $BaCO_3$ to form $Ba_3Cl_4CO_3$:

$$2 * BaCl_2 + BaCO_3 \rightleftarrows Ba_3Cl_4CO_3 \quad (5.2)$$

$Ba_3Cl_4CO_3$ was first described in 1967 and synthesized by a solid-state reaction between $BaCl_2$ and $BaCO_3$ at 1123 K [100; 101]. Under the experimental conditions used here, this reaction clearly occurs at a lower temperature. P-XRD analysis confirmed the formation of $Ba_3Cl_4CO_3$ in the sample heated to 1023 K.

Subsequent reaction steps were not fully resolved, but analysis of the sample heated to 1043 K revealed the formation of $Ba_3EuIr_2O_9$, accompanied by residual Eu_2O_3, $BaCO_3$, $BaIrO_3$, and $Ba_3Cl_4CO_3$.

Further distinct signals appeared at approximately 1063 K and 1073 K. These reactions were accompanied by a mass loss, which continued as the temperature increased. The first peak, around 1063 K, is likely due to the thermal decomposition of $Ba_3Cl_4CO_3$ with the release of CO_2. The calculated initial CO_2 content is 4.6%, which is about 3% higher than the observed mass loss. This discrepancy suggests incomplete reaction of $BaCO_3$ to form $Ba_3Cl_4CO_3$, consistent with the detection of $BaCO_3$ in the sample heated to 1043 K.
The sharp peak at 1073 K is attributed to the formation of a melt. While the melting point of pure $BaCl_2$ is known to be 1235 K [98], it appears to be significantly lowered in this multicomponent system. No melting point was observed at 1233 K, indicating that melting occurs at a lower temperature. The gradual mass loss following the melting peak is attributed to the volatile behavior of $BaCl_2$ melt, which has also been reported for pure $BaCl_2$ [98].
P-XRD analysis of the sample heated to 1073 K revealed the presence of $Ba_3EuIr_2O_9$, $BaCO_3$, $BaIrO_3$, and $BaCl_2$ in the final composition.

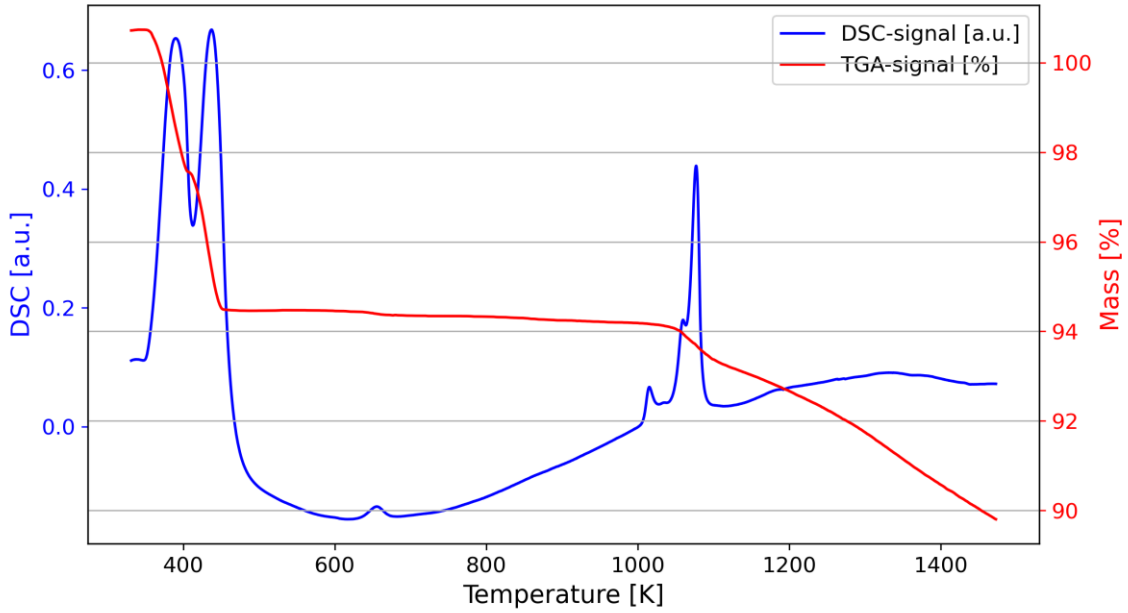

Figure 5.4: Shown is the STA signal of a sample with the molar composition 4 $BaCO_3$: 0.5 Eu_2O_3 : 3 $BaIrO_3$: 7 $BaCl_2{\cdot}2H_2O$. The TGA signal is shown in red and the DSC signal in blue. Several reaction steps can be observed during heating, initially, dehydration of $BaCl_2{\cdot}2H_2O$ occurs, followed by the decomposition of $Ba(ClO_3)_2$ at approximately 653 K. Around 1003 K, $Ba_3Cl_4CO_3$ forms, which decomposes again at around 1043 K. Finally, the melting peak of $BaCl_2$ is observed at 1073 K.

Crystal growth investigations:

The BaO–Eu_2O_3–IrO_2 system was further investigated through two different synthesis approaches, distinguished by their choice of starting materials. In the first approach (S-ID 1-28), $BaCO_3$, Eu_2O_3, and IrO_2 were used, while in the second (S-ID 29-38), $BaCO_3$, Eu_2O_3, and $BaIrO_3$ served as starting materials. Unless otherwise specified, Ir and Eu were combined in a 3 : 1 molar ratio. All experimental parameters and results are summarized in Table 5.2 and Table 5.3.

S-ID 1-6: In the first two experimental series, IrO_2 : Eu_2O_3 : $BaCO_3$ were combined in a molar ratio of 3 : 0.5 : x with x = 4.5, 7.0 and 10, respectively, and subsequently mixed with $BaCl_2{\cdot}2H_2O$ in relative molar amounts of 2 and 3, respectively. The applied temperature program was inspired by conditions for iridate compounds synthesized via $BaCl_2$ flux methods in literature. For example, $Ba_4Ir_3O_{10}$ has been successfully grown at 1673 K and 1733 K [102; 103]. In the present work, the samples were heated to 1673 K and cooled to 1073 K at a rate of 4.1 K/h.

In all samples with a crystal : flux ratio of 1 : 3 (S-ID 1-3), a phase mixture of IrO_2 and

$EuAlO_3$ was observed. The same phase composition was detected in S-ID 4 with relative molar amount of 4.5 $BaCO_3$ and a crystal : flux ratio of 1 : 2. $EuAlO_3$ crystallized with cube-shaped morphology and was chemically analyzed via EDX (see Figure 5.5). The presence of aluminum is attributed to leaching from the alumina crucibles, supported by severe corrosion observed at the crucible bottom. The extent of crucible degradation increased with rising $BaCO_3$ and $BaCl_2$ contents, confirming earlier findings from 1989 on the reactivity of $BaCO_3$/BaO with Al_2O_3 in the presence of $BaCl_2$ flux [104]. Samples containing $BaCO_3$ in relative molar amounts of 7.5 and 10, along with 2 molar equivalents of $BaCl_2$ flux (S-ID 5 and 6), predominantly yielded $Ba_3EuIr_2O_9$, accompanied by minor amounts of $Ba_4EuIr_3O_{12}$.

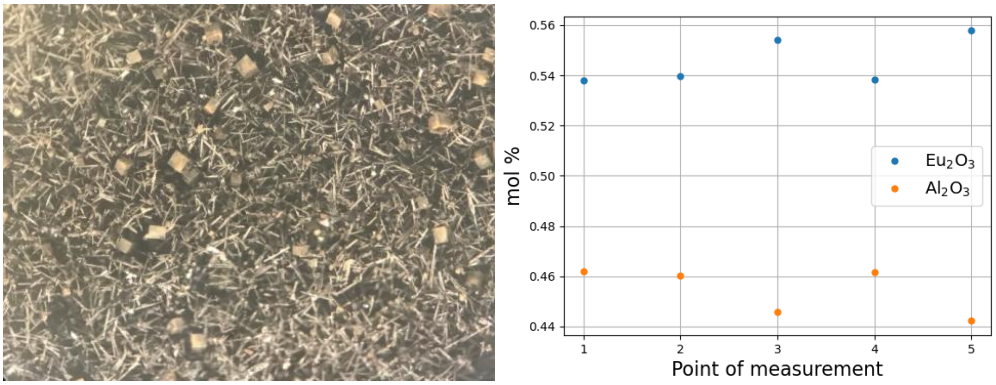

Figure 5.5: a) Cube-shaped $EuAlO_3$ crystals with needle-like intergrown IrO_2 crystals observed in experiment S-ID 1. b) EDX analysis of a cube-shaped $Eu_{1+x}Al_{1-x}O_3$ crystal.

S-ID 7-18: Follow-up syntheses were conducted at a reduced temperature of 1573 K. At a crystal : flux ratio of 1 : 2.2, all samples crystallized as $Ba_3EuIr_2O_9$ (S-ID 7-11). When the flux content was increased to 2.5 relative molar amounts and the $BaCO_3$ content was set to 4.5 and 7 relative molar equivalents, a mixture of $EuAlO_3$ and IrO_2 was observed (S-ID 12 and 13). In contrast, the sample containing 9.5 relative molar equivalents of $BaCO_3$ yielded IrO_2 along with a compound whose P-XRD pattern matched the cubic double perovskite Ba_2PrIrO_6 (ICSD database), strongly suggesting the formation of cubic Ba_2EuIrO_6 (S-ID 14). The same phase combination was detected in samples with crystal : flux ratio 1 : 3 and a $BaCO_3$ content of 7 relative molar equivalents (S-ID 16). In comparison, samples with an increased $BaCO_3$ content of 9.5 relative molar equivalents predominantly formed $Ba_3EuIr_2O_9$ (S-ID 17). Based on the observation that $Ba_3EuIr_2O_9$ forms preferentially at lower flux content, whereas no reaction between $BaCO_3$ and IrO_2 or Eu_2O_3 is observed at higher flux levels, the hypothesis was formulated that $BaCO_3$ primarily reacts with $BaCl_2$. This implies that the formation of perovskite phases is only possible when the flux content is low, or the $BaCO_3$ content is sufficiently high.

S-ID 19–28: To further investigate the proposed hypothesis, the crystal-to-flux ratio was reduced to 1 : 1.8. Under these conditions, $Ba_3EuIr_2O_9$ consistently formed as the primary phase for approaches with a nominal molar fraction of $BaCO_3$ between 4.5 and 6.5. In some cases, minor quantities of $Ba_4EuIr_3O_{12}$ were detected. For an increased $BaCO_3$ contend the primary phase changed to $Ba_4EuIr_3O_{12}$ (S-ID 23 and 24). Attempts to reproduce this result were disrupted by the crystallization of $Ba_5(PO_4)_3Cl$. The crystallization of $Ba_5(PO_4)_3Cl$ is caused by the ceramic glue used and was studied in more detail in the $BaO–CeO_2–IrO_2$ system.

As $BaCl_2$ was found to react with $BaCO_3$ and promote aluminum dissolution from the crucible, the system can no longer be considered ternary. Instead, $BaCl_2$ must be regarded as a reactive component, effectively making the system quaternary. This complexity is further increased by crucible interactions, introducing aluminum as an additional component and thereby expanding the system to quinary.
When considering all experiments, the trend indicates that a higher $BaCO_3$ content combined with a lower $BaCl_2$ content favors the formation of $Ba_4EuIr_3O_{12}$. It appears that $BaCO_3$ is consumed by its reaction with $BaCl_2$, rendering it unavailable to react with IrO_2 and Eu_2O_3. This depletion of barium causes a barium deficiency, resulting in the formation of $Ba_3EuIr_2O_9$ instead of $Ba_4EuIr_3O_{12}$. This means, that $BaCl_2$ is necessary to promote melt formation and facilitate single-crystal growth, whereas an excess of barium carbonate is required to enable perovskite phase crystallization. To address this issue, IrO_2 was replaced by $BaIrO_3$, thereby introducing a barium-containing component that is presumably less reactive with $BaCl_2$.

S-ID	Educts (molar ratio)				Total weight [g]	Time to T_{max} [h]	T_{max} [K]	Time at T_{max} [h]	T_{min} [K]	Rate [K/h]	Products identified by P-XRD
	$BaCO_3$	Eu_2O_3	IrO_2	$BaCl_2 \cdot 2H_2O$							
1	4.5	0.5	3	3	1	30	1673	24	1073	4.1	IrO_2 + $EuAlO_3$
2	7.5	0.5	3	3	1	30	1673	24	1073	4.1	IrO_2
3	10	0.5	3	3	1	30	1673	24	1073	4.1	IrO_2
4	4.5	0.5	3	2	1	30	1673	24	1073	2.1	IrO_2 + $EuAlO_3$
5	7.5	0.5	3	2	1	30	1673	24	1073	4.1	$Ba_3EuRu_2O_9$ + $Ba_4EuIr_3O_{12}$
6	10	0.5	3	2	1	30	1673	24	1073	4.1	$Ba_3EuRu_2O_9$ + $Ba_4EuIr_3O_{12}$
7	5.25	0.5	3	2.2	1	24	1573	24	1073	4.1	$Ba_3EuRu_2O_9$
8	6	0.5	3	2.2	1	24	1573	24	1073	4.1	$Ba_3EuRu_2O_9$
9	6.5	0.5	3	2.2	1	24	1573	24	1073	4.1	$Ba_3EuRu_2O_9$
10	7	0.5	3	2.2	1	24	1573	24	1073	4.1	$Ba_3EuRu_2O_9$ + X
11	7.5	0.5	3	2.2	1	24	1573	24	1073	4.1	$Ba_3EuRu_2O_9$ + $Ba_4EuIr_3O_{12}$
12	4.5	0.5	3	2.5	1	24	1573	35	1073	2.1	IrO_2 + $EuAlO_3$
13	7	0.5	3	2.5	1	24	1573	35	1073	2.1	IrO_2 + $EuAlO_3$
14	9.5	0.5	3	2.5	1	24	1573	35	1073	2.1	Ba_2EuIrO_6 + IrO_2
15	4.5	0.5	3	3	1	24	1573	35	1073	2.1	IrO_2 + $EuAlO_3$
16	7	0.5	3	3	1	24	1573	35	1073	2.1	Ba_2EuIrO_6 + IrO_2
17	9.5	0.5	3	3	1	24	1573	35	1073	2.1	$Ba_3EuRu_2O_9$
18	4.5	0.5	3	15	1	24	1573	20	1073	4.1	IrO_2
19	4.5	0.5	3	1.8	1	24	1573	20	1073	4.1	$Ba_3EuRu_2O_9$ + $Ba_4EuIr_3O_{12}$ + X
20	5.25	0.5	3	1.8	1	24	1573	20	1073	4.1	$Ba_3EuRu_2O_9$
21	6	0.5	3	1.8	1	24	1573	20	1073	4.1	$Ba_3EuRu_2O_9$ + $Ba_4EuIr_3O_{12}$
22	6.5	0.5	3	1.8	1	24	1573	20	1073	4.1	$Ba_3EuRu_2O_9$ + $Ba_4EuIr_3O_{12}$
23	7	0.5	3	1.8	1	24	1573	20	1073	4.1	$Ba_4EuIr_3O_{12}$ + $Ba_3EuRu_2O_9$
24	7.5	0.5	3	1.8	1	24	1573	20	1073	4.1	$Ba_4EuIr_3O_{12}$ + $Ba_3EuRu_2O_9$
25	7.5	0.5	3	1.8	1	24	1573	20	1073	4.1	$Ba_3EuRu_2O_9$ + $Ba_5(PO_4)_3Cl$
26	8	0.5	3	1.8	1	24	1573	20	1073	4.1	$Ba_3EuRu_2O_9$ + $Ba_5(PO_4)_3Cl$
27	9	0.5	3	1.8	1	24	1573	20	1073	4.1	$Ba_3EuRu_2O_9$ + $Ba_3EuRu_2O_9$ + $Ba_5(PO_4)_3Cl$
28	10	0.5	3	1.8	1	24	1573	20	1073	4.1	$Ba_3EuRu_2O_9$ + $Ba_4EuIr_3O_{12}$+ $BaIrO_3$

Table 5.2: Growth conditions of all crystal growth experiments in the $BaO–Eu_2O_3–IrO_2$ system using the educts $BaCO_3$, Eu_2O_3, IrO_2 and $BaCl_2 \cdot 2H_2O$. An "X" indicates a phase that was clearly visible in the powder pattern but could not be identified.

S-ID 29-38: $BaIrO_3$ was synthesized by conventional solid-state reaction at 1573 K and employed as a substitute for IrO_2. This substitution was intended to increase the overall barium content by introducing a pre-synthesized phase with reduced reactivity toward the flux. The results of this experimental series are summarized in Table 5.3.

A general trend emerged in which $Ba_4EuIr_3O_{12}$ appeared in higher quantities in certain compositions or crystallized alongside with $BaAlO_2$ (S-ID 30). Even slight compositional variations altered the stability fields and led to different phase assemblages. Additionally, the crystallization of an unidentified phase was observed. This phase appeared in experiments S-ID 10, 19 and 32. However, no consistent chemical correlation could be established between the experimental conditions and the appearance of this unknown phase.
It also became apparent that the substitution of IrO_2 with $BaIrO_3$ does not lead to consistent results either, as long as additional $BaCO_3$ is introduced into the system. The reaction between $BaCO_3$ and the flux $BaCl_2$ proceeded uncontrollably, complicating the maintenance of accurate barium stoichiometry and ultimately hindering reproducibility under these conditions.

Building on the improved outcomes with $BaIrO_3$, the experimental approach was further refined by using pre-sintered $Ba_4EuIr_3O_{12}$ as the starting material without additional $BaCO_3$. The reaction temperature was reduced to 1373 K, and the amount of flux was increased to promote melt formation. Since no additional $BaCO_3$ was added, significant crucible interactions were not observed. Reactions were carried out in 50 mL Al_2O_3 crucibles, sealed within alumina boxes. This strategy aimed to foster crystal growth under chemically stable and well-defined conditions.
After flux removal, the resulting crystals were identified as $Ba_4EuIr_3O_{12}$. Most crystals measured less than 100 µm, with one specimen reaching approximately 200 µm, see Figure 5.6.

S-ID	Educts (molar ratio)				Total weight [g]	Time to T_{max} [h]	T_{max} [K]	Time at T_{max} [h]	T_{min} [K]	Rate [K/h]	Products identified by P-XRD
	$BaCO_3$	Eu_2O_3	$BaIrO_3$	$BaCl_2 \cdot 2H_2O$							
29	1.5	0.5	3	2	1	20	1573	24	1073	16	$Ba_3EuRu_2O_9$ + $BaIrO_3$ + $Eu_2Ir_2O_/$
30	4.5	0.5	3	2	1	20	1573	24	1073	16	$Ba_4EuIr_3O_{12}$ + $BaAl_2O_4$
31	4.5	0.5	4	2	1	20	1573	24	1073	16	$EuO/Eu_2Ir_2O_7$ + Ir + $BaIrO_3$
32	4.5	0.5	5	2	1	20	1573	24	1073	16	$BaIrO_3$+ $Ba_3EuRu_2O_9$ + Ir + X
33	4.5	0.5	3	15	1	24	1573	24	1073	3	IrO_2 + Ir
34	10	0.5	3	2.5	1	24	1573	24	1073	4.1	$BaIrO_3$+ $Ba_3EuRu_2O_9$
35	4.5	0.5	3	200	10	24	1573	24	1073	4.1	IrO_2 + Ir
36	4.5	0.5	3	2.5	1	24	1573	24	1073	4.1	$Ba_4EuIr_3O_{12}$ + $Ba_3EuRu_2O_9$ + $BaIrO_3$
37	4.5	0.5	4	2.5	1	24	1573	24	900	4.1	$Ba_4EuIr_3O_{12}$

S-ID	Educts (molar ratio)		Total weight [g]	Time to T_{max} [h]	T_{max} [K]	Time at T_{max} [h]	T_{min} [K]	Rate [K/h]	Products identified by P-XRD
	$Ba_4EuIr_3O_{12}$	$BaCl_2 \cdot 2H_2O$							
38	1	30	10	24	1373	24	1173	1	$Ba_4EuIr_3O_{12}$ + $BaIrO_3$

Table 5.3: Growth conditions of all crystal growth experiments in the $BaO–Eu_2O_3–IrO_2$ system, using the educts $BaCO_3$, Eu_2O_3, $BaIrO_3$/$Ba_4EuIr_3O_{12}$ and $BaCl_2 \cdot 2H_2O$. An "X" indicates a phase that was clearly visible in the powder pattern but could not be identified.

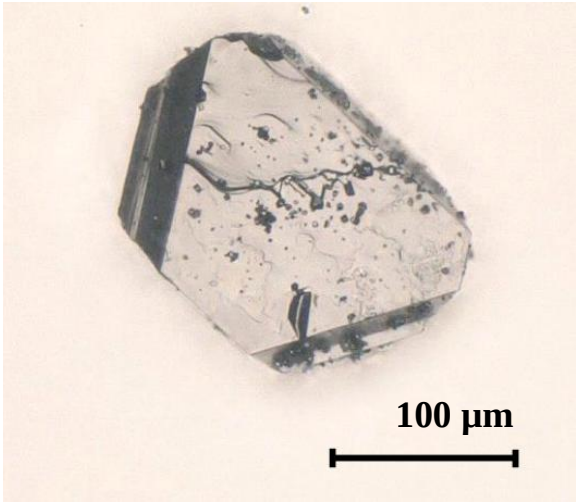

Figure 5.6: Image of a $Ba_4EuIr_3O_{12}$ single crystal taken from experiment with S-ID 38. After dissolving the flux with distilled water, the crystal could be mechanically detached from the crucible bottom.

5.1.2 $BaO – CeO_2 – IrO_2$

Perovskite type compounds of the type Ba_2CeIrO_6, $Ba_3CeIr_2O_9$ and $Ba_4CeIr_3O_{12}$ have been reported in the $BaO–CeO_2–IrO_3$ system [48; 28]. The synthesis of powder samples was performed analogously to the Eu-based perovskite type phases [48; 28]. Single crystals of Ba_2CeIrO_6 and $Ba_3CeIr_2O_9$ were successfully grown from a $BaCl_2$ flux (crystal-to-flux ratio 1 : 15), using CeO_2, IrO_2, and $BaCO_3$ as starting materials in stoichiometric composition [105].
This study investigated the influence of different pre-synthesized phases, IrO_2 (S-ID 1-4), $BaIrO_3$ (S-ID 5-12), $BaCeO_3$ (S-ID 13-16), $Ba_3CeIr_2O_9$ (S-ID 16-23), and $Ba_4CeIr_3O_{12}$ (S-ID 24), on the crystallization behavior. In addition, various crucible shapes and crucible materials were examined to assess their influence on the growth process.

Solid state reaction experiments:
A composition of $BaCO_3$, CeO_2 and IrO_2 corresponding to $Ba_4CeIr_3O_{12}$ was heated to 1573 K over 20 hours and held at that temperature for 40 hours. As observed in the equivalent system with europium, the dimer phase $Ba_3CeIr_2O_9$ formed under these conditions. The same composition processed at 1373 K resulted in the formation of single phase $Ba_4CeIr_3O_{12.}$ This suggests that the system behaves similarly to the europium-based system, where the dimer phase represents the high-temperature phase. $Ba_3CeIr_2O_9$ was also formed from stoichiometric composition at 1373 K.

Crystal growth experiments:
S-ID 1–4: In the first four experiments, $BaCO_3$, CeO_2, and IrO_2 were used as starting materials (see Table 5.4). Experiments S-ID 1 and 2 were conducted with a crystal-to-flux ratio of 1:15 at 1573 K. Under these conditions, the high flux content combined with a lower $BaCO_3$ content primarily led to the crystallization of IrO_2. This behavior is similar to what was observed in the $BaO–Eu_2O_3–IrO_2$ system, where this reaction likely causes a barium deficiency that inhibits the crystallization of perovskite phases.
In contrast, experiments S-ID 3 and 4 employed a crystal-to-flux ratio of 1:2 at 1673 K, where the flux concentration was kept below the $BaCO_3$ content in order to prevent the formation of $Ba_3Cl_4CO_3$. Both crucibles were sealed and placed in additional sealed crucibles to maintain a closed reaction environment. Nevertheless, IrO_2 was again observed as the primary crystallization product in combination with CeO_2.
Furthermore, a pronounced reaction was observed between volatile species and the glue used to seal the crucibles, which consists of aluminum oxide, water, and 10–25% phosphate (see data sheet [106]). This reaction led to the formation of $Ba_5(PO_4)_3Cl$, also known as the mineral alforsite [107] (see Figure 5.7). The formation of substantial amounts of

$Ba_5(PO_4)_3Cl$ can be attributed to the high volatility of $BaCl_2$ at the elevated temperature of 1673 K [97].
Since this reaction was prevented by using a new adhesive of same composition, it is likely that the chemical composition of the original adhesive changed over time, making it more susceptible to chemical attack.

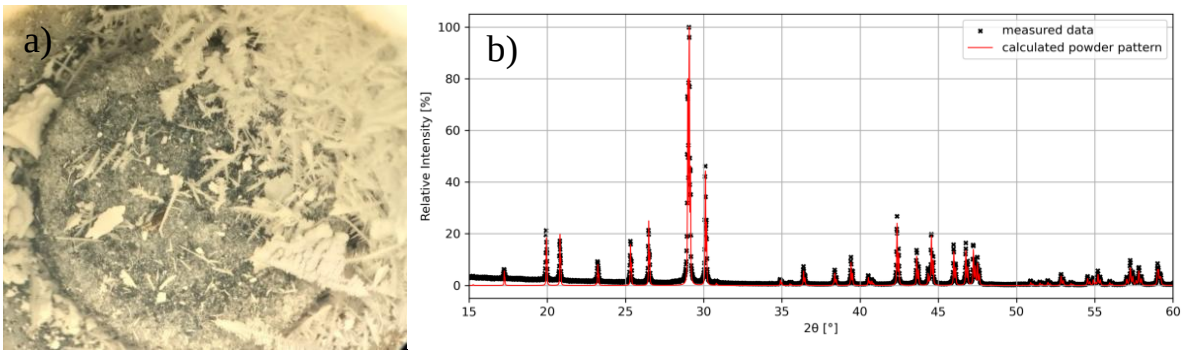

Figure 5.7: a) Image of the experiment S-ID 3. Bottom formation of IrO_2 with minor amounts of $Ba_3CeIr_2O_9$. The white phase, is dendritic crystalline $Ba_5(PO_4)_3Cl$, as confirmed by the P-XRD measurements shown in b).

S-ID	Educts (molar ratio)				Total weight [g]	Time to T_{max} [h]	T_{max} [K]	Time at T_{max} [h]	T_{min} [K]	Rate [K/h]	Products identified by P-XRD
	$BaCO_3$	CeO_2	IrO_2	$BaCl_2 \cdot 2H_2O$							
1	4.5	1	3	15	1	24	1573	20	1073	4.1	IrO_2 + CeO_2
2	8	1	3	15	1	24	1573	20	1073	4.1	IrO_2 + CeO_2
3	7.5	1	3	2	2	24	1673	24	1073	2	IrO_2 + $Ba_5(PO_4)_3Cl$
4	7.5	1	2.6	2	3	24	1673	24	1073	2	IrO_2 + CeO_2 $Ba_5(PO_4)_3Cl$

Table 5.4: Growth conditions of experiments in the BaO–CeO_2–IrO_2 system with $BaCO_3$, CeO_2 and IrO_2 as starting materials. $BaCl_2 \cdot 2H_2O$ was used as the source for the $BaCl_2$ flux.

S-ID 5-12: To enhance the reactivity of the iridium source, IrO_2 was replaced with $BaIrO_3$ (see Table 5.5). In experiments with the lowest $BaCO_3$ content (S-ID 6 and 7), only small amounts of $Ba_3CeIr_2O_9$ were formed. In contrast, slightly higher $BaCO_3$ concentrations led to the primary crystallization of $Ba_3CeIr_2O_9$. In experiments using 13 to 37 molar equivalents of $BaCO_3$ and 1.8 equivalents of $BaCl_2$, the high $BaCO_3$ content appeared to enhance aluminum solubility from the Al_2O_3 crucible, leading to the preferential formation of $BaAl_2O_4$ and $Ba_5AlIr_2O_{11}$.
It appears that a high $BaCO_3$ concentration may promote the crystallization of $Ba_4CeIr_3O_{12}$. However, this also increases the reactivity with the Al_2O_3 leading to the

formation of competing phases such as $BaAl_2O_4$ and $Ba_5AlIr_2O_{11}$ thereby hindering the growth of the target phase. For this reason, the crucible shape and material were examined in order to counteract the reaction between $BaCl_2$/BaO and Al_2O_3.

S-ID	Educts (molar ratio)				Total weight [g]	Time to T_{max} [h]	T_{max} [K]	Time at T_{max} [h]	T_{min} [K]	Rate [K/h]	Products identified by P-XRD
	$BaCO_3$	CeO_2	$BaIrO_3$	$BaCl_2 \cdot 2H_2O$							
5	4.5	1	3.3	2.5	1	24	1573	24	1073	4.1	$Ba_3CeIr_2O_9$ + $Ba_4CeIr_3O_{12}$
6	3.5	1	3.3	2.5	1	20	1573	24	973	18	$Ba_3CeIr_2O_9$ + CeO_2 + IrO_2 + Ir
7	2	1	2	2.5	1	20	1573	24	973	18	$Ba_3CeIr_2O_9$ + CeO_2 + IrO_2 + Ir
8	4	1	1.6	2.3	10	24	1573	24	1023	2	$Ba_3CeIr_2O_9$
9	13	1	3	1.8	0.5	20	1573	20	1073	3	$BaAl_2O_4$ + IrO_2 + CeO_2
10	20	1	3	1.8	0.5	20	1573	20	1073	3	$Ba_4CeIr_3O_{12}$ + $BaAl_2O_4$ + $Ba_3CeIr_2O_9$
11	22.5	1	3	1.8	0.5	20	1573	20	1073	3	empty
12	37	1	3	1.8	0.5	20	1573	20	1073	3	$BaAl_2O_4$ + $Ba_5AlIr_2O_{11}$

Table 5.5: Growth conditions of experiments in the BaO–CeO_2–IrO_2 system with $BaCO_3$, CeO_2 and $BaIrO_3$ starting materials. $BaCl_2 \cdot 2H_2O$ was used as the source for the $BaCl_2$ flux.

S-ID 13-16: To evaluate the influence of crucible geometry, a single batch was distributed across three Al_2O_3 crucibles of different shapes and one 10 mL platinum crucible (see Table 5.6). In the platinum crucible (S-ID 13), crystals of a new phase with sizes up to 500 µm were obtained. While the structure could not be identified by powder X-ray diffraction (PXRD), EDX analysis revealed a composition close to $Ba_3CeIrPtO_9$, see Figure 5.8. This exemplary experiment clearly demonstrates that platinum metal crucibles are not inert for the system BaO–CeO_2–IrO_2, but rather act as reactive component. This finding is consistent with previous literature [108].
In S-ID 14 and 16, a conical crucible with an aspect ratio (crucible width / crucible height) of 0.76 and a cylindrical crucible with an aspect ratio of 0.60 were used, respectively. In both cases, $Ba_3CeIr_2O_9$ crystallized as the dominant phase. By contrast, in S-ID 15 a crucible with a lower aspect ratio of 0.51 was used and $Ba_4CeIr_3O_{12}$was the main phase. These findings highlight that crucible geometry significantly influences phase formation, with narrower crucibles favoring the crystallization of the trimer phase. However, it

remains unclear whether this effect is due to the reduced surface area (resulting in lower evaporation rates) or a smaller contact area between melt and crucible (leading to reduced aluminum contamination).

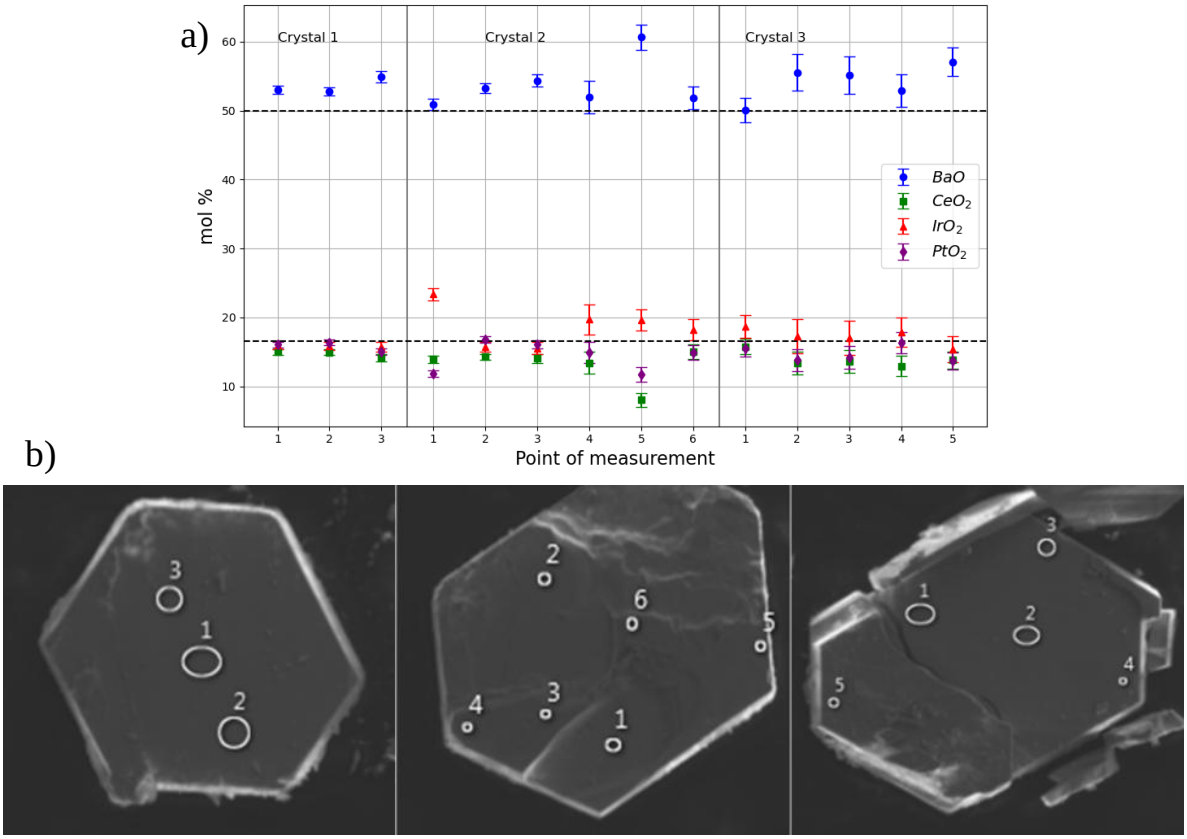

Figure 5.8: a) Shown is the chemical composition of three crystals from experiment S-ID 13, measured by EDX analysis. The determined molar fractions of BaO (blue), CeO_2 (red), IrO_2 (green), and PtO_2 (purple) correspond to the stoichiometry of $Ba_3PtCeIrO_9$. The dashed lines indicate the ideal molar fractions in this compound: 50 % for BaO and 16.7 % each for CeO_2, IrO_2, and PtO_2. The analyzed crystals and measurement points are shown in (b).

S-ID	Educts (molar ratio)				Total weight [g]	Time to T_{max} [h]	T_{max} [K]	Time at T_{max} [h]	T_{min} [K]	Rate [K/h]	Products identified by P-XRD
	$BaCO_3$	$BaCeO_3$	IrO_2	$BaCl_2 \cdot 2H_2O$							
13	11	1	3.2	1.8	0.74	20	1573	20	1073	3	$Ba_3CeIrPtO_9$
14	11	1	3.2	1.8	0.74	20	1573	20	1073	3	$BaAl_2O_4$ + $Ba_3CeIr_2O_9$
15	11	1	3.2	1.8	0.74	20	1573	20	1073	3	$Ba_4CeIr_3O_{12}$ + $Ba_3CeIr_2O_9$
16	11	1	3.2	1.8	0.74	20	1573	20	1073	3	$Ba_3CeIr_2O_9$ + $BaAl_2O_4$ +

Table 5.6: Growth conditions of experiments in the $BaO–CeO_2–IrO_2$ system with $BaCO_3$, $BaCeO_3$ and IrO_2 as starting materials. $BaCl_2 \cdot 2H_2O$ was used as the source for the $BaCl_2$ flux.

S-ID 17–23: Building on the previous experiments, the starting materials were further adjusted, and pre-synthesized $Ba_3CeIr_2O_9$ was used in combination with $BaCO_3$ and IrO_2 or $BaIrO_3$, see Table 5.7. In experiments S-ID 17–20 and S-ID 23, $Ba_3CeIr_2O_9$ was used as educt in combination with 4.0, 6.5, or 7.5 relative molar amounts of $BaCO_3$. In all cases, $Ba_4CeIr_3O_{12}$ crystallized, accompanied by $BaAl_2O_4$. The samples exhibited a microcrystalline matrix with hexagonal $Ba_4CeIr_3O_{12}$ single crystals of approximately 100 µm in size as shown in Figure 5.9.

Experiments conducted without $BaCO_3$ or with only 2 equivalents resulted in the formation of $Ba_3CeIr_2O_9$ and IrO_2 (S-ID 21), and $Ba_3CeIr_2O_9$ along with $BaAl_2O_4$ (S-ID 22).

These results suggest that the stability of the trimer phase $Ba_4CeIr_3O_{12}$ is enhanced at higher $BaCO_3$ concentrations compared to the dimer phase $Ba_3CeIr_2O_9$, however, $BaCO_3$ also promotes the dissolution of aluminum from the crucible, and the role of aluminum in the crystallization process remains unclear. Similar to the Eu-based system, the reaction between $BaCl_2$/BaO and Al_2O_3 is crucial and prevents the system from being considered ternary.

S-ID24: The experiment that was most successful for the Eu-based system did not achieve the desired result here. Using pre-sintered $Ba_4CeIr_3O_{12}$ as a starting material mixed with $BaCl_2$ in a ratio 1 : 30 led to the crystallization of $Ba_3CeIr_2O_9$.

S-ID	Educts (molar ratio)				Total weight [g]	Time to T_{max} [h]	T_{max} [K]	Time at T_{max} [h]	T_{min} [K]	Rate [K/h]	Products identified by P-XRD
	$BaCO_3$	$Ba_3CeIr_2O_9$	IrO_2	$BaCl_2 \cdot 2H_2O$							
17	6.5	1	1	1.8	1	24	1573	24	1023	3	$Ba_4CeIr_3O_{12}$ + $BaAl_2O_4$ + $BaIrO_3$
18	6.5	1	1	1.8	1	24	1573	24	1023	3	$Ba_4CeIr_3O_{12}$ + $BaAl_2O_4$ + $BaIrO_3$
19	6.5	1	1	1.8	1	24	1573	24	1023	3	$Ba_4CeIr_3O_{12}$ + $BaAl_2O_4$
20	4	1	1	1.8	1.3	24	1573	24	1023	2	$Ba_4CeIr_3O_{12}$ + $BaAl_2O_4$
S-ID	**Educts (molar ratio)**				**Total weight [g]**	**Time to T_{max} [h]**	**T_{max} [K]**	**Time at T_{max} [h]**	**T_{min} [K]**	**Rate [K/h]**	**Products identified by P-XRD**
	$BaCO_3$	**$Ba_3CeIr_2O_9$**	**$BaIrO_3$**	**$BaCl_2 \cdot 2H_2O$**							
21	0	1	2	1.8	1	24	1573	24	1073	3	$Ba_3CeIr_2O_9$ + IrO_2
22	2	1	2	1.8	1	24	1573	24	1073	3	$Ba_3CeIr_2O_9$ + $BaAl_2O_4$
23	7.5	1	2	1.8	1	24	1573	24	1073	3	$Ba_4CeIr_3O_{12}$ + $BaAl_2O_4$

S-ID	Educts (molar ratio)		Total weight [g]	Time to T_{max} [h]	T_{max} [K]	Time at T_{max} [h]	T_{min} [K]	Rate [K/h]	Products identified by P-XRD
	$Ba_4CeIr_3O_{12}$	$BaCl_2 \cdot 2H_2O$							
24	1	30	10	24	1373	24	1123	1	$Ba_3CeIr_2O_9$

Table 5.7: Growth conditions of experiments in the $BaO–CeO_2–IrO_2$ system with $BaCO_3$, $Ba_3CeIr_2O_9$ and IrO_2 resp. $BaIrO_3$ as starting materials. $BaCl_2 \cdot 2H_2O$ was used as the source for the $BaCl_2$ flux.

Figure 5.9: $Ba_4CeIr_3O_{12}$ single crystal with ~150µm in size. The crystal was isolated by dissolution of $BaCl_2$ with distilled water and taken from experiment S-ID 18.

5.1.3 $BaO – Nb_2O_5 – IrO_2$

In the $BaO–Nb_2O_5–IrO_2$ system, both the dimer and trimer phases are known in literature and have been successfully grown with $BaCl_2$ flux [30; 50]. $Ba_3NbIr_2O_9$ was initially synthesized with solid state reaction and subsequently mixed with $BaCl_2$ [50].
Solid state reaction experiments of $Ba_4NbIr_3O_{12}$ are first mentioned in 1991 by J. Wilkens and Müller-Buschbaum [53]. A detailed description for the crystal growth is given by Gohil S. Thakur et al. [30]. It is reported that $Ba_4NbIr_3O_{12}$ single crystals in combination with $Ba_5Nb_4O_{15}$ and elemental Ir can be obtained directly from stoichiometric mixtures of $BaCO_3$, Nb_2O_5, and IrO_2 with the addition of $BaCl_2$ as a flux [30]. When $Ba_4NbIr_3O_{12}$ was used as educt, no secondary phases were observed, and the crystal size increased. In general, a higher flux content and a lower cooling rate seem to favor crystal growth in this system [30].

Crystal growth experiments:

For the synthesis of $Ba_4NbIr_3O_{12}$ in this work, a similar approach as described in [30] was used. All experiments, unless otherwise specified, were carried out in sealed 10 mL Al_2O_3 crucibles (30 mm height x 23 mm width) placed inside a sealed Al_2O_3 box. The temperature profile was limited to a maximum of 1373 K, as $Ba_4NbIr_3O_{12}$ decomposes at higher temperatures (see chapter 6.2.2). However, the crystal growth proved significantly more challenging than expected. The information of growth conditions are summarized in Table 5.8. Solid state reaction experiments to form $Ba_4NbIr_3O_{12}$ from the starting materials $BaCO_3$, Nb_2O_5, and IrO_2 at 1373 K were successful, so that $Ba_4NbIr_3O_{12}$was used as starting material.

S-ID 1 and 2: The first two crystallization experiments were based on comparable experimental conditions but yielded markedly different results. In the first experiment, crystals of $Ba_4NbIr_3O_{12}$ up to 0.5 mm in size (see Figure 5.11) were identified alongside $BaIrO_3$, suggesting partial phase separation. Notably, almost the entire amount of $BaCl_2$ flux had evaporated from the crucible during the process, indicating a high volatility of the flux under the applied conditions.
In contrast, the second experiment retained most of the $BaCl_2$ within the crucible. Small black crystals were observed near the upper rim of the crucible, suggesting a possible vapor-phase transport of iridium species. However, only a small amount of microcrystalline $Ba_4NbIr_3O_{12}$ could be recovered after flux dissolution.

S-ID 3 and 4: Subsequent experiments were carried out with a crystal-to-flux ratio of 1 : 5 to investigate the influence of an additional $BaCO_3$ component on the crystallization process. In both trials, the transport of iridium species along the crucible wall was again evident from dark deposits near the upper regions of the crucibles (see Figure 5.10). Simultaneously, both crucibles exhibited a dense, intergrown microcrystalline layer at the bottom, consisting of $Ba_4NbIr_3O_{12}$, with no visible residues of $BaCl_2$ flux. This observation suggests that complete melting may not have occurred, and the flux likely evaporated prior to or during crystallization.

Figure 5.10: Formation of black crystallites on the upper inner crucible wall (experiment S-ID 3), indicating gas-phase transport during the synthesis process.

S-ID 5–9: To investigate the potential influence of the sealing glue Ceramabond 503 on the synthesis process, a controlled experimental series was conducted. The objective was to systematically evaluate how varying degrees of sealing affect the composition and nature of the resulting crystallization products. A homogenous powder mixture of $Ba_4NbIr_3O_{12}$ and $BaCl_2$ was divided and distributed into five identical Al_2O_3 crucibles, each subjected to different sealing conditions.

The first crucible (S-ID 5) was completely sealed using 0.32 mL of adhesive. Under these conditions, crystals of $Ba_4Nb_4O_{15}$ and $BaNb_2O_6$ formed. IrO_2 and $BaCl_2$ were also detected as minor phases, but only in trace amounts compared to the original quantities used. Notably, the adhesive showed clear signs of chemical degradation, indicating active involvement in the reaction (see Figure 5.12). P-XRD analysis of the glue could not be matched with the structure database. In S-ID 6, the crucible was half-sealed with 0.14 mL of glue. In this approach, residual IrO_2 and elemental Ir were present, while all of the $BaCl_2$ had volatilized. The third crucible (S-ID 7) was sealed to three-quarters using 0.6 mL of glue, with a resulting phase composition similar to S-ID 6, but partial deposition was observed on the surface of the crucible lid. In contrast, the fourth crucible (S-ID 8) was not sealed but merely covered with a loosely fitting lid. In this setup, a solidified $BaCl_2$ melt

was observed (see Figure 5.12). After dissolving the $BaCl_2$ with distilled water small amounts of residual microcrystalline $Ba_4NbIr_3O_{12}$ was obtained.
The fifth crucible (S-ID 9) was left completely open and subjected to heat treatment at 1373 K for 330 hours. The initial aim of this approach was to evaporate $BaCl_2$ from the system in order to supersaturate the melt and thereby promote the crystallization of $Ba_4NbIr_3O_{12}$. For this, the crucible was placed inside an Al_2O_3 tube, which was positioned in the vertical tube furnace so that its upper end protruded from the furnace. This setup allowed the opening to be narrowed down to the diameter of a hose, enabling controlled channeling and filtration/condensation of gases generated during the experiment. However, contrary to expectations, the majority of the $BaCl_2$ remained within the crucible, while iridium and niobium volatilized completely and escaped from the system. After the flux removal procedure, only $BaCO_3$ was detected, which likely resulted from the reaction of residual barium oxide with atmospheric CO_2 during the washing process. It is conceivable that chloride-containing phases may have initially crystallized, but subsequently decomposed during cleaning, making them no longer detectable.

This experimental series clearly demonstrates the significant volatility of system components under different sealing conditions. The results indicate that the ceramic glue and the method of crucible sealing actively influence the evaporation of $BaCl_2$ at elevated temperatures. Moreover, both niobium and iridium were observed to volatilize from the system, though the mechanisms governing the selective volatilization, with iridium predominating in S-ID 5 and niobium in S-IDs 6 and 7, remain unclear.
The complex volatility behavior and elemental interactions cannot be fully explained based on the available experimental data alone. To comprehensively interpret these findings, additional data on transport mechanisms and the formation of volatile species within the system are required.

In the open system configuration, S-ID 8, the presence of microcrystalline $Ba_4NbIr_3O_{12}$ residue suggests that no homogeneous melt was formed. Instead, $Ba_4NbIr_3O_{12}$ appears to decompose gradually, generating volatile species in conjunction with $BaCl_2$ which then escape from the system. Nb_2O_5 or $NbCl_5$ likely serve as transport agents facilitating iridium volatilization.
$BaCl_2$ undergoes partial dissociation at elevated temperatures, releasing reactive chloride ions (Cl^-) [109]. Niobium metal and Nb_2O_5 can both react with Cl^-, forming $NbCl_5$ and $NbOCl_3$, respectively, both of which are highly volatile species (Equation 5.4) [94]. $NbCl_5$ is commonly employed as a transport agent for niobium, by a reduction reaction to $NbCI_4$ (Equation 5.3 and 5.5) [94]. Therefore, it is conceivable that $NbCl_5$ forms a volatile species

in combination with iridium. However, experimental transport data on $NbCl_5$ outside the Nb–O–Cl system are limited.

$$Nb + 4\ NbCl_{5(g)} = 5\ NbCI_{4(g)} \quad (5.3)$$

$$Nb_2O_5 + 3\ C1_2 = 2\ NbOCl_{3(g)} + 3/2\ 0_2 \quad (5.4)$$

$$Nb_2O_5 + 3\ NbCl_{5(g)} = 5\ NbOCl_{3(g)} \quad (5.5)$$

Iridium itself can form $IrCl_3$ species, which are volatile and also used as a transport species in chemical vapor transport reactions [110]. However, since such high volatility was not observed in the $BaO–Eu_2O_3–IrO_2$ and $BaO–CeO_2–IrO_2$ systems, even at elevated temperatures of up to 1573 K, it is more likely that the niobium is key for the transport in this system.

In addition, the formation of complex chloride phases, such as $Ba_6IrNb_2O_{12}Cl_2$, cannot be ruled out. The crystallization of this compound has also been reported from a $BaCl_2$ flux, underscoring the notion that $BaCl_2$ should be considered an active component in this system rather than an inert flux [111].

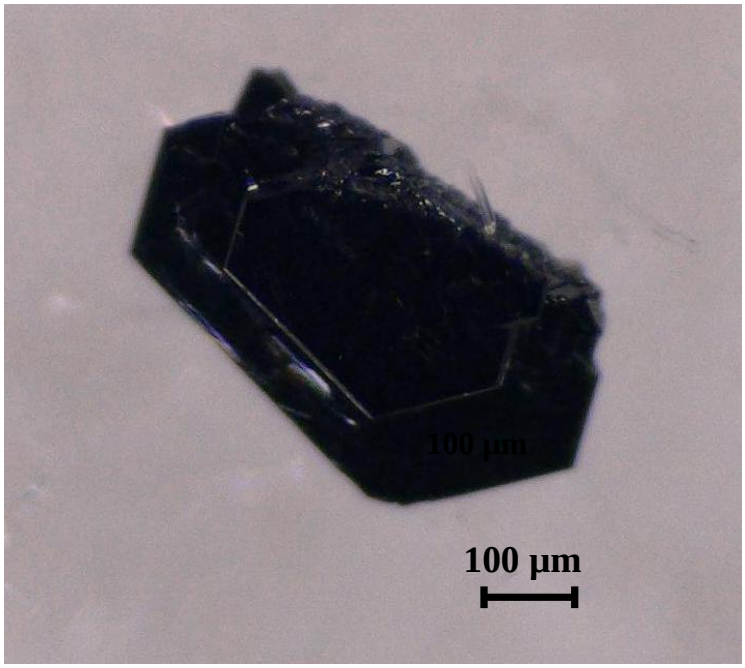

Figure 5.11: $Ba_4NbIr_3O_{12}$ single crystal with ~500µm in size. The crystal was isolated and taken from experiment S-ID 1. After dissolving the $BaCl_2$ with distilled water, the crystal could be mechanically isolated.

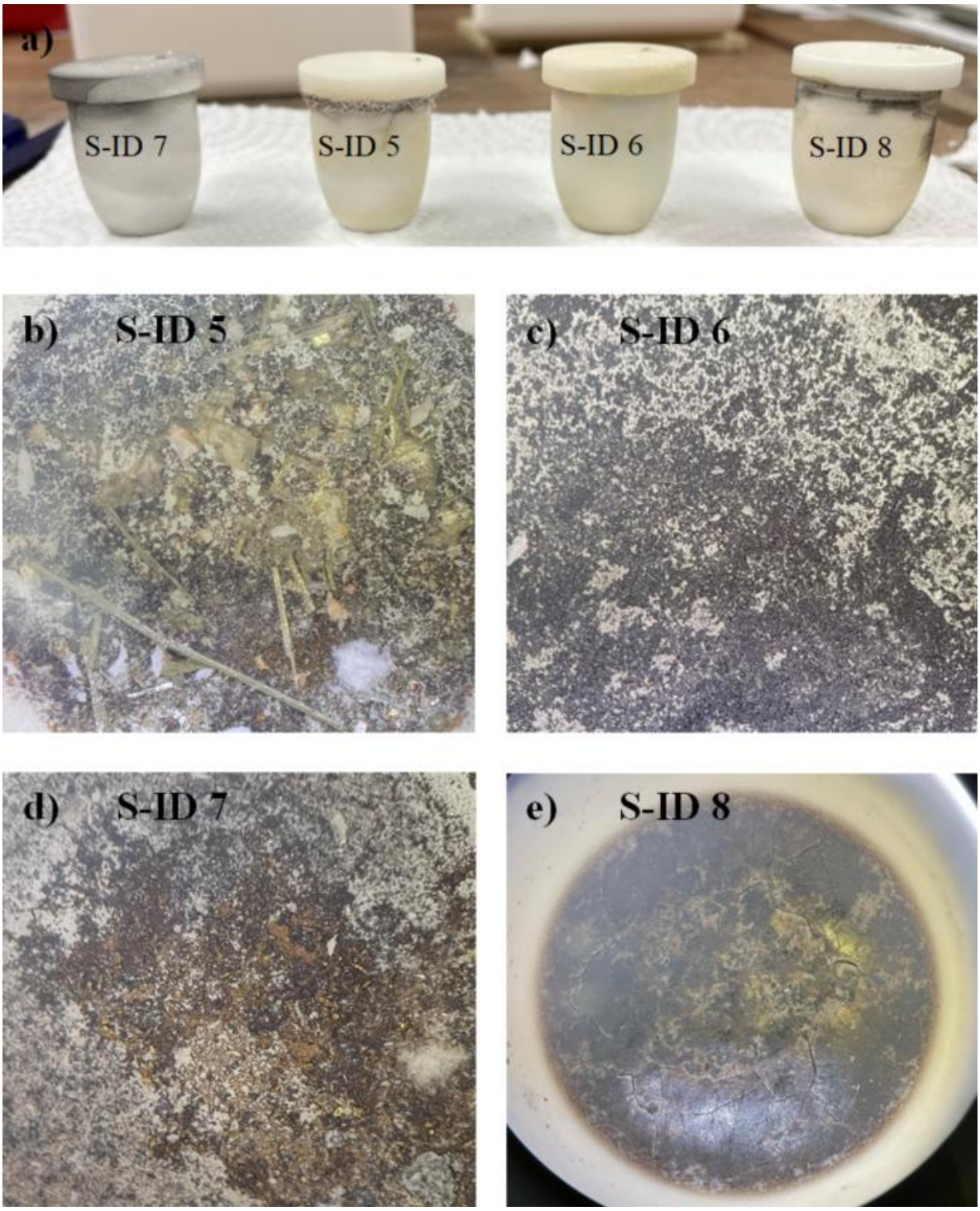

Figure 5.12: a) Image of the crucibles after the experiment. It is clearly visible that in experiment S-ID 5, the glue reacted strongly. Additionally, the crucibles with S-ID 7 and S-ID 8 exhibits black deposits on the outer part of the crucible. b) Image of green, prismatic $Ba_4Nb_4O_{15.33}$ crystals from experiment S-ID 5. c) and d) Image of IrO_2 crystals in experiment S-ID 6 and 7. e) Image of the crystallized gray/brown $BaCl_2$ melt in experiment S-ID 8.

S-ID	Educts	Crystal to flux ratio	Total weight [g]	Time to T_{max} [h]	T_{max} [K]	Time at T_{max} [h]	T_{min} [K]	Rate [K/h]	Products identified by P-XRD	Comment
1	$Ba_4NbIr_3O_{12}$	1:35	5	24	1373	24	950	0.8	$Ba_4NbIr_3O_{12}$ + $BaIrO_3$	- Crystal size 0.5 - No remaining $BaCl_2$
2	$Ba_4NbIr_3O_{12}$	1:30	2.1	24	1373	24	950	0.85	IrO_2	- residual $BaCl_2$
3	$Ba_4NbIr_3O_{12}$ + $BaCO_3$	1:5	0.4	24	1373	24	930	1	$Ba_4NbIr_3O_{12}$	- No remaining $BaCl_2$
4	$Ba_4NbIr_3O_{12}$	1:5	0.3	24	1373	24	930	1	$Ba_4NbIr_3O_{12}$	- No remaining $BaCl_2$
5	$Ba_4NbIr_3O_{12}$	1:35	2.25	12	1373	24	950	0.85	Ir + IrO_2 + $BaNb_2O_6$ + $Ba_5Nb_4O_{15.3}$	- No remaining $BaCl_2$ - 0.32 mL glue
6	$Ba_4NbIr_3O_{12}$	1:35	2.25	12	1373	24	950	0.85	IrO_2 + Ir	- No remaining $BaCl_2$ - 0.14 mL glue
7	$Ba_4NbIr_3O_{12}$	1:35	2.25	12	1373	24	950	0.85	$Ba_4NbIr_3O_{12}$	- No remaining $BaCl_2$ - 0.6 mL glue
8	$Ba_4NbIr_3O_{12}$	1:35	2.25	12	1373	24	950	0.85	$BaCO_3$	- remaining $BaCl_2$ - unsealed
9	$Ba_4NbIr_3O_{12}$	1:35	3	24	1373	336	-	50	$BaCl_2$	- unsealed
10	$Ba_4NbIr_3O_{12}$	1:35	2.8	12	1373	20	950	0.9	$Ba_4NbIr_3O_{12}$	- Crucible-in-crucible, double-sealed
11	$Ba_4NbIr_3O_{12}$	1:30	7.5	20	1373	24	900	1	$Ba_5Nb_4O_{15}$ + $Ba_4NbIr_3O_{12}$	- Tube crucible

Table 5.8: Growth conditions and resulting phases observed in the $BaO–Nb_2O_5–IrO_2$ system. $Ba_4NbIr_3O_{12}$ was used as a starting material, in combination with $BaCl_2·2H_2O$ as a flux source.

5.1.4 $BaO – Ta_2O_5 – IrO_2$

The $BaO–Ta_2O_5–IrO_2$ system is largely unexplored, and, to the best of the author's knowledge, the compounds $Ba_3TaIr_2O_9$ and $Ba_4TaIr_3O_{12}$ have not been reported in the literature to date. Due to the close chemical relationship of Nb_2O_5 and Ta_2O_5, it is reasonable to hypothesize that the systems $BaO–Ta_2O_5–IrO_2$ and $BaO–Nb_2O_5–IrO_2$ exhibit comparable behaviors.

Solid state reaction experiments:

Initial attempts focused on synthesizing $Ba_4TaIr_3O_{12}$ by solid-state reaction using a molar ratio of 4 $BaCO_3$: 1/2 Ta_2O_5 : 3 IrO_2 at 1273 K. This method successfully and reproducibly yielded phase-pure $Ba_4TaIr_3O_{12}$. Its structure was refined via the Rietveld method using the initial $Ba_4NbIr_3O_{12}$ structure model [30], which confirmed the structural similarity between these two compounds (see 6.2.3). Similarly, the solid-state product of the $Ba_3TaIr_2O_9$ composition could be matched with the calculated powder pattern of $Ba_3CoIr_2O_9$, indicating a structural relationship and thus supporting the formation of $Ba_3TaIr_2O_9$. The stoichiometries corresponding to the sum formulas Ba_2TaIrO_6 led to phases that could not be identified using the ICSD database. The search was restricted to compounds containing barium, any TM, REEs, and oxygen in arbitrary compositions.

Sample	Educts (molar ratio)			T_{max} [K]	Products
	$BaCO_3$	Ta_2O_5	IrO_2		
IRTA 1	2	0.5	1	1373	New phase
IRTA 2	3	0.5	2	1373	$Ba_3TaIr_2O_9$
IRTA 3	4	0.5	3	1373	$Ba_4TaIr_3O_{12}$

Table 5.9: Chemical composition of all solid state experiments in the $BaO–Ta_2O_5–RuO_2$ system.

Crystal growth experiments:

Each experiment was conducted inside a sealed alumina box. The used Al_2O_3 crucibles themselves were covered with a loose-fitting lid. A total of eight experiments were conducted, all using sintered $Ba_4TaIr_3O_{12}$ as educts and T_{max} of 1273 K. The details of the growth conditions are given in Table 5.10.

S-ID 1-4: The first four experiments were conducted using $Ba_4TaIr_3O_{12}$ as starting material with crystal to flux ratios ranging from of 1 : 5 to 1 : 35. All syntheses were carried out in conical 10 mL Al_2O_3 crucibles with an aspect ratio of 1.3 at the top. In experiments with a crystal-to-flux ratio of 1 : 5 (S-ID 1 and 2) and 1 : 30 (S-ID 3), no noticeable reaction between $Ba_4TaIr_3O_{12}$ and the $BaCl_2$ melt was observed. In contrast to the Nb-based system,

the $BaCl_2$ had nearly completely evaporated, leaving $Ba_4TaIr_3O_{12}$ behind as a microcrystalline residue. In experiment S-ID 4 the crucible was placed in a second sealed crucible to slightly reduce the volume relative to the Al_2O_3 box. Here, significant deposition of black crystalline material on the outer crucible walls was observed, indicative of a transport reaction between $BaCl_2$ and the reactants. The black color of the deposited crystals suggests the possible transport of an iridium-containing phase (see Figure 5.13). Despite this transport behavior, a partially solidified $BaCl_2$ melt remained in the crucible. After dissolving the flux with distilled water, well-formed $Ba_4TaIr_3O_{12}$ crystals up to 500 µm in size (see Figure 5.14) were observed on the crucible bottom, indicating a heterogeneous nucleation process.

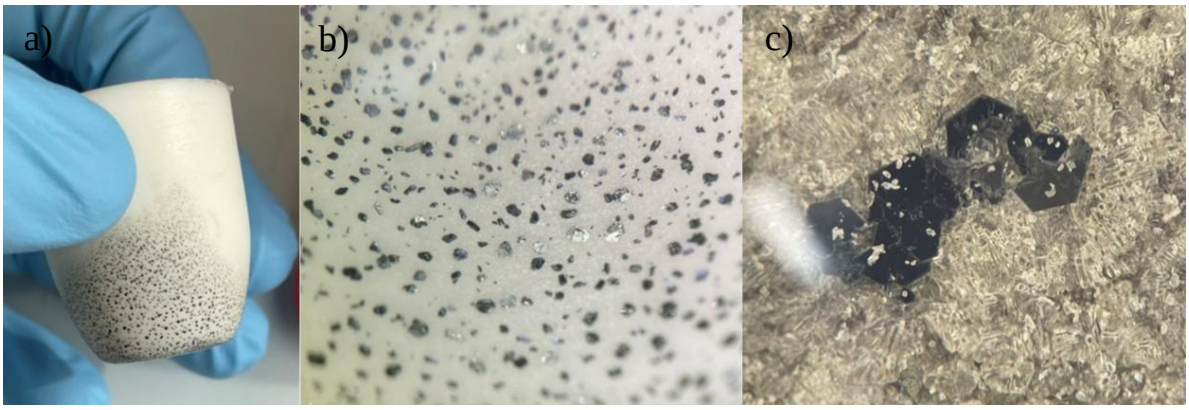

Figure 5.13: a) and b) black crystals on the outer part of the crucible of the experiment S-ID 4. c) shows black hexagonal $Ba_4TaIr_3O_{12}$ on the surface of $BaCl_2$ in the crucible.

S-ID 5–7: In experiments S-ID 5–7, the chemical composition was systematically varied to evaluate its influence on phase formation and crystal growth. A total mass of 10 g was used for each experiment. Therefore, large cylindrical Al_2O_3 crucibles with a volume of 90 mL and an aspect ratio of approximately 1.9 were selected. The increased cross-sectional area of these crucibles (44 mm) was intended to promote the nucleation of a high number of crystals across the crucible bottom.

For this purpose, the sintered products corresponding to the initial ratios of $BaCO_3$, Ta_2O_5 and IrO_2 with 2 : 0.5 : 1 (S-ID 5), 3 : 0.5 : 2 (S-ID 6), and 4 : 0.5 : 3 (S-ID 7) were used as starting materials.

All of these experiments showed similarities to experiments S-ID 1–3, in which the primary observation was the evaporation of the $BaCl_2$ flux. Even though small $Ba_4TaIr_3O_{12}$ crystals formed in experiment S-ID 6 and 7, the majority of the initially $BaCl_2$ had volatized.

Notably, in comparison to the intended starting compositions, the resulting phases exhibited a higher BaO + IrO_2 content. X-ray diffraction (XRD) analysis of a sample prepared with a

nominal Ba_2TaIrO_6 crystallized to the $Ba_3TaIr_2O_9$ phase. The initial sintered product corresponding to $3\,BaCO_3 : 0.5\,Ta_2O_5 : 2\,IrO_2$ formed small $Ba_4TaIr_3O_{12}$ crystals in combination with $Ba_3TaIr_2O_9$.
Compared to the previous experiments, the holding time at 1273 K was increased from 24 to 48 hours to promote more effective melt formation. It is conceivable that the opposite occurred, and that the high volatility in combination with the observed transport of iridium species processes continued for the extended time at elevated temperature.

S-ID 8: In a final experiment, a tube-shaped crucible with an aspect ratio of approximately 4 (6 mm height × 1.5 mm width) was used. The open end was wedged with a second, slightly larger tube crucible in order to reduce evaporation without using ceramic glue, which reacts with the vapor phase. The holding time was reduced again to 24 hours, and a crystal-to-flux ratio of 1:30 was applied. After the experiment, black deposits were again observed on the outer surface of the crucible. Upon dissolution of the flux, $Ba_4TaIr_3O_{12}$ crystals with sizes up to 200 µm were successfully isolated. Based on previous observations from experiment S-ID 4, where crystallization likely occurred via heterogeneous nucleation at the crucible wall rather than through homogeneous nucleation in the melt, it is reasonable to assume a similar mechanism here. The narrow cross-section of the crucible likely reduced the number of available nucleation sites and thereby limited the overall crystal yield in this experiment.

The experimental findings indicate that vapor-phase dynamics play a critical role in the crystallization behavior of $Ba_4TaIr_3O_{12}$. In open systems, volatilization processes dominate, preventing crystallization. Crystallization is only observed when the system volume is sufficiently reduced, allowing a dynamic equilibrium between the vapor phase and the melt to form. This equilibrium effectively limits the volatility of key species and thus facilitates crystal formation.
Due to the reactivity of volatile species with the ceramic glue, such materials introduce an uncontrollable variable that is difficult to quantify, as previously observed in the Nb-based system. Consequently, the implementation of a protective crucible emerged as the most reliable strategy to suppress evaporation and promote targeted crystallization.

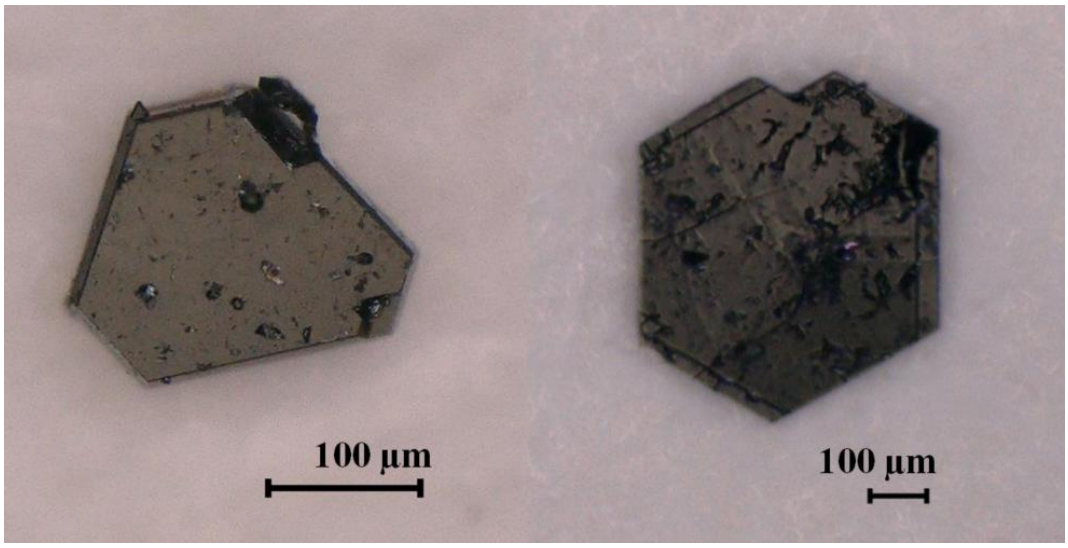

Figure 5.14: $Ba_4TaIr_3O_{12}$ single crystals with up to 500 µm in size. The crystal were isolated and taken from experiment S-ID 4.

S-ID	Educts	Crystal to flux ratio	Total weight [g]	Time to T_{max} [h]	T_{max} [K]	Time at T_{max} [h]	T_{min} [K]	Rate [K/h]	Products identified by P-XRD	Comment
1	$Ba_4TaIr_3O_{12}$ + 4 $BaCO_3$	1:5	0.4	24	1373	24	1203	1	$Ba_4TaIr_3O_{12}$	- 10 mL crucible - No remaining $BaCl_2$
2	$Ba_4TaIr_3O_{12}$	1:5	0.3	24	1373	24	1203	1	$Ba_4TaIr_3O_{12}$	- 10 mL crucible - No remaining $BaCl_2$
3	$Ba_4TaIr_3O_{12}$	1:30	2	24	1373	24	1223	0.8	$Ba_4TaIr_3O_{12}$	- 10 mL crucible
4	$Ba_4TaIr_3O_{12}$	1:35	3	12	1373	20	1223	0.9	$Ba_4TaIr_3O_{12}$	- 10 mL crucible - Crucible in a second sealed crucible - 0.5 mm crystals
5	Sinter product of RUTA1	1:30	10	48	1373	48	1223	0.76	$Ba_3TaIr_2O_9$	- 90 mL crucible
6	Sinter product of RUTA2	1:30	10	48	1373	48	1223	0.76	$Ba_3TaIr_2O_9$ + $Ba_4TaIr_3O_{12}$	- 90 mL crucible - 0.2 mm crystals
7	$Ba_4TaIr_3O_{12}$	1:30	10	48	1373	48	1223	0.76	$Ba_4TaIr_3O_{12}$	- 90 mL crucible
8	$Ba_4TaIr_3O_{12}$	1:30	7.5	20	1373	24	1173	1	$Ba_4TaIr_3O_{12}$	- Tube crucible - 0.2 mm crystals

Table 5.10 Growth conditions and resulting phases observed in the $BaO–Ta_2O_5–IrO_2$ system.

5.2 Ruthenium based systems

Building on insights gained from experiments with iridium-based systems, it was determined that the most effective approach for crystallizing perovskite compounds is the use of pre-synthesized phases. Accordingly, solid-state reactions were performed for the ruthenium-based systems, and the resulting products served as starting materials for subsequent crystal growth experiments. These studies revealed that ruthenate phases require higher temperatures for their formation compared to their iridate counterparts. As a result, the solid-state syntheses were conducted at an elevated temperature of 1573 K.

All solid-state reactions were carried out in sealed, conical 10 mL Al_2O_3 crucibles. For crystal growth, cylindrical 50 mL Al_2O_3 crucibles with dimensions of 60 mm height and 39 mm diameter (aspect ratio ~ 1.53) were employed. Each crucible was covered with a loosely fitting lid and enclosed within a sealed Al_2O_3 box.

In all systems, except for M = Ta, the compounds $Ba_3MRu_2O_9$ and $Ba_4MRu_3O_{12}$ are reported in literature. There, the dimer phases were prepared under ambient conditions from stoichiometric mixtures of $BaCO_3$ and the corresponding metal oxides with solid state reactions [44; 45; 29]. The trimer phases were synthesized analogously to the iridates, using platinum crucibles sealed in evacuated quartz ampoules [33; 6]. Due to contamination with the dimer phase and pyrochlore-type compounds, an excess of $BaRuO_3$ was employed to favor the formation of the trimer phase [33; 6].

The goal of the following section was the crystallization of ruthenium-based dimer and trimer phases incorporating differently valent elements on the M site in order to modulate the number of electrons within the dimer and trimer clusters.

5.2.1 $BaO – Eu_2O_3 – RuO_2$

Solid state reaction investigations:

Solid-state experiments were conducted using $BaCO_3$, Eu_2O_3, and RuO_2 in molar ratios ranging from 3 : 0.5 : 2 to 5 : 0.5 : 4, as summarized in Table 5.11. The composition corresponding to the 3 : 0.5 : 2 molar ratio yielded single-phase $Ba_3EuRu_2O_9$, in agreement with previously reported results [29]. The 4 : 0.5 : 3 molar ratio composition resulted in a mixture of dimer and trimer phases, suggesting that the dimer phase remains the dominant stable phase under these conditions. Further increasing the $BaCO_3$ and RuO_2 content to a nominal 5 : 0.5 : 4 ratio led to the formation of both the trimer phase and $BaRuO_3$. These results suggest that the dimer phase is stable over a broad compositional range extending up to the nominal trimer stoichiometry, while stabilization of the trimer phase requires a significant excess of ruthenium oxide under these conditions.

Sample	Educts ratio			T_{max} [K]	Products
	$BaCO_3$	Eu_2O_3	RuO_2		
RUEU1	9	0.5	2	1373	$Ba_5Ru_2O_{10}$ + $BaCO_3$
RUEU2	3	0.5	2	1573	$Ba_3EuRu_2O_9$
RUEU3	4	0.5	3	1573	$Ba_3EuRu_2O_9$ + $Ba_4EuRu_3O_{12}$
RUEU4	5	0.5	4	1573	$Ba_4EuRu_3O_{12}$+ $BaRuO_3$

Table 5.11: Chemical composition of all solid state experiments in the $BaO–Eu_2O_3–RuO_2$ system.

Crystal growth investigations:

The detailed growth conditions are summarized in Table 12. Representative images of $Ba_3EuRu_2O_9$ single crystals are shown in Figure 5.15.

Six crystal growth experiments were performed, two of which included an excess of barium oxide. In experiment S-ID 1, excess $BaCO_3$ was used during the solid-state reaction, while in S-ID 5, $BaCO_3$ was added to the pre-synthesized phase after sintering. In both cases, the reaction between the melt and the reactants appeared to be suppressed, preventing any crystal growth. Based on previous observations, it is assumed that the excess barium carbonate reacts with $BaCl_2$, thereby inhibiting its function as a flux in this system.

In experiments S-ID 2–4 and 6, primarily $Ba_3EuRu_2O_9$ crystallized. For experiments using the nominal composition of $Ba_4EuRu_3O_{12}$, the excess $BaRuO_3$ also crystallized alongside with the dimer phase. The crystal size of $Ba_3EuRu_2O_9$ was slightly larger in experiments employing excess $BaRuO_3$ compared to those using a stoichiometric mixture. Crystallization of the trimer phase from stoichiometric compositions was not achieved. Considering the findings from the solid-state experiments, it was already evident that a significant excess of $BaRuO_3$ is required to stabilize the trimer phase. However, even

growth experiments using the solid-state product from RUEU4 resulted in the crystallization of $Ba_3EuRu_2O_9$.

S-ID	Educts	Crystal to flux ratio	Total weight [g]	Time to T_{max} [h]	T_{max} [K]	Time at T_{max} [h]	T_{min} [K]	Rate [K/h]	Products identified by P-XRD	Crystal size [mm]
1	Product from RUEU1:	1:20	2.7	8	1573	24	1173	3	$Ba_3EuRu_2O_9$	<0.1
2	Product from RUEU2:	1:30	5	10	1573	20	1173	2	$Ba_3EuRu_2O_9$	0.4
3	Product from RUEU2:	1:30	6	24	1623	48	1173	2	$Ba_3EuRu_2O_9$	0.5
4	Product from RUEU3:	1:30	5	10	1573	20	1173	2	$Ba_3EuRu_2O_9$ + $BaRuO_3$	0.7
5	Product from RUEU3 + $BaCO_3$ in ratio 1:4	1:30	4	10	1623	20	1223	2	$Ba_3EuRu_2O_9$	<0.1
6	Product from RUEU4:	1:30	2.6	15	1573	24	1223	2	$Ba_3EuRu_2O_9$	0.3

Table 5.12: Experimental conditions and resulting phases observed in the $BaO–Eu_2O_3–RuO_2$ system.

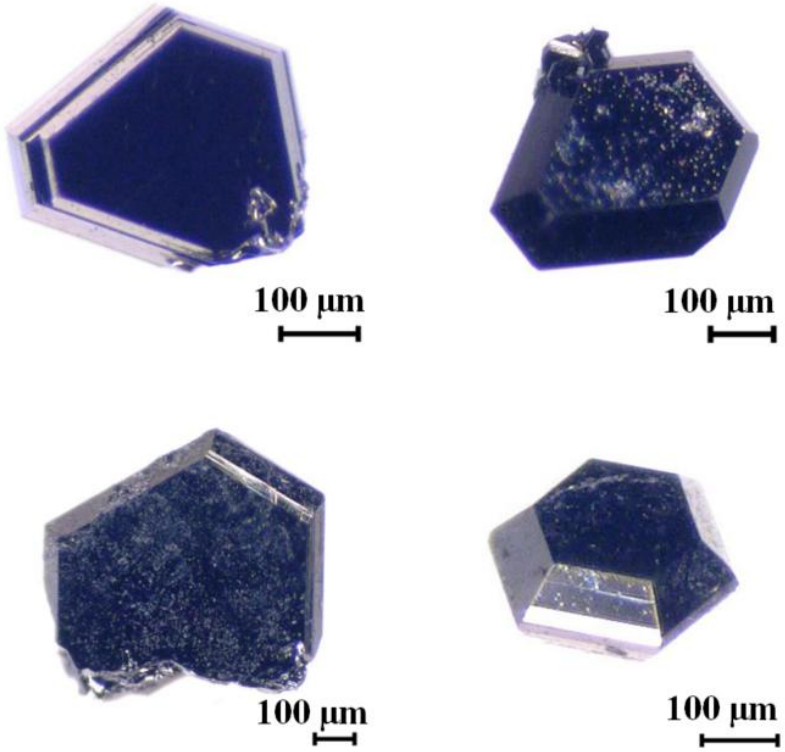

Figure 5.15: Image of $Ba_3EuRu_2O_9$ single crystals with a view along the [001] direction. The pronounced hexagonal symmetry is clearly visible. The morphology corresponds to a flattened hexagonal bipyramid.

5.2.2 $BaO – CeO_2 – RuO_2$

Solid state reaction investigations:

Solid-state reaction experiments conducted at 1373 K led to the formation of $Ba_5Ru_3O_{10}$ and $BaCeO_3$ (see Table 5.13), indicating that quaternary perovskite phases were not formed under these conditions. To further explore phase formation, additional syntheses were performed at 1573 K using $BaCO_3$, CeO_2, and RuO_2 in molar ratios ranging from 2 : 1 : 1 to 5 : 1 : 4. At a 2 : 1 : 1 ratio, $Ba_3CeRu_2O_9$ and $BaCeO_3$ formed. A 3 : 1 : 2 ratio composition produced $Ba_3CeRu_2O_9$ as the major phase, with $Ba_4CeRu_3O_{12}$ and $BaCeO_3$ as minor phases. Pure $Ba_4CeRu_3O_{12}$ crystallized at a 4 : 1 : 3 ratio, while higher $BaCO_3$ and RuO_2 contents led to mixtures of $Ba_4CeRu_3O_{12}$ and $BaRuO_3$.

These results indicate that the trimer phase is stable over a broad compositional range, extending from the dimer stoichiometry up to the nominal $Ba_5CeRu_4O_{15}$ composition. In contrast, $Ba_3CeRu_2O_9$ appears to be stabilized under $BaRuO_3$ deficient conditions. The relative stability of the dimer and trimer phases in the Ce-based system thus differs significantly from that of the europium analogue, suggesting distinct phase stability fields depending on the choice of rare-earth element.

Sample	Educts (molar ratio)			T_{max} [K]	Products
	$BaCO_3$	CeO_2	RuO_2		
RUCE1	9	1	2	1373	$B_5Ru_3O_{10}$ + $BaCeO_3$
RUCE2	2	1	1	1573	$Ba_3CeRu_2O_9$ + $BaCeO_3$
RUCE3	3	1	2	1573	$Ba_3CeRu_2O_9$+ $Ba_4CeRu_3O_{12}$+ $BeCeO_3$
RUCE4	4	1	3	1573	$Ba_4CeRu_3O_{12}$
RUCE5	5	1	4	1573	$Ba_4CeRu_3O_{12}$ + $BaRuO_3$

Table 5.13: Chemical composition of all solid state experiments in the $BaO–CeO_2–RuO_2$ system.

Crystal growth investigations:

A total of 12 crystal growth experiments were conducted, with detailed conditions summarized in Table 5.14. Representative images of the crystallized crystals are shown in Figure 5.18. In experiments S-ID 1–3, the pre-crystallized product obtained from the RUCE2 composition, corresponding to the nominal stoichiometry Ba_2CeRuO_6, was used. In all cases, the resulting phase crystallized as $Ba_4CeRu_3O_{12}$ along with CeO_2. The crystal sizes varied significantly between S-ID 1 and S-ID 2: while S-ID 1 yielded crystals smaller than 0.1 mm, S-ID 2 produced crystals up to 2 mm in size. This variation is likely due to differences in synthesis temperature. A higher temperature of 1623 K appears to enhance solubility and reactivity, facilitating the formation of larger crystals.

Several larger crystals exhibited surface coverage by a secondary phase. Electron microprobe EDX analysis identified this phase as Al_2O_3, indicating minor contamination

from the crucible material (see Figure 5.16).

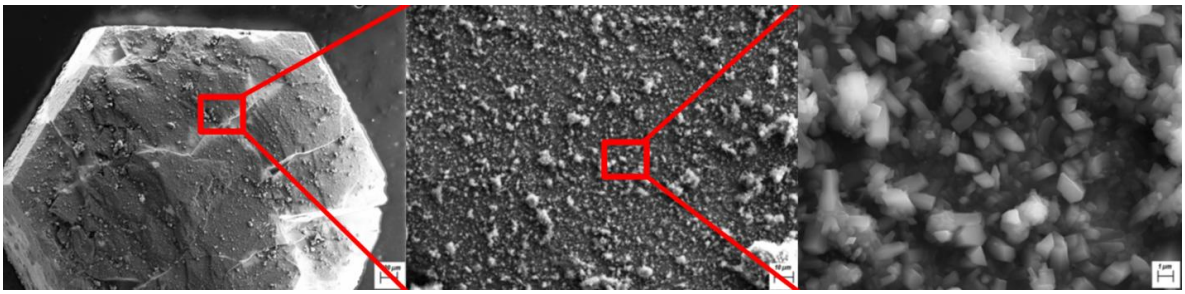

Figure 5.16: Electron beam microscope image of microcrystalline Al_2O_3 on a $Ba_4CeRu_3O_{12}$ crystal from experiment S-ID 2.

Moreover, many of the large $Ba_4CeRu_3O_{12}$ crystals were heavily intergrown with CeO_2, typically localized on the bottom side of the crystals. This observation suggests that the high CeO_2 concentration led to early precipitation or incomplete dissolution, forming a solid layer upon which $Ba_4CeRu_3O_{12}$ crystals subsequently nucleated. During growth, CeO_2 was partially incorporated as inclusions (see Figure 5.17).

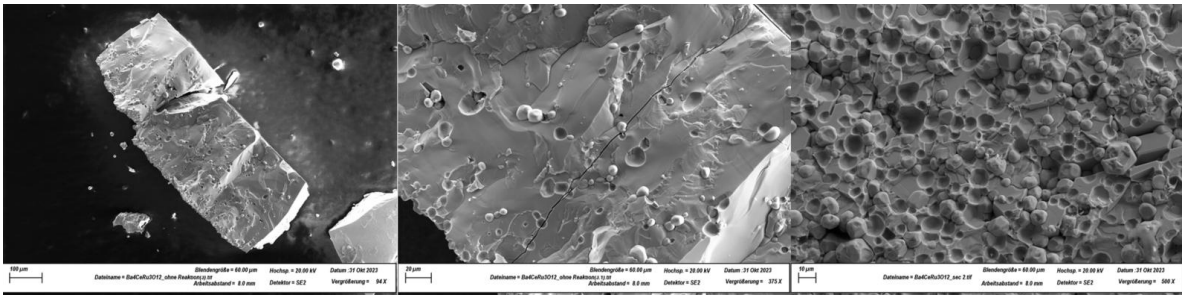

Figure 5.17: Electron beam microscope image of CeO_2 inclusions in a $Ba_4CeRu_3O_{12}$ single crystal from experiment S-ID 2. The inclusions are particularly concentrated at the bottom of the crystal and decrease as crystallization progresses.

In experiments S-ID 4–8, the product of the solid-state experiment from RUCE3 with the nominal stoichiometry $Ba_3CeRu_2O_9$ was used as educt. These experiments yielded inconsistent phase outcomes. S-ID 4 and 5 predominantly formed $Ba_3CeRu_2O_9$ with crystals up to 0.9 mm in size, along with minor amounts of $Ba_4CeRu_3O_{12}$. Conversely, S-ID 6 and 7 exclusively yielded $Ba_4CeRu_3O_{12}$ with CeO_2, with no trace of the dimer phase. The determining parameter responsible for favoring either phase could not be identified. Even slight changes in experimental conditions appear sufficient to shift the phase equilibrium.
In experiments S-ID 9–11, phase-pure $Ba_4CeRu_3O_{12}$ was used as educt. In all cases, $Ba_4CeRu_3O_{12}$ crystallized successfully, accompanied only by minor amounts of CeO_2. The resulting crystals exhibited smooth growth surfaces, and no Al_2O_3 contamination was

detected. In experiment S-ID 12, $Ba_4CeRu_3O_{12}$ was used as the starting material with additional $BaCO_3$ in a molar ratio of 1:4. Unexpectedly, $Ba_3CeRu_2O_9$ crystallized as the resulting phase instead of the originally used trimer phase. Since the effect of the reaction between $BaCO_3$ and the flux $BaCl_2$ on crystallization is unclear, it cannot be conclusively determined whether the increased BaO content is the cause of the phase formation or a consequence of the reaction between the flux and $BaCO_3$. In either case, this experiment demonstrates that $BaCO_3$ appears to significantly influence the stability of $Ba_4CeRu_3O_{12}$ within the system.

As previously observed in the europium-based system, elevated temperatures strongly promote the crystallization of perovskite phases. The high phase stability of $Ba_4CeRu_3O_{12}$ observed in solid-state experiments is mirrored in the growth trials. The consistent formation of the trimer phase from compositions that notably differ from the nominal stoichiometry ($BaCO_3 : CeO_2 : RuO_2 = 2 : 1 : 1$) and the inconsistent formation behavior at $BaCO_3 : CeO_2 : RuO_2 = 3 : 1 : 2$ is surprising.
Due to the use of pre-reacted starting materials which do not result in a homogeneous phase for RUCE1 and RUCE2, the precise molar ratios of the components involved are not well defined. It is conceivable that the different phases exhibit varying reactivity with the $BaCl_2$ flux. For example, a reaction between $BaCl_2$ and $BaCeO_3$ may facilitate the dissolution of Al_2O_3 from the crucible material, analogous to the known reactivity between $BaCl_2$ and $BaCO_3$. Notably, the quantity of $BaCeO_3$ was highest in experiments with the highest initial CeO_2 content (RUCE2), the same experiments in which Al_2O_3 contaminations were detected.
These findings suggest that, similar to the Ir-based systems, BaO availability may play a decisive role in the formation and stabilization of the trimer phase. However, this hypothesis is primarily based on experimental observations and should be validated through further investigation. Nevertheless, the proposed mechanism presents a plausible contributing factor to be considered when analyzing phase stability in the system.

S-ID	Educts	Crystal to flux ratio	Total weight [g]	Time to T_{max} [h]	T_{max} [K]	Time at T_{max} [h]	T_{min} [K]	Rate [K/h]	Products identified by P-XRD	Crystal size [mm]
1	Product of RUCE2:	1:50	12	10	1473	40	1173	1	$Ba_4CeRu_3O_{12}$ + CeO_2	<0.1
2	Product of RUCE2:	1:20	20	8	1623	20	1223	1	$Ba_4CeRu_3O_{12}$ + CeO_2	2
3	Product of RUCE2:	1:30	15	24	1623	48	1173	1.7	$Ba_4CeRu_3O_{12}$ + CeO_2	0.6
4	Product of RUCE3:	1:30	5	10	1573	20	1173	2	$Ba_3CeRu_2O_9$	0.9
5	Product of RUCE3:	1:20	20	8	1623	20	1223	1	$Ba_3CeRu_2O_9$ + $Ba_4CeRu_3O_{12}$	0.8
6	Product of RUCE3:	1:50	10	15	1623	20	1123	2	$Ba_4CeRu_3O_{12}$+ CeO_2	1.4
7	Product of RUCE3:	1:20	14	40	1623	48	1173	1.7	$Ba_4CeRu_3O_{12}$+ CeO_2	0.5
8	Product of RUCE1	1:35	4	8	1573	24	1173	3	$Ba_4CeRu_3O_{12}$+ CeO_2	0.5
9	Product of RUCE4:	1:50	20	10	1473	40	1173	1	$Ba_4CeRu_3O_{12}$ + CeO_2	<0.1
10	Product of RUCE4:	1:30	5	10	1573	20	1173	2	$Ba_4CeRu_3O_{12}$+ CeO_2	0.6
11	Product of RUCE4:	1:20	20	8	1623	20	1223	1	$Ba_4CeRu_3O_{12}$ + CeO_2	0.8
12	Product of RUCE4: +$BaCO_3$ in ratio 1:4	1:30	4	10	1623	20	1223	2	$Ba_3CeRu_2O_9$	0.8

Table 5.14: Growth conditions and resulting phases observed in the BaO–CeO_2–RuO_2 system.

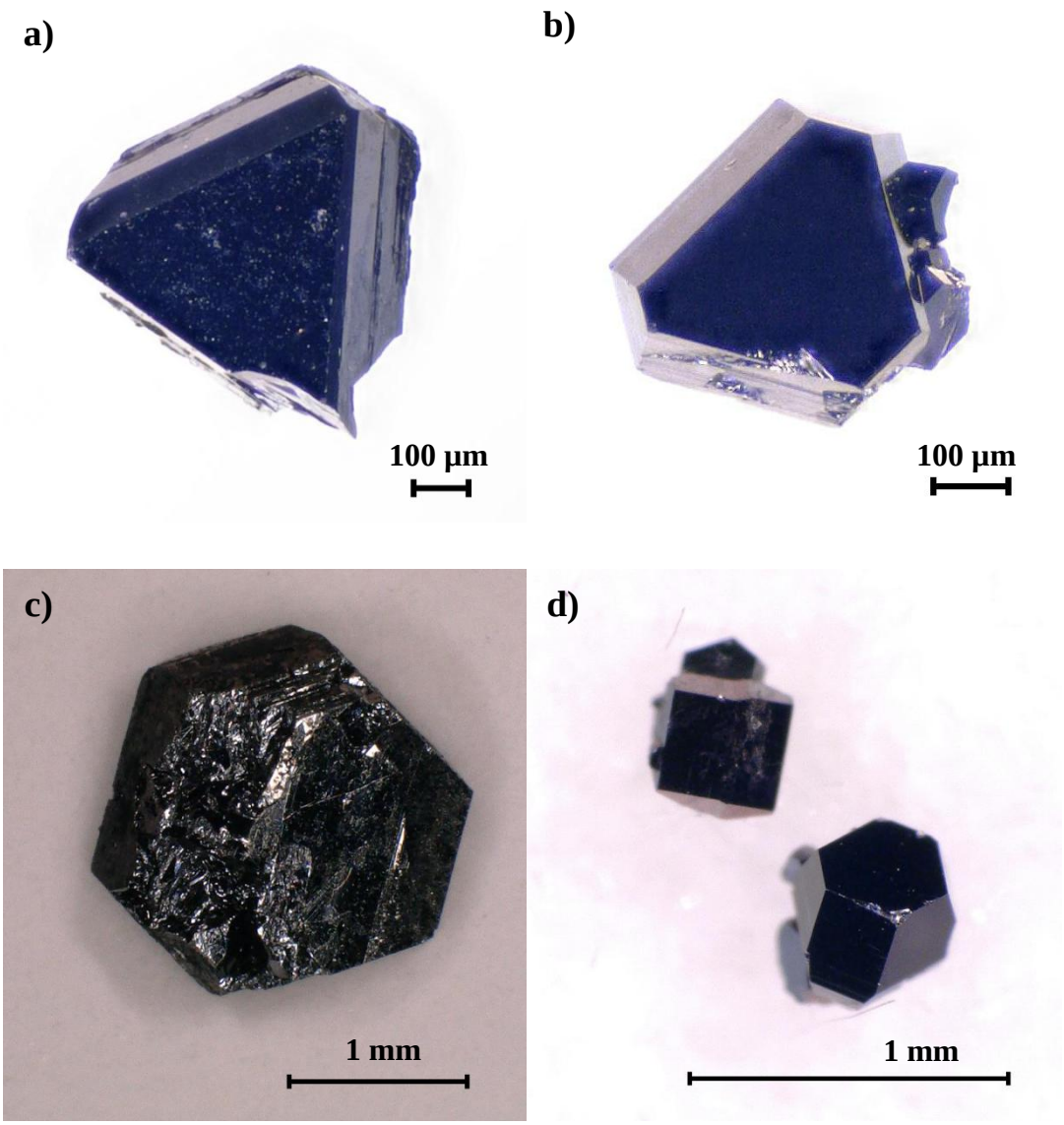

Figure 5.18: The images a) and b) show $Ba_3CeRu_2O_9$ single crystals of the experiment S-ID 3. The images c) and d) show $Ba_4CeRu_3O_{12}$ single crystals of the experiment S-ID 2 and 9. The quality of the $Ba_4CeRu_3O_{12}$ crystals varies significantly between the experiments. In S-ID 2, the crystal is larger but shows less well-developed growth faces compared to the crystals in experiment S-ID 9.

5.2.3 $BaO – Pr_6O_{11} – RuO_2$

Solid state reaction investigation:

The compositions and results of the solid-state experiments are summarized in Table 5.15. Two phases were successfully synthesized as single-phase products: the cubic double perovskite Ba_2PrRuO_6 and the trimer phase $Ba_4PrRu_3O_{12}$. Both phases were obtained from compositions, similar to [33; 112]. The dimer phase $Ba_3PrRu_2O_9$ [45] could not be detected. When the $BaRuO_3$ content was increased, $Ba_4PrRu_3O_{12}$ was identified in combination with $BaRuO_3$.

Sample	Educts (molar ratio)			T_{max} [K]	Products
	$BaCO_3$	Pr_6O_{11}	RuO_2		
RUPR1	2	1/6	1	1573	Ba_2PrRuO_6
RUPR2	4	1/6	3	1573	$Ba_4PrRu_3O_{12}$
RUPR3	5	1/6	4	1573	$Ba_4PrRu_3O_{12}$ + $BaRuO_3$

Table 5.15: Chemical composition of all solid state experiments in the $BaO–Pr_2O_3–RuO_2$ system.

Crystal growth investigations:

Three crystallization experiments were conducted using the products of the solid state experiments as starting materials (Table 5.16).

In the first experiment, the $BaRuO_3$ crystals up to 1 mm in size were obtained. Since $BaRuO_3$ can crystallize in different structural modifications depending on the growth conditions, it should be noted that this corresponds to the 9R modification [113]. The 9R-perovskite crystal structure consists of corner-connected $[Ru_3O_{12}]$-trimer units. The structure is thus similar to the 12L perovskite structure described in Section 2.1.2, but without the separating monolayer of $[MO_6]$-octahedra. Chemical investigations regarding a possible mixed occupancy between Ru and Pr are planned.

The second and third experiments resulted in the formation of $Ba_4PrRu_3O_{12}$ crystals along with $BaRuO_3$ (S-ID 2) or $Ba_3PrRu_2O_9$ (S-ID 3). It is not possible to distinguish between primary and secondary crystallites, as there is no clear epitaxy of either phase. Furthermore, the crystals are of similar size. Differentiating between these phases based on morphology is challenging. However, $Ba_4PrRu_3O_{12}$ crystals tend to exhibit a slightly prismatic growth habit, while $BaRuO_3$ and $Ba_3PrRu_2O_9$ crystals generally display a flatter morphology. Additionally, some $Ba_4PrRu_3O_{12}$ crystals show signs of twinning, indicating the presence of two intergrown individuals. Representative single crystals of both $BaRuO_3$ and $Ba_4PrRu_3O_{12}$ are shown in Figure 5.19.

S-ID	Educts	Crystal to flux ratio	Total weight [g]	Time to T_{max} [h]	T_{max} [K]	Time at T_{max} [h]	T_{min} [K]	Rate [K/h]	Products identified by P-XRD	Crystal size [mm]
1	Product from RUPR1: Ba_2PrRuO_6	1:30	15	8	1623	40	1173	1.5	$BaRuO_3$	1
2	Product from RUPR2: $Ba_4PrRu_3O_{12}$	1:30	10	10	1573	20	1223	1	$Ba_4PrRu_3O_{12}$ + $BaRuO_3$	0.3
3	Product from RUPR3: $Ba_4PrRu_3O_{12}$	1:30	2.6	15	1573	24	1223	2	$Ba_4PrRu_3O_{12}$ + $Ba_3PrRu_2O_9$	0.3

Table 5.16: Growth conditions and resulting phases observed in the $BaO–Pr_2O_3–RuO_2$ system.

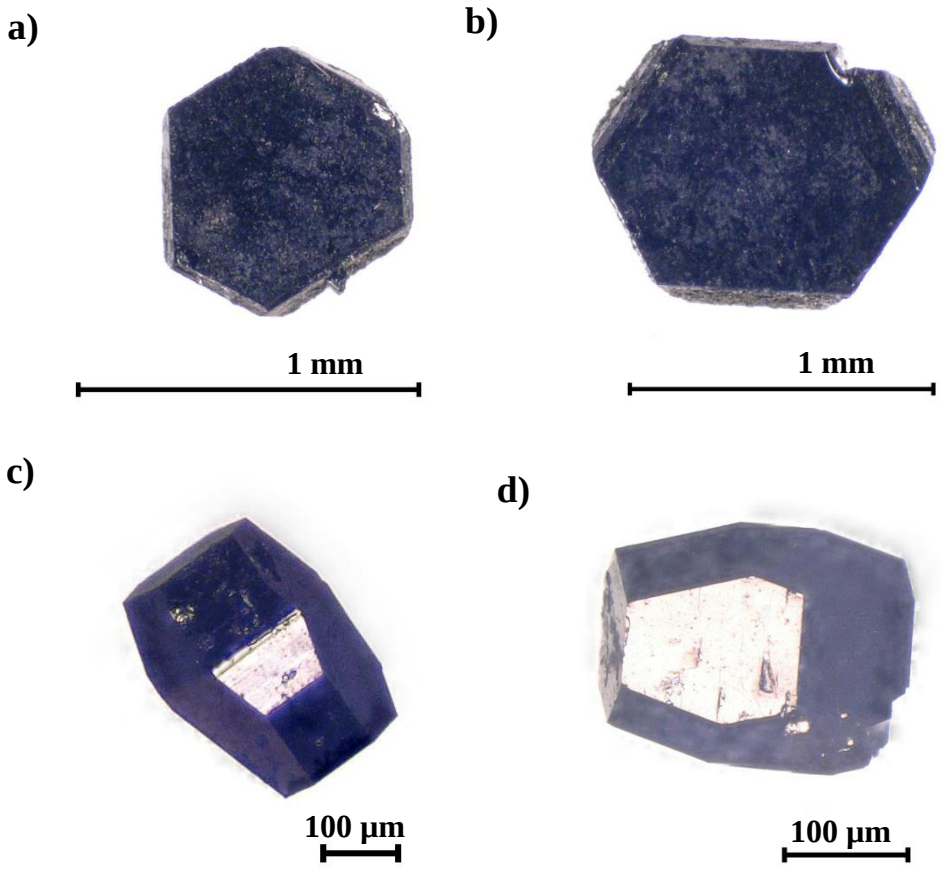

Figure 5.19: The images (a) and (b) show single crystals of the 9R perovskite type modification of $BaRuO_3$. (c) Twinned $Ba_4PrRu_3O_{12}$ single crystal, with the reflection clearly indicating the intergrowth of two individuals. (d) Untwinned $Ba_4PrRu_3O_{12}$ crystal.

5.2.4 $BaO – Ta_2O_5 – RuO_2$

Solid state reaction investigation:

Similar to the Ce- and Eu-based systems, a synthesis temperature of 1373 K is insufficient to form quaternary perovskite phases. Experiments using $BaCO_3 : Ta_2O_5 : RuO_2$ ratios of 2 : 1/2 : 1 and 3 : 1/2 : 2 resulted in the formation of a hexagonal 8H-perovskite stacking variant alongside $Ba_4TaRu_3O_{12}$. The 8H-type perovskite structure has been reported for compounds such as $Ba_8Ta_4Ru_{8/3}Co_{2/3}O_{24}$ [114], suggesting that the composition of the observed phase is likely close to $Ba_8Ta_4Ru_4O_{24}$. In contrast, $Ba_4TaRu_3O_{12}$ was successfully obtained as a single phase when using $BaCO_3 : Ta_2O_5 : RuO_2$ ratios of 4 : 1/2 : 3 and 5 : 1/2 : 4. The absence of detectable $BaRuO_3$ in the final products may be attributed to the observed volatility of reactants during synthesis, which may alter the effective Ta : Ru ratio in the resulting phases.

Sample	Educts (molar ratio)			T_{max} [K]	Products
	$BaCO_3$	Ta_2O_5	RuO_2		
RUTA1	9	1	2	1373	$Ba_5Ru_2O_{10}$ + $Ba_4Ta_2O_9$
RUTA2	2	1	1	1573	$Ba_8Ta_4Ru_3O_{24}$ + $Ba_4TaRu_3O_{12}$
RUTA3	3	1	2	1573	$Ba_8Ta_4Ru_3O_{24}$ + $Ba_4TaRu_3O_{12}$
RUTA4	4	1	3	1573	$Ba_4TaRu_3O_{12}$
RUTA5	5	1	4	1573	$Ba_4TaRu_3O_{12}$

Table 5.17: Chemical composition of all solid state experiments in the $BaO–Ta_2O_5–RuO_2$ system.

Crystal growth investigation:

The details and results of the crystal growth experiments within the $BaO–Ta_2O_5–RuO_2$ system are summarized in Table 9.

Attempts to crystallize the 8H-perovskite phase were unsuccessful. Instead, the Cl-phases such as $Ba_5RuTaO_9Cl_2$ and $Ba_8Ru_{3.33}Ta_{1.67}O_{18}Cl_2$ were formed, both of which dissolved during the flux removal process. The discrepancies between the simulated and experimental diffraction patterns suggest that the crystallized phases may differ chemically from the calculated models, potentially exhibiting altered lattice parameters due to compositional variations.

The remaining experiments revealed a clear trend concerning the growth temperature. All attempts conducted at 1573 K or lower failed to produce crystals. However, experiments performed at an elevated temperature of 1623 K resulted in the crystallization of $Ba_4TaRu_3O_{12}$. Even the $BaRuO_3$-deficient composition from sample RUTA03 produced $Ba_4TaRu_3O_{12}$ crystals. Increasing the temperature to 1673 K did not yield successful crystallization. The excessively high temperature appears to significantly enhance the volatility of the phases, with nearly the entire sample evaporating from the crucible. The significant influence of volatility in this system was particularly evident in experiment S-

ID 10. In this case, the amount of material was sufficiently large that crystalline deposits could be collected from the crucible lid and analyzed by X-ray diffraction. The resulting phases consisted of $Ba_8Ta_4Ru_3O_{24}$ and $Ba_5Ta_4O_{15}$. As previously observed in the iridium-based system, tantalum oxide appears to react with $BaCl_2$ to form volatile species. It is likely that volatile tantalum chloride species act as transport agents for ruthenium, facilitating the crystallization of quaternary phases from the gas phase. Even though the role of tantalum as a transport agent cannot be definitively proven, it is nevertheless likely that it reacts similarly to Nb_2O_5, as discussed in Section 5.1.4. Furthermore, the transport of tantalum via halogen species is well known and has been thoroughly documented [95].

S-ID	Educts	Crystal to flux ratio	Total weight [g]	Time to T_{max} [h]	T_{max} [K]	Time at T_{max} [h]	T_{min} [K]	Rate [K/h]	Products identified by P-XRD	Crystal size [mm]
1	Product from RUTA1:	1:20	2,7	8	1573	24	1173	3	$Ba_4TaRu_3O_{12}$	0.5
2	Product from RUTA2:	1:30	15	24	1623	40	1173	1.5	$BaCl_2Ba_3Ru_2O_{10}$	Soluble in H_2O
3	Product from RUTA2:	1:30	10	48	1623	48	1223	1	$Ba_5RuTaO_9Cl_2$ + $Ba_8Ru_{3.33}$-$Ta_{1.67}O_{18}Cl_2$	Soluble in H_2O
4	Product from RUTA3:	1:30	5	10	1573	20	1173	2	$Ba_4TaRu_3O_{12}$	<0.1
5	Product from RUTA3:	1:30	6	24	1623	40	1173	2	$Ba_4TaRu_3O_{12}$	0.3
6	Product from RUEU4: $Ba_4TaRu_3O_{12}$	1:30	5	10	1573	20	1173	2	$Ba_4TaRu_3O_{12}$	<0.1
7	Product from RUTA4 + $BaCO_3$ in ratio 1:4	1:30	4	10	1623	20	1223	2	$Ba_4TaRu_3O_{12}$ + $BaRuO_3$	0.3
8	Product from RUTA4: $Ba_4TaRu_3O_{12}$	1:50	10	15	1673	20	1123	2	emty-crucible	-
9	Product from RUTA4: $Ba_4TaRu_3O_{12}$	1:50	10	10	1473	40	1173	1	$Ba_4TaRu_3O_{12}$	0.3
10	Product from RUTA5: $Ba_4TaRu_3O_{12}$	1:30	10	48	1623	48	1223	1	$BaRuO_3$	-

Table 5.18: Growth conditions and resulting phases observed in the $BaO–Ta_2O_5–RuO_2$ system.

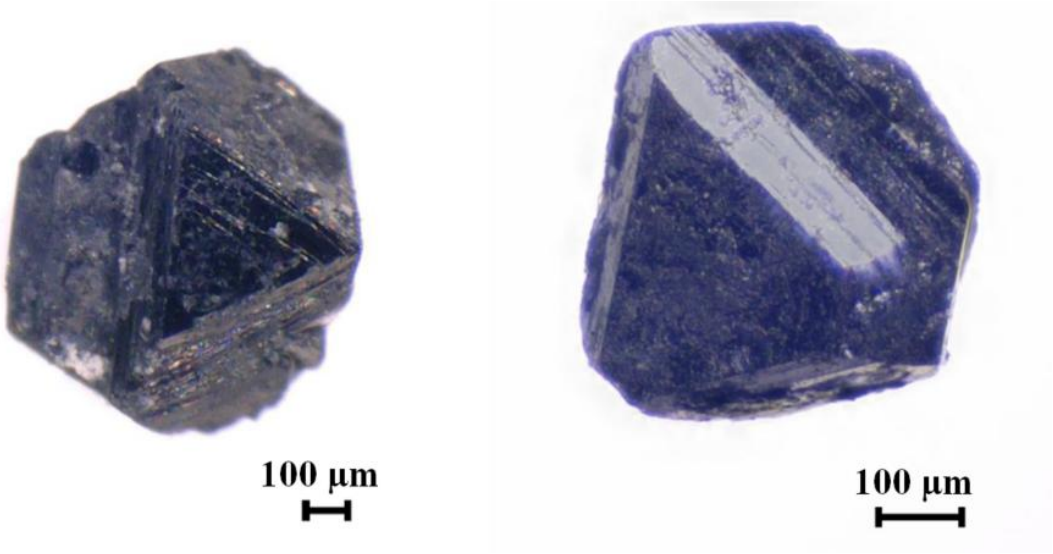

Figure 5.20: (a) $Ba_4TaRu_3O_{12}$ single crystal from experiment S-ID 1, exhibiting a flat morphology with a well-defined (001) face. The surfaces of type (hkl) and (h0l) or (0kl) show a characteristic stepped growth pattern. (b) $Ba_4TaRu_3O_{12}$ crystal from experiment S-ID 7, displaying smaller size but better-developed morphology.

5.2.5 BaO – M_xO_y – RuO_2 with M_xO_y = Sc_2O_3, Y_2O_3, Tb_4O_7, Yb_2O_3 and Lu_2O_3

Solid state reaction investigation:

Based on the insights gained from previous experiments, solid-state reactions were conducted within the BaO–M_xO_y–RuO_2 systems, where M_xO_y corresponds to Sc_2O_3, Y_2O_3, Tb_4O_7, Yb_2O_3, and Lu_2O_3. The molar ratios of the starting materials ($BaCO_3$: M_xO_y : RuO_2) were selected to correspond to the nominal composition of the trimer phase, typically using a ratio of 4 : 0.5 : 3. For terbium, a reduced amount of 0.25 equivalents was employed to account for the higher oxidation state (Tb^{4+}) present in Tb_4O_7.

The results indicated that the formation of the trimer phase was only successful in the BaO–Tb_4O_7–RuO_2 system. In this case, the trimer phase was observed alongside the dimer phase, suggesting a partial stabilization of the desired compound. In contrast, all other systems exclusively produced the dimer phase in coexistence with $BaRuO_3$ and, in the systems with Yb_2O_3 resp. Lu_2O_3, $Ba_4Ru_2O_{10}$.

Sample	Educts (molar ratio)			T_{max} [K]	Products
	$BaCO_3$	M_xO_y	RuO_2		
RUSC1	4	½ Sc_2O_3	3	1573	$Ba_3ScRu_2O_9$ + $BaRuO_3$
RUY1	4	½ Y_2O_3	3	1373	$Ba_3YRu_2O_9$ + $BaRuO_3$
RUTB1	4	¼ Tb_4O_7	3	1573	$Ba_3TbRu_2O_9$ + $Ba_4TbRu_3O_{12}$
RUYB1	4	½ Yb_2O_3	3	1573	$Ba_3YbRu_2O_9$ + $Ba_4Ru_2O_{10}$ + $BaRuO_3$
RULU1	4	½ Lu_2O_3	3	1573	$Ba_3LuRu_2O_9$ + $Ba_4Ru_2O_{10}$ + $BaRuO_3$ + Lu_2O_3

Table 5.19: Chemical composition of all solid state experiments in the systems BaO–*M*–RuO_2 with *M* = Sc_2O_3, Y_2O_3, Tb_4O_7, Yb_2O_3 and Lu_2O_3.

Crystal growth investigation:

The addition of $BaCl_2$ flux to the respective pre-synthesized phases (given in Table 5.19) enabled the successful crystallization of several dimer compounds. The results and growth conditions are summarized in Table 5.20.

All systems exhibited similar behavior. In each attempt, the dimer phase was detected alongside with $BaRuO_3$. However, the crystal size and the number of crystals formed varied significantly between experiments. In the system with M_xO_y = Sc_2O_3 no macroscopic single crystals were obtained. In contrast, the equivalent system with the 4d element Yttrium produced small crystals up to 150µm in size.

Crystal growth experiments involving lutetium (M_xO_y = Lu_2O_3) did not yield any crystals, similar to the Sc_2O_3 based system. However, for M_xO_y = Yb_2O_3, crystals up to 200 µm in size were successfully isolated in a microcrystalline matrix of $Ba_3YbRu_2O_9$. The system

with M_xO_y = Tb_4O_7 demonstrated the most extensive crystallization, with the entire sample crystallizing to form crystals of up to 200 µm in size, see Figure 5.21.

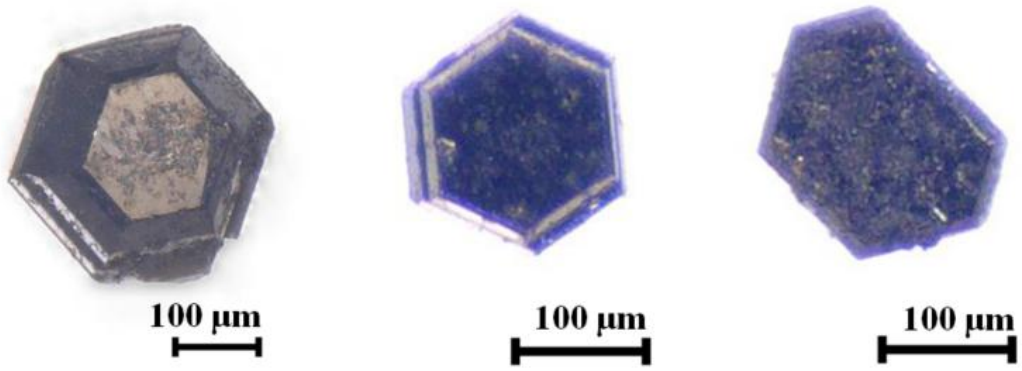

Figure 5.21: (a) $Ba_3YRu_2O_9$ crystal, (b) $Ba_3TbRu_2O_9$ crystal, and (c) $Ba_3YbRu_2O_9$ crystal.

S-ID	Educts	Crystal to flux ratio	Total weight [g]	Time to T_{max} [h]	T_{max} [K]	Time at T_{max} [h]	T_{min} [K]	Rate [K/h]	Products identified by P-XRD	Crystal size [mm]
1	Product from RUSC1:	1:30	3	40	1623	48	1223	2	$Ba_3ScRu_2O_9$ + $BaRuO_3$	<0.1
2	Product from RUY1:	1:30	3	40	1623	48	1223	2	$Ba_3YRu_2O_9$ + $BaRuO_3$	0.15
3	Product from RUTB1:	1:30	10	10	1573	20	1223	1	$Ba_3TbRu_2O_9$ +	0.2
4	Product from RUYB1:	1:30	3	40	1623	48	1223	2	$Ba_3YbRu_2O_9$	0.2
5	Product from RULU1:	1:30	3	40	1623	48	1223	2	$Ba_3LuRu_2O_9$ + $Ba_5Ru_2O_{10}$	<0.1

Table 5.20: Growth conditions and resulting phases observed in the systems BaO–*M*–RuO_2 with *M* = Sc_2O_3, Y_2O_3, Tb_2O_3, Yb_2O_3 and Lu_2O_3.

6 Characterization Iridates

Following the successful synthesis and growth of various 12L-perovskite compounds, this chapter focuses on the comprehensive characterization of the resulting single crystals. While the preceding sections primarily discussed the optimization of growth parameters and flux interactions, the focus now shifts to the structural, chemical, and thermal properties of the obtained materials. A range of analytical techniques was employed to assess compositional homogeneity, thermal stability, and structural features.

6.1 $Ba_4Ir_3O_{10}$

The first synthesis and structural description of $Ba_4Ir_3O_{10}$ dates back to 1991 [115]. In the study [115] for the synthesis, a mixture of $BaCO_3$, IrO_2, and $BaCl_2 \cdot 2H_2O$ in a molar ratio of 1 : 1 : 10 had been used. Due to the thermal decomposition of the hydrate, BaO is partially formed, which allows $Ba_4Ir_3O_{10}$ to crystallize even from a composition that is nominally undersaturated with respect to barium [115]. The $BaCl_2$ flux was evaporated, and small crystals of $Ba_4Ir_3O_{10}$ had been obtained and analyzed using X-ray diffraction. The structure was initially described in the monoclinic space group $P2_1/a$, attributed to a tilting of the octahedral units [115]. Later studies proposed an undistorted structure with higher symmetry, assigning the compound to the orthorhombic space group Cmca [116]. However, upon closer inspection, this structure appears to correspond to $Ba_7Ir_6O_{19}$ [117]. Subsequent investigations in 2021 and 2022 confirmed the presence of monoclinic distortions and supported the assignment of space group $P2_1/a$ [103] [102].

Two approaches for synthesizing single crystals of $Ba_4Ir_3O_{10}$ larger than 1 mm^3 are reported in the literature. In both methods, $BaCO_3$, IrO_2, and $BaCl_2 \cdot 2H_2O$ are used as starting materials and heated in a platinum crucible. One approach employs a molar ratio of 1 : 10 : 2.7, a maximum temperature of 1733 K, and a cooling rate of 4 K/h [118]. The second approach uses a molar ratio of 3 : 1 : 5, a maximum temperature of 1623 K, and a slower cooling rate of 1 K/h [103]. Since iridium is significantly rarer than $BaCO_3$, the second approach without IrO_2 excess was chosen for crystal growth. A mixture of $BaCO_3$

and IrO_2 with $BaCl_2 \cdot 2H_2O$ in a molar ratio of 3 : 1 : 5 was homogenized and placed in a sealed alumina crucible. The mixture was then cooled from 1623 K to 1223 K at a rate of 1 K/h. After dissolving the flux with distilled water, single crystals of $Ba_4Ir_3O_{10}$ were successfully obtained.

S-ID	Educts [molar ratio]			Total weight [g]	Time to T_{max} [h]	T_{max} [K]	Time at T_{max} [h]	T_{min} [KC]	Rate [K/h]	Product identified by P-XRD	Crystal size [mm]
	$BaCO_3$	IrO_2	$BaCl_2 \cdot 2H_2O$								
1	3	1	5	3	10	1623	10	1223	1	$Ba_4Ir_3O_{10}$	>1

Table 6.1: Summary of the crystal growth conditions for $Ba_4Ir_3O_{10}$.

Figure 6.1: $Ba_4Ir_3O_{10}$ single crystals obtained from $BaCl_2$ flux growth, exhibiting well-defined morphology and sizes in the millimeter range. Scale bar: 1 mm

6.1.1 Elemental analysis

To ensure comparability between different analytical methods, $Ba_4Ir_3O_{10}$ crystals were analyzed using two different systems: a SEM equipped with an EDX detector, and an EPMA equipped with a WDX detector system. The $Ba_4Ir_3O_{10}$ crystal was embedded in epoxy resin and polished to a planar surface, minimizing surface roughness and ensuring optimal flatness. An additional crystal was mounted on carbon adhesive tape with a planar crystal face oriented perpendicular to the electron beam as described in Section 3.3. This allowed for a comparison between EPMA and SEM data, as well as an assessment of the influence of sample preparation on the measurement results.

A comparison of the datasets reveals that the SEM systematically reports slightly higher BaO content and a lower IrO_2 content compared to the microprobe. The EPMA analysis yielded an average BaO concentration of 58.24 mol% and an IrO_2 concentration of 41.67 mol%, with a standard deviation of 0.17 mol% for both elements. In contrast, the SEM measurements indicated a BaO concentration of 60.04 mol% and an IrO_2 concentration of 39.96 mol%, with a standard deviation of 0.33 mol% for both elements. This suggests that SEM consistently overestimates barium by approximately 2 mol% and underestimates iridium by the same amount. The strong correlation is likely an artifact resulting from the normalization of measured values to 100 %, inherent to the internal data processing. The discrepancy between the EDX and WDX data is likely due to a combination of the lower accuracy of the EDX technique and sample preparation, as discussed in detail in Section 3.3. When comparing the measured concentrations to the nominal stoichiometry of the $Ba_4Ir_3O_{10}$ compound, even the microprobe data show slightly elevated barium content and correspondingly reduced iridium content. This deviation suggests that the actual stoichiometry does not precisely match the ideal formula, potentially indicating structural defects within the crystal lattice.

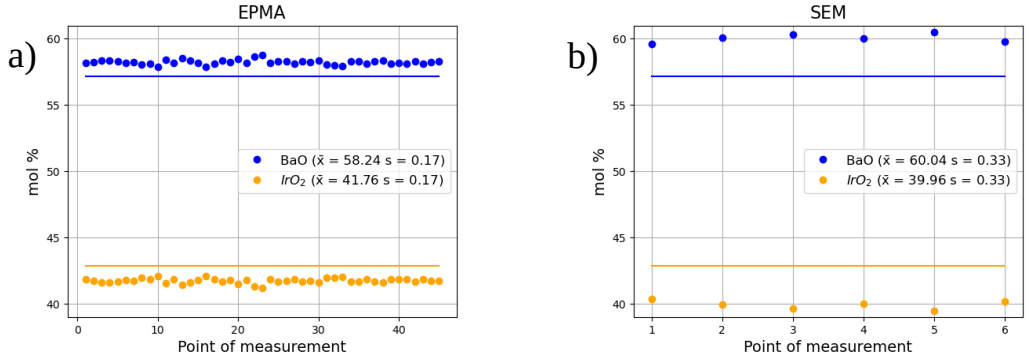

Figure 6.2: a) Quantitative chemical composition of $Ba_4Ir_3O_{10}$ determined by WDX analysis using EPMA. b) Corresponding EDX analysis using SEM. In both plots, the nominal stoichiometry of BaO : IrO_2 = 4 : 3 in $Ba_4Ir_3O_{10}$ is indicated by horizontal lines for comparison. The mean of all data points is denoted by $\bar{x}$, and the standard deviation by s.

6.1.2 Structural analysis

$Ba_4Ir_3O_{10}$ represents the first known ternary compound with this specific stoichiometry [115]. The unit cell is based on one iridium atom located at the origin on the 2a Wyckoff position, forming a C-centered Bravais lattice. A second iridium atom is located on a general position, resulting in the formation of a three-dimensional framework of corner-sharing $[Ir_3O_{12}]$ clusters through translational repetition. In $Ba_4Ir_3O_{10}$, a tilting of the $[Ir_3O_{12}]$ units leads to a monoclinic distortion of the structure, which crystallizes in the space group $P2_1/a$ [115]. The undistorted orthorhombic symmetry is reported for the quaternary compound $Ba_4Ir_{1.45}Ti_{1.55}O_{10}$ [119].

Between the $[Ir_3O_{12}]$ clusters the structure is stabilized by barium atoms, which also occupy two general Wyckoff positions. Additionally, five oxygen atoms located on general positions complete the coordination environment, forming $[IrO_6]$ octahedra around each iridium center.

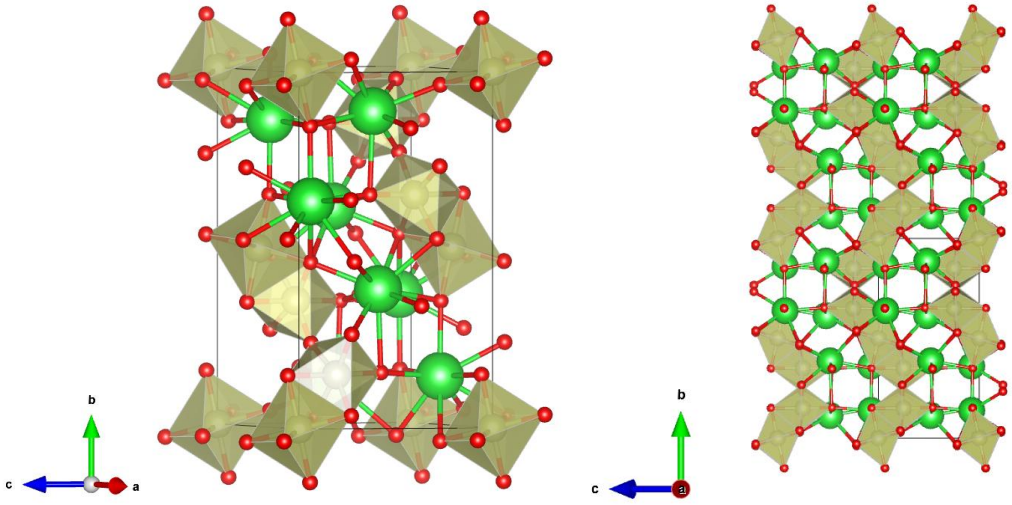

Figure 6.3: Representation of the $Ba_4Ir_3O_{10}$ crystal structure. Left: the primitive unit cell with a c-centered iridium based Bravais lattice. Right: the extended structure generated by translation, highlighting the corner-sharing connectivity between $[Ir_3O_{12}]$ units. (Data taken from [115], Visualization created using VESTA)

A single crystal of $Ba_4Ir_3O_{10}$ was ground into powder and analyzed via P-XRD. As previously discussed, the monoclinic distortion was clearly confirmed. The structure model obtained through Rietveld refinement based on data from [115] shows excellent agreement with the experimental data. The refinement included lattice parameters, atomic positions, and isotropic ADPs. The final model yielded a goodness-of-fit (*GOF*) value of 1.24, confirming the high quality of the structural solution.

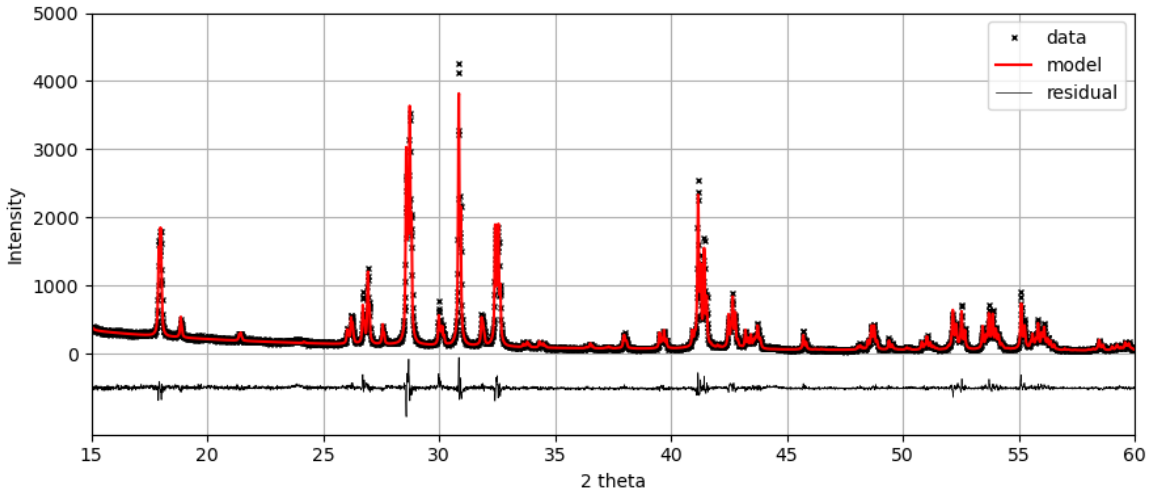

Figure 6.4: Experimental powder X-ray diffraction (P-XRD) pattern of $Ba_4Ir_3O_{10}$ (black) measured at room temperature, shown together with the calculated pattern from Rietveld refinement (red) and the difference curve below. The refinement confirms the monoclinic symmetry (space group $P2_1/a$) and shows excellent agreement with the experimental data.

Metric	$P2_1/a$	a = 5.78177 Å	b = 13.20345 Å	c = 7.23790 Å	β = 113.145 °
Atoms	**Site**	**x**	**y**	**z**	B_{eq}
Ba1	4e	0.97025	0.63920	0.92951	0.82
Ba2	4e	0.26268	0.61207	0.52104	0.63
Ir1	2a	0	0	0	1.12
Ir2	4e	0.13076	0.84991	0.25067	0.94
O1	4e	0.02853	0.16029	0.06751	3.06
O2	4e	0.67631	0.03889	0.77640	2.73
O3	4e	0.12343	0.04650	0.79771	0.87
O4	4e	0.74278	0.15462	0.45495	0.02
O5	4e	0.57442	0.23706	0.70080	5.70
					***GOF* = 1.24** R_{Bragg} **= 2.4**

Table 6.2: Crystallographic data and structural parameters for $Ba_4Ir_3O_{10}$ obtained from Rietveld refinement of powder X-ray diffraction data. The table includes lattice parameters, atomic coordinates and isotropic ADPs.

6.2 $Ba_4MIr_3O_{12}$ (*M* = Ce, Eu, Nb, Ta)

6.2.1 Elemental analysis

EDX spectroscopy was employed to assess the chemical composition and homogeneity of $Ba_4MIr_3O_{12}$ single crystals grown within the BaO–*M*–IrO_2 systems, where *M* = Eu, Ce, Nb, or Ta. Idiomorphic crystals with *M* = Eu, Ce, and Nb were mounted on carbon adhesive pads with their dominant (001) face oriented perpendicular to the electron beam and analyzed using SEM. In contrast, $Ba_4TaIr_3O_{12}$ crystals were embedded in epoxy resin, mechanically polished, and examined with EPMA using WDX analysis.

The measured data are shown in Figure 6.5. The plots show the molar percentages of the oxide components within the crystals. To improve comparability between different compositions, the measured molar amounts of Eu_2O_3, Nb_2O_5, and Ta_2O_5 were recalculated based on the corresponding monometallic oxides EuO, $NbO_{2.5}$, and $TaO_{2.5}$. All investigated crystals exhibited homogeneous elemental distributions, with standard deviations below 0.7 %, indicating high compositional uniformity. No aluminum contamination was detected within the detection limits. To highlight potential deviations from the ideal stoichiometry (Ba = 50 %, Ir = 37.5 % and *M* = 12.5 %), horizontal dashed lines representing the nominal values were added to the corresponding plots Figure 6.5.
For crystals with *M* = Eu, Ce, and Nb, the measurements revealed a slight relative excess of barium (~3 mol%) accompanied by a corresponding deficit in Ir and *M*. This deviation may be attributed to systematic measurement uncertainties, as previously discussed for $Ba_4Ir_3O_{10}$. In contrast, crystals containing tantalum (*M* = Ta), measured with the EPMA, closely matched the nominal composition, confirming accurate incorporation of the target stoichiometry during synthesis.

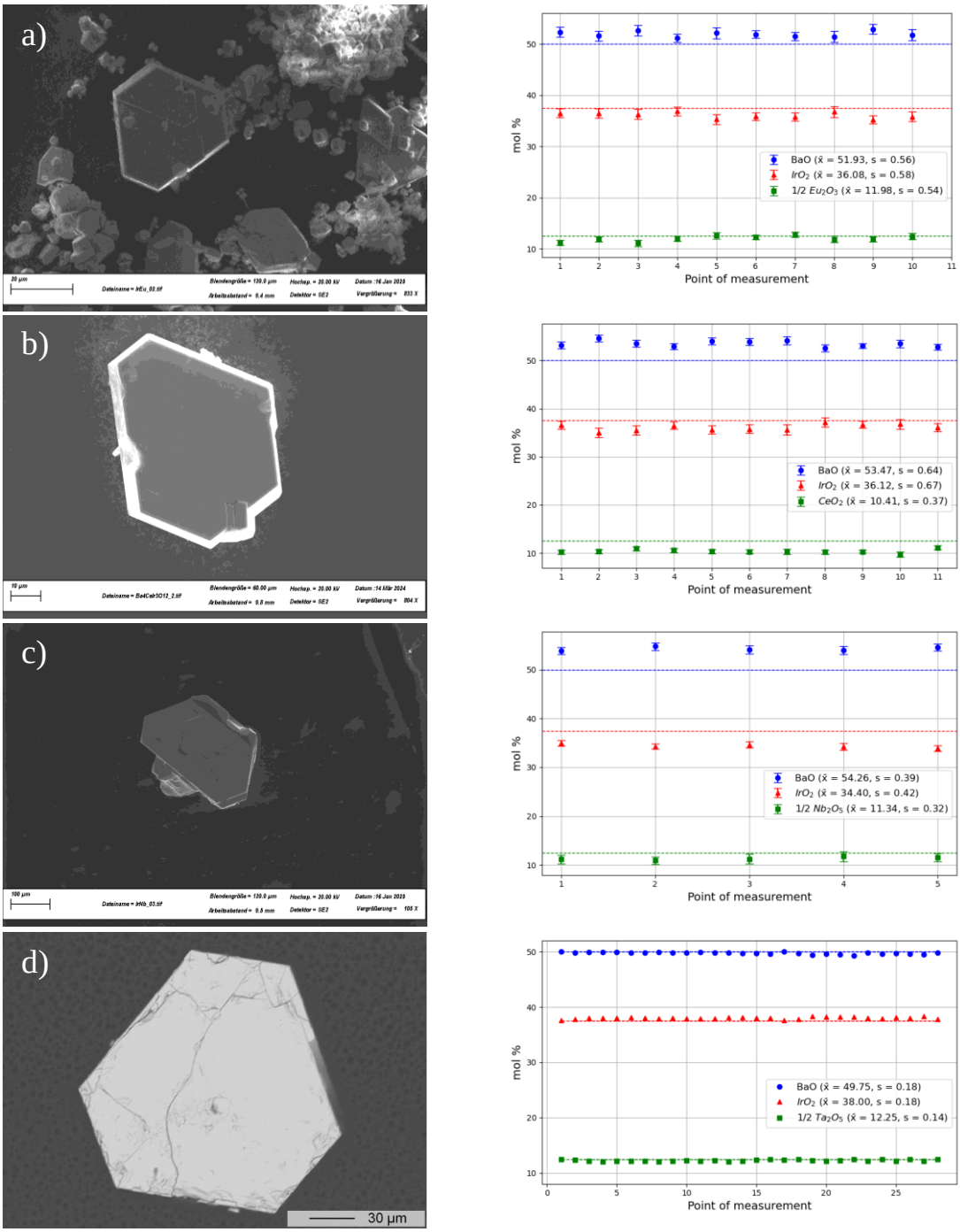

Figure 6.5: a–c) EDX analyses of $Ba_4EuIr_3O_{12}$, $Ba_4CeIr_3O_{12}$, and $Ba_4NbIr_3O_{12}$ single crystals, each measured on the (001) surface. d) WDX data for a $Ba_4TaIr_3O_{12}$ crystal. The EDX measurements indicate slightly elevated barium content across all samples, which is attributed to non-ideal measurement geometry, an effect previously observed in $Ba_4Ir_3O_{10}$ as well. When accounting for this systematic deviation, all measured compositions are in good agreement with the expected stoichiometry.

6.2.2 Thermal analysis

Thermal analysis was conducted on homogeneous powder samples of $Ba_4MIr_3O_{12}$ (*M* = Eu, Ce, Nb and Ta). Approximately 50 mg of each sample was analyzed using STA. The samples were placed in Al_2O_3 crucibles with a loosely fitting lid, heated at a rate of 20 K/min to 1673 K, held at this temperature for 5 minutes, and then cooled at the same rate to 1073 K. The data are shown in Figure 6.6.

All compounds exhibited a single endothermic decomposition reaction, with no indication of a structural phase transition.

- $Ba_4EuIr_3O_{12}$ showed a minor mass loss of approximately 1.33 wt%, a T_{onset} of 1468 K, and an endothermic signal intensity of $9.3*10^3$ µV/mmol.
- $Ba_4CeIr_3O_{12}$ decomposed at a higher temperature, with a T_{onset} of 1535 K, a mass loss of 1.41 wt% and a lower signal intensity of $8*10^3$ µV/mmol.
- In contrast, $Ba_4NbIr_3O_{12}$ showed a T_{onset} of 1496 K, a significantly higher mass loss of 3.98 wt%, and a markedly stronger thermal signal of $8.8*10^4$ µV/mmol.
- Similarly, $Ba_4TaIr_3O_{12}$ decomposed at 1465 K, with a mass loss of 3.89 wt% and an endothermic signal intensity of $8.8*10^4$ µV/mmol.

These values indicate that the decomposition of the Nb- and Ta-containing phases is more extensive in terms of mass loss and significantly more energy-intensive compared to the Ce- and Eu-analogues. The much higher thermal signal intensities, increased by roughly a factor of ten, point to a substantially greater enthalpy change during decomposition. While their decomposition temperatures are similar or even slightly lower, this does not necessarily imply reduced thermal stability but rather a more energetically demanding decomposition process for $Ba_4NbIr_3O_{12}$ and $Ba_4TaIr_3O_{12}$.

Post-experimental P-XRD analysis confirmed the decomposition of all trimer phases. $Ba_4EuIr_3O_{12}$ and $Ba_4CeIr_3O_{12}$ exhibit partial decomposition to a dimer-type phase before undergoing complete breakdown at higher temperatures. In contrast, the decomposition products of $Ba_4NbIr_3O_{12}$ and $Ba_4TaIr_3O_{12}$ could not be matched to any known entries in the ICSD database. However, all samples clearly showed the presence of elemental iridium as a secondary phase.

The decomposition at high temperatures indicates that the phases do not melt congruently, which complicates crystallization at elevated temperatures, as previously discussed in the crystal growth section.

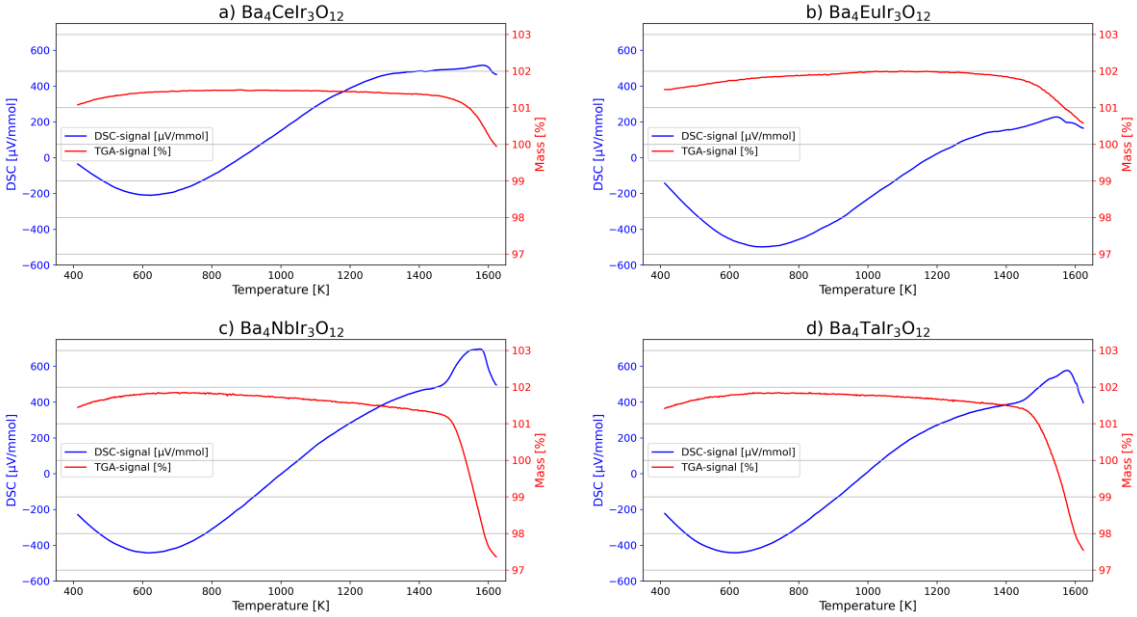

Figure 6.6: Shown are STA data for (a) $Ba_4CeIr_3O_{12}$, (b) $Ba_4EuIr_3O_{12}$, (c) $Ba_4NbIr_3O_{12}$, and (d) $Ba_4TaIr_3O_{12}$. The TGA signal is displayed in red, while the DSC signal is shown in blue. All phases exhibit an endothermic decomposition around 1473 K, accompanied by a mass loss detected in the TGA signal.

6.2.3 Structural analysis

6.2.3.1 P-XRD:

Structural analysis of $Ba_4MIr_3O_{12}$ (M = Eu, Ce, Nb, Ta) was performed using powder X-ray diffraction in a temperature range of 300 K to 12 K, with a step size of 0.015° and an exposure time of 1 s per step. The angular range covered was 10°–120° in 2θ. Structural refinements were conducted using the Rietveld method (program: TOPAS [64]), based on the models of $Ba_4EuIr_3O_{12}$ [60] and $Ba_4NbIr_3O_{12}$ [30]. The measured data and corresponding Rietveld refinement at 290 K are presented in Figure 6.7, the low-temperature measurement is provided in Appendix B.

P-XRD analysis confirmed a phase-pure product for the compounds $Ba_4MIr_3O_{12}$ (M = Eu, Nb and Ta) sample. In the Ce-containing compound, weak reflections corresponding to residual CeO_2 were observed.
The lattice parameters obtained for $Ba_4MIr_3O_{12}$ (M = Eu, Ce, Nb) showed good agreement with the literature [60; 53], while $Ba_4TaIr_3O_{12}$ is isotypic to $Ba_4NbIr_3O_{12}$. All compounds exhibited similar structural trends upon cooling: the a- and b-axes contracted with decreasing temperature, while the c-axis remained largely unchanged. For M = Eu and Ce,

the monoclinic angle β increased slightly at lower temperatures, indicating an enhancement of the monoclinic distortion.

A comparison of the monoclinic structures with *M* = Eu and Ce to the rhombohedral variants with *M* = Nb and Ta clearly reveals the reduction in symmetry. This is particularly evident from the fact that the monoclinic angle β deviates from 90°. As a result, a doubling of diffraction peaks is observed in the 2θ range between 15° and 20°. In the rhombohedral phase, the reflections in this region are described by symmetry-equivalent planes of the forms {101} and {012}. Upon transformation to the monoclinic setting the corresponding reflections are described by the planes $\{20\bar{1}\}$ and {111}, or $\{11\bar{2}\}$ and {202}, respectively. These planes are sensitive to changes in the monoclinic angle β. As β deviates from 90°, their interplanar spacings (*d*-values) diverge slightly, resulting in distinct diffraction angles in the P-XRD pattern. The same effect is also observed in the region between 26° and 29° 2θ, where additional peak splitting occurs due to further divergence of previously overlapping reflections.

The temperature-dependent measurements for *M* = Eu, Ce reveal a slight increase in the monoclinic angle β upon cooling. This indicates that the monoclinic distortion becomes more pronounced at lower temperatures, leading to a further separation of the corresponding split reflections. In contrast, for the phases with *M* = Nb and Ta, no peak splitting is observed even at low temperatures. This suggests that the rhombohedral symmetry is preserved throughout the temperature range investigated. The results of the Rietveld refinement are summarized in Table 6.3.

Compound	*a* [Å]	*b* [Å]	*c* [Å]	β [°]	R_{Bragg}	*GOF*
$Ba_4CeIr_3O_{12}$ [290 K]	10.17721(4)	5.87944(2)	29.48772(2)	91.2080(8)	6.02	2.37
$Ba_4CeIr_3O_{12}$ [12 K]	10.16401(9)	5.87164(3)	29.46632(1)	91.6769(3)	7.07	2.45
$Ba_4EuIr_3O_{12}$ [290 K]	10.18938(7)	5.88039(5)	29.63825(6)	92.4559(2)	4.61	2.15
$Ba_4EuIr_3O_{12}$ [12 K]	10.17479(4)	5.87015(3)	29.63378(6)	92.8288(6)	2.99	1.96
$Ba_4NbIr_3O_{12}$ [290 K]	5.76745(6)	-	28.72555(9)	-	6.11	2.6
$Ba_4NbIr_3O_{12}$ [12 K]	5.76072(1)		28.68215(6)		6.44	2.74
$Ba_4TaIr_3O_{12}$ [290 K]	5.7719(6)	-	28.71670(6)	-	3.92	2.41
$Ba_4TaIr_3O_{12}$ [12 K]	5.7649(4)		28.67080(4)		4.09	2.45

Table 6.3: Results of the Rietveld refinements for $Ba_4CeIr_3O_{12}$, $Ba_4EuIr_3O_{12}$, $Ba_4NbIr_3O_{12}$ and $Ba_4TaIr_3O_{12}$ based on P-XRD data. The lattice parameters *a*, *b*, *c*, and β at 290 K and 12 K are listed, along with the corresponding R_{Bragg} and *GOF* values.

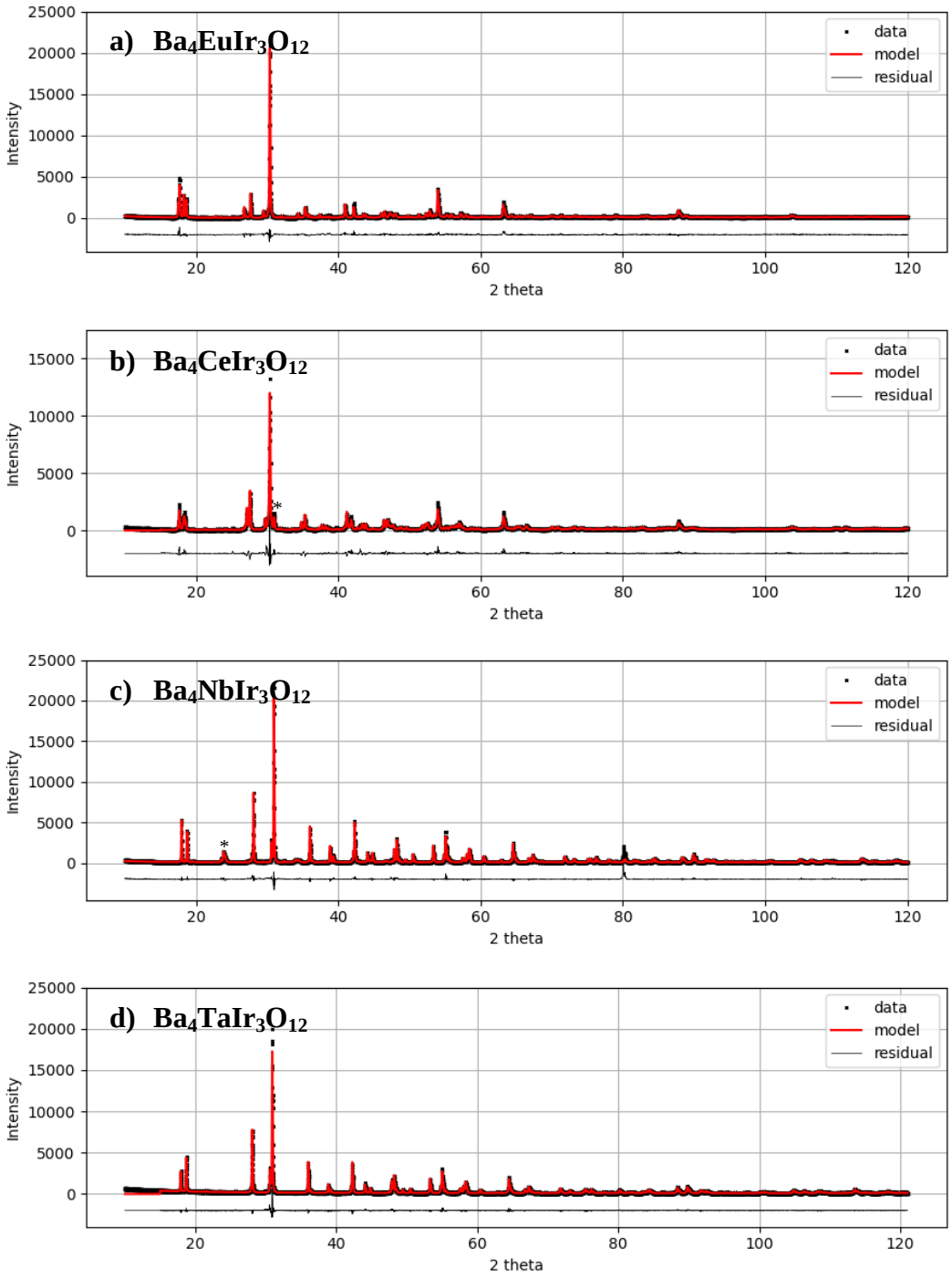

Figure 6.7: Plots (a) - (d) show Rietveld refinements for $Ba_4EuIr_3O_{12}$ (a), $Ba_4CeIr_3O_{12}$ (b), $Ba_4NbIr_3O_{12}$ (c), and $Ba_4TaIr_3O_{12}$ (d). In each case, the measured powder diffraction data are shown in black, the calculated model in red, and the difference (residual) is plotted below. Peaks from impurity phases, $BaIrO_3$ for $Ba_4CeIr_3O_{12}$ and $BaCO_3$ for $Ba_4NbIr_3O_{12}$, are marked with an asterisk (*).

6.2.3.2 SC-XRD:

Attempts to obtain single-crystal data for $Ba_4EuIr_3O_{12}$ and $Ba_4CeIr_3O_{12}$ were unsuccessful. The structures of all examined crystals appeared to be highly disordered. While the *a* and *b* axis could be reliably indexed, determining the *c* axis proved difficult, see Figure 6.8. The 12-layer stacking sequence appears to be significantly disrupted by stacking faults, preventing indexing of the data with sufficient quality. Only for $Ba_4TaIr_3O_{12}$ was it possible to obtain high-quality single-crystal data.

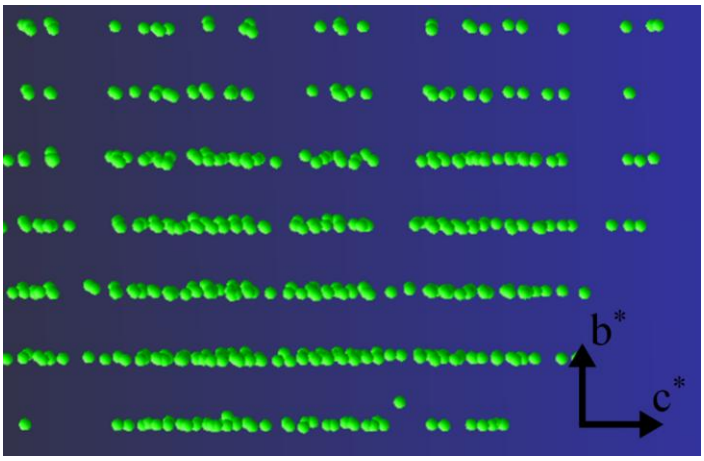

Figure 6.8: Shown are the measured reflections of a $Ba_4EuIr_3O_{12}$ single crystal as points in reciprocal space, viewed along a*. It is clearly visible that the periodicity along b* is largely undisturbed, whereas the periodicity along c* exhibits distinct disruptions. Due to these disturbances, it was not possible to reliably index the measured data or process them with sufficient accuracy.

During the selection of a suitable $Ba_4TaIr_3O_{12}$ crystal, it was observed that most crystals exhibited reflections indicative of a hexagonal superstructure. These reflections arise from twinning of obverse and reverse domains and do not correspond to a true hexagonal symmetry of the crystal. A twofold axis parallel to the threefold axis or parallel to the *a*-*b* plane can serve as the twin law, resulting in so-called obverse/reverse twinning [120]. In the hexagonal setting, the reflection condition for the first domain (obverse) is $-h+k+l=3n$, while for the second domain (reverse) it is $h-k+l=3n$ [120]. The structural solution was carried out using a monodomain crystal that did not exhibit hexagonal superstructure reflections.

For the single-crystal analysis, a 0.03 × 0.03 × 0.04 mm crystal was measured at 250 K. A total of 74016 reflections were collected and reduced to 6752 after scaling in Laue group -1. Further scaling using Jana2020 in space group $R\bar{3}m$ yielded 1335 unique reflections with an R_{int} value of 6.01 %. The precession map revealed clear trigonal symmetry, with no evidence of hexagonal superstructure reflections. The data agree well with a structural

model isotypic to $Ba_4NbIr_3O_{12}$.
A model with fully occupied atomic positions was assumed, in accordance with the measured chemical composition. All atoms were refined anisotropically. The full structural model is summarized in Table 6.4.

In comparison a structure model with a mixed atomic occupancy between tantalum and iridium results in a minor improvement of the wR_2-values by approximately 0.2 %. This model suggests that the 3b site is almost fully occupied by iridium, while approximately 26 % of the 6c site is occupied by tantalum. Conversely, the 3a site of tantalum shows a partial substitution of about 57 % by iridium. As the estimated errors are below 8 %, the mixed occupancies in the model can be considered statistically significant. However, the chemical analysis reveals a stoichiometric 1 : 3 ratio of Ta and Ir which do not fit with this model. In general, distinguishing between Ta (Z = 73) and Ir (Z = 77) remains challenging due to their high atomic numbers and the relatively small difference in electron count, resulting in similar scattering power.

While there are indications of mixed site occupancy, a full occupation of the trimer units by iridium appears more likely based on the results of the chemical analysis.

General Information	
Compound	$Ba_4TaIr_3O_{12}$
Space group	$R\bar{3}m$ (166)
Z	3
a, b, c	5.7724 (3) Å; 5.7724 (3) Å; 28.7081 (16) Å
V	828.405(11) $Å^3$
p_{calc}	9.0139 g/cm^3
T	250 K
Radiation wavelength	0.71073 Å
Crystal information	
Colour/shape	black, plate
Size	0.030 mm x 0.034 mm x 0.041 mm
Data collection	
Index ranges	-13 < h <13, -14 < k 13, -64 < l <65
Total reflections	74016
Independent reflections	1335
R_{int}	0.0602
Data reduction	
Absorption correction	multi scan
Absorption coefficient μ	59.930 mm^{-1}
F(000)	1872
Refined parameters	28
Final R indices	
all data	R_1 = 0.0267, wR_2 = 0.0434, GOF = 2,56
data with I > 3sigma(I)	R_1 = 0.0245, wR_2 = 0.0431, GOF = 2,64
GII:	**0.1672**

Atom	Site	x	y	z	U_{eq}
Ir1	3b	0	0	0.5	0.00416(7)
Ir2	6c	0	0	0.411587(8)	0.00434(5)
Ta1	3a	0	0	0	0.00345(7)
Ba1	6c	0	0	0.285811(16)	0.00719(8)
Ba2	6c	0	0	0.129037(16)	0.00842(9)
O1	18h	0.4908(3)	0.5092(3)	0.12248(12)	0.0077(8)
O2	18h	0.5045(3)	0.4955(3)	0.29406(11)	0.0091(9)

Atom	U11	U22	U33	U12	U13	U23
Ir1	0.00431(8)	0.00431(8)	0.00386(11)	0.00216(4)	0	0
Ir2	0.00447(7)	0.00447(7)	0.00407(9)	0.00224(3)	0	0
Ta1	0.00351(8)	0.00351(8)	0.00332(11)	0.00176(4)	0	0
Ba1	0.00701(10)	0.00701(10)	0.00754(14)	0.00351(5)	0	0
Ba2	0.00767(10)	0.00767(10)	0.00993(17)	0.00384(5)	0	0
O1	0.0092(8)	0.0092(8)	0.0078(10)	0.007(1)	0.0000(4)	0.0000(4)
O2	0.0094(9)	0.0094(9)	0.0115(12)	0.0069(11)	-0.0030(5)	0.0030(5)

Table 6.4: Atomic coordinates and anisotropic ADPs of $Ba_4TaIr_3O_{12}$ refined from SC-XRD data.

7 Characterization Ruthenates

7.1 $Ba_4MRu_3O_{12}$ (*M* = Ce, Pr, Ta)

7.1.1 Elemental analysis

For chemical analysis, $Ba_4CeRu_3O_{12}$ and $Ba_4TaRu_3O_{12}$ were measured using WDX spectroscopy while $Ba_4PrRu_3O_{12}$ was analyzed using the EDX. The results are shown in Figure 7.1.

The measured composition of $Ba_4CeRu_3O_{12}$ shows good agreement with the nominal stoichiometry. The average values for RuO_2 lie within the experimental error of their expected molar ratios. CeO_2 exhibits a slight deficiency of approximately 1 mol% while the BaO exhibits a slight excess of approximately 1 mol%. The $L\alpha_1$ lines of Ba (4.465 Å) and Ce (4.839 Å) lie in close proximity, making precise peak separation challenging and thereby complicating quantitative analysis. As a result, the measured data may indicate approximately 1 % vacancies on the Ce site, although this may alternatively result from the limited resolution in distinguishing these two elements. The composition of $Ba_4PrRu_3O_{12}$ is also consistent with the nominal stoichiometry within the standard deviation. Similar to the $Ba_4Ir_3O_{10}$ crystal, the measured values for barium show reduced precision and correlate with those of ruthenium. Further measurements using the EMPA are planned to clarify whether this reflects a chemical feature or is merely an artifact of the suboptimal measurement geometry. In any case, the measurement conditions appear to affect the determination of BaO and RuO_2 content much more strongly than that of Pr_6O_{11}. The standard deviation for Ba and Ru is approximately three times higher than for Pr.

In contrast, the measured composition of $Ba_4TaRu_3O_{12}$ shows a significant deviation from the ideal stoichiometry. While the barium content averages 50.36 mol% (s = 0.3 mol%), ruthenium shows an excess of +4.34 mol%, and tantalum a corresponding deficiency of -4.71 mol%. This suggests mixed occupancy at the tantalum site by ruthenium.

a) $Ba_4CeRu_3O_{12}$

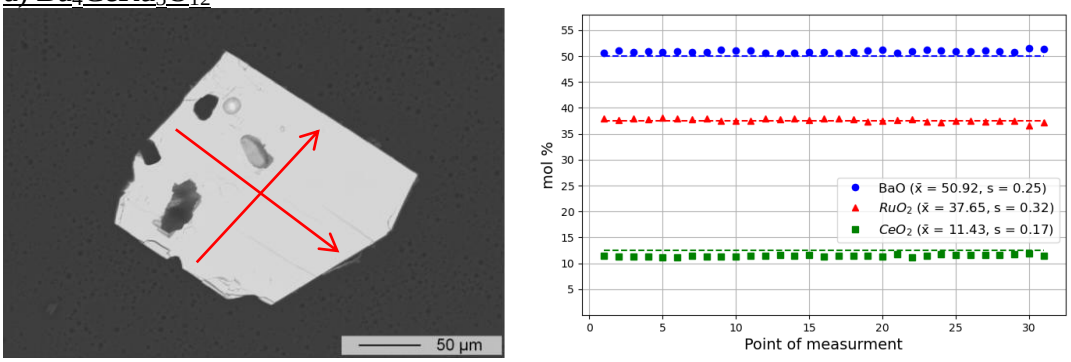

b) $Ba_4TaRu_3O_{12}$

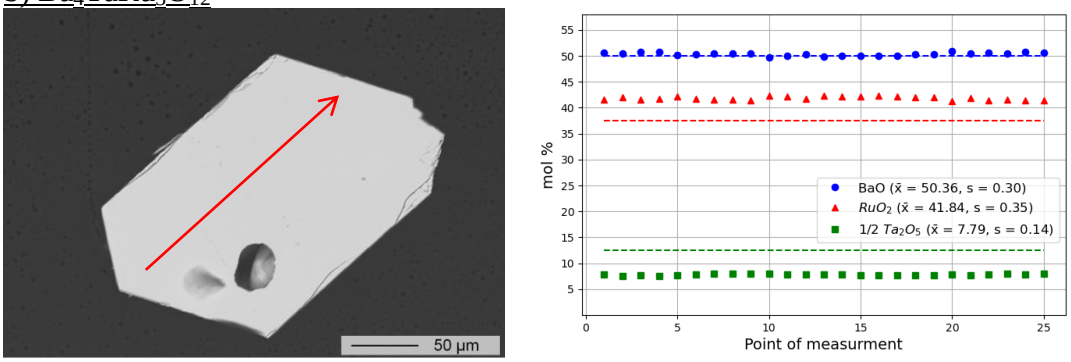

c) $Ba_4PrRu_3O_{12}$

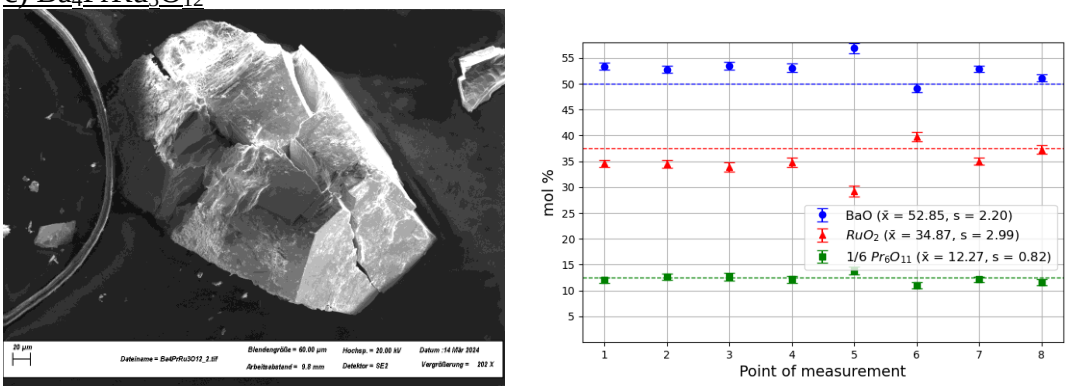

Figure 7.1: Elemental analyses of $Ba_4MRu_3O_{12}$ compounds are shown. Samples (a) $Ba_4CeRu_3O_{12}$ and (b) $Ba_4TaRu_3O_{12}$ were analyzed by WDX while sample (c) $Ba_4PrRu_3O_{12}$ was analyzed by EDX. For $Ba_4CeRu_3O_{12}$, a slight cerium deficiency is detected. In the case of $Ba_4PrRu_3O_{12}$, the data quality is insufficient to draw conclusions regarding site occupancy. The composition measured for $Ba_4TaRu_3O_{12}$ indicates partial substitution between Ta and Ru. Dashed lines indicate the nominal molar content of each oxide in the compound. For multi-metal oxides, the values were normalized to the number of metal atoms per formula unit.

7.1.2 Structural analysis

7.1.2.1 P-XRD:

Powder X-ray diffraction data of $Ba_4MRu_3O_{12}$ compounds with M = Ce, Pr, and Ta were collected analogously to the Ir-based systems. Structural models of $Ba_4PrRu_3O_{12}$ [51] and $Ba_4NbRu_3O_{12}$ [121] were used as starting points for the Rietveld refinement. Measurements were carried out across a temperature range from 300 K to 12 K. The measured data and corresponding Rietveld refinement at 290 K are presented in Figure 7.2, the low-temperature measurement is provided in Appendix B. The results of the Rietveld refinement are summarized in Table 7.1.
Both $Ba_4CeRu_3O_{12}$ and $Ba_4PrRu_3O_{12}$ are consistent with the monoclinic 12L-perovskite type structure. As these compounds are isotypic to their Ir-based analogues, clear monoclinic peak splitting is observed as discussed for $Ba_4EuIr_3O_{12}$ and $Ba_4CeIr_3O_{12}$ (see Figure 7.2 (a/b), resp. (c)). The degree of distortion increases with decreasing temperature and is reflected by an increase in the β angle specifically, by 0.9° in $Ba_4CeRu_3O_{12}$ and 0.7° in $Ba_4PrRu_3O_{12}$ between 300 K and 12 K. Simultaneously, all lattice parameters (*a*, *b*, and *c*) contract due to reduced thermal motion. The *c*-axis is proportionally less affected than *a*- and *b*-axes, as its length is coupled to the β angle. As thermal motion decreases, atomic packing becomes more efficient.
In contrast, $Ba_4TaRu_3O_{12}$ can be accurately modeled in the rhombohedral space group and shows no evidence of monoclinic distortion. Even at 12 K, no peak splitting is observed, and the lattice parameters contract uniformly, resulting only in a shift of reflections toward higher 2θ values. Introducing a partial substitution of Ta by Ru at the Ta site led to a notable improvement of the R_{Bragg} value of 0.2 % and aligns well with the chemical composition obtained from elemental analysis.

A comparison of powder X-ray diffraction patterns of a solid-state sample of $Ba_4CeRu_3O_{12}$ and a single crystal reveals notable differences. The *a*- and *c*-axes are shortened by approximately 0.1 %, while the *b*-axis is reduced by around 0.04 %. The β angle decreases from 90.98° to 90.66°, reflecting a reduction of 0.3 %. These changes indicate a significant reduction of monoclinic distortion in the single crystal. The findings support the interpretation that this distortion is induced by structural defects. Single crystals grown under near equilibrium conditions exhibit fewer defects and consequently show reduced distortion. In contrast, solid-state samples, whose crystallization is driven by high temperatures and rapid cooling, are often far from equilibrium, leading to a higher density of crystal defects and a more distorted structure.

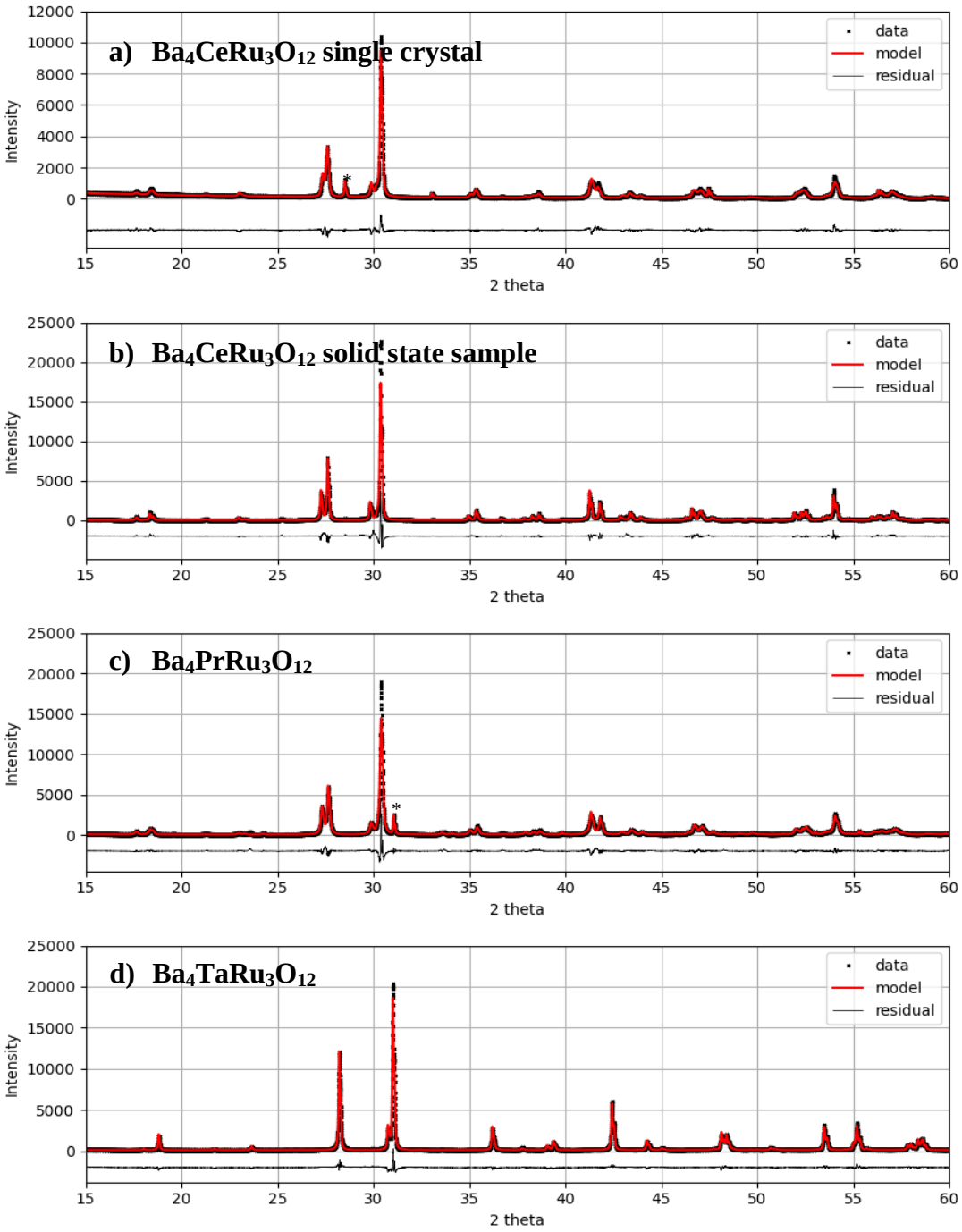

Figure 7.2: Plots a-d show Rietveld refinements of $Ba_4MRu_3O_{12}$ compounds. Panels (a) and (b) correspond to $Ba_4CeRu_3O_{12}$, with a showing data from a single crystal and a sintered sample. Clear differences in peak splitting are observed between 25–30° 2θ and 43–49° 2θ. Panel (c) shows the refinement for $Ba_4PrRu_3O_{12}$, while (d) presents the pattern for $Ba_4TaRu_3O_{12}$. Peaks from impurity phases, CeO_2 for $Ba_4CeRu_3O_{12}$ and $BaRuO_3$ for $Ba_4PrRu_3O_{12}$, are marked with an asterisk (*).

Compound	*a* [Å]	*b* [Å]	*c* [Å]	*β* [°]	R_{Bragg}	*GOF*
$Ba_4CeRu_3O_{12}$ [290 K]	10.17406(5)	5.87902(7)	29.39051(7)	90.9828(4)	5.07	2.7
$Ba_4CeRu_3O_{12}$ [12 K]	10.15047(7)	5.86821(4)	29.37951(8)	91.8228(8)	6.49	2.81
$Ba_4PrRu_3O_{12}$ [290 K]	10.16350(6)	5.87093(2)	29.32037(3)	90.9186(1)	3.76	2.39
$Ba_4PrRu_3O_{12}$ [12 K]	10.14654(9)	5.864250	29.31122(1)	91.5590(5)	4.52	2.54
$Ba_4TaRu_3O_{12}$ [290 K]	5.75903(9)	5.75903(9)	28.56621(7)	-	3.32	1.64
$Ba_4TaRu_3O_{12}$ [12 K]	5.75085(7)	5.75085(7)	28.53676(8)	-	3.36	1.67

Table 7.1: Results of the Rietveld refinements for $Ba_4CeRu_3O_{12}$, $Ba_4PrRu_3O_{12}$, and $Ba_4TaRu_3O_{12}$ based on P-XRD data. The lattice parameters *a*, *b*, *c*, and *β* at 290 K and 12 K are listed, along with the corresponding R_{Bragg} and *GOF* values.

7.1.2.2 SC-XRD:

Since single crystal structure data of $Ba_4TaRu_3O_{12}$ and $Ba_4CeRu_3O_{12}$ are not available in literature, the crystal structures of those compounds were determined here.

$Ba_4TaRu_3O_{12}$:

For single-crystal X-ray diffraction, a crystal of dimensions 0.03 × 0.03 × 0.04 mm³ was measured at 250 K using Mo-Kα radiation (λ = 0.71073 Å). Due to the presence of hexagonal superstructure reflections, obverse/reverse twinning was suspected and the integration was performed in the hexagonal setting. A total of 351681 reflections were collected, of which 20022 remained after intensity scaling in Laue group $\bar{1}$. Refinement in space group $R\bar{3}m$ using Jana2020 yielded 2201 unique reflections with an internal agreement factor of R_{int} = 8.78 %.
Refinement of the volume fractions of the twin domains revealed an approximate ratio of 1:1. All atoms were refined with anisotropic ADPs, and an isotropic extinction correction (type 1, Gaussian model) was applied in the final refinement cycle.

The initial model was based on the published structure of $Ba_4NbRu_3O_{12}$ [121]. Introducing a partial occupancy of ~25 % Ru on the Ta site improved the refinement quality, reducing R_1(obs) from 6.33 % to 4.8%, and the weighted *R*-factor wR_2(obs) from 11.3 % to 7.68 %. This is consistent with chemical analysis of $Ba_4TaRu_3O_{12}$ crystals, which showed a Ru excess of 4.34 mol% and a Ta deficiency of 4.71 mol%.

Single-crystal studies on $Ba_4Nb_{1-x}Ru_{3+x}O_{12}$ in literature showed good agreement with space group $R\bar{3}m$, but suggested a possible symmetry reduction to $R\bar{3}$ [34]. A refinement of the data for $Ba_4TaRu_3O_{12}$ in the present work in the lower-symmetry group $R\bar{3}$ indeed reduced R_1(obs) further to 4.36 % and wR_2(obs) to 6.39 %, but introduced physically implausible parameters, such as negative ADPs for the oxygen atoms.
This instability is attributed to the lack of symmetry constraints on general positions in $R\bar{3}$,

which causes the oxygen atoms to drift from idealized positions, resulting in overfitting and non-physical ADPs.

Taken together, the data strongly support space group $R\bar{3}m$ as the correct description of the crystal structure.

General information

Compound	$Ba_4TaRu_3O_{12}$
Space group	$R\bar{3}m$ (166)
Z	3
a, b, c	5.7482 (7) Å; 5.7482(7) Å; 28.587(4) Å
V	818.01 $Å^3$
p_{calc}	7.4639 g/cm^3
T	250 K
Radiation wavelength	0.71073 Å

Crystal information

Colour/shape	black, plate
Size	0.030 mm x 0.034 mm x 0.041 mm

Data collection

Index ranges	-13 < h <13, -14 < k 13, -64 < l <65
Total reflections	351681
Independent reflections	2201
R_{int}	0.0803
Data reduction	
Absorption correction	multi scan
Absorption coefficient μ	28.28 mm^{-1}
F(000)	1551
Refined parameters	29

Final *R* indices

all data	R_1 = 0.0486, wR_2 = 0.0768, GOF = 4.84
data with I > 3sigma(I)	R_1 = 0.0480, wR_2 = 0.0768, GOF = 4.87
GII:	**0.183**

Atom	Site	Occ	x	y	z	U_{eq}
Ru1	3b	1	0	0	0.5	0.00293(10)
Ru2	6c	1	0	0	0.411757 (15)	0.00332(8)
Ta1	3a	0.734(4)	0	0	0	0.00347(8)
Ru3	3a	0.259(4)	0	0	0	0.00347(8)
Ba1	6c	1	0	0	0.128388(14)	0.00769(8)
Ba2	6c	1	0	0	0.286860(13)	0.00581(7)
O1	18h	1	0.4891(3)	0.5109(3)	0.12203(10)	0.0079(6)
O2	18h	1	0.5022(3)	0.4978(3)	0.29433(10)	0.0087(6)

Atom	U11	U22	U33	U12	U13	U23
Ru1	0.00248	0.00248	0.00383	0.00124	0	0
Ru2	0.00341	0.00341	0.00315	0.00171	0	0
Ta1	0.00318	0.00318	0.00405	0.00159	0	0
Ru3	0.00318	0.00318	0.00405	0.00159		
Ba1	0.00627	0.00627	0.01054	0.00313	0	0
Ba2	0.00518	0.00518	0.00708	0.00259	0	0
O1	0.00700	0.00700	0.01260	0.00570	0.00050	-0.00050
O2	0.00650	0.00650	0.01440	0.00420	-0.00090	0.00090

Table 7.2: Atomic coordinates and anisotropic ADPs of $Ba_4TaRu_3O_{12}$ refined from SC-XRD data.

$Ba_4CeRu_3O_{12}$:

Single-crystal X-ray diffraction data of a $Ba_4CeRu_3O_{12}$ crystal was readily indexed in the rhombohedral crystal system. Due to the presence of hexagonal superstructure reflections, attributed twinning domains, similar to the observations in $Ba_4TaIr_3O_{12}$ and $Ba_4TaRu_3O_{12}$, the data were integrated in the hexagonal setting. After intensity scaling in Jana2020 using space group $R\bar{3}m$, yielded an internal agreement factor R_{int} of 7.49 %. Notably, powder X-ray diffraction patterns of both a sintered sample and a finely ground large single crystal confirm monoclinic symmetry. However, refinement of the unit cell parameters shows that the monoclinic angle β is significantly reduced in the single crystal. Assuming superior crystallinity and fewer structural defects in the single crystal, this observation suggests a correlation between monoclinic distortion and defect density. A crystal with a diameter of approximately 50 µm may thus represent a near-ideal structure, exhibiting higher symmetry.

As a starting model, the structure was refined in space group $R\bar{3}m$ using $Ba_4HoRu_3O_{12}$ as a reference model [51]. A fully ordered model employing isotropic ADPs, including an obverse–reverse twin component with a refined volume fraction of approximately 3.7 %,

yielded a weighted residual $wR_2(obs)$ = 15 %. Anisotropic refinement yielded a marginal further improvement (~1 %) without introducing artifacts.

Transforming the isotropic model into the monoclinic space group C2/m resulted in a significantly lower R_{int} = 6.7 % and residual of $wR_2(obs)$ = 9 %, indicating the presence of monoclinic distortions. Allowing for anisotropic ADPs for all atoms further reduced the residual to $wR_2(obs)$ = 6 %. However, the increased number of parameters and reduced symmetry led to refinement instabilities. The Ce atom (originally on 3a) and Ru (on 3b) were split into symmetry-independent positions. The less-constrained sites developed non-positive definite ADPs, and six of twelve oxygen atoms also showed negative eigenvalues. All remaining atoms retained physically meaningful, positive-definite ADPs. To stabilize the model, the Ce atom, Ru atoms at the 3b site, and all oxygen atoms were subsequently refined isotropically.
Occupancy refinement of the Ce atom on the 4i site indicated approximately 5% vacancies, which slightly improved the model. The final refinement yielded R_1(all) = 10 %, significantly higher than R_1(obs) = 6 %, suggesting inconsistencies at high diffraction angles. Applying a resolution cut-off at $\sin(\theta)/\lambda = 0.9$ reduced R_1(all) to 6.5 %, while the weighted *R*-factors remained largely unaffected. This confirms a loss in data quality at high angles. The cut-off reduced the number of independent reflections from 21357 to 10640.

In summary, the crystal structure of $Ba_4CeRu_3O_{12}$ shows a slight monoclinic distortion, allowing for indexing in the rhombohedral space group. This contrasts with the powder X-ray diffraction (P-XRD) data obtained from solid-state samples, which indicate a more pronounced deviation from ideal symmetry, particularly in the β angle. The monoclinic model fits the data quantitatively better, though it becomes increasingly sensitive to instability due to the higher number of free parameters and the absence of symmetry constraints. Poor data quality at high diffraction angles may indicate the presence of structural defects. Such defects can also compromise the reliability of the refined ADPs, potentially leading to inaccurate thermal factors. The monoclinic distortion manifests as a rotation of the octahedral units, as discussed in Section 2.1.2. This is primarily reflected in the transformation of the oxygen atomic positions, while the positions of the heavier atoms remain largely unaffected.

General information	
Compound	$Ba_4CeRu_3O_{12}$
Space group	*C*2/*m* (12)
Z	6
a, b, c	10.16367 (9) Å; 5.868 (1) Å; 29.3028(6) Å
V	1747 $Å^3$
p_{calc}	6.7545 g/cm^3
T	250 K
Radiation wavelength	0.71073 Å
Crystal information	
Colour/shape	black, plate
Size	
Data collection	
Index ranges	-13 < h <13, -14 < k 13, -64 < l <65
Total reflections	324193
Independent reflections	21357
R_{int}	0.0672
Data reduction	
Absorption correction	multi scan
Absorption coefficient μ	20.946 mm^{-1}
F(000)	3060
Refined parameters	165
Final R indices	
all data	R_1 = 0.1003, wR_2 = 0.0701, *GOF* = 1.96
data with I > 3sigma(I)	R_1 = 0.0624, wR_2 = 0.0701, *GOF* = 2.30
Resolution cut-off applied:	
all data	R_1 = 0.0625, wR_2 = 0.0636, *GOF* = 2.34
data with I > 3sigma(I)	R_1 = 0.0490, wR_2 = 0.0605, *GOF* = 2.48
GII:	**0.133**

Atom	Site	Occ	x	y	z	U_{eq}
Ru1_1	2c	1	0	0	-0.5	0.00335(14)
Ru1_2	4i	1	-0.16815(7)	0.5	-0.833516(14)	0.00761(13)
Ru2_1	4i	1	-0.00387(7)	0	-0.414073(14)	0.00453(11)
Ru2_2	4i	1	-0.17041(7)	0.5	-0.747396(14)	0.00437(11)
Ru2_3	4i	1	0.16207(8)	0.5	-1.080268(17)	0.01136(15)
Ce1_1	2a	1	0	0	0	0.00474(9)
Ce1_2	4i	1	-0.16970(6)	0.5	-0.332996(10)	0.00149(7)
Ba1_1	4i	1	0.00111(6)	0	-0.283888(12)	0.00914(10)
Ba1_2	4i	1	-0.16580(6)	0.5	-0.617080(12)	0.00976(10)
Ba1_3	4i	1	0.16763(7)	0.5	-0.950801(13)	0.01534(14)
Ba2_1	4i	1	0.00142(7)	0	-0.130621(13)	0.01420(13)
Ba2_2	4i	1	-0.16624(5)	0.5	-0.463587(11)	0.00784(10)
Ba2_3	4i	1	0.16595(7)	0.5	-0.796944(14)	0.01416(12)
O1_1	4i	1	0.0164(8)	0.5	-0.1287(4)	0.035(3)
O1_2	4i	1	-0.1521(5)	1	-0.46222(15)	-0.0006(8)
O1_3	4i	1	0.1776(5)	1	-0.79068(17)	0.0035(13)
O1_4	8j	1	-0.2448(4)	-0.2646(8)	0.12281(13)	0.0097(10)
O1_5	8j	1	-0.0788(4)	0.2313(7)	-0.54470(10)	0.0058(8)
O1_6	8j	1	-0.4088(4)	0.2347(8)	-0.20934(15)	0.0148(12)
O2_1	4i	1	0.0172(7)	0.5	-0.2938(3)	0.020(2)
O2_2	4i	1	-0.1552(6)	1	-0.62841(16)	0.0048(11)
O2_3	4i	1	0.1815(7)	1	-0.9612(3)	0.0196(18)
O2_4	8j	1	-0.2490(4)	-0.2581(6)	0.28915(14)	0.0091(9)
O2_5	8j	1	-0.0823(4)	0.2371(8)	-0.37907(12)	0.0109(10)
O2_6	8j	1	-0.4140(5)	0.2385(9)	-0.04504(14)	0.0152(13)

Table 7.3: Atomic coordinates and isotropic ADPs of $Ba_4CeRu_3O_{12}$ refined from SC-XRD data.

7.2 $Ba_3MRu_2O_9$ (*M* = Ce, Eu, Tb, Yb and Y)

7.2.1 Elemental analysis

For chemical analysis, single crystals of $Ba_3MRu_2O_9$ (*M* = Eu, Ce, Tb, Yb, and Y) were investigated using a SEM equipped with an EDX system. Each crystal was mounted with its well-developed (001) face facing upward and fixed onto a piece of carbon adhesive tape. All analyzed crystals could clearly be assigned to the $Ba_3MRu_2O_9$ composition. Results of the analysis are presented in Figure 7.3.

$Ba_3CeRu_2O_9$ exhibits a CeO_2 deficiency of approximately 1 mol%, similar to that observed in $Ba_4CeRu_3O_{12}$ using WDX analysis. This may again result from the spectral overlap of characteristic X-ray emission lines of Ba and Ce in the EDX measurement. For all other compounds, the measured metal content on the *M* site agrees well with the nominal stoichiometry within an estimated experimental uncertainty of 5 to 15 % for elements present at concentrations above 5 mol%. The RuO_2 content is also consistent with the expected values for Ru atoms occupying the *M′* site.
The BaO content appears slightly elevated, likely due to the measurement geometry and imperfectly planar crystal surfaces, as previously discussed for $Ba_4Ir_3O_{10}$. Due to the relatively high experimental error, the data quality is insufficient to resolve minor vacancies. Nonetheless, within this limitation, the measurements agree well with the ideal stoichiometry and show no indication of substitution between the *M* and *M′* sites. The measured elemental compositions show no evidence of, thereby confirming the chemical homogeneity and phase purity of the samples within the limits of experimental uncertainty.

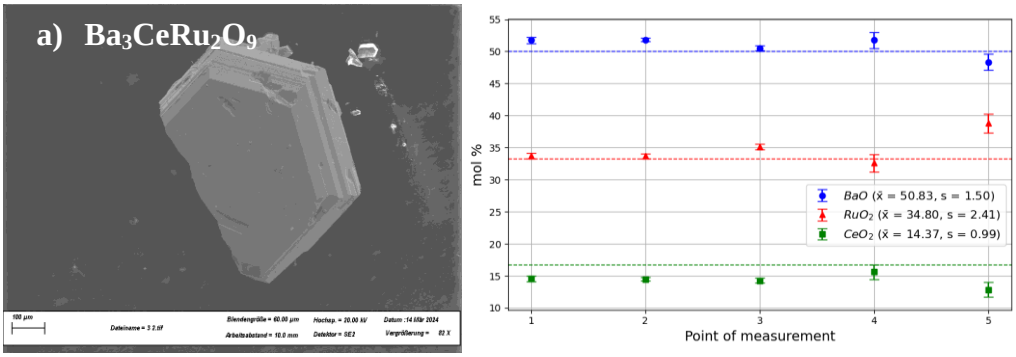

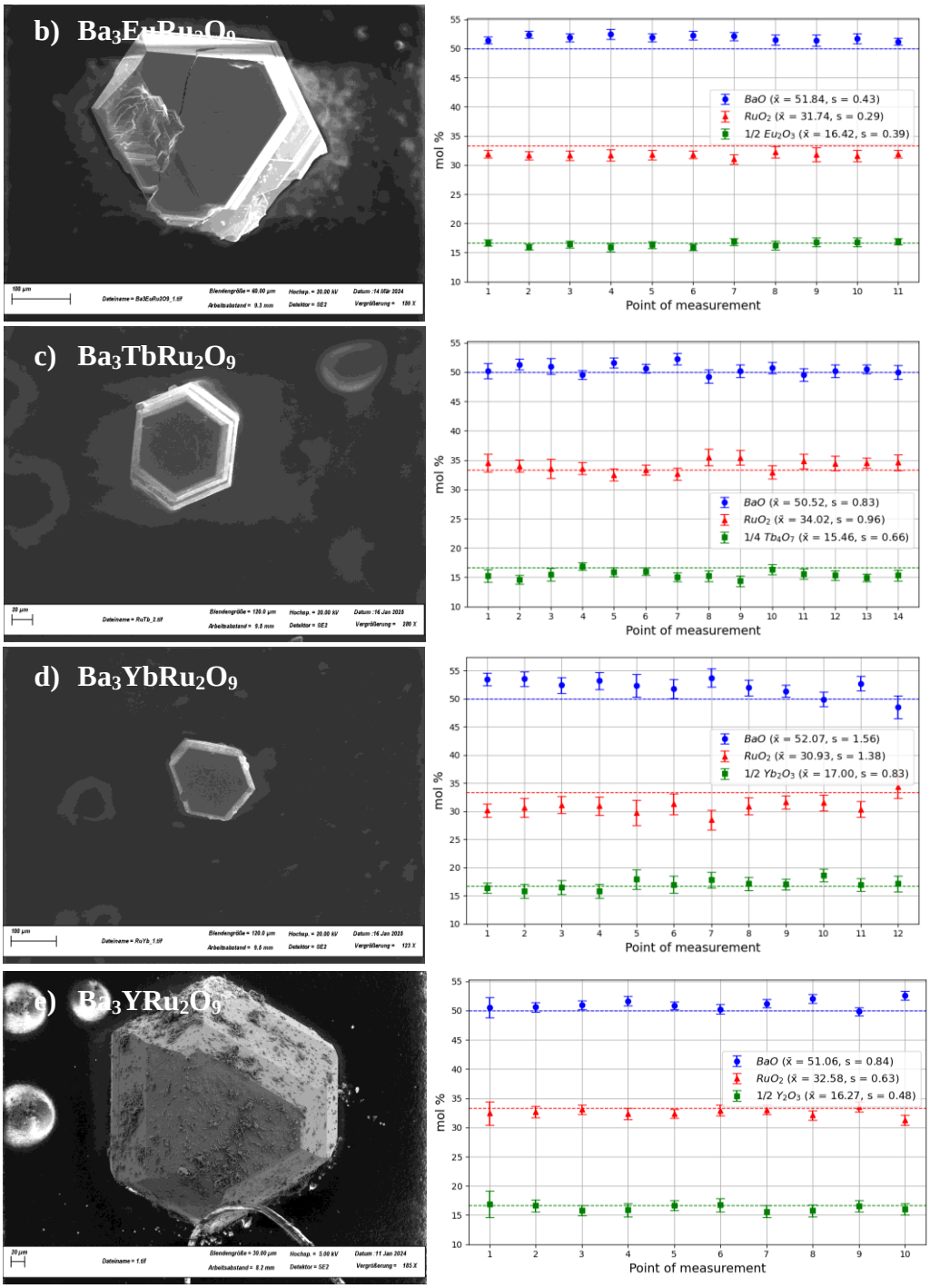

Figure 7.3: EDX-derived elemental compositions of $Ba_3MRu_2O_9$ single crystals with (a) M = Ce, (b) M = Eu, (c) M = Tb, (d) M = Yb, and (e) M = Y. The measurements confirm the expected stoichiometry within experimental error and indicate chemical homogeneity across all samples. Dots with error bars give measured data, lines indicate the nominal values expected from the stoichiometry $Ba_3MRu_2O_9$.

7.2.2 Structural analysis

7.2.2.1 P-XRD:

The compounds $Ba_3YRu_2O_9$ and $Ba_3YbRu_2O_9$ crystallized alongside $BaRuO_3$ and could not be sufficiently isolated for reliable structural analysis. Therefore, only the single phase powder diffraction data of $Ba_3EuRu_2O_9$, $Ba_3CeRu_2O_9$, and $Ba_3TbRu_2O_9$ were refined using the Rietveld method. All compounds are isotypic and crystallize in the hexagonal space group $P6_3/mmc$, consistent with previous reports and the findings of this study [45; 29]. Given their structural similarity, $Ba_3EuRu_2O_9$ was used as the initial model for all refinements, with appropriate adjustments made to the Eu site. The refinements were carried out sequentially, including lattice parameters, sample displacement, and atomic positions. Isotropic ADPs B_{eq} were fixed at 0.4 $Å^2$ for metal atoms and 0.6 $Å^2$ for oxygen atoms. The refined lattice constants agree well with values reported in the literature (see Table 7.4). Elemental analysis confirms an ideal 1 : 2 stoichiometry between the *M*-site metal and ruthenium. Introducing a mixed-occupancy model for the *M* and Ru sites did not improve the refinement, indicating that the Ru_2O_9 dimer units are fully occupied by ruthenium. Low-temperature measurements of $Ba_3CeRu_2O_9$ at 12 K reveal that the structure remains stable without any indications of structural distortion. The *a*-axis contracts by approximately 0.24 %, while the *c*-axis remains largely unaffected by thermal changes, shortening by only 0.01 %.
For clarity, only the 2θ range from 15° to 60° is shown in the Figure 7.4. Full diffraction datasets and the final structure models are provided in the Appendix B.

Compound	*a* [Å]	*c* [Å]	*GOF*	R_{Bragg}
$Ba_3CeRu_2O_9$ [at 290 K]	5.8883(4)	14.6378(4)	2.31	3.85
$Ba_3CeRu_2O_9$ [at 12 K]	5.8742(8)	14.6358(7)	2.42	4.56
literature [45]	5.8894(2)	14.6476(4)		
$Ba_3EuRu_2O_9$	5.8744(8)	14.5418(9)	1.48	3.63
Literature [29]	5.9133(3)	14.6346(6)		
$Ba_3TbRu_2O_9$	5.8371(2)	14.4319(2)	1.38	2.99
Literature [122]	5.8365(5)	14.4257(9)		

Table 7.4: Comparison of the refined lattice parameters with literature values, along with a summary of refinement quality indicators (*R*-factors) from the respective Rietveld analyses.

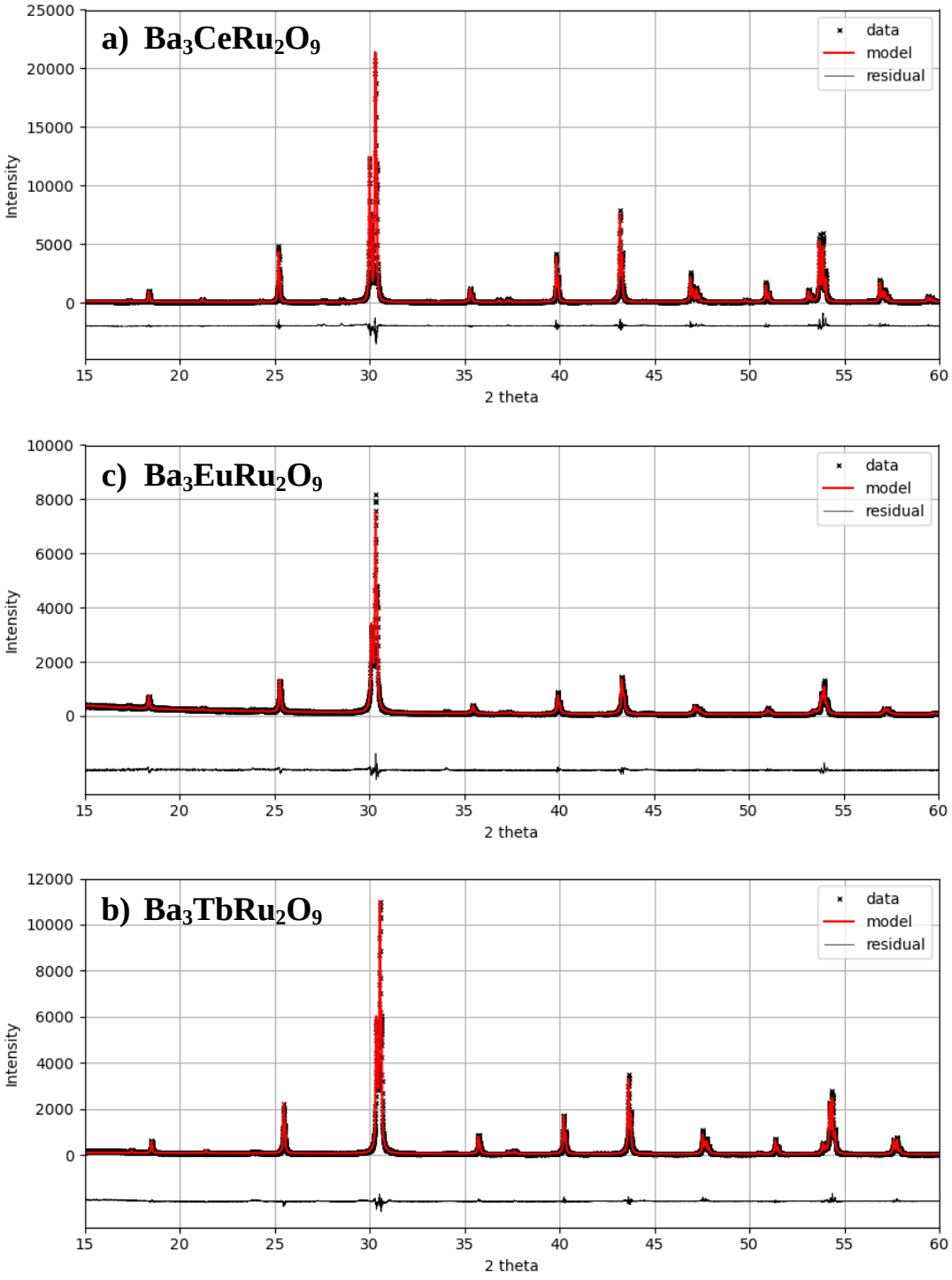

Figure 7.4: Rietveld refinements of powder diffraction data for (a) $Ba_3CeRu_2O_9$ (b) $Ba_3EuRu_2O_9$, and (c) $Ba_3TbRu_2O_9$. Shown are the measured patterns (black), calculated profiles (red), and the difference plots below.

7.2.2.2 SC-XRD:

Single-crystal diffraction data for $Ba_3MRu_2O_9$ (*M* = Ce, Yb, Y, Eu, Tb) were collected at 250 K and processed using the Jana2020 software suite for data scaling and structural refinement [66; 67]. All refinements initially employed the hexagonal structure type of $Ba_3MRu_2O_9$, as similar to the Rietveld refinement.

For the high-symmetry space group $P6_3/mmc$, the structures of $Ba_3CeRu_2O_9$, $Ba_3YbRu_2O_9$ and $Ba_3YRu_2O_9$ could be successfully solved. All atoms were refined anisotropically, achieving good agreement between the final model and experimental data with wR_2(obs) below 5 %. Allowing partial occupancy refinement on the *M*-site revealed approximately 1.5 % vacancies, which improved the wR_2(obs) by around 0.2 %. Ruthenium positions were fully occupied.
In contrast, for $Ba_3EuRu_2O_9$ and $Ba_3TbRu_2O_9$, the $wR2_{obs}$ values were higher (~7 %), and the oxygen atom at the 6H site exhibited negative eigenvalues during anisotropic ADPs refinement. Negative ADPs may indicate incorrect site assignments arising from symmetry mis-specification. Consequently, possible structural distortions were investigated. The quality values of models refined in respective space groups are summarized in Table 7.5. The description of symmetry lowering is exemplified using $Ba_3EuRu_2O_9$ but applies equally to $Ba_3TbRu_2O_9$.

The space group $P6_3/mmc$ is defined by a mirror plane perpendicular to the *c*-axis at z = 0.25 and 0.75, which constrains both the 6h oxygen position (O1) and Ba1 along the *c*-axis. Breaking this mirror plane reduces the symmetry to the non-centrosymmetric subgroup $P6_3mc$. This space group is already known for related compounds such as $Ba_3IrTi_2O_9$ or $Ba_3RuTi_2O_9$ [123; 124]. To explore possible symmetry lowering, the high symmetry hexagonal phase structural model including anisotropic ADPs for metal atoms and isotropic ADPs for oxygen atoms was transformed into $P6_3mc$

Upon the transformation to $P6_3mc$, the atomic sites 4f (Ru, Ba2) and 12k (O2) split. Since the symmetry breaking is assumed to originate from oxygen displacements, as observed in similar structures, all parameters except oxygen atomic positions and isotropic ADPs were fixed during refinement [50]. This led to a reduction of the wR_2(obs) value from approximately 6 % to 4 %. Attempts to refine the ADPs of the oxygen atoms anisotropically again resulted in negative eigenvalues. The final model refined all parameters with isotropic displacement constraints on oxygen atoms.

To further characterize the distortion, symmetry-mode analysis was carried out using the ISODISTORT software package [125; 126]. ISODISTORT systematically decomposes the structural distortion into symmetry-adapted modes based on group–subgroup relationships, enabling the identification of specific atomic displacement patterns responsible for the observed symmetry breaking. In this context, Gamma modes (GM) refer to distortions at the center of the Brillouin zone (k = 0), representing uniform atomic displacements within the unit cell. Both structural models were compared to identify active distortion modes contributing to the symmetry lowering. The analysis revealed that the symmetry reduction is described by the non-polar $GM1^+$ and the polar $GM2^-$ modes.

The $GM1^+$ modes correspond to symmetric, non-polar displacements predominantly involving oxygen atoms. For instance, the O1:h:A_1 mode amplitude is 0.03386 Å, while O2:k:A'_1 and A'_2 modes contribute 0.01064 Å and –0.05830 Å, respectively, to the structural relaxation. The notation O1:h:A_1 refers to the oxygen atom O1 located at the Wyckoff position h, whose displacements transform according to the irreducible representation A_1. In contrast, contributions from cations are significantly smaller (Ba1:f:A_1 = 0.00424 Å, Ru1:f:A_1 = 0.00205 Å), indicating only minor cation displacement. Thus, the distortion is primarily driven by displacive movements within the oxygen sublattice.
Crucial for the symmetry lowering and the breaking of inversion symmetry are the $GM2^-$ modes. The mode amplitudes O1:h:B_1 = –0.10252 Å, O2:k:A'_1 = 0.19684 Å, and O2:k:A'_2 = 0.13130 Å confirm the dominant role of oxygen displacements in this process. A smaller yet noticeable contribution arises from Ba2:b:A_2'' = –0.01200 Å, whereas transition metal contributions remain minor (Ru1:f:A_1 = –0.01083 Å, Eu1:a:A_2u = 0.0 Å). This suggests that the symmetry lowering is mainly driven by displacements in the anion sublattice, with a minor influence from the alkaline earth sublattice, whereas the transition metal centers largely retain their structural positions.
The oxygen displacements are illustrated in Figure 7.5. Since the oxygen movements range between 0.01 and 0.2 Å, displacement vectors were scaled by a factor of 10 to improve visibility.

Finally, a possible monoclinic distortion to space group *C2/c*, as reported for $Ba_3InIr_2O_9$, was investigated [50]. The refinement procedure was analogous, focusing on oxygen atoms. Since the monoclinic distortion involves a larger symmetry break, the cell was transformed accordingly as described in Section 2.1.1. However, no improvement in the refinement quality was observed and even isotropic ADPs for oxygen yielded negative eigenvalues.

In summary, for *M* = Ce, Yb, and Y, the data favor the hexagonal symmetry $P6_3/mmc$. In contrast, for *M* = Eu and Tb, a non-centrosymmetric model with $P6_3mc$ symmetry significantly improved the data fitting. It should be noted that the distorted structure provides a better fit to the measurement data but this is not definitive proof of symmetry breaking and merely indicates its possible presence. Evidence for the loss of the inversion symmetry and the presence of space group $P6_3mc$ could be obtained through crystal-physical investigations of crystal acentricity. Suitable methods include for example the Second Harmonic Generation (SHG) powder tests or measurements of the piezoelectric effect. However, due to the black color and small size of the crystals, we were unable to perform optical or physical measurements.

By breaking the mirror planes perpendicular to the c-axis and breaking inversion symmetry, the atomic positions of the oxygen atoms are better described. This improves the wR_2(obs) values by approximately 2 %. However, attempts to refine oxygen atoms anisotropically resulted in unphysical negative ADPs in all tested models.

The observed distortion in these compounds can be explained by an ionic size mismatch. The coordination environment of the barium atom at the 4f site is influenced by the size of the metal atom at the 2a site. The larger ionic radii of Eu^{3+} (95 pm) and Tb^{3+} (92 pm), compared to Ce^{4+} (87 pm) and Yb^{3+} (87 pm), exceed the ideal size for the hexagonal lattice, creating a structural void partially filled by the barium atom in response. In compounds such as $Ba_3CeRu_2O_9$, which retain perfect hexagonal symmetry, this mismatch is compensated by pronounced thermal anisotropy along the *c*-axis, stabilizing the structure.

However, in $Ba_3EuRu_2O_9$, the mismatch exceeds the compensation possible by thermal vibration alone. Consequently, the structure undergoes a subtle distortion that allows oxygen atoms to shift closer to barium, relieving local strain and stabilizing the coordination environment. The distortion is very small and barely reflected in the Global Instability Index (GII), which decreases slightly from 0.2634 in $P6_3/mmc$ to 0.2618 in $P6_3mc$ for $Ba_3EuRu_2O_9$.

Space group	R_1(obs)	R_1(all)	wR_2(obs)	wR_2(all)	*GOF*(obs)	*GOF*(all)
$P6_3/mmc$ Nr. 194	3.37	3.82	6.09	6.19	3.97	3.85
$P6_3mc$ Nr. 186	2.75	3.31	4.06	4.2	2.43	2.34
$P\bar{3}1c$ Nr.163	2.88	3.42	4.7	4.81	2.86	2.74
C2/c Nr. 15	4.62	6.12	5.05	5.22	2.24	1.99

Table 7.5: Comparison of *R*-values for structural models of $Ba_3EuRu_2O_9$ refined in different space groups. In the initial model ($P6_3/mmc$), The ADPs of all metal atoms were refined anisotropically, while oxygen atoms were refined isotropically. In all other lower-symmetry models, only the oxygen positions and isotropic ADPs were refined, all other parameters were fixed to exclusively assess the influence of oxygen atoms on the structure. In the monoclinic space group, the isotropic ADPs could not be refined to physically meaningful values.

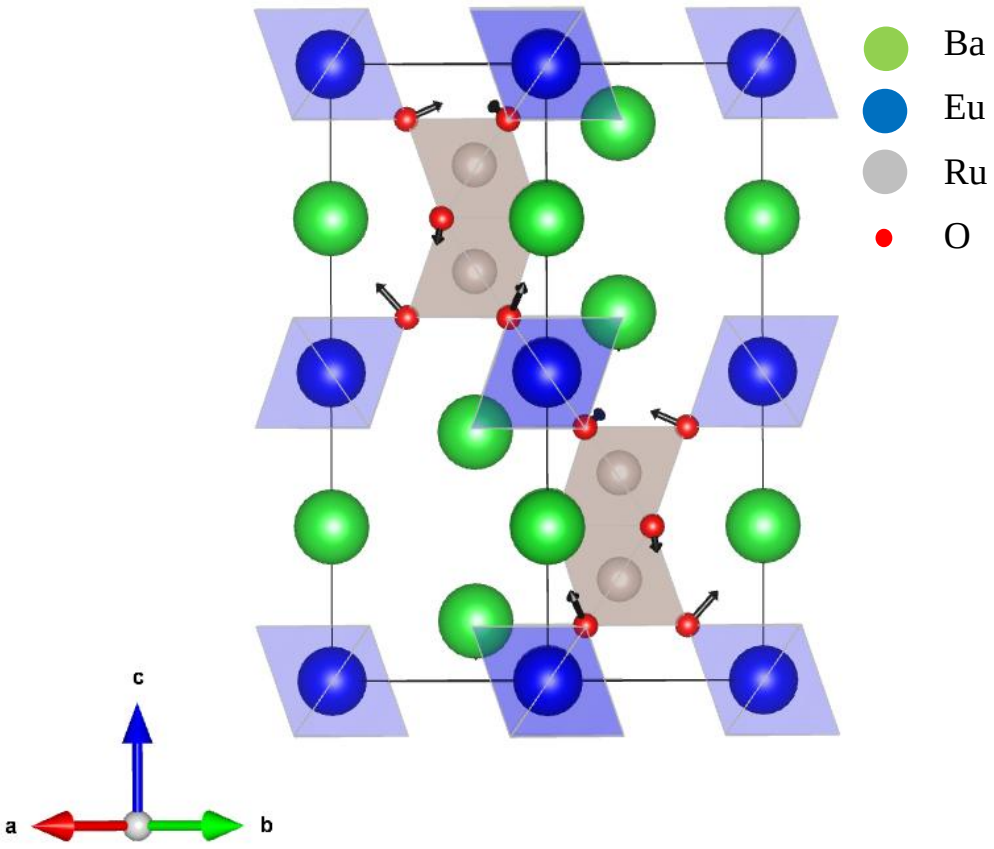

Figure 7.5: Visualization of the hexagonal $P6_3/mmc$ structure of $Ba_3EuRu_2O_9$, showing the displacement vectors of the oxygen atoms (black arrows) relative to the model in space group $P6_3mc$. The vectors are scaled by a magnified of 10 for better visibility. The distortions primarily involve oxygen atoms and result from a combination of the $GM1^+$ and $GM2^-$ active modes.

General Information	
Compound	$Ba_3CeRu_2O_9$
Space group	$P6_3/mmc$ (194)
Z	2
a, b, c	5.88770(10) Å; 5.88770(10) Å; 14.6392(4) Å
V	439.480(16) $Å^3$
p_{calc}	6.7886 g/cm^3
T	250 K
Radiation wavelength	0.71073 Å
Crystal information	
Color/shape	black, plate
Size	0.030 mm x 0.034 mm x 0.041 mm
Data collection	
Index ranges	-12 < h <13, -14 < k < 13, -33 < l <33
Total reflections	45434
Independent reflections	1084
R_{int}	0.0615
Data reduction	
Absorption correction	multi scan
Absorption coefficient μ	21.672 mm^{-1}
F(000)	769
Refined parameters	21
Final *R* indices	
all data	R_1 = 0.0367, wR_2 = 0.0350, GOF = 1.67
data with I > 3 sigma(I)	R_1 = 0.0229, wR_2 = 0.0312, GOF = 1.72

Atom	Site	x	y	z	U_{eq}
Ru1	**4f**	**1/3**	**2/3**	**0.16513(2)**	**0.00402(6)**
Ce1	**2a**	**0**	**0**	**0**	**0.00403(6)**
Ba1	**2b**	**0**	**0**	**0.25**	**0.00814(7)**
Ba2	**4f**	**1/3**	**2/3**	**0.90192(2)**	**0.00908(6)**
O1	**6h**	**0.4872(2)**	**0.9744(4)**	**0.25**	**0.0072(6)**
O2	**12k**	**0.17422(17)**	**0.3484(3)**	**0.41271(15)**	**0.0102(5)**

Table 7.6: Atomic coordinates and isotropic ADPs of $Ba_3CeRu_2O_9$ refined from SC-XRD data.

General Information	
Compound	$Ba_3EuRu_2O_9$
Space group	$P6_3/mmc$ (194)
Z	2
a, b, c	5.91110(10) Å; 5.91110(10) Å; 14.6346(3) Å
V	442.841(14) $Å^3$
p_{calc}	6.8259 g/cm^3
T	250 K
Radiation wavelength	0.71073 Å
Crystal information	
Color/shape	black, plate
Size	0.030 mm x 0.034 mm x 0.041 mm
Data collection	
Index ranges	-13 < h <13, -13 < k < 13, -33 < l <33
Total reflections	159251
Independent reflections	1088
R_{int}	0.0535
Data reduction	
Absorption correction	multi scan
Absorption coefficient μ	23.45 mm^{-1}
F(000)	782
Refined parameters	17
Final *R* indices	
all data	R_1 = 0.0318, wR_2 = 0.0570, GOF = 3.93
data with I > 3 sigma(I)	R_1 = 0.0279, wR_2 = 0.0563, GOF = 4.0

Atom	Site	x	y	z	U_{eq}
Ru1	**4f**	**1/3**	**2/3**	**0.16355(3)**	**0.00347(8)**
Eu1	**2a**	**0**	**0**	**0**	**0.00419(8)**
Ba1	**2b**	**0**	**0**	**0.25**	**0.00770(9)**
Ba2	**4f**	**1/3**	**2/3**	**0.90314(3)**	**0.00975(8)**
O1	**6h**	**0.4855(2)**	**0.5145(3)**	**0.25**	**0.0062(8)**
O2	**12k**	**0.1757(2)**	**0.3513(5)**	**0.4107(2)**	**0.0108(6)**

Table 7.7: Atomic coordinates and isotropic ADPs of $Ba_3EuRu_2O_9$ refined from SC-XRD data.

General Information	
Compound	$Ba_3TbRu_2O_9$
Space group	$P6_3/mmc$ (194)
Z	2
a, b, c	5.8233(3) Å; 5.8233(1) Å; 14.4190(8) Å
V	439.6(11) Å^3
p_{calc}	7.1930 g/cm^3
T	100 K
Radiation wavelength	0.5608 Å
Crystal information	
Color/shape	black, plate
Size	0.06 mm x 0.06 mm x 0.03 mm
Data collection	
Index ranges	-13 < h <13, -13 < k < 13, -32 < l <32
Total reflections	39147
Independent reflections	1027
R_{int}	0.0627
Data reduction	
Absorption correction	multi scan
Absorption coefficient μ	25.468 mm^{-1}
F(000)	786
Refined parameters	17
Final *R* indices	
all data	R_1 = 0.0408, wR_2 = 0.0752, GOF = 4.74
data with I > 3 sigma(I)	R_1 = 0.0346, wR_2 = 0.0742, GOF = 4.7

Atom	Site	x	y	z	U_{eq}
Ru1	**4f**	**1/3**	**2/3**	**0.16374(3)**	**0.0022(1)**
Tb1	**2a**	**0**	**0**	**0**	**0.00228(9)**
Ba1	**2b**	**0**	**0**	**0.25**	**0.00355(11)**
Ba2	**4f**	**1/3**	**2/3**	**0.90636(3)**	**0.00377(9)**
O1	**6h**	**0.4854(3)**	**0.9708(7)**	**0.25**	**0.0017(6)**
O2	**12k**	**0.1713(3)**	**0.3425(5)**	**0.4150(2)**	**0.0057(6)**

Table 7.8: Atomic coordinates and isotropic ADPs of $Ba_3TbRu_2O_9$ refined from SC-XRD data.

General Information	
Compound	$Ba_3YRu_2O_9$
Space group	$P6_3/mmc$ (194)
Z	2
a, b, c	5.88185(10) Å; 5.88185(10) Å; 14.50056(26) Å
V	428.79(11) $Å^3$
p_{calc}	6.4757 g/cm^3
T	250 K
Radiation wavelength	0.71073 Å
Crystal information	
Color/shape	black, plate
Size	0.030 mm x 0.034 mm x 0.041 mm
Data collection	
Index ranges	-13 < h <13, -13 < k < 13, -32 < l <32
Total reflections	169210
Independent reflections	1067
R_{int}	0.0535
Data reduction	
Absorption correction	multi scan
Absorption coefficient μ	23.396 mm^{-1}
F(000)	734
Refined parameters	23
Final *R* indices	
all data	R_1 = 0.0293, wR_2 = 0.0491, GOF = 3.39
data with I > 3 sigma(I)	R_1 = 0.0259, wR_2 = 0.0485, GOF = 3.49

Atom	Site	x	y	z	U_{eq}
Ru1	**4f**	**1/3**	**2/3**	**0.16253(2)**	**0.00456(6)**
Y1	**2a**	**0**	**0**	**0**	**0.00449(9)**
Ba1	**2b**	**0**	**0**	**0.25**	**0.00838(7)**
Ba2	**4f**	**1/3**	**2/3**	**0.90616(2)**	**0.00986(6)**
O1	**6h**	**0.48593(19)**	**0.9719(4)**	**0.25**	**0.0078(5)**
O2	**12k**	**0.17460(16)**	**0.3492(3)**	**0.41196(15)**	**0.0118(4)**

Table 7.9: Atomic coordinates and isotropic ADPs of $Ba_3YRu_2O_9$ refined from SC-XRD data.

General Information	
Compound	$Ba_3YbRu_2O_9$
Space group	$P6_3/mmc$ (194)
Z	2
a, b, c	5.8565(1) Å; 5.8565(1) Å; 14.4358(8) Å
V	439.6(11) Å^3
p_{calc}	7.2128 g/cm^3
T	250 K
Radiation wavelength	0.71073 Å
Crystal information	
Color/shape	black, plate
Size	0.06 mm x 0.06 mm x 0.03 mm
Data collection	
Index ranges	-13 < h <13, -13 < k < 13, -32 < l <32
Total reflections	39147
Independent reflections	1036
R_{int}	0.0401
Data reduction	
Absorption correction	multi scan
Absorption coefficient μ	27.809 mm^{-1}
F(000)	760
Refined parameters	23
Final *R* indices	
all data	R_1 = 0.0396, wR_2 = 0.0504, GOF = 2.67
data with I > 3 sigma(I)	R_1 = 0.0345, wR_2 = 0.0492, GOF = 2.76

Atom	Site	x	y	z	U_{eq}
Ru1	**4f**	**1/3**	**2/3**	**0.16374(3)**	**0.0022(1)**
Yb1	**2a**	**0**	**0**	**0**	**0.00228(9)**
Ba1	**2b**	**0**	**0**	**0.25**	**0.00355(11)**
Ba2	**4f**	**1/3**	**2/3**	**0.90636(3)**	**0.00377(9)**
O1	**6h**	**0.4854(3)**	**0.9708(7)**	**0.25**	**0.0017(6)**
O2	**12k**	**0.1713(3)**	**0.3425(5)**	**0.4150(2)**	**0.0057(6)**

Table 7.10: Atomic coordinates and isotropic ADPs of $Ba_3YbRu_2O_9$ refined from SC-XRD data.

8 Crystal growth of Ni_2InSbO_6

Ni_3TeO_6 was first reported in 1967 [127] and remains the only known member of the M_3TeO_6 family (with M = Mn, Co, Ni, Cu) that crystallizes in the polar, trigonal space group *R3* [128; 129; 130; 131; 132]. The chirality of this crystal structure implies the absence of mirror planes or inversion centers, so that its symmetry elements consist solely of rotational and screw axes. This lack of inversion symmetry is key to its chiral character and gives rise to unconventional physical phenomena.
In this context, right- and left-handed magnons are of particular importance. Magnons are quantized collective excitations of spin waves in magnetically ordered systems. Depending on the direction of their spin precession, they can be classified as right- or left-handed. In chiral crystals such as Ni_3TeO_6, these magnon modes remain degenerate in the absence of a magnetic field [133]. However, the chirality of the crystal allows them to interact differently with circularly polarized light.

As part of CRC 1238 *"Control and Dynamics of Quantum Materials"*, Ni_3TeO_6 was investigated with a focus on non-reciprocal optical effects, in which the interaction between light and the material depends on the direction of light propagation along the optical axis [133]. These effects manifest most prominently as strong natural optical activity in the terahertz frequency range. The underlying mechanism is the dynamic magnetoelectric effect, where electric and magnetic dipole excitations are coupled [133]. This interaction leads to substantial polarization rotation of transmitted light. Notably, these effects occur even in the absence of an external magnetic field and directly result from the interplay between the chiral crystal structure and magnon excitations [133].

The structure of Ni_3TeO_6 is built from three crystallographically distinct nickel atoms and one tellurium atom occupying 3a Wyckoff positions, along with two oxygen atoms located on 9b positions [127]. The presence of three separate Ni sites in the structure allows for the formation of structurally analogous compounds of the type $M_2M'SbO_6$, in which the Te

atom is substituted by Sb, and one Ni position is replaced by a different cation. Compounds with M = Mn, Ni and M' = Sc, In have all been shown to adopt the same isotypic structure with the polar trigonal space group $R3$ [134; 135].
In this context, the compound Ni_2InSbO_6 is of particular interest. Due to its structural similarity to Ni_3TeO_6, it shares the same chiral space group and thus provides a comparable crystallographic environment for studying collective excitations. At the same time, substitution of Te by Sb and one Ni atom by In significantly modifies the electronic configuration and magnetic properties. This makes Ni_2InSbO_6 an ideal candidate to investigate the influence of chemical substitution on the magnetoelectric coupling and non-reciprocal optical phenomena .

For the investigation of these non-reciprocal optical effects, high-quality single crystals are essential. Since the measurements are performed along the optical axis (*c*-axis), it is necessary to obtain crystals from which specimens with a (001) surface orientation and an area of approximately 1 mm² can be prepared. Therefore, a key objective was to optimize the crystal growth process in order to produce crystals of the required size and quality.

8.1 Crystal growth investigation

8.1.1 Theoretical background and modeling

Crystal growth of Ni_2InSbO_6 is expected to be achievable via chemical transport reactions (CTR) as suitable transport reactions for the constituent oxides NiO, In_2O_3 and Sb_2O_5 can be found in literature [82]. Based on the crystal growth experiments described in [136], Ni_2InSbO_6 was synthesized by the CTR method with chloride as transport agent.
The details of all transport experiments, including the use of the precision balance, the mathematical foundations of CVTRANS, and the method to estimate thermodynamic data, are described in detail in Section 0.
Within this experimental setup, the transported mass m_1 can be derived from the measured value m_{mes} by applying the lever law:

$$m_1 = m_{mes} * \frac{\Delta S}{L} \tag{8.1}$$

By plotting the transported mass as a function of time, the transport rate can be extracted from the slope of a linear fit to the data.
The calculation of the transport rates was carried out using the program CVTRANS [137]. CVTRANS determines the partial pressures based on the thermodynamic data of all species

present at both the source and sink side of the ampoule. Using this information, the program solves the Schäfer equation (see eq. 4.13) to calculate the transport rate. The required input parameters include the diffusion path length in the growth ampoule, the cross-sectional area of the ampoule, the temperature gradient along the diffusion path, the molar amounts of the substances involved, as well as their thermodynamic data and the mean diffusion coefficient.

All thermodynamic data were obtained from Binnewiese et al. [85], with the relevant literature cited accordingly. The full set of thermodynamic parameters applied is listed in Appendix D. Since no thermodynamic data are available for Ni_2InSbO_6, an estimation was performed using the Dulong–Petit law and the Neumann–Kopp rule. The standard enthalpy of formation for Ni_2InSbO_6 was estimated by summing the standard enthalpies of formation for the reactants NiO, Sb_2O_5, and In_2O_3 in the appropriate stoichiometric ratios as given in eq. 8.2. To this sum, an additional value, referred to as the stabilization enthalpy $\Delta_R H°$, must be added. For simple oxides, a value of -20 to -30 kJ/mol per metal atom is generally a good approximation. This results in a stabilization enthalpy for Ni_2InSbO_6 of -80 to -120 kJ/mol.

$$\Delta_F H°_{Ni_2InSbO_6} = 2 * \Delta_F H°_{NiO} + \frac{1}{2} * \Delta_F H°_{In_2O_3} + \frac{1}{2} * \Delta_F H°_{Sb_2O_5} + \Delta_R H° \tag{8.2}$$

Each volatile species has its own diffusion coefficient, which is difficult to measure and is known for only a few molecular species. Schäfer proposed an average diffusion coefficient of 0.1 cm²/s [83], which is a good approximation for nitrogen (N_2) molecules. However, subsequent investigations have shown that for real systems containing larger and heavier molecules, a lower diffusion coefficient of 0.025 cm²/s is more appropriate [82; 138; 139]. Nevertheless, even with this reduced value, the calculated transport rates exceed the experimentally observed rates by a factor of approximately 2.5. As the thermodynamic data of Ni_2InSbO_6 and the diffusion coefficient are the only uncertain or estimated parameters affecting the model, their influence was systematically analyzed through sensitivity studies. In general, the transport rate increases with decreasing standard enthalpy of formation of Ni_2InSbO_6. In order for any transport to occur at all, a minimum stabilization enthalpy of -50 kJ/mol is required. However, even with this minimal stabilization and assuming a diffusion coefficient of 0.025 cm²/s, the resulting transport rate remains more than twice as large as the measured values. This suggests that the diffusion coefficient is the more critical parameter in this context. Under a more realistic stabilization enthalpy of -80 kJ/mol, the diffusion coefficient must be reduced to 0.01 cm²/s in order for the computed transport rates

to align with experimental observations.
With all these parameters known, the Schäfer equation can be solved to calculate the partial pressures of all species involved and the transport rates.

8.1.2 Experimental procedures and results

The experiments were monitored using a precision transport balance to analyze the transport rate as a function of temperature profiles and ampoule geometry. High-purity silica ampoules were used to tolerate the elevated temperatures required for these reactions. The starting material, Ni_2InSbO_6, was synthesized by solid-state reaction at 1373 K for 12 hours, using stoichiometric amounts of NiO, In_2O_3, and Sb_2O_5, which were homogenized in an agate mortar. The resulting product was ground and loaded into a silica ampoule under an argon atmosphere inside a glovebox, in the presence of $PtCl_4$ as the transport agent precursor.
Thermal analysis of $PtCl_4$ under a chlorine atmosphere revealed a three-step decomposition at approximately 655 K, 723 K, and 788 K, accompanied by the release of Cl_2 gas [140]. Above these temperatures, no platinum chlorides remain thermodynamically stable; as a result, the residual platinum remained at the source and did not participate in further transport processes. Therefore, it was not included in subsequent calculations. The ampoule was subsequently evacuated, sealed under vacuum, and thermally processed.
To calibrate measurement accuracy and account for external factors such as balance drift, laboratory access, mechanical vibrations, and general measurement uncertainty, a blank experiment using an evacuated ampoule was performed under transport conditions (T_1 = 1273 K, T_2 = 1173 K) for approximately 9 days. The results reached a stable equilibrium after approximately 60 h, showing consistent oscillations of ±0.01 g and a period of about 40 hours (see Figure 8.1).

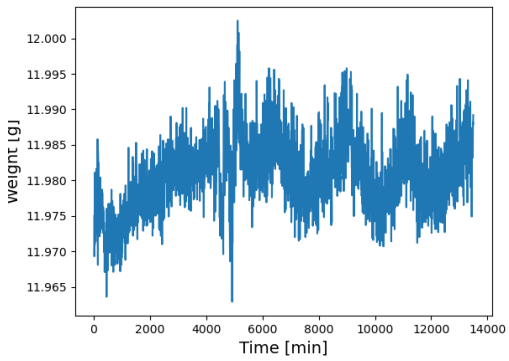

Figure 8.1: Baseline measurement of the transport balance under transport conditions (T_1 = 1273 K, T_2 = 1173 K) to determine baseline stability. Shown is the temporal progression of the measured mass using an empty ampoule. The resulting fluctuations of ±0.01 g with a period of approximately 40 hours serve as a reference for the balance's accuracy.

In total, four transport experiments were conducted to compare the measured transport rates n_{mes} with theoretical calculations n_{calc} and to study their influence on crystallization. The detailed experimental conditions are provided in Table 8.1. The measurement data from the transport balance, along with the corresponding fit used for calculating the transport rates can be found in Appendix D.

S-ID	Ni_2InSbO_6 [g]	$PtCl_4$ [g]	Length [mm]	Diameter [mm]	T_1 [K]	T_2 [K]
1	0.91	0.03	160	17	1273	1223
2	0.967	0.035	170	17	1273	1223
3	0.962	0.035	185	17	1233	1173
					1253	1203
4	0.967	0.034	175	12	1273	1223

Table 8.1: Summary of experimental conditions and results for the synthesis of Ni_2InSbO_6 by CVTR. T_1 and T_2 indicate the set temperatures during the experiments, which may differ from the actual temperatures and can explain the differences between the calculated and measured transport rates.

Experiments S-ID 1 and S-ID 2 achieved transport rates exceeding 3 mg/h, which promoted the growth of large crystals at the sink side. However, these crystals were highly intergrown, making it impossible to isolate individual specimens. To address this, experiment S-ID 3 utilized a longer ampoule (185 mm) to reduce the transport rate, aiming for the formation of isolated crystals over a larger area. After approximately one week, the transport rate was assessed, and the temperature gradient was reduced from 60 to 50 K to further suppress the transport rate. This adjustment resulted in an approximately 50% reduction in transport rate, and compared to S-ID 1 and S-ID 2, a greater number of isolated crystals could be recovered. Finally, the experiment S-ID 4 was conducted using a narrower ampoule (12 mm instead of 17 mm), which resulted in a transport rate n_{mes} = 0.9 mg/d , with isolated crystals of up to 2 mm in size Figure 8.2.

The calculated transport rates for all experiments are of the same order of magnitude as the experimentally measured ones. The deviations can have several causes. In particular, the temperature gradient in the furnace plays a key role, as it directly influences the transport rate. The temperature gradient varies with the length and position of the ampoule as well as the T_1 and T_2 temperatures, see Figure 4.3. The calculations were always carried out using the target temperatures, which, however, may slightly differ from the actual temperatures. A deviation in the temperature gradient of 15 K is sufficient to explain all discrepancies between the calculated and experimentally measured transport rates.

The calculations identified the following transport-active species: $NiCl_2$, $InCl_3$ and $SbCl_3$.

All other species exhibit partial pressures at least three orders of magnitude lower and can therefore be neglected. The results are summarized in Table 8.2.

S-ID	$p(Cl_2)$ [atm]	$p(NiCl_2)$ [atm]	$p(InCl_3)$ [atm]	$p(SbCl_3)$ [atm]	$p(O_2)$ [atm]	p(total) [atm]	n‘(cal) [mg/h]	n‘(mes) [mg/h]
1	$5.9*10^{-2}$	$4.3*10^{-2}$	$1.4*10^{-1}$	$1.3*10^{-1}$	$3.0*10^{-1}$	0.69	2.89	3.21
2	$6.2*10^{-2}$	$4.5*10^{-2}$	$1.5*10^{-1}$	$1.4*10^{-1}$	$3.2*10^{-1}$	0.72	2.7	3.48
3	$7.1*10^{-2}$	$3.8*10^{-2}$	$1.2*10^{-1}$	$1.2*10^{-1}$	$2.7*10^{-1}$	0.63	3.15	3.16
	$6.3*10^{-2}$	$4.0*10^{-2}$	$1.3*10^{-1}$	$1.3*10^{-1}$	$2.8*10^{-1}$	0.65	2.52	1.74
4	$1.5*10^{-1}$	$7.7*10^{-2}$	$2.8*10^{-1}$	$2.7*10^{-1}$	$5.9*10^{-1}$	1.38	1.22	0.91

Table 8.2: Partial pressures on the source side for all transport-active species in experiments S-ID1 to S-ID4 are listed. Additionally, the calculated partial pressures of O_2 and Cl_2, as well as the total pressure in the ampoule, are provided. The calculated and measured transport rates show good agreement, with discrepancies attributable to temperature differences between the actual conditions and those assumed in the calculations.

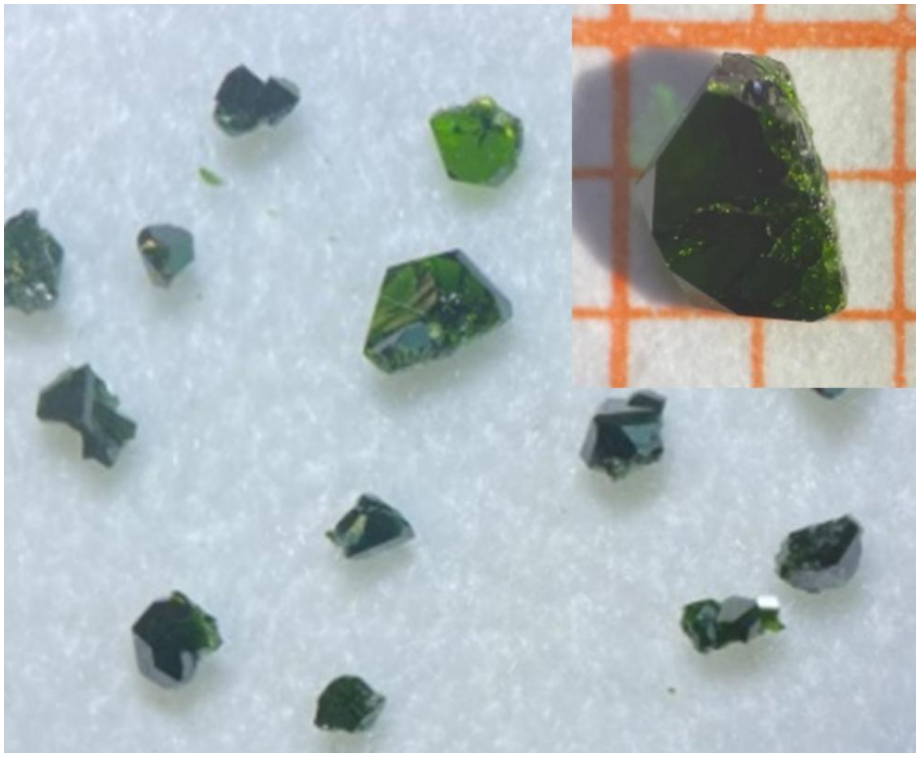

Figure 8.2: Image of grown Ni_2InSbO_6 single crystals grown using the chemical transport reaction (CTR) method with chlorine as the transport gas. The crystals, reaching sizes of up to 2 mm, were obtained from experiment S-ID4 and mechanically isolated. The measured transport rate was 0.91 mg/d, which is in good agreement with the calculated value of 1.22 mg/d.

8.2 Elemental analysis

A Ni_2InSbO_6 crystal from experiment S-ID 3 was embedded in epoxy and polished for chemical analysis. Horizontal and vertical line scans were performed using WDX analysis to accurately assess the chemical composition. In the BSE image, the crystal appears chemically homogeneous. However, chemical analysis reveals a slight but abrupt change in the In/Ni composition ratio along the horizontal scan. The Sb concentration remains uniform across all measured points. Initially, the horizontal scan shows a minor deficit of approximately 0.5 mol% In, which then increases to the target value of 25 mol%, accompanied by a deficit of about 1 mol% Ni. In contrast, the vertical scan shows no significant changes in composition.

The observed compositional variations can be attributed to temperature changes during the growth process, specifically an increase in the T_1 temperature from 1233 K to 1253 K and the T_2 temperature from 1173 K to 1203 K. The calculations of the partial pressures of the most transport-reactive species on the source side reveal a crossover of $InCl_3$ and $SbCl_3$ at approximately 1218 K (see Figure 8.3). This indicates that the growth temperature influences the crystal's composition of the grown crystal. Moreover, the analysis demonstrates that the compound tolerates slight chemical variations and grows chemically very homogeneously under constant growth conditions.

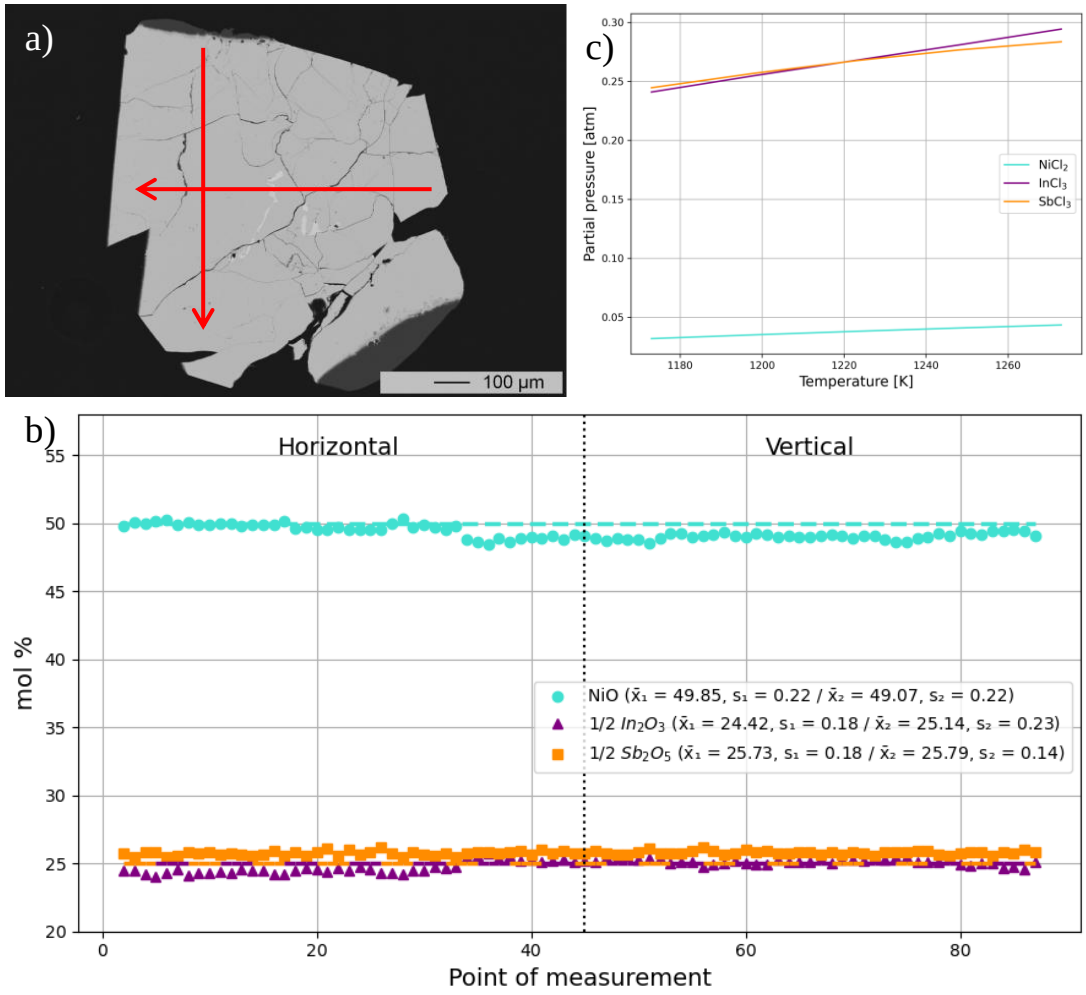

Figure 8.3: a) Backscattered electron (BSE) image of a Ni_2InSbO_6 crystal with the measured lines indicating horizontal and vertical chemical composition scans. b) Plot of the measured chemical composition along the marked lines with dashed lines indicate the nominal composition. The mean values $\bar{x}$ and standard deviations s for regions where the crystal is chemically homogeneous ($x_1 = 0$ to 33, $x_2 = 34$ to 87) are shown in the legend. c) Calculated partial pressures of the transport-reactive species at the source side at different temperatures under the experimental conditions of experiment S-ID 3.

8.3 Structural analysis

For structural characterization, a powder sample obtained from a Ni_2InSbO_6 single crystal was investigated in the temperature range from 300 K down to 12 K. The Rietveld fit of the diffraction data collected at 290 K is shown in Figure 8.4. The results and quality indicators are shown in Table 8.3. The refined structural model at low temperature is included in Appendix B.

The data were refined based on the structural model published by M. Weil et al [136]. During the refinement, lattice parameters, atomic positions, isotropic ADPs and sample displacement were adjusted, resulting in a high-quality fit to the experimental data. The refined lattice constants at room temperature show excellent agreement with those reported by Weil et al. [136]. Throughout the entire temperature range studied, no evidence for a structural phase transition was found. As expected from thermal contraction, both the *a*- and *c*-axes decrease slightly with decreasing temperature, by approximately 0.05 % and 0.06 %, respectively.

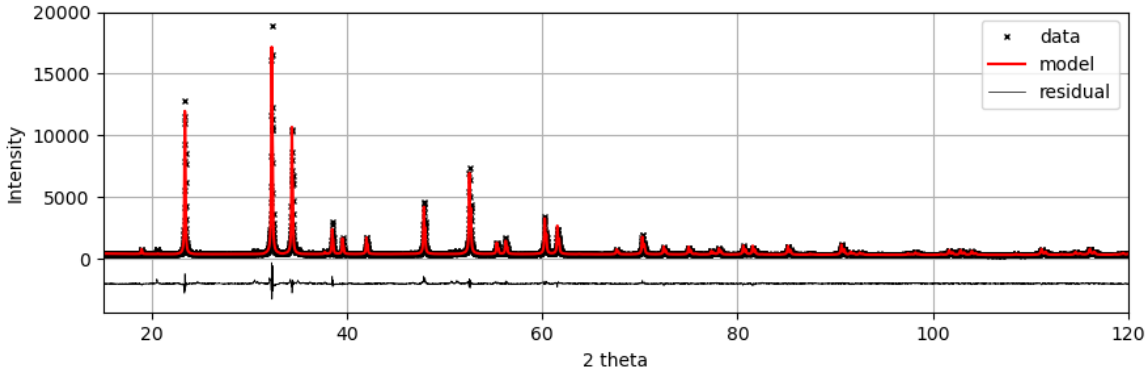

Figure 8.4: Rietveld refinements of Ni_2InSbO_6 at (a) 300 K and (b) 12 K in the 2θ range from 10° to 120°. The measured data are shown in black, the calculated fit in red, and the difference (residual) is plotted below each pattern (Structural model taken from [136]).

Temperature	*a* [Å]	*c* [Å]	R_{Bragg}	*GOF*
290 K	5.21282(1)	14.01409(4)	2.22	1.74
12 K	5.21014(2)	14.00628(6)	1.84	1.81
Weil et al.	5.2164	14.0142		

Table 8.3: Comparison of the lattice parameters of Ni_2InSbO_6 obtained by Rietveld refinement with literature values from M. Weil et al. [136]. Additionally, the refined lattice parameters at 12 K and the corresponding quality factors R_{Bragg} and *GOF* for the refinements at 290 K and 12 K are listed.

Figure 8.5 illustrates the crystal structure of Ni_2InSbO_6, which crystallizes in the polar space group *R*3. The symmetry of this space group is defined by a threefold rotation axis aligned with the *c*-axis at the origin (0 0 0), with additional threefold axes located at fractional coordinates (1/3 1/3 0) and (2/3 2/3 0). Threefold screw axes are present at (1/3 0 0), (2/3 0 0), (0 1/3 0), (0 2/3 0), (1/3 2/3 0), and (2/3 1/3 0).

In the crystal structure, a total of six Wyckoff positions are occupied. Two nickel atoms, one antimony atom, and one indium atom each occupy 3a positions, while two distinct oxygen atoms occupy 9b positions. This results in a layered structure of octahedra arranged in an edge-sharing honeycomb lattice. Each honeycomb layer is half-filled with nickel, while the remaining sites are alternately occupied by antimony or indium. The stacking of these layers is such that the nickel-centered octahedra collectively form a corner-sharing honeycomb network throughout the structure [141].

Due to the absence of inversion symmetry, the octahedra units are strongly anisotropic, and the metal atoms are displaced from the octahedral centers.

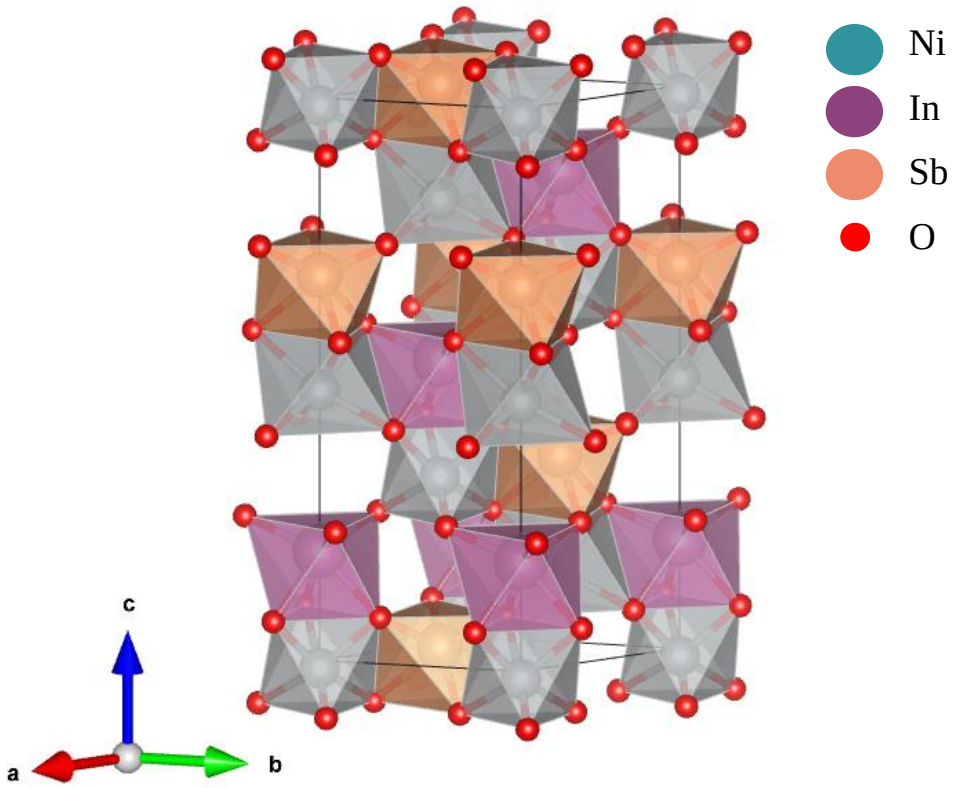

Figure 8.5: Crystal structure of Ni_2InSbO_6 [136]. The image shows the anisotropically distorted, chiral structure in space group *R*3. Nickel, indium, and antimony centers are coordinated by oxygen in distorted octahedra, forming an edge-sharing honeycomb lattice. (Visualization created using VESTA)

8.4 Thermal analysis

Two thermal analyses of Ni_2InSbO_6 were conducted, one on a solid-state sample and another on a single crystal sample. The solid-state sample was heated to 1673 K and exhibited two distinct endothermic reactions at approximately 1323 K and 1463 K, followed by decomposition at around 1473 K. This decomposition was accompanied by a significant mass loss of about 25 wt% up to 1673 K, indicating that the compound underwent complete breakdown, including partial volatilization. Post-measurement P-XRD revealed the absence of Ni_2InSbO_6, instead showing a decomposition product not consistent with any known phases in the ICSD database.

To clarify the origin of the endothermic signals observed prior to decomposition, a single crystal was heated to 1473 K and subsequently analyzed by P-XRD. In this case, no endothermic events were detected during heating, and the diffraction pattern confirmed that the Ni_2InSbO_6 structure remained intact and thermally stable under these conditions.

These findings suggest that the endothermic peaks observed in the solid-state sample likely originate from secondary phases, which formed during the solid-state synthesis, rather than from intrinsic transformations of the Ni_2InSbO_6 phase.

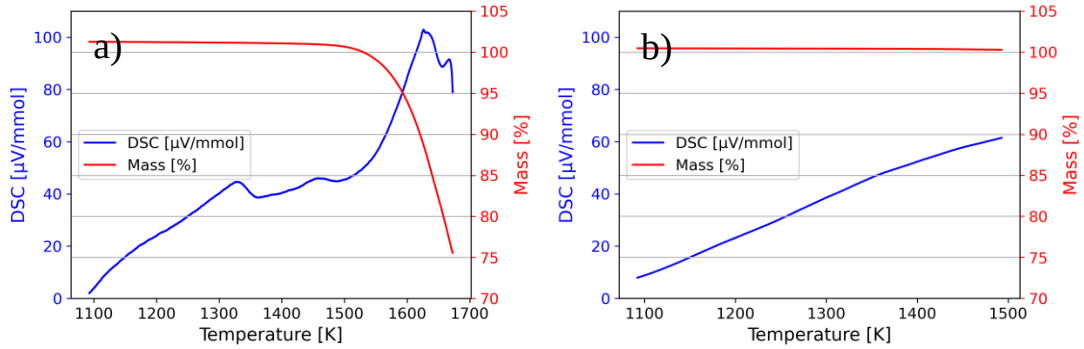

Figure 8.6: Simultaneous thermal analysis (STA) of Ni_2InSbO_6, with the TGA signal shown in red and the DSC signal in blue. (a) Measurement of a Ni_2InSbO_6 sintered powder sample up to 1673 K. Two distinct endothermic peaks at approximately 1323 K and 1463 K can be observed, followed by a decomposition event around 1673 K. (b) In contrast, a Ni_2InSbO_6 single crystal measured up to 1500 K shows no thermal events, indicating that the reactions observed in (a) are not attributable to Ni_2InSbO_6 itself.

8.5 Optical analysis

The chiral symmetry in Ni_2InSbO_6 gives rise to optical activity, meaning that the polarization plane of light rotates as it passes through the crystal. This investigation focuses specifically on this reciprocal effect, which contrasts with non-reciprocal optical phenomena where the response depends on the direction of light propagation. In optical activity, the effect is identical for both propagation directions and arises solely from the chiral, non-centrosymmetric crystal structure.

This effect is most pronounced when observed along the optical axis, which corresponds to the [001] direction in Ni_2InSbO_6. For optically inactive crystals, this orientation would correspond to the extinction position under crossed polarizers, where no light is transmitted regardless of the rotation angle of the crystal. In contrast, in optically active media, the polarization plane is rotated as light passes through the crystal, allowing part of the light to pass through the analyzer. Consequently, complete extinction only occurs when the crystal is rotated by the same angle as the optical rotation. The rotation angle depends on the strength of the optical activity and the thickness of the crystal.

Trigonal chiral space groups often exhibit enantiomorphic twin domains. These domains exhibit opposite handedness, resulting in optical rotation of opposite signs, either left- or right-handed. Through polarization microscopy, these enantiomorphic domains become visible because they do not share the same extinction orientation (see Figure 8.7). As a result, they appear as regions of differing brightness under crossed polarizers, as a direct consequence of the opposite sense of optical rotation in each domain.

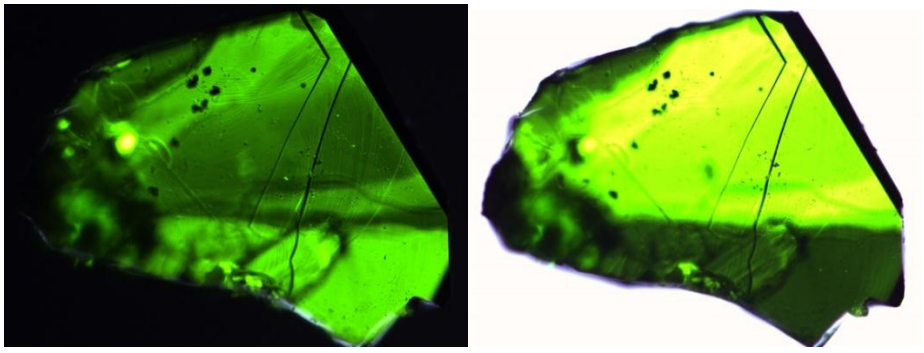

Figure 8.7: Polarized light microscopy image of a Ni_2InSbO_6 crystal viewed along the [100] direction under crossed polarizers. The image reveals enantiomorphic twin domains with opposite handedness. Bright and dark regions correspond to right- and left-handed domains, respectively, which rotate the polarization plane in opposite directions due to their optical activity.

9 Discussion

The objective of this work was to gain insights into ternary oxide systems containing the 4d and 5d transition metals Ru and Ir, with the aim of enabling the crystallization of perovskite-type compounds of the general formulas $Ba_3MM'O_9$ and $Ba_4MM'O_{12}$. The synthesis pathway was systematically investigated, with a particular emphasis on the flux growth method using a $BaCl_2$ flux. This approach allowed for the successful growth of a range of single crystals, which could be structurally characterized by single-crystal X-ray diffraction and chemically analyzed by EPMA WDX and SEM EDX analysis.

In addition, the chemical transport reaction method was employed for the synthesis of Ni_2InSbO_6 crystals. Through the combination of thermodynamic modeling and experimental validation, deeper insight into the reaction mechanism and growth behavior under transport conditions was achieved.

Initial synthesis experiments, for the crystal growth of Ir and Ru containing compounds, using the metallic oxides, $BaCO_3$, and $BaCl_2 \cdot 2H_2O$ showed pronounced chemical reactions between $BaCl_2$ and $BaCO_3$, indicating that $BaCl_2$ cannot be considered chemically inert under these conditions. The reaction product, in turn, appeared to be inert toward the metallic oxides, effectively depleting the system of barium required for the crystallization of perovskite phases. This significantly influences the reproducibility of the synthesis experiments. This finding demonstrated that the systems, based on the chosen starting materials, cannot be considered quasi-ternary. Furthermore, it was observed that high $BaCO_3$ content, corresponding to elevated BaO concentrations in combination with $BaCl_2$ at high temperatures, promoted the dissolution of Al_2O_3 from the crucible material, leading to the crystallization of Al-containing impurity phases, such as $BaAl_4O_4$ and $EuAlO_3$.
Platinum crucibles were found to be unsuitable for these syntheses, as platinum acted as a reactive component and was incorporated into the perovskite crystal structure. Although ZrO_2 crucibles were not tested in this study, they may provide advantages in future work due to their likely increased resistance to attack by BaO-rich melts.

To mitigate the strong interactions between flux and crucible/reactants, a modified approach was employed in which the target phase was first synthesized by solid-state reaction and then used as starting material for subsequent crystal growth. This method yielded significantly better and reproducible results in both Ir- and Ru-based systems.

Solid-state reaction experiments revealed that the Ir-based trimer phases $Ba_4MIr_3O_{12}$ are thermodynamically stable at lower temperatures than the corresponding dimer phases $Ba_3MIr_2O_9$. This observation was corroborated by simultaneous thermal analysis and powder X-ray diffraction. In contrast, the Ru-based systems were stable at higher temperatures above 1573 K. Higher synthesis temperatures favored single crystal growth, likely due to improved solubility and increased reactivity. However, excessively high temperatures promoted the volatilization of $BaCl_2$ and of the metal oxides Ta_2O_5 and Nb_2O_5, setting an upper thermal limit.

Both Ta_2O_5 and Nb_2O_5 showed strong reactivity with $BaCl_2$, forming volatile species. These species also appeared to act as transport agents for Ir and Ru, leading to the formation of quaternary perovskite-type compounds such as $Ba_8Ta_4Ru_3O_{24}$ deposited near the lid of the crucibles. In general, the vapor pressure in systems containing M = Nb_2O_5 or Ta_2O_5 appears to play a crucial role. In an open system, where no equilibrium between melt and vapor phase can be established, the volatility of the perovskite phases seems to dominate, and no crystal growth is observed. As has been shown, the ceramic glue also reacts with the vapor phase, meaning that sealing the system introducing an additional, unidentified factor that influences the crystal growth process.
The observations suggest that the synthesis of $Ba_8Ta_4Ru_3O_{24}$ via CVT could be a viable approach. However, such experiments require careful preparation and consideration, as temperatures exceeding 1573 K prevent the use of silica ampoules. Additionally, pre-sintered starting materials would be necessary in a closed system, since the decomposition of $BaCO_3$ generates excessive pressure within a sealed ampoule. For these reasons, conducting transport reactions in an open system would likely be more practical.

While crystals of $Ba_4MIr_3O_{12}$ tended to be smaller than their ruthenium-based analogs, clear differences were still observed depending on the choice of the *M*-cation. Crystals with M = Eu or Ce remained below 200 µm, likely due to the lower growth temperature (1373 K) and limited solubility of rare earth oxides in $BaCl_2$. By contrast, systems with M = Nb and Ta crystallized more readily but presented challenges related to volatility and phase competition.

Despite these limitations, single crystals of the novel compound $Ba_4TaIr_3O_{12}$ were successfully synthesized and structurally characterized via SC-XRD. The structure is isotypic to $Ba_4NbIr_3O_{12}$ and crystallizes in the space group $R\bar{3}m$. In contrast to $Ba_4NbIr_3O_{12}$, where significant Ir/Nb site disorder is known, no such substitution was observed in $Ba_4TaIr_3O_{12}$. This conclusion was supported by both chemical analysis and diffraction data, which showed excellent agreement with the nominal stoichiometry. It is therefore assumed that the structure is composed of fully ordered, isolated $[Ir_3O_{12}]$-trimer units.

The ruthenium analog, $Ba_4TaRu_3O_{12}$, also represents a novel compound. It was synthesized and characterized in this work. Elemental and structural analysis revealed that this material exhibits significant substitutional disorder, with approximately 25 % of the Ta site occupied by Ru.

Further ruthenium-based trimer phases were successfully grown, including $Ba_4CeRu_3O_{12}$ and $Ba_4PrRu_3O_{12}$. Crystals of $Ba_4CeRu_3O_{12}$ reached sizes greater than 1 mm and were structurally characterized via SC-XRD. A comparison between sintered and single-crystal samples revealed pronounced structural differences. In particular, the monoclinic distortion was significantly more pronounced in sintered samples. It is therefore hypothesized that this distortion may arise from structural stacking faults or anti-phase boundaries. Single crystals grown closer to equilibrium conditions may better represent the ideal, less defective structure.

For $Ba_4PrRu_3O_{12}$, single-crystal structure determination was not possible. Similar to the compounds $Ba_4EuIr_3O_{12}$ and $Ba_4CeIr_3O_{12}$, the c-axis could not be indexed, suggesting substantial stacking disorder.

A comparison of the *M*-cations used in this study revealed that $M = CeO_2$ and Pr_4O_7 (containing tetravalent cations) strongly favor the formation of trimer phases of the type $Ba_4MRu_3O_{12}$, whereas larger trivalent cations $M = Eu_2O_3$, Yb_2O_3, Tb_4O_7, and Y_2O_3 led to the formation of the dimer phase of the type $Ba_3MM'_2O_9$. This behavior appears to correlate not only with the valency but also with the ionic radii of the *M*-cations. All dimer-phase crystals were structurally and chemically characterized. They exhibited clear hexagonal symmetry, though in the cases of *M* = Eu and Tb, a potential distortion to the polar space group $P6_3mc$ is under discussion. A possible loss of inversion symmetry could, in principle, be verified by measuring physical properties such as second-harmonic generation or

piezoelectricity, but this was not feasible due to the small crystal size and lack of optical transparency.

In the final part of this work, an additional system was investigated that differs significantly from the Ir- and Ru-based cluster materials, both chemically and crystallographically. Thermodynamic modeling of the CTR system for Ni_2InSbO_6 using chloride transport agents revealed two unknown parameters that had to be estimated: the diffusion coefficient and the thermodynamic data for Ni_2InSbO_6. Comparison with experimentally measured transport rates indicated that a lower diffusion coefficient was necessary to reconcile calculated rates with measured values. Adjusting the thermodynamic data for Ni_2InSbO_6 alone did not yield satisfactory agreement unless the diffusion coefficient was also decreased.

Growth experiments showed that low transport rates (~1 mg/d) were optimal for producing large, well-formed single crystals. Higher transport rates (~3 mg/d) led to large but heavily intergrown crystals. The most effective way to control the transport rate was by reducing the cross-sectional area of the ampoule. Alternatively, decreasing the temperature gradient also proved effective.

Further analysis showed that the active transport species in this system were dominated by volatile chlorides of In, Sb and Ni, such as $InCl_3$, $SbCl_3$ and $NiCl_2$. The chemical composition of the crystals varied slightly depending on the partial pressure ratios of these species. This was observed by analyzing two different regions of the same crystal, which had formed under slightly different local transport conditions. The partial pressures of $InCl_3$ and $SbCl_3$ were of similar magnitude and showed a temperature-dependent crossover point. In contrast, the partial pressure of $NiCl_2$ was found to be an order of magnitude lower, indicating that Ni transport is rate-limiting in this system.

These investigations underscore the complexity of perovskite phase formation in multi-component systems, particularly under high-temperature and reactive conditions. The successful synthesis of several novel compounds and the identification of key reaction mechanisms provide a strong foundation for targeted crystal growth strategies in future studies.

Bibliography

[1] B. Yuan, B. H. Kim, Q. Chen, D. Dobrowolski, M. Azmanska, G. M. Luke, S. Fan, V. Bisogni, J. Pelliciari, and J. P. Clancy, "Highly tunable Ru-dimer molecular orbital state in 6H-perovskite $Ba_3MRu_2O_9$," *arXiv*:2405.09418 (2024).

[2] A. Revelli, M. Moretti Sala, G. Monaco, M. Magnaterra, J. Attig, L. Peterlini, T. Dey, A. A. Tsirlin, P. Gegenwart, T. Fröhlich, M. Braden, C. Grams, J. Hemberger, P. Becker, P. H. M. van Loosdrecht, D. I. Khomskii, J. van den Brink, M. Hermanns, and M. Grüninger, "Quasimolecular electronic structure of the spin-liquid candidate $Ba_3InIr_2O_9$," *Phys. Rev. B* **106**, 195128 (2022).

[3] M. Magnaterra, A. Sandberg, H. Schilling, P. Warzanowski, L. Pätzold, E. Bergamasco, Ch. J. Sahle, B. Detlefs, K. Ruotsalainen, M. M. Sala, G. Monaco, P. Becker, Q. Faure, G. S. Thakur, M. Songvilay, C. Felser, P. H. M. van Loosdrecht, J. van den Brink, M. Hermanns, and M. Grüninger, "Quasimolecular electronic structure of the trimer iridate $Ba_4NbIr_3O_{12}$," *Phys. Rev. B* **111**, 085122 (2025).

[4] S. N. Khanna and P. Jena, "Atomic clusters: Building blocks for a class of solids," *Phys. Rev. B* **51**, 13705 (1995).

[5] I. A. M. Ibrahim and C.-Y. Chung, "Lead-free double perovskites: How divalent cations tune the electronic structure for photovoltaic applications," *J. Mater. Chem. C* **10**, 12276 (2022).

[6] Y. Shimoda, Y. Doi, M. Wakeshima, and Y. Hinatsu, "Magnetic and electrical properties of quadruple perovskites with 12 layer structures $Ba_4LnM_3O_{12}$ (Ln = rare earths; M = Ru, Ir): The role of metal–metal bonding in perovskite-related oxides," *J. Solid State Chem.* **183**, 1962 (2010).

[7] R. Gross and A. Marx, *Festkörperphysik*, de Gruyter GmbH, Berlin, 2017, ISBN 978-3-11-055822-7.

[8] R. Winkler, *Spin–Orbit Coupling Effects*, Springer, Heidelberg, 2003, pp. 1–2, ISBN 3-540-01187-0.

[9] D. J. Griffiths, *Introduction to Quantum Mechanics*, 2nd ed., Prentice Hall, Upper Saddle River, 2005, pp. 246–266, ISBN 0-13-191175-9.

[10] D. D. Sarma "Nature of dependence of spin-orbit splittings on atomic number," *Proc. Indian Acad. Sci. Chem. Sci.*, **90**, 19–26 (1981).

[11] C. Du, H. Wang, F. Yang, and P. C. Hammel, "Systematic variation of spin-orbit coupling with d-orbital filling: Large inverse spin Hall effect in 3d transition metals," *Phys. Rev. B* **90**, 140425 (2014).

[12] G. L. Stamokostas and G. A. Fiete, "Mixing of t_{2g}–e_g orbitals in 4d and 5d transition metal oxides," *Phys. Rev. B* **97**, 045114 (2018).

[13] A. Revelli, M. Moretti Sala, G. Monaco, P. Becker, L. Bohaty, M. Hermanns, T. C. Koethe, T. Fröhlich, P. Warzanowski, T. Lorenz, S. V. Streltsov, P. H. M. van Loosdrecht, D. I. Khomskii, J. van den Brink, and M. Grüninger, "Resonant inelastic x-ray incarnation of Young's double-slit experiment," *Science Advances* **5**, eaav4020 (2019).

[14] H.-S. Kim, J. Im, M. J. Han, and H. Jin, "Spin-orbital entangled molecular je states in lacunar spinel compounds," *Nature Communications* **5**, 3988 (2014).

[15] J. P. Clancy, N. Chen, C. Y. Kim, W. F. Chen, K. W. Plumb, B. C. Jeon, T. W. Noh, and Y.-J. Kim, "Spin-orbit coupling in iridium-based 5d compounds probed by x-ray absorption spectroscopy," *Phys. Rev. B* **86**, 195131 (2012).

[16] E. Riedel and C. Janiak, *Anorganische Chemie*, Walter de Gruyter GmbH, Berlin/Boston, 2022, ISBN 978-3-11-069604-2.

[17] P. Jena and S. N. Khanna, "Physics of cluster assembled materials," *Materials Science and Engineering: A* **217–218**, 218–222 (1996).

[18] M. Magnaterra, J. Attig, L. Peterlini, M. Hermanns, M. H. Upton, J. Kim, L. Prodan, V. Tsurkan, I. Kezsmárki, P. H. M. van Loosdrecht, and M. Grüninger, "Quasimolecular J_{tet}=3/2 moments in the cluster Mott insulator $GaTa_4Se_8$," *Phys. Rev. Lett.* **133**, 036401 (2024).

[19] Y. Okamoto, H. Amano, N. Katayama, H. Sawa, K. Niki, R. Mitoka, H. Harima, T. Hasegawa, N. Ogita, Y. Tanaka, M. Takigawa, Y. Yokoyama, K. Takehana, Y. Imanaka, Y. Nakamura, H. Kishida, and K. Takenaka, "Regular-triangle trimer and charge order preserving the Anderson condition in the pyrochlore structure of CsW_2O_6," *Nature Communications* **11**, 4614 (2020).

[20] R. Nakamura, D. Takegami, A. Melendez-Sans, L. H. Tjeng, M. Okawa, T. Miyoshino, N. L. Saini, M. Kitamura, D. Shiga, H. Kumigashira, M. Yoshimura, K. D. Tsuei, Y. Okamoto, and T. Mizokawa, "Electronic structure reconstruction by trimer formation in CsW_2O_6 studied by x-ray photoelectron spectroscopy," *Phys. Rev. B* **106**, 195131 (2022).

[21] Y. Okamoto, "Electronic self-organization in the β-pyrochlore oxide CsW_2O_6," *J. Phys. Soc. Jpn.* **93**, 044701 (2024).

[22] T. Hikihara and Y. Motome, “Orbital and spin interplay in spin-gap formation in pyroxene $ATiSi_2O_6$ (A = Na, Li),” *Phys. Rev. B* **70**, 214404 (2004).

[23] S. A. Nikolaev, I. V. Solovyev, and S. V. Streltsov, “Quantum spin liquid and cluster Mott insulator phases in the Mo_3O_8 magnets,” *npj Quantum Materials* **6**, 12 (2021).

[24] A. Akbari-Sharbaf, R. Sinclair, A. Verrier, D. Ziat, H. D. Zhou, X. F. Sun, and J. A. Quilliam, “Tunable quantum spin liquidity in the 1/6-filled breathing kagome lattice,” *Phys. Rev. Lett.* **120**, 227201 (2018).

[25] T.-H. Yang, S. Kawamoto, T. Higo, S. G. Wang, M. B. Stone, J. Neuefeind, J. P. C. Ruff, A. M. M. Abeykoon, Y.-S. Chen, S. Nakatsuji, and K. W. Plumb, “Bond ordering and molecular spin-orbital fluctuations in the cluster Mott insulator $GaTa_4Se_8$,” *Phys. Rev. Research* **4**, 013088 (2022).

[26] M. Y. Jeong, S. H. Chang, B. H. Kim, J.-H. Sim, A. Said, D. Casa, T. Gog, E. Janod, L. Cario, S. Yunoki, M. J. Han, and J. Kim, “Direct experimental observation of the molecular $J_e$ff = 3/2 ground state in the lacunar spinel $GaTa_4Se_8$,” *Nature Communications* **8**, 782 (2017).

[27] A. J. Browne, S. A. J. Kimber, and J. P. Attfield, “Persistent three- and four-atom orbital molecules in the spinel AlV_2O_4,” *Phys. Rev. Materials* **1**, 054406 (2017).

[28] Y. Shimoda, Y. Doi, M. Wakeshima, and Y. Hinatsu, “Synthesis and magnetic properties of 12L-perovskites $Ba_4LnIr_3O_{12}$ (Ln = lanthanides),” *J. Solid State Chem.* **182**, 2873–2879 (2009).

[29] Y. Doi, K. Matsuhira, and Y. Hinatsu, “Crystal structures and magnetic properties of 6H-perovskites $Ba_3MRu_2O_9$ (M = Y, In, La, Sm, Eu, and Lu),” *J. Solid State Chem.* **165**, 317–323 (2002).

[30] G. S. Thakur, S. Chattopadhyay, T. Doert, T. Herrmannsdörfer, and C. Felser, “Crystal growth of spin-frustrated $Ba_4Nb_{0.8}Ir_{3.2}O_{12}$: a possible spin liquid material,” *Cryst. Growth Des.* **20**, 2871–2876 (2020).

[31] Y. Li, A. A. Tsirlin, T. Dey, P. Gegenwart, R. Valentí, and S. M. Winter, “Soft and anisotropic local moments in 4d and 5d mixed-valence M_2O_9 dimers,” *Phys. Rev. B* **102**, 235142 (2020).

[32] A. Nag, S. Bhowal, M. M. Sala, A. Efimenko, I. Dasgupta, and S. Ray, “Hopping-induced ground-state magnetism in 6H perovskite iridates,” *Phys. Rev. Lett.* **123**, 017201 (2019).

[33] Y. Shimoda, Y. Doi, M. Wakeshima, and Y. Hinatsu, "Magnetic properties of quadruple perovskites $Ba_4LnRu_3O_{12}$ (Ln = La, Nd, Sm–Gd, Dy–Lu)," *J. Solid State Chem.* **183**, 33–40 (2010).

[34] H. Zhao, Y. Zhang, P. Schlottmann, R. Nandkishore, L. E. DeLong, and G. Cao, "Transition between heavy-fermion-strange-metal and quantum spin liquid in a 4d-electron trimer lattice," *Phys. Rev. Lett.* **132**, 076401 (2024).

[35] G. Rose, "Ueber einige neue Mineralien des Urals, 1. Der Perowskit, eine neue Mineralspecies," *J. Prakt. Chem.* **19**, 459–460 (1840).

[36] T. Barth, "Die Kristallstruktur von Perowskit und verwandten Verbindungen," *Norsk Geol. Tidsskr.* **8**, 201–216 (1925).

[37] H. D. Megaw, "Crystal structure of double oxides of the perovskite," *Proc. Phys. Soc.* **58**, 133–152 (1946).

[38] R. H. Mitchell, *Perovskites: Modern and Ancient*, (Almaz Press Inc., Canada, 2002), ISBN: 0-9689411.

[39] A. M. Glazer, "The classification of tilted octahedra in perovskites," *Acta Cryst. B* **28**, 3384–3392 (1972).

[40] Y. Takeda, F. Kanamaru, M. Shimada, and M. Koizumi, "The crystal structure of $BaNiO_3$," *Acta Cryst. B* **32**, 2464–2466 (1976).

[41] R. D. Burbank and H. T. Evans, "The crystal structure of hexagonal barium titanate," *Acta Cryst.* **1**, 330–336 (1948).

[42] Ch. Lang and H. K. Müller-Buschbaum, "Ba_2EuIrO_6 – Eine Kristallstrukturuntersuchung an einer 6L-Perowskitstapelvariante," *J. Less-Common Met.* **161**, 1–6 (1990).

[43] L. T. Nguyen and R. J. Cava, "Hexagonal perovskites as quantum materials," *Chem. Rev.* **121**, 2935–2965 (2021).

[44] Y. Hinatsu and Y. Doi, "Structures and magnetic properties of double perovskites A_2LnMO_6 and 6H-perovskites $Ba_3LnRu_2O_9$ (A = Sr, Ba; Ln = Y, lanthanides; M = Nb, Ta, Ru)," *Bull. Chem. Soc. Jpn.* **76**, 1093–1113 (2003).

[45] Y. Doi, M. Wakeshima, Y. Hinatsu, A. Tobo, K. Ohoyama, and Y. Yamaguchi, "Crystal structures and magnetic properties of the 6H-perovskites $Ba_3LnRu_2O_9$ (Ln = Ce, Pr and Tb)," *J. Mater. Chem.* **11**, 3135–3140 (2001).

[46] P. Lightfoot and P. D. Battle, “The crystal and magnetic structures of $Ba_3NiRu_2O_9$, $Ba_3CoRu_2O_9$ and $Ba_3ZnRu_2O_9$,” *J. Solid State Chem.* **89**, 174–183 (1990).

[47] J. T. Rijssenbeek, Q. Huang, R. W. Erwin, H. W. Zandbergen, and R. J. Cava, “The crystal structure of $Ba_3CuRu_2O_9$ and comparison to $Ba_3MRu_2O_9$ (M = In, Co, Ni, Fe),” *J. Solid State Chem.* **146**, 65–72 (1999).

[48] Y. Doi, M. Wakeshima, Y. Hinatsu, A. Tobo, K. Ohoyama, and Y. Yamaguchi, “Structural and magnetic characterization of 6H-perovskite-type oxides $Ba_3LnIr_2O_9$ (Ln = Y, lanthanides),” *J. Mater. Chem.* **11**, 3135–3140 (2001).

[49] T. Sakamoto, Y. Doi, and Y. Hinatsu, “Crystal structures and magnetic properties of 6H-perovskite-type oxides $Ba_3MIr_2O_9$ (M = Mg, Ca, Sc, Ti, Zn, Sr, Zr, Cd and In),” *J. Solid State Chem.* **179**, 2595–2601 (2006).

[50] T. Fröhlich, *Structural aspects of systems with spin–orbit coupling*, Dissertation, Köln (2020).

[51] Y. Shimoda, Y. Doi, and Y. Hinatsu, “Synthesis, crystal structures, and magnetic properties of new 12L-perovskites $Ba_4LnRu_3O_{12}$ (Ln = lanthanides),” *Chem. Mater.* **20**, 4512–4518 (2008).

[52] J. M. Longo, L. Katz, and R. Ward, “Rhenium-containing complex metal oxides of the formula type $AII_4ReVII_2MII\ O_{12}$,” *Inorg. Chem.* **4**, 235 (1965).

[53] J. Wilkens and H. K. Müller-Buschbaum, “$Ba_{12}Ir_{2-x}Nb_xO_{36}$ (x = 2, 4) – Eine neue Verbindung mit 12R-Perowskit-Stapelvariante,” *J. Alloys Compd.* **176**, 141–146 (1991).

[54] P. E. R. Blanchard, K. W. Chapman, S. M. Heald, M. Zbiri, M. R. Johnson, B. J. Kennedy, and C. D. Ling, “Direct observation of pressure-driven valence electron transfer in $Ba_3BiRu_2O_9$, $Ba_3BiIr_2O_9$ and $Ba_4BiIr_3O_{12}$,” *Inorg. Chem.* **55**, 11 (2016).

[55] M. Wojciech, M. T. Dunstan, Z. Huang, Z. Mohamed, B. J. Kennedy, M. Avdeev, and C. D. Ling, “Complex 5d magnetism in a novel S = 1/2 trimer system, the 12L hexagonal perovskite $Ba_4BiIr_3O_{12}$,” *Inorg. Chem.* **52**, 12181–12854 (2013).

[56] L. T. Nguyen and R. J. Cava, “The trimer-based spin liquid candidate $Ba_4NbIr_3O_{12}$,” *Phys. Rev. Mater.* **3**, 014412 (2018).

[57] A. Bandyopadhyay, S. Lee, D. T. Adroja, G. B. G. Stenning, A. Berlie, M. R. Lees, R. A. Saha, D. Takegami, A. Melendez-Sans, G. Poelchen, M. Yoshimura, K. D. Tsuei, Z. Hu, C.-W. Kao, Y.-C. Huang, T.-S. Chan, and K.-Y. Choi, “Novel quantum spin liquid ground state in the trimer rhodate $Ba_4NbRh_3O_{12}$,” *Phys. Rev. B* **109**, 054405 (2024).

[58] L. T. Nguyen, T. Kong, and R. J. Cava, “Trimers of MnO_6 octahedra and ferrimagnetism of $Ba_4NbMn_3O_{12}$,” *Materials Research Express* (2019).

[59] A. Ali, H.-S. Kim, P. Yadav, S. Lee, D. Yoon, and S. Choi, “Partial molecular orbitals in face-sharing 3d manganese trimer: Comparative studies on $Ba_4TaMn_3O_{12}$ and $Ba_4NbMn_3O_{12}$,” *Phys. Rev. Research* **6** (2024).

[60] Y. Shimoda, Y. Doi, M. Wakeshima, and Y. Hinatsu, “Crystal structures and characterizations of mixed valence 12L-perovskites $Ba_4EuM_3O_{12}$ (M = Ru and Ir),” *Inorg. Chem.* **48**, 9952–9957 (2009).

[61] W. Masser, *Kristallstrukturbestimmung*, Springer Spektrum, 2013. ISBN 978-3-658-09411-9.

[62] W. H. Bragg and W. L. Bragg, “The reflection of X rays by crystals,” *Proc. R. Soc. Lond. A* **88**, 428–438 (1913).

[63] B. D. Cullity and S. R. Stock, *Elements of X-ray Diffraction*, 3rd ed., Pearson Education, 2001. ISBN 1-292-04054-8.

[64] A. Coelho, *TOPAS Academic V5*, Coelho Software, Brisbane, Australia (2012).

[65] Bruker, *APEX3 Software Suite*, Bruker AXS Inc., Madison, WI, USA (2016).

[66] V. Petríček, L. Palatinus, J. Plášil, and M. Dušek, “Jana2020 — a new version of the crystallographic computing system Jana,” *Z. Kristallogr.* **238**, 271–282 (2023).

[67] V. Petríček, M. Dušek, and L. Palatinus, “Crystallographic computing system JANA2006: General features,” *Z. Kristallogr.* **229**, 345–352 (2014).

[68] P. Gabbott, *Principles and Applications of Thermal Analysis*, Blackwell Publishing, 2003. ISBN 978-1-4051-3171-1.

[69] P. J. Potts, J. F. W. Bowles, S. J. B. Reed, and M. R. Cave, *Microprobe Techniques in the Earth Sciences*, Chapman and Hall, 1995. ISBN 978-0-412-55100-0.

[70] J. I. Goldstein, D. E. Newbury, J. R. Michael, N. W. M. Ritchie, J. H. J. Scott, and D. C. Joy, *Scanning Electron Microscopy and X-Ray Microanalysis*, 4th ed., Springer Verlag GmbH, 2018. ISBN 978-1-4939-6674-5.

[71] X. Llovet, A. Moy, P. T. Pinard, and J. H. Fournelle, “Electron probe microanalysis: A review of recent developments and applications in materials science and engineering,” *Prog. Mater. Sci.* **120**, 1–90 (2021).

[72] K. Th. Wilke and J. Böhm, *Kristallzüchtung*, J. A. Barth, Leipzig (1993).

[73] D. Elwell and H. J. Scheel, *Crystal Growth from High-Temperature Solutions*, Academic Press, London (1975).

[74] T. Nishinaga, *Handbook of Crystal Growth, Fundamentals: Thermodynamics*, Vol. 1, Elsevier, Japan, 2014. ISBN 978-0444563699.

[75] A. K. Jha, *Solid-State Chemistry – A Modern Approach*, Apple Academic Press, 2023, pp. 1–8. ISBN 978-1-77491-197-6.

[76] L. Kerkhoff, *Crystal Growth and Structural Aspects of Alkali Iridates and Ruthenates of Lithium and Sodium*, Dissertation, Köln (2021).

[77] J. W. Gibbs, "On the equilibrium of heterogeneous substances," *Trans. Conn. Acad. Arts Sci.* **3**, 108–248 (1878).

[78] J. W. Gibbs, "On the equilibrium of heterogeneous substances (concluded)," *Trans. Conn. Acad. Arts Sci.*, 343–524 (1878).

[79] W. Ostwald, "Studien über die Bildung und Umwandlung fester Körper," *Z. Phys. Chem.* **22**, 1–42 (1897).

[80] W. Kossel, *Nachrichten von der Gesellschaft der Wissenschaften zu Göttingen* (1928).

[81] P. C. Canfield and Z. Fisk, "Growth of single crystals from metallic fluxes," *Philos. Mag. B* **65**, 1117–1123 (1992).

[82] M. Binnewies, R. Glaum, M. Schmidt, and P. Schmid, *Chemische Transportreaktionen*, Walter de Gruyter GmbH & Co. KG (2011).

[83] H. Schäfer, *Chemische Transportreaktionen: Der Transport anorganischer Stoffe über die Gasphase und seine Anwendungen*, Chemie GmbH, Weinheim (1963).

[84] M. Lindner, *Kristallzüchtung im System Cu-V-O: Aufbau einer CTR-Zuchtungsanlage, Kristallzüchtung und -charakterisierung*, Diplomarbeit Köln (2006).

[85] M. Binnewies and E. Milke, *Thermodynamical Data of Elements and Compounds*, Wiley-VCH, Weinheim, 2002. ISBN 3-527-30524-6.

[86] V. Plies, T. Kohlmann, and R. Grühn, "Eine Methode zur kontinuierlichen Bestimmung von Transportraten: Experimente im System $GeO_2/WO_2/H_2O$ und $NiSO_4/PbSO_4/PbCl_2$," *Z. Anorg. Allg. Chem.* **568**, 62–72 (1989).

[87] K. S. Pedersen, J. Bendix, A. Tressaud, E. Durand, H. Weihe, Z. Salman, T. J. Morsing, D. N. Woodruff, Y. Lan, W. Wernsdorfer, C. Mathonière, S. Piligkos, S. I. Klokishner, S. Ostrovsky, K. Ollefs, F. Wilhelm, A. Rogalev, and R. Clerac, "Iridates from the molecular side," *Nat. Commun.* **7**, 1–7 (2016).

[88] A. A. Aczel, Q. Chen, J. P. Clancy, C. dela Cruz, D. Reig-i-Plessis, G. J. MacDougall, C. J. Pollock, M. H. Upton, T. J. Williams, N. LaManna, J. P. Carlo, J. Beare, G. M. Luke, and H. D. Zhou, "Spin-orbit coupling controlled ground states in the double perovskite iridates A_2BIrO_6 (A=Ba, Sr; B=Lu, Sc)," *Phys. Rev. Mater.* **6**, 094409 (2022).

[89] P. Kayser, M. J. Martínez-Lope, J. A. Alonso, M. Retuerto, M. Croft, A. Ignatov, and M. T. Fernández-Díaz, "Crystal structure, phase transitions, and magnetic properties of iridium perovskites Sr_2MIrO_6 (M = Ni, Zn)," *Inorg. Chem.* **52**, 11013–11022 (2013).

[90] Y. Gong, M. Zhou, M. Kaupp, and S. Riedel, "Formation and characterization of the iridium tetroxide molecule with iridium in the oxidation state +VIII," *Angew. Chem. Int. Ed.* **48**, 7879–7883 (2009).

[91] T. Aharen, *Crystal structure and magnetic properties of geometrically frustrated face-centered cubic (fcc) double perovskites* (2010).

[92] C. I. Hiley, M. R. Lees, J. M. Fisher, D. Thompsett, S. Agrestini, R. I. Smith, and R. I. Walton, "Ruthenium(V) oxides from low-temperature hydrothermal synthesis," *Angew. Chem. Int. Ed.* **53**, 4423–4427 (2014).

[93] I. Arvanitidis, D. Sichen, and S. Seetharaman, "A study of the thermal decomposition of $BaCO_3$," *Metall. Mater. Trans.* **27**, 409–416 (1996).

[94] H. Schäfer, "Über die Darstellung der Nioboxide und ihren Transport im Temperaturgefälle," *Z. Anorg. Allg. Chem.* **317**, 321–333 (1962).

[95] J. H. E. Jeffes and T. N. R. Marples, "The thermodynamics of chemical transport reaction with special references to the transport of tantalum by iodine," *J. Cryst. Growth* **17**, 46–52 (1972).

[96] M. Magnaterra, M. Moretti Sala, G. Monaco, P. Becker, M. Hermanns, P. Warzanowski, T. Lorenz, D. I. Khomskii, P. H. M. van Loosdrecht, J. van den Brink, and M. Grüninger, "RIXS interferometry and the role of disorder in the quantum magnet $Ba_3Ti_{3-x}Ir_xO_9$," *Phys. Rev. Res.* **5** (2023).

[97] M. Esthaku Peter, A. Addisu Dabulo, and T. Gurumurthi, "Growth and characterization of barium chloride dihydrate crystal," *Int. J. Sci. Res.* **8**, 1775–1779 (2019).

[98] I. R. Bellobono, B. Maracandalli, E. Selli, and R. Lancia, "Thermodynamic analysis of the reaction of barium chloride with water vapour from 1173 K to 1473 K," *Mater. Chem. Phys.* **10**, 163–174 (1984).

[99] K. H. Stern, *"*High Temperature Properties and Decomposition of Inorganic Salts*," J. Phys. Chem. Ref. Data - Part 4. Oxy-Salts of the Halogens* **3**, 488–489 (1974).

[100] P. Leyva-Bailen, P. Vaqueiro, and A. V. Powell, "Ionothermal synthesis of the mixed-anion material, $Ba_3Cl_4CO_3$," *J. Solid State Chem.* **182**, 2333–2337 (2009).

[101] B. Frit, B. Tanguy, and P. Hagenmuller, *Bull. Soc. Chim. Fr.* **1**, 234–237 (1967).

[102] Y. Shen, J. Sears, G. Fabbris, A. Weichselbaum, W. Yin, H. Zhao, D. G. Mazzone, H. Miao, M. H. Upton, D. Casa, R. Acevedo-Esteves, C. Nelson, A. M. Barbour, C. Mazzoli, G. Cao, and M. P. M. Dean, "Emergence of spinons in layered trimer iridate $Ba_4Ir_3O_{10}$," *Phys. Rev. Lett.* **129**, 207201 (2022).

[103] X. Chen, Y. He, S. Wu, Y. Song, D. Yuan, E. Bourret-Courchesne, J. P. C. Ruff, Z. Islam, A. Frano, and R. J. Birgeneau, "Structural and Magnetic Transitions in the Planar Antiferromagnet $Ba_4Ir_3O_{10}$," *Phys. Rev.* **103**, 224420 (2021).

[104] C. Lang and H. Müller-Buschbaum, "$Ba_5AlIr_2O_{11}$: Eine neue Verbindung mit Iridium (IV,V)," *Z. Anorg. Allg. Chem.* **568** (1989).

[105] A. Revelli, C. C. Loo, D. Kiese, P. Becker, T. Fröhlich, T. Lorenz, M. M. Sala, G. Monaco, F. L. Buessen, J. Attig, M. Hermanns, S. V. Streltsov, D. I. Khomskii, J. van den Brink, M. Braden, P. H. M. van Loosdrecht, S. Trebst, A. Paramekanti, and M. Grüninger, "Spin-orbit entangled j = 1/2 moments in Ba_2CeIrO_6: A frustrated fcc quantum magnet," *Phys. Rev.* **100**, 085139 (2019).

[106] Kager Industrieprodukte GmbH, *Sicherheitsdatenblatt: Ceramabond 503*.

[107] D. Nötzold and H. Wulff, "Structural and Optical Properties of the System (Sr, Ba, Eu)$_5$(PO_4)$_3$Cl," *Phys. Stat. Sol.* **158**, 303–311 (1996).

[108] K. Manna, G. Aslan-Cansever, A. Maljuk, S. Wurmehl, S. Seiro, and B. Büchner, "Flux growth of $Sr_{n+1}Ir_nO_{3n+1}$ (n = 1, 2, ∞) crystals," *J. Cryst. Growth* **540**, 125657 (2020).

[109] D. L. Hildenbrand, "Dissociation Energies and Chemical Bonding in the Alkaline-Earth Chlorides from Mass Spectrometric Studies," *J. Chem. Phys.* **52**, 11 (1970).

[110] J. R. V. Garcia and T. Goto, "Chemical Vapor Deposition of Iridium, Platinum, Rhodium and Palladium," *Materials Transactions* **44**, 1717–1728 (2003).

[111] J. Wilkens and H. K. Müller-Buschbaum, "Röntgenstrukturanalyse verzwillingter Einkristalle von $Ba_6IrNb_2O_{12}Cl_2$," *J. Alloys Compd.* **179**, 187–193 (1992).

[112] J.-W. Chen, K. R. Chiou, A.-C. Hsueh, and C.-R. Chang, "Dielectric relaxation of the double perovskite oxide Ba_2PrRuO_6," *RSC Adv.* **9**, 12319–12324 (2019).

[113] J. G. Zhao, L. X. Yang, Y. Yu, F. Y. Li, R. C. Yu, Z. Fang, L. C. Chen, and C. Q. Jin, "Structural and physical properties of the 6H $BaRuO_3$ polymorph synthesized under high pressure," *J. Solid State Chem.* **180**, 2816–2823 (2007).

[114] E. M. Kopnin, A. A. Belik, R. V. Shpanchenko, E. V. Antipov, F. Izumi, E. Takayama-Muromachi, and J. Hadermann, "Synthesis, crystal structure, and magnetic properties of new layered hexagonal perovskite $Ba_8Ta_4Ru_{8/3}Co_{2/3}O_{24}$," *J. Solid State Chem.* **177**, 3499–3504 (2004).

[115] J. Wilken and H. K. Müller-Buschbaum, "Zur Kenntnis von $Ba_4Ir_3O_{10}$," *Z. Anorg. Allg. Chem.* **592**, 79–83 (1991).

[116] K. E. Stitzer, M. D. Smith, and H.-C. zur Loye, "Crystal growth, structure determination and magnetic properties of $Ba_4Ir_3O_{10}$ and $Ba_4(Co_{0.4}Ir_{0.6})Ir_2O_{10}$," *J. Alloys Compd.* **338**, 104–111 (2002).

[117] C. Lang and H. Müller-Buschbaum, "Über ein neues Oxoiridat(IV): $Ba_7Ir_6O_{19}$," *Monatsh. Chem.* **120**, 705–710 (1989).

[118] G. Cao, H. Zheng, H. Zhao, Y. Ni, C. A. Pocs, Y. Zhang, F. Ye, C. Hoffmann, X. Wang, M. Lee, M. Hermele, and I. Kimchi, "Quantum liquid from strange frustration in the trimer magnet $Ba_4Ir_3O_{10}$," *Quantum Materials* **26** (2020).

[119] M. Neubacher, "Ein neues Verknüpfungsmuster von Ir_3O_{12}-Oktaedertripeln in $Ba_4Ir_{3-x}Ti_xO_{10}$ (x = 1,55)," *Z. Anorg. Allg. Chem.* **586**, 87–92 (1990).

[120] R. Herbst-Irmer and G. M. Sheldrick, "Refinement of obverse/reverse twins," *Acta Cryst.* **58**, 477–481 (2002).

[121] L. T. Nguyen, T. Halloran, W. Xie, T. Kong, C. L. Broholm, and R. J. Cava, "Geometrically frustrated trimer-based Mott insulator," *Phys. Rev. Mater.* **2**, 054414 (2018).

[122] Y. Doi, M. Wakeshima, Y. Hinatsu, A. Tobo, K. Ohoyama, and Y. Yamaguchi, "Magnetic and calorimetric studies on 6H-perovskite $Ba_3TbRu_2O_9$," *J. Alloys Compd.* **344**, 166–169 (2002).

[123] T. Dey, A. V. Mahajan, P. Khuntia, M. Baenitz, Koteswararao, and F. C. Chou, "Spin-liquid behavior in J_eff = -1/2 triangular lattice compound $Ba_3IrTi_2O_9$," *Phys. Rev.* **86**, 140405 (2012).

[124] C. Maunders, J. Etheridge, N. Wright, and H. J. Whitfield, "Structure and microstructure of hexagonal $Ba_3Ti_2RuO_9$ by electron diffraction and microscopy," *Acta Cryst.* **61**, 154–159 (2005).

[125] H. T. Stokes, D. M. Hatch, and B. J. Campbell, *ISODISTORT, ISOTROPY Software Suite*, iso.byu.edu.

[126] B. J. Campbell, H. T. Stokes, D. E. Tanner, and D. M. Hatch, "ISODISPLACE: An Internet Tool for Exploring Structural Distortions," *J. Appl. Cryst.* **39**, 607–614 (2006).

[127] R. E. Newnham and E. P. Meagher, "Crystal Structure of Ni_3TeO_6," *Mater. Res. Bull.* **2**, 549–554 (1967).

[128] S. A. Ivanov, P. Nordblad, R. Mathieu, R. Tellgren, C. Ritter, N. V. Golubko, E. D. Politova, and M. Weil, "New type of incommensurate magnetic ordering in Mn_3TeO_6," *Mater. Res. Bull.* **46**, 1870–1877 (2011).

[129] S. A. Ivanov, R. Tellgren, C. Ritter, P. Nordblad, R. Mathieu, G. Andre, N. V. Golubko, E. D. Politova, and M. Weil, "Temperature-dependent multi-k magnetic structure in multiferroic Co_3TeO_6," *Mater. Res. Bull.* **47** (2012).

[130] I. Zivkovic, K. Prša, O. Zaharko, and H. Berger, "Ni_3TeO_6 - a collinear antiferromagnet with ferromagnetic honeycomb planes," *J. Phys.: Condens. Matter* **22** (2010).

[131] K. Y. Choi, P. Lemmens, E. S. Choi, and H. Berger, "Lattice anomalies and magnetic excitations of the spin web compound Cu_3TeO_6," *J. Phys.: Condens. Matter* **20** (2008).

[132] R. Mathieu, S. A. Ivanov, P. Nordblad, and M. Weil, "Enhancement of antiferromagnetic interaction and transition temperature in M_3TeO_6 (M = Mn, Co, Ni, Cu)," *Eur. Phys. J. B* **86**, 1–4 (2013).

[133] D. Maluski, K. Gawęda, J. Debray, F. Damay, S. Petit, and A. H. Moudden, "Giant natural optical rotation from chiral electromagnons in a collinear antiferromagnet," arXiv:2312.02733 (2023).

[134] S. Ivanov, P. Nordblad, R. Mathieu, R. Tellgren, E. Politova, G. André, „Short-Range Spin Order and Frustrated Magnetism in Mn_2InSbO_6 and Mn_2ScSbO_6,“ *ChemInform*. **43**, (2012).

[135] S. A. Ivanov, R. Mathieu, P. Nordblad, R. Tellgren, C. Ritter, E. Politova, G. Kaleva, A. Mosunov, S. Stefanovich, M. Weil, “Spin and Dipole Ordering in Ni_2InSbO_6 and Ni_2ScSbO_6 with Corundum-Related Structure,” *Chem. Mater.* **25**, 935–945 (2013).

[136] M. Weil, R. Mathieu, P. Nordblad, S. A. Ivanov, “Crystal growth experiments in the systems Ni_2MSbO_6 (M = Sc, In) using chemical vapour transport reactions: Ni_2InSbO_6 and $Ni_2Sb_2O_6$ crystals in the millimeter range,” *Cryst. Res. Technol.* **49**, 142–151 (2013).

[137] R. Glaum, O. Trappe, “Das Computerprogramm CVTRANS zur Modellierung chemischer Transportexperimente,” (1999).

[138] H. Schornstein, R. Gruehn, “Zum chemischen Transport von MoO_2 und Mo_4O_{11} mit dem Transportmittel $HgCl_2$: Experimente und Modellrechnungen,” *Z. Anorg. Allg. Chem.* **587**, 129–144 (1990).

[139] M. Ritschel, H. Oppermann, “On the Chemical Transport of Molybdenum Dioxide with Tellurtetrahalogens,” *Krist. Tech.* **15**, 395–401 (1980).

[140] C. Horike, K. Morita, T. H. Okabe, “Effective Dissolution of Platinum by Using Chloride Salts,” *Metall. Mater. Trans. B* **43**, 1300–1307 (2012).

[141] Z. Liu, Y. Araki, T. Arima, S. Itoh, S. Asai, T. Masuda, “Spin Excitation in Coupled Honeycomb Lattice Ni_2InSbO_6,” *Phys. Rev.* **107** (2023).

[142] A. A. Bolzan, C. Fong, B. J. Kennedy, C. J. Howard, “Structural studies of rutile-type metal dioxides,” *Acta Crystallogr. B* **53** (1997).

[143] S. Geller, V. B. Bala, “Crystallographic studies of perovskite-like compounds. II. Rare earth aluminates,” *Acta Crystallogr.* **9** (1956).

[144] A. J. Perrotta, J. V. Smith, “The crystal structure of $BaAl_2O_4$,” *Bull. Soc. Fr. Minéral. Cristallogr.* **91** (1968).

[145] J. P. R. de Villiers, “Crystal structures of aragonite, strontianite, and witherite,” *Am. Mineral.* **56** (1971).

[146] T. Siegrist, B. L. Chamberland, “The crystal structure of $BaIrO_3$,” *J. Less-Common Met.* **170** (1991).

[147] H. E. Swanson, N. T. Gilfrich, G. M. Ugrinic, "Standard X-ray diffraction powder patterns," *Natl. Bur. Stand. Circ.* **539** (1995).

[148] M. L. Foo, Q. Huang, J. W. Lynn, W.-L. Lee, T. Klimczuk, I. S. Hagemann, N. P. Ong, R. J. Cava, "Synthesis, structure and physical properties of Ru ferrites: BaM Ru_5O_{11} (M = Li and Cu) and BaM′$_2$ Ru_4O_{11} (M′ = Mn, Fe and Co)," *J. Solid State Chem.* **179** (2006).

[149] W. T. Wu, D. J. W. Ijdo, "On the symmetry and structure of the double perovskites Ba_2LnRuO_6 (Ln = La, Pr and Nd)," *Solid State Commun.* **136**, 456–461 (2005).

[150] E. M. Kopnin, A. A. Belik, R. V. Shpanchenko, E. V. Antipov, F. Izumi, "Synthesis, crystal structure, and magnetic properties of new layered hexagonal perovskite $Ba_8Ta_4Ru_{8/3}Co_{2/3}O_{24}$," *J. Solid State Chem.* **177**, 3499–3504 (2004).

[151] Y. Ma, Y. Ma, G. Giuli, H. Euchner, A. Groß, G. O. Lepore, F. d'Acapito, D. Geiger, J. Biskupek, U. Kaiser, H. M. Schütz, A. Carlsson, T. Diemant, R. J. Behm, M. Kuenzel, S. Passerini, D. Bresser, „Introducing highly redox-active atomic centers into insertion-type electrodes for lithium-ion batteries," *Adv. Energy Mater.* **10**, 2000783 (2020).

[152] E. B. Brackett, T. E. Brackett, R. L. Sass, „The crystal structures of barium chloride, barium bromide and barium iodide," *J. Phys. Chem.* **67**, 2132–2135 (1963).

[153] V. M. Padmanabhan, W. R. Busing, H. A. Levy, „Barium chloride dihydrate by neutron diffraction," *Acta Crystallogr. B* **34**, 2290–2292 (1978).

[154] S. Pagola, G. Polla, G. Leyva, M. T. Casais, J. A. Alonso, I. Rasines, R. E. Carbonio, „Crystal structure refinement of $Ba_5Nb_4O_{15}$ and $Ba_5Nb_4O_{15-x}$ by Rietveld analysis of neutron and X-ray diffraction data," *Mater. Sci. Forum* **228**, 819–824 (1996).

[155] J. Wilkens, H. K. Müller-Buschbaum, „Darstellung und Strukturaufklärung von $Ba_8Ru_{3.33}Ta_{1.67}O_{18}Cl_2$," *J. Alloys Compd.* **184**, 195–201 (1992).

[156] J. Wilkens, H. K. Müller-Buschbaum, „Über Halogenooxo-Ruthenate: Zur Kenntnis von $Ba_5RuTaO_9Cl_2$," *J. Less-Common Met.* **171**, 255–262 (1991).

[157] H. L. Yakel, „A refinement of the crystal structure of monoclinic europium sesquioxide," *Acta Crystallogr. B* **35**, 564–569 (1979).

[158] P. Schmidt, M. Binnewies, R. Glaum, M. Schmidt, "Advanced Topics on Crystal Growth," (2013).

Appendix A

The following section presents the measured powder X-ray diffraction (P-XRD) patterns from all experiments described in Section 5. For each sample, the measured data are shown together with the calculated diffraction peaks of the corresponding reference phases. To ensure clarity and avoid excessive overlap, the intensities of the reference data have been scaled down by a factor of 1/3. The reference diffraction patterns are based on selected literature values and serve for phase identification and validation :
IrO_2 [142], $EuAlO_3$ [143], $BaAl_2O_4$ [144], $BaCO_3$ [145], $Ba_3EuIr_2O_9$ [48], $Ba_3CeIr_2O_9$ [48] , $Ba_4EuIr_3O_{12}$ [60], $Ba_4NbIr_3O_{12}$ [30], $BaIrO_3$ [146], Ir [147], $BaRuO_3$ [148], $Ba_5Ru_2O_{10}$, $Ba_3CeRu_2O_9$ [45], $Ba_3EuRu_2O_9$ [29], $Ba_3TbRu_2O_9$ [47], $Ba_3YRu_2O_9$ [29], $Ba_4EuRu_3O_{12}$ [51], $Ba_4CeRu_3O_{12}$ [51], $Ba_4PrRu_3O_{12}$ [51], Ba_2PrRuO_6_cubic [149], $Ba_8Ta_4Ru_{8/3}Co_{2/3}O_{24}$ [150], CeO_2 [151], $BaCl_2$ [152], $BaCl_2$*$2H_2O$ [153], $Ba_5Nb_4O_{15}$ [154], $Ba_8Ru_{3.33}Ta_{1.67}O_{18}Cl_2$ [155], $Ba_5RuTaO_9Cl_2$ [156], Eu_2O_3 [157], CeO_2 [151].

$BaO – Eu_2O_3 – IrO_2$

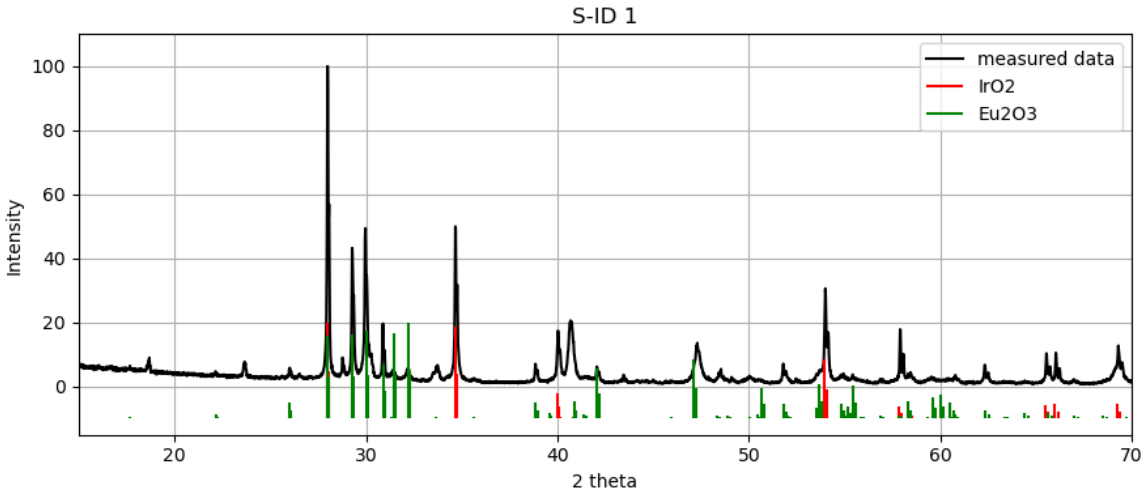

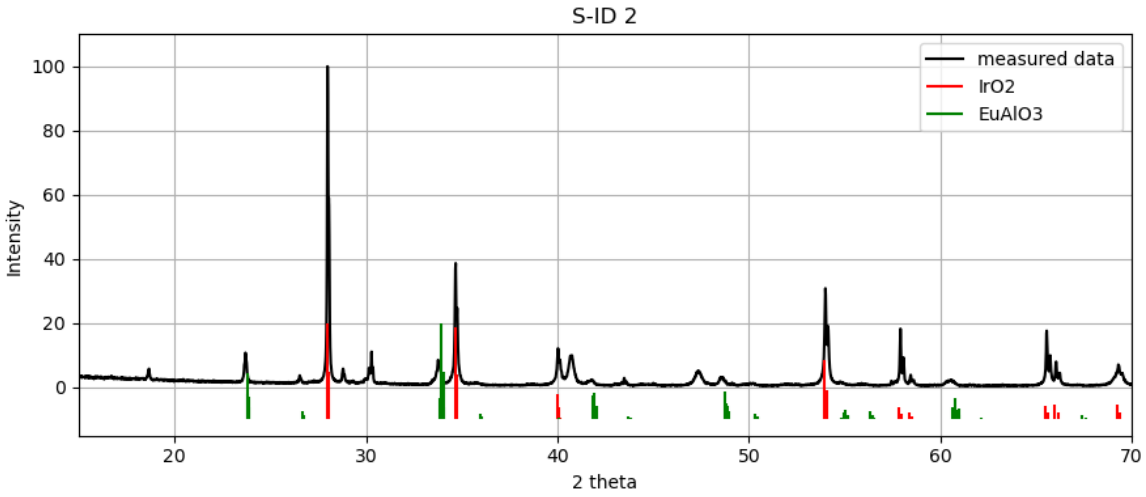
S-ID 2
measured data
IrO2
EuAlO3
Intensity
2 theta

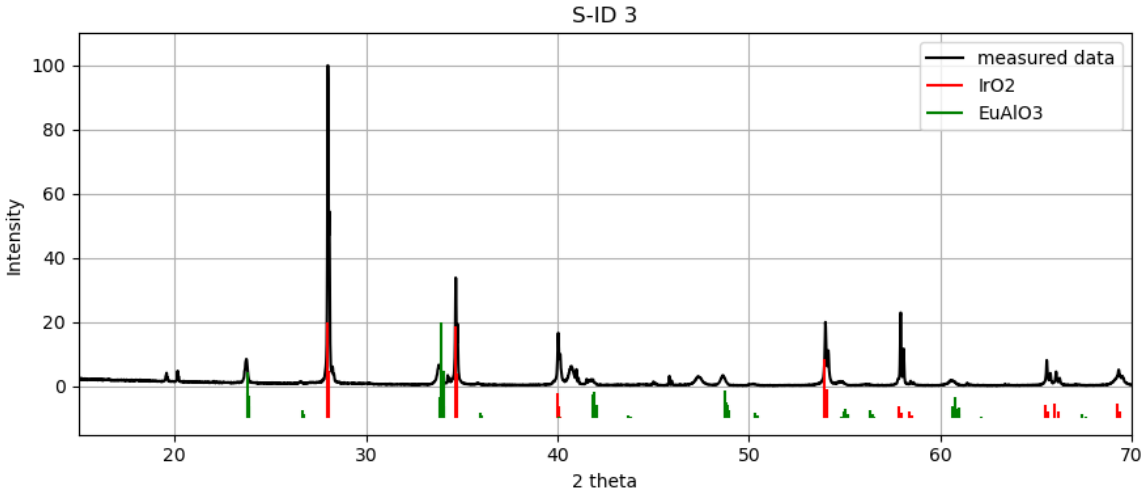
S-ID 3
measured data
IrO2
EuAlO3
Intensity
2 theta

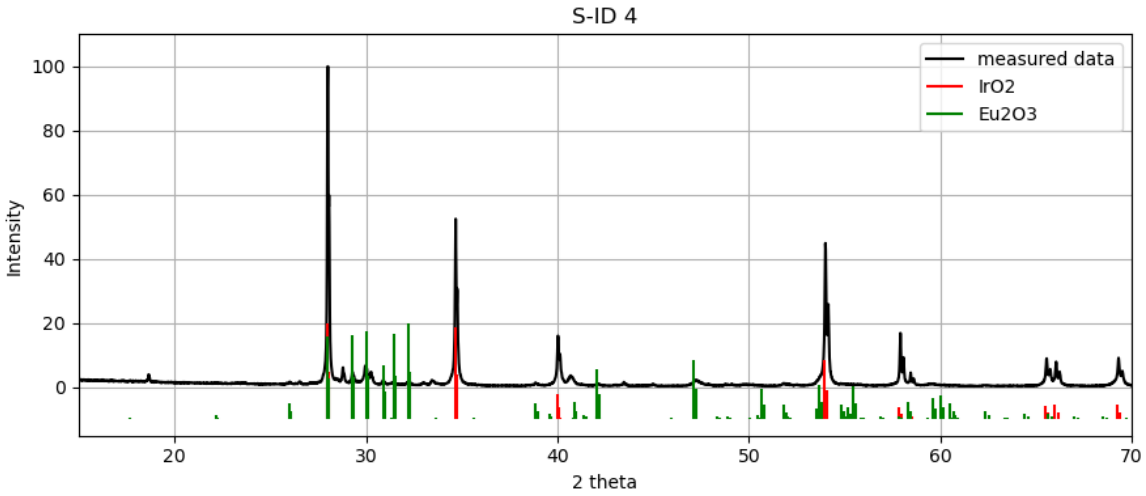
S-ID 4
measured data
IrO2
Eu2O3
Intensity
2 theta

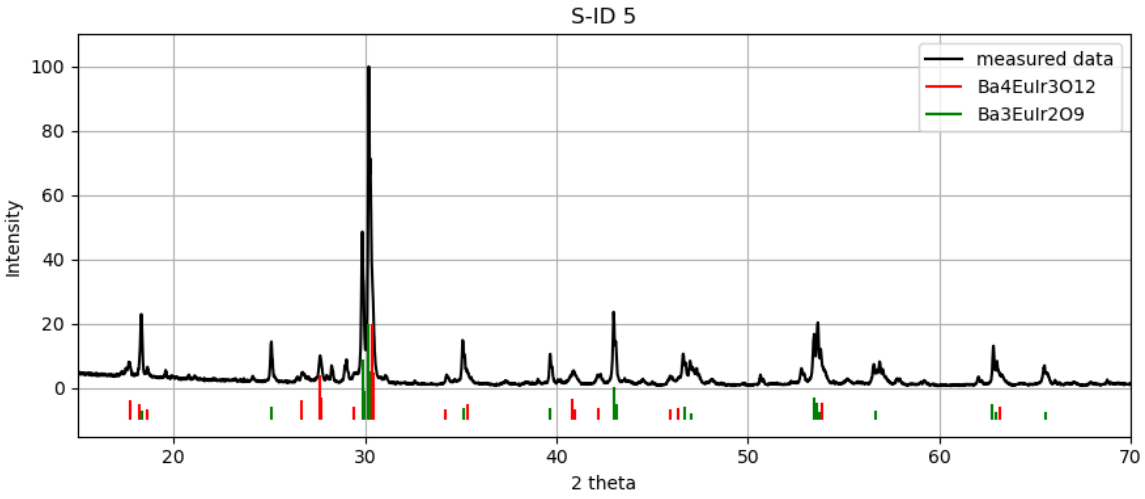
S-ID 5
measured data
Ba4EuIr3O12
Ba3EuIr2O9
Intensity
2 theta

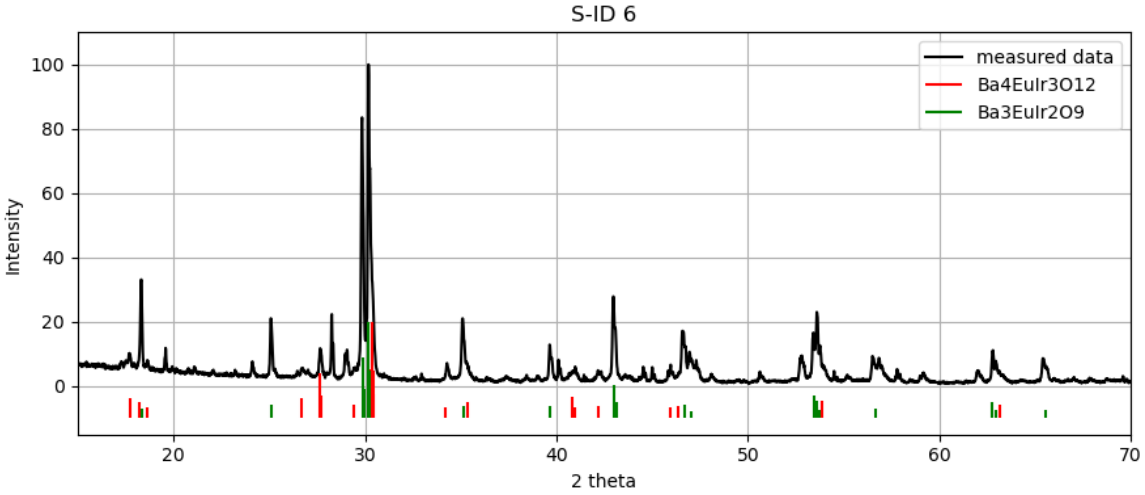
S-ID 6
measured data
Ba4EuIr3O12
Ba3EuIr2O9
Intensity
2 theta

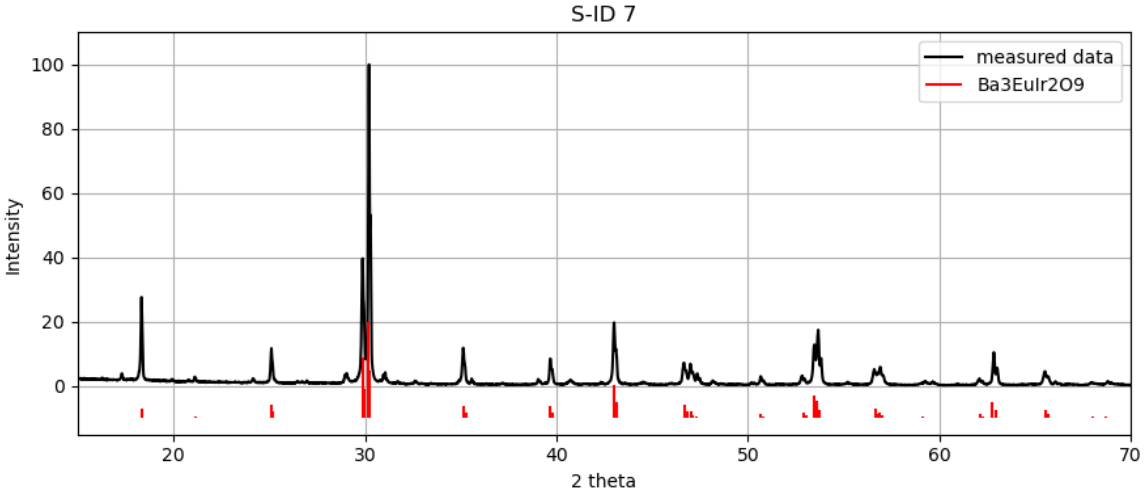
S-ID 7
measured data
Ba3EuIr2O9
Intensity
2 theta

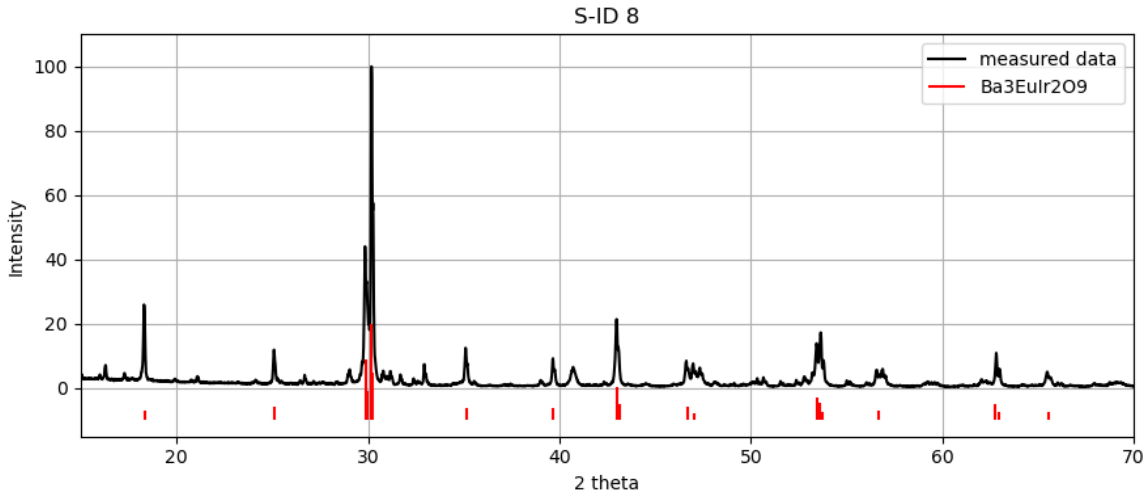
S-ID 8
measured data
Ba3EuIr2O9
Intensity
2 theta

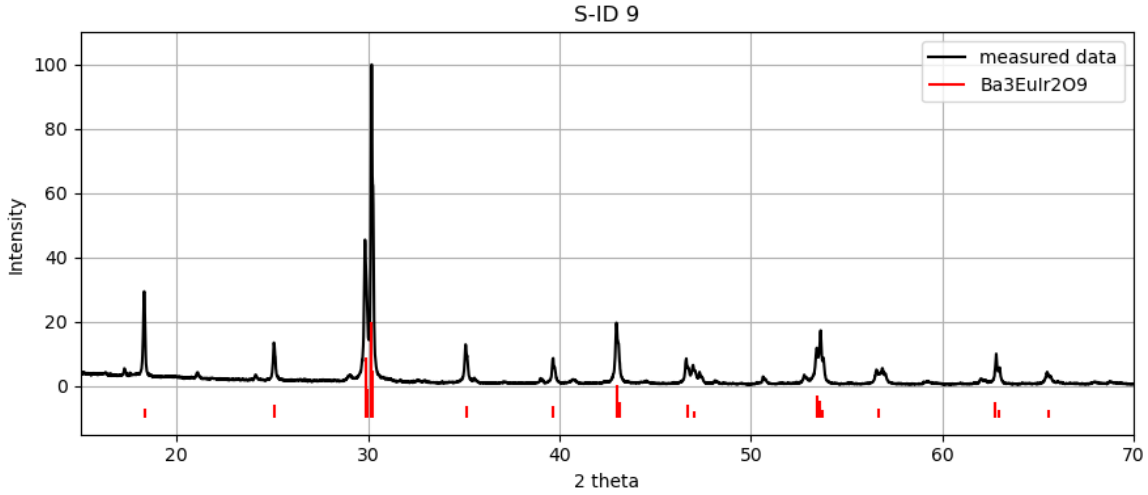
S-ID 9
measured data
Ba3EuIr2O9
Intensity
2 theta

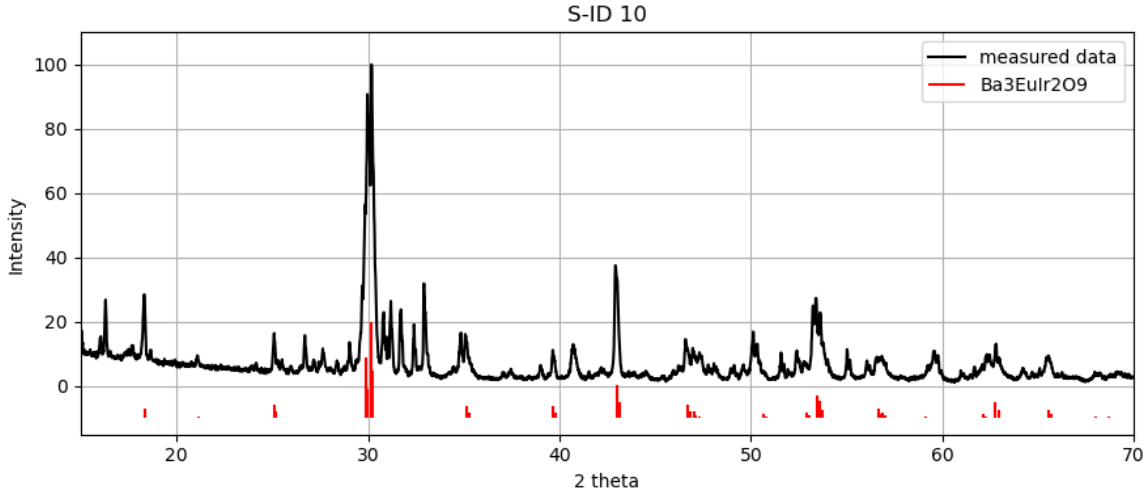
S-ID 10
measured data
Ba3EuIr2O9
Intensity
2 theta

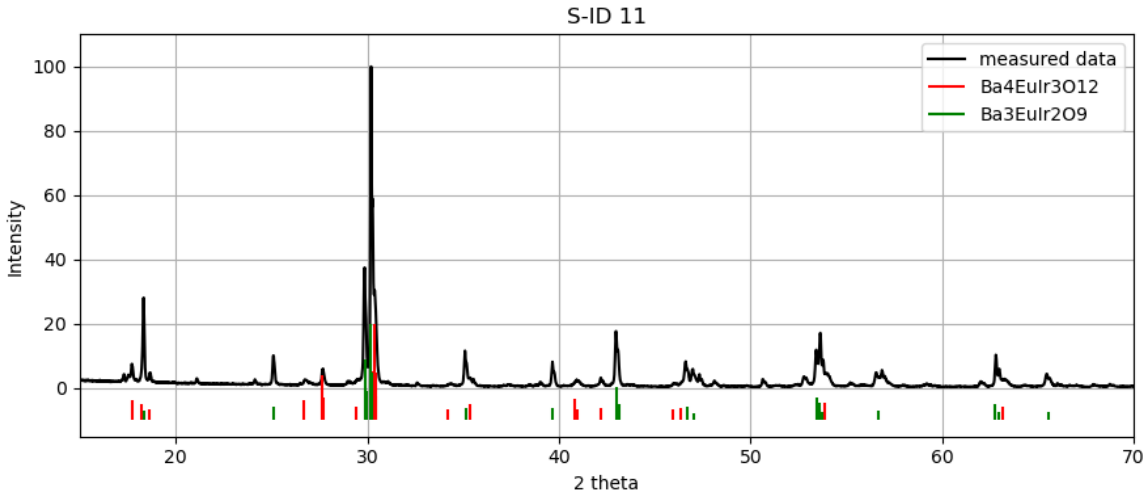
S-ID 11
measured data
Ba4EuIr3O12
Ba3EuIr2O9
Intensity
2 theta

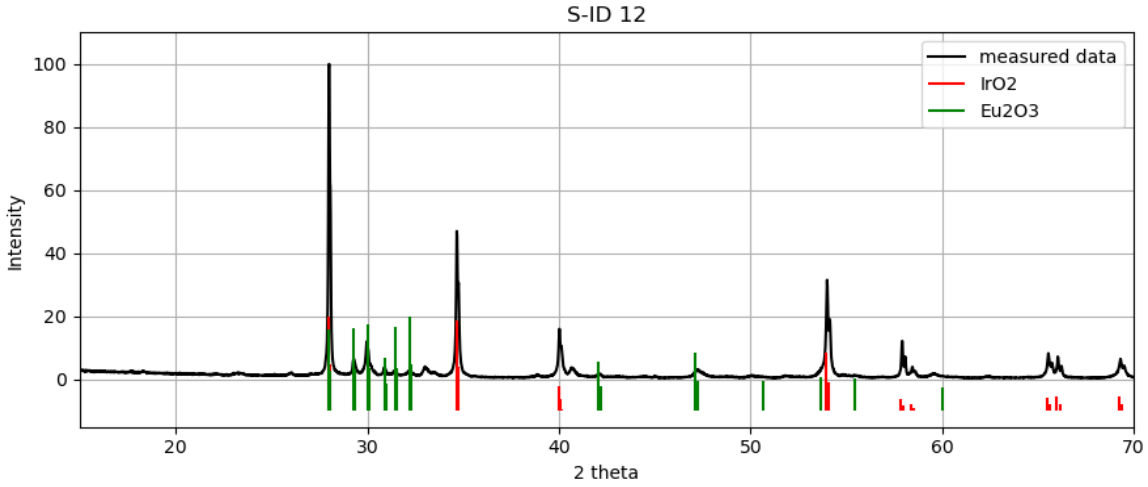
S-ID 12
measured data
IrO2
Eu2O3
Intensity
2 theta

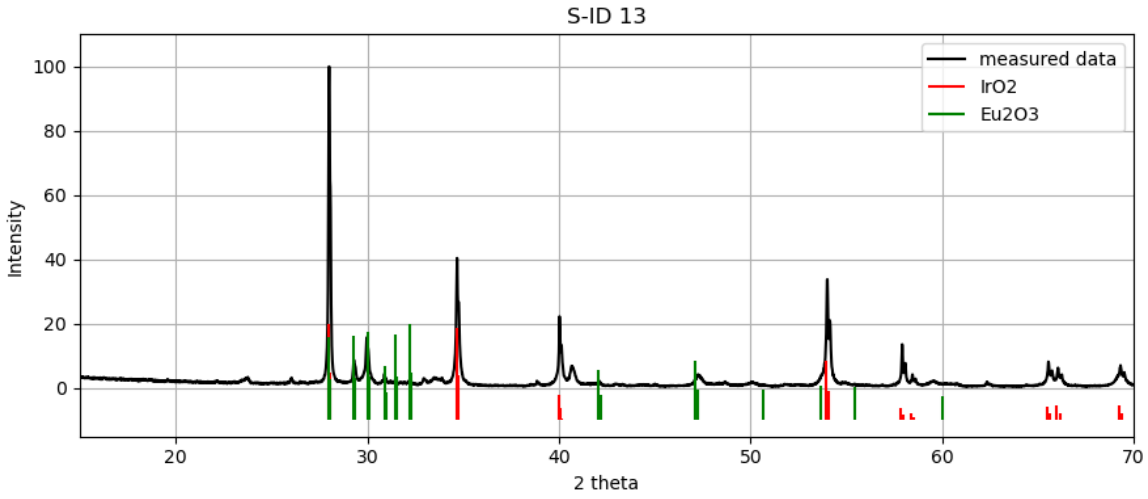
S-ID 13
measured data
IrO2
Eu2O3
Intensity
2 theta

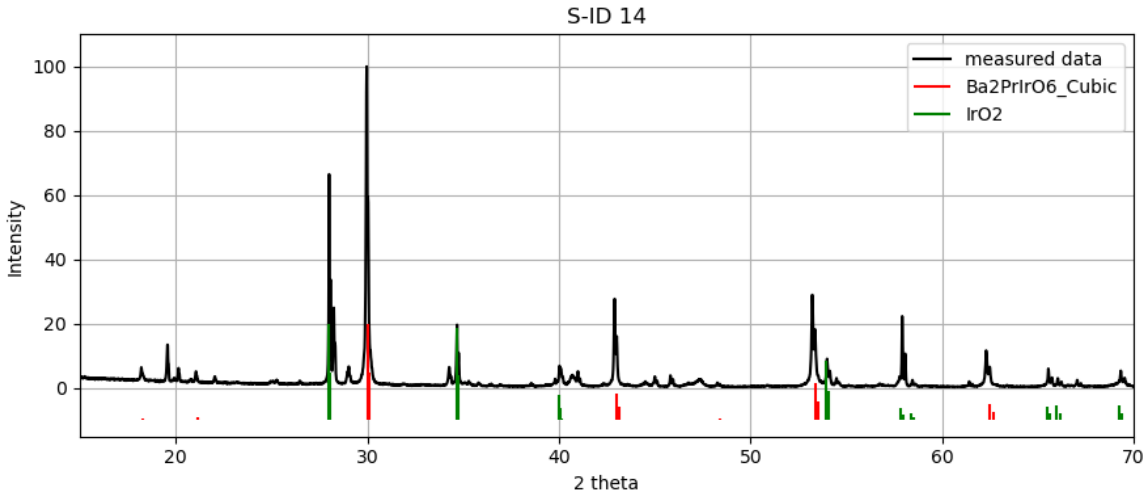
S-ID 14
measured data
Ba2PrIrO6_Cubic
IrO2
Intensity
2 theta

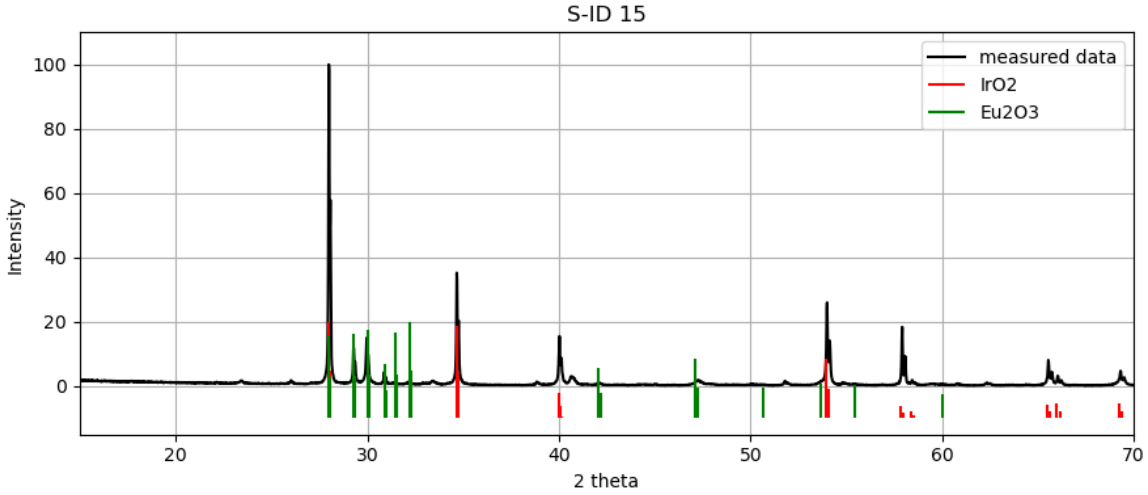
S-ID 15
measured data
IrO2
Eu2O3
Intensity
2 theta

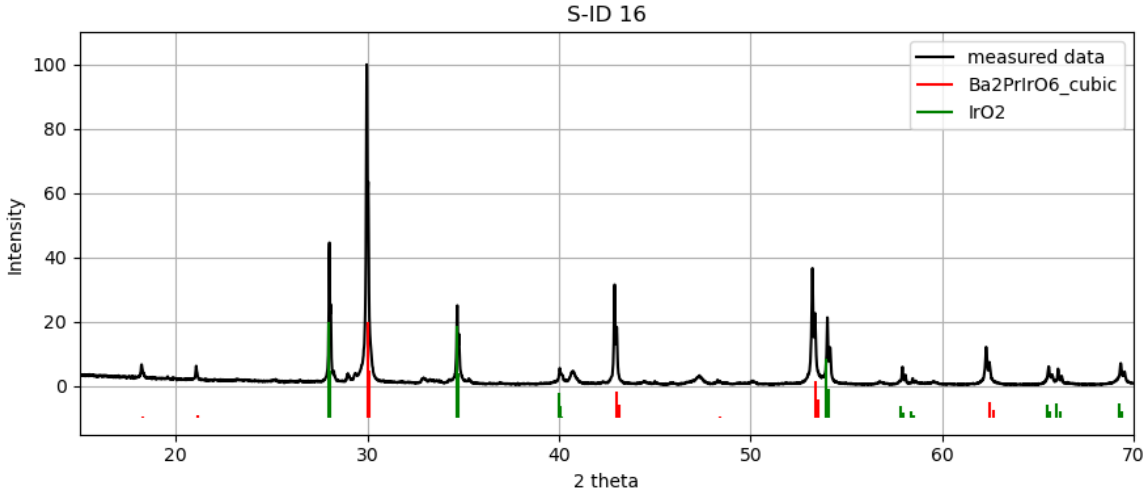
S-ID 16
measured data
Ba2PrIrO6_cubic
IrO2
Intensity
2 theta

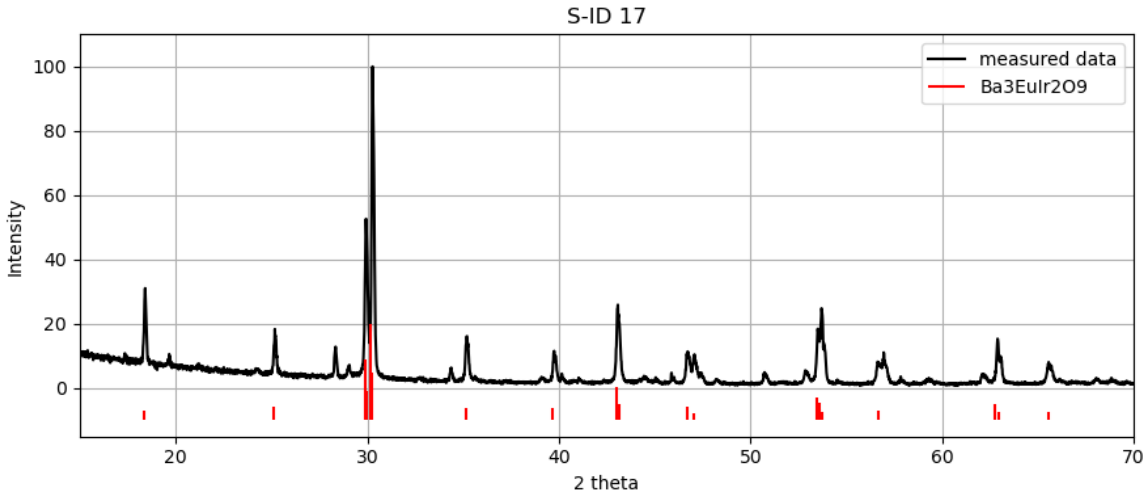
S-ID 17
measured data
Ba3EuIr2O9
Intensity
2 theta

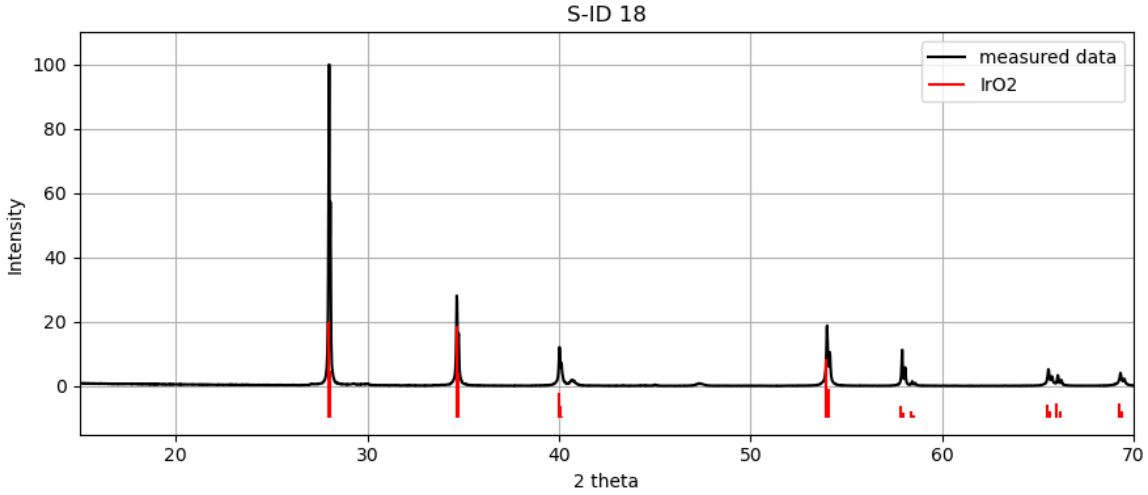
S-ID 18
measured data
IrO2
Intensity
2 theta

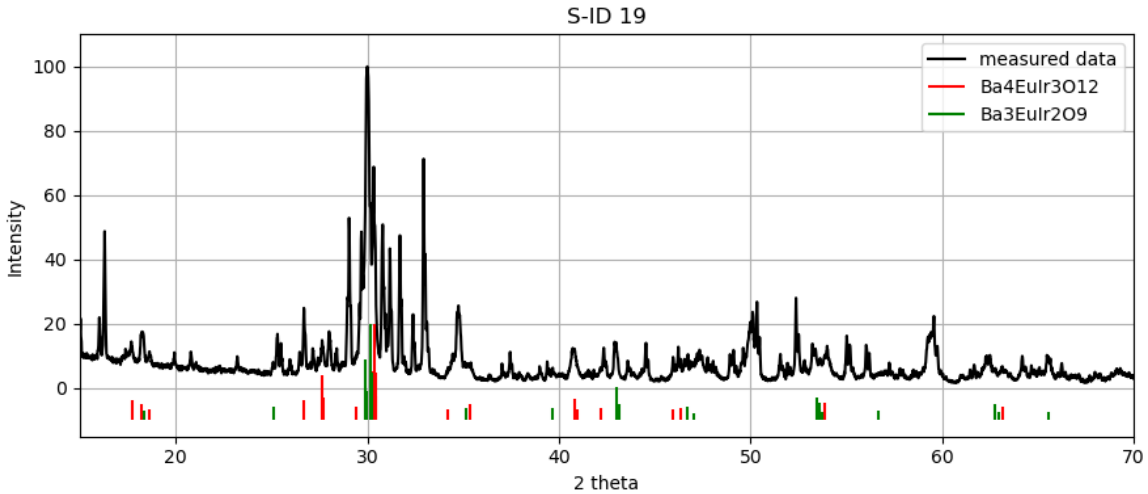
S-ID 19
measured data
Ba4EuIr3O12
Ba3EuIr2O9
Intensity
2 theta

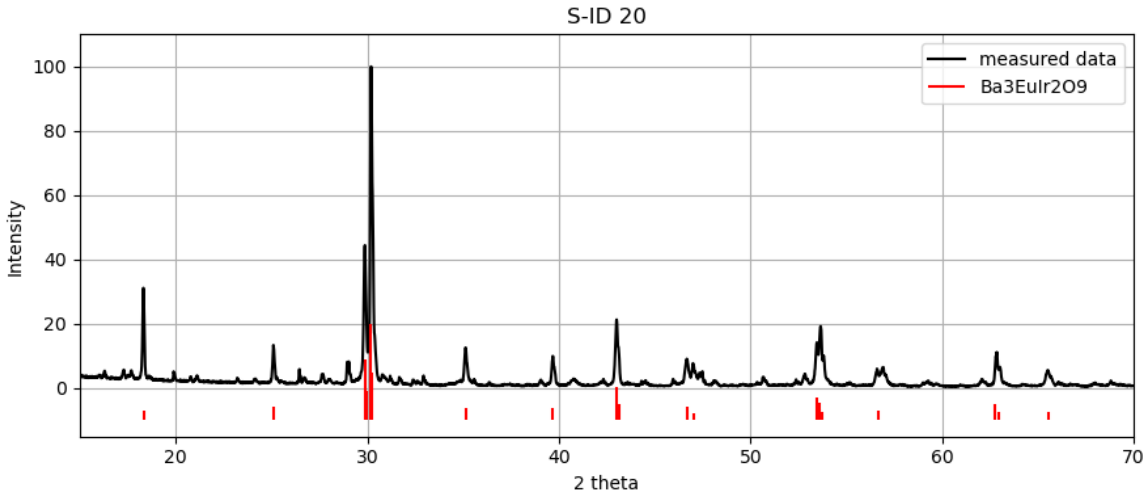
S-ID 20
measured data
Ba3EuIr2O9
Intensity
2 theta

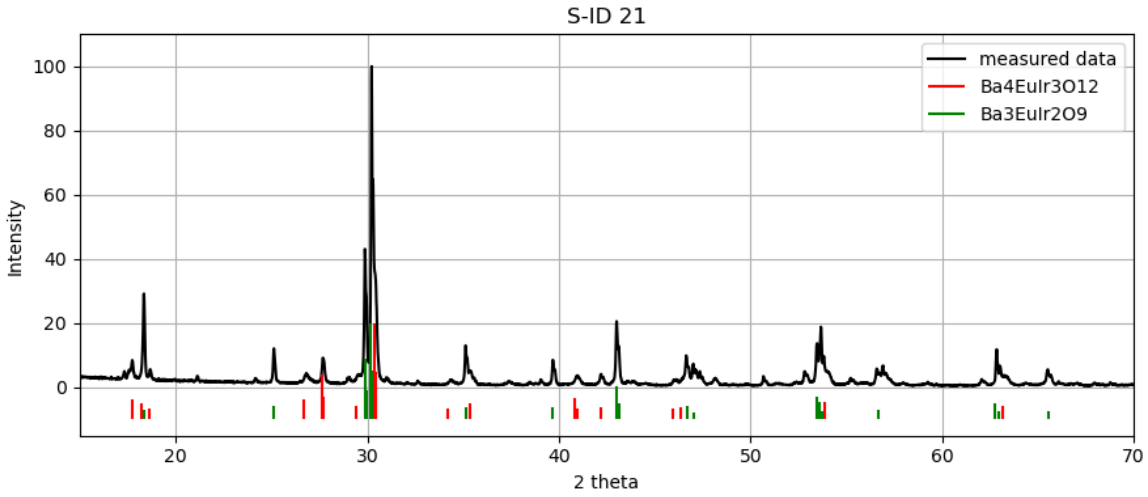
S-ID 21
measured data
Ba4EuIr3O12
Ba3EuIr2O9
Intensity
2 theta

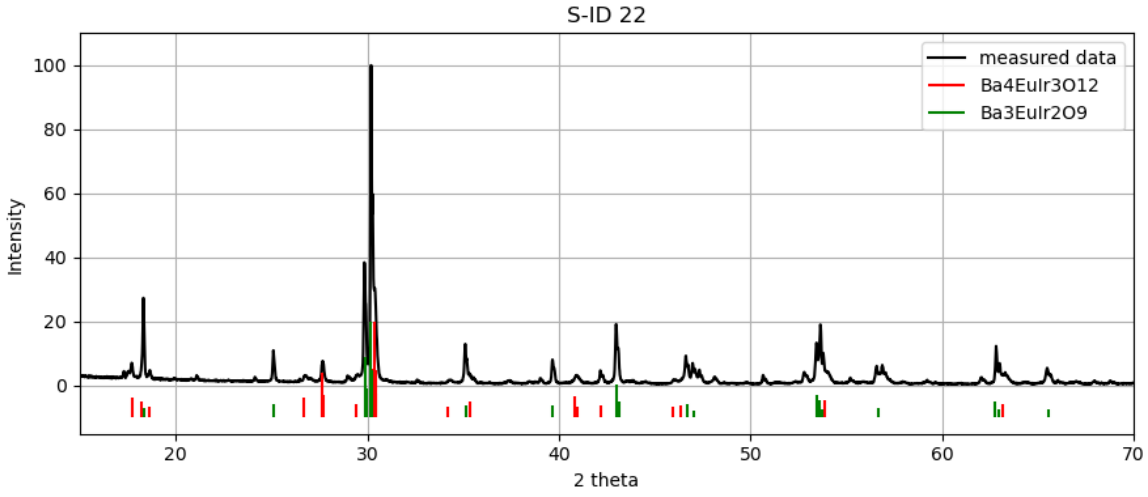
S-ID 22
measured data
Ba4EuIr3O12
Ba3EuIr2O9
Intensity
2 theta

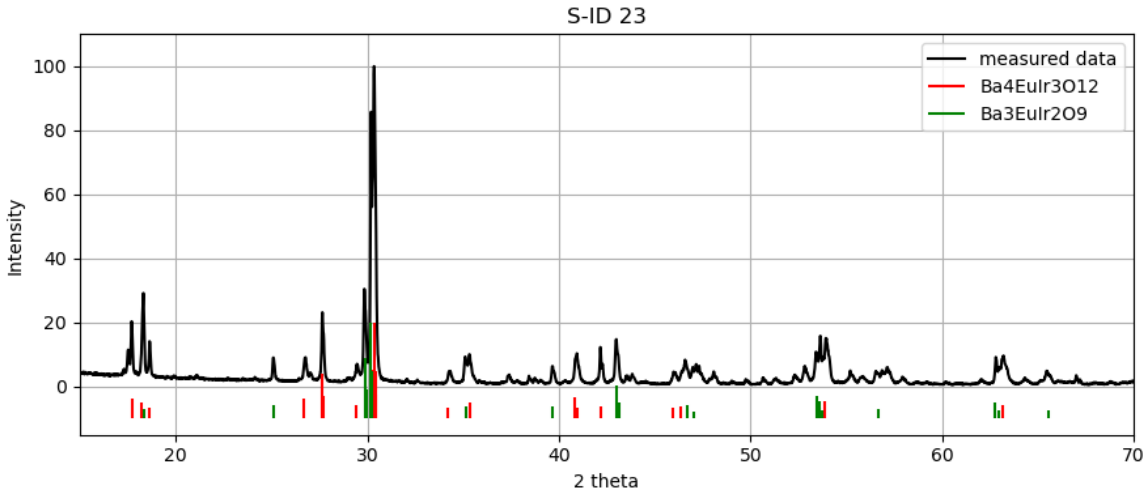
S-ID 23
measured data
Ba4EuIr3O12
Ba3EuIr2O9
Intensity
2 theta

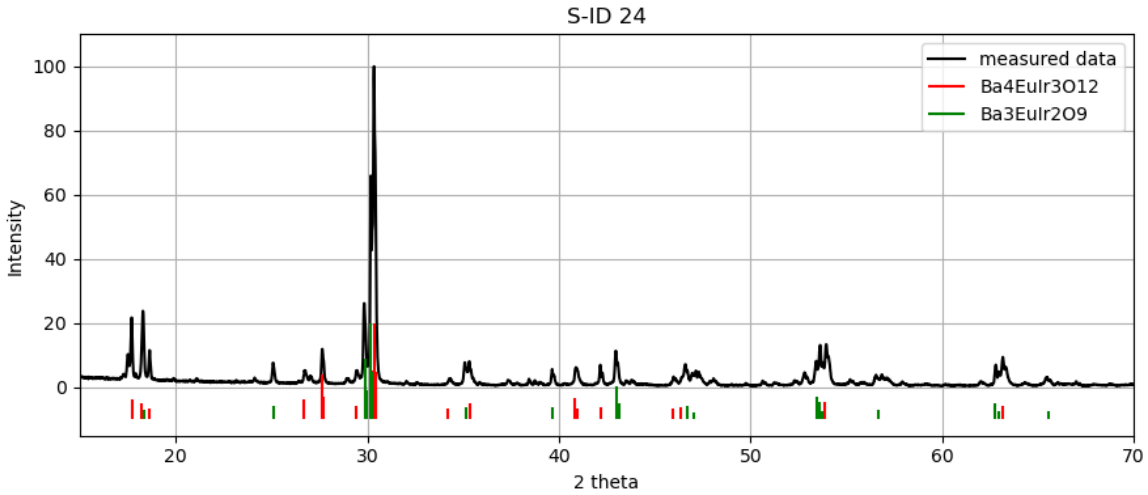
S-ID 24
measured data
Ba4EuIr3O12
Ba3EuIr2O9
Intensity
2 theta

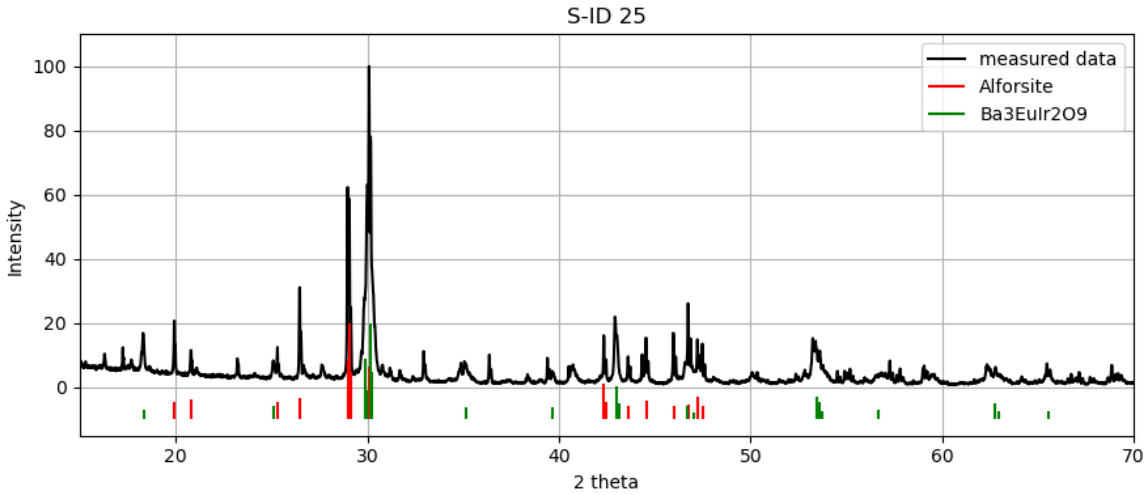
S-ID 25
measured data
Alforsite
Ba3EuIr2O9
Intensity
2 theta

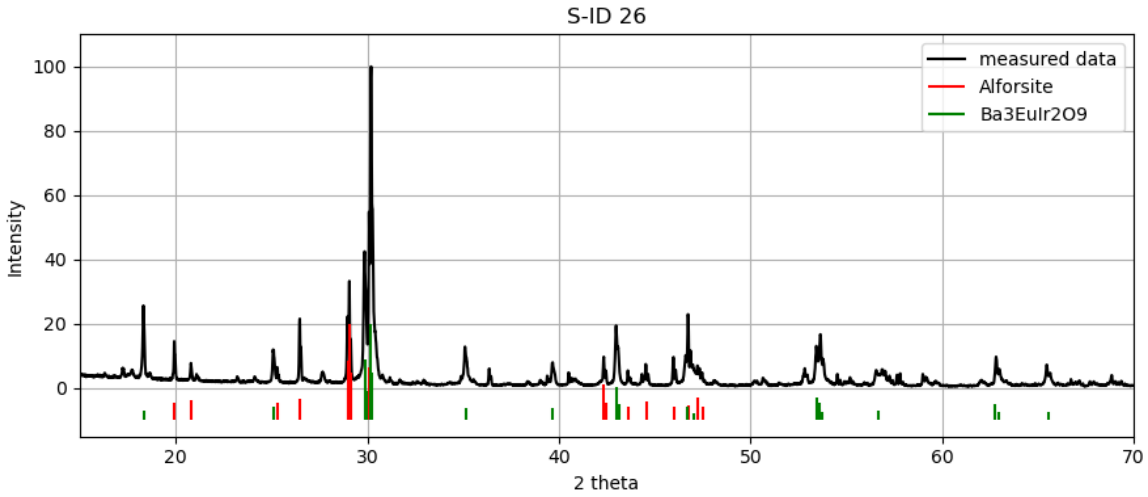
S-ID 26
measured data
Alforsite
Ba3EuIr2O9
Intensity
2 theta

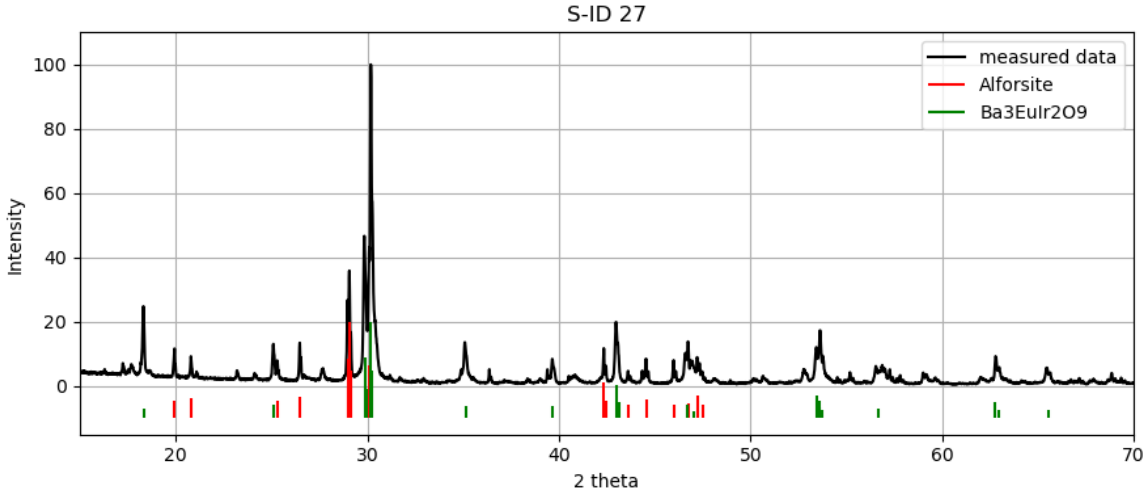
S-ID 27
measured data
Alforsite
Ba3EuIr2O9
Intensity
2 theta

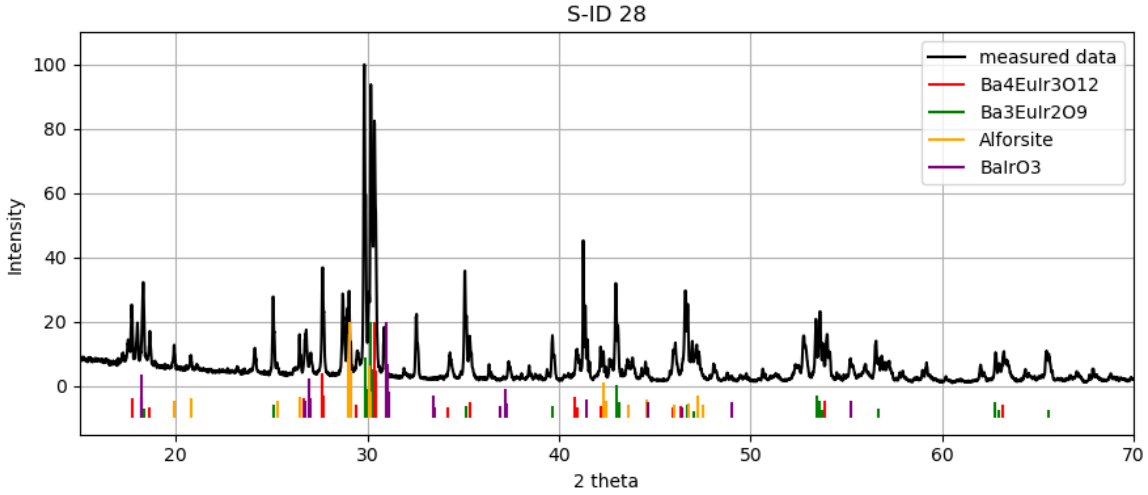
S-ID 28
measured data
Ba4EuIr3O12
Ba3EuIr2O9
Alforsite
BaIrO3
Intensity
2 theta

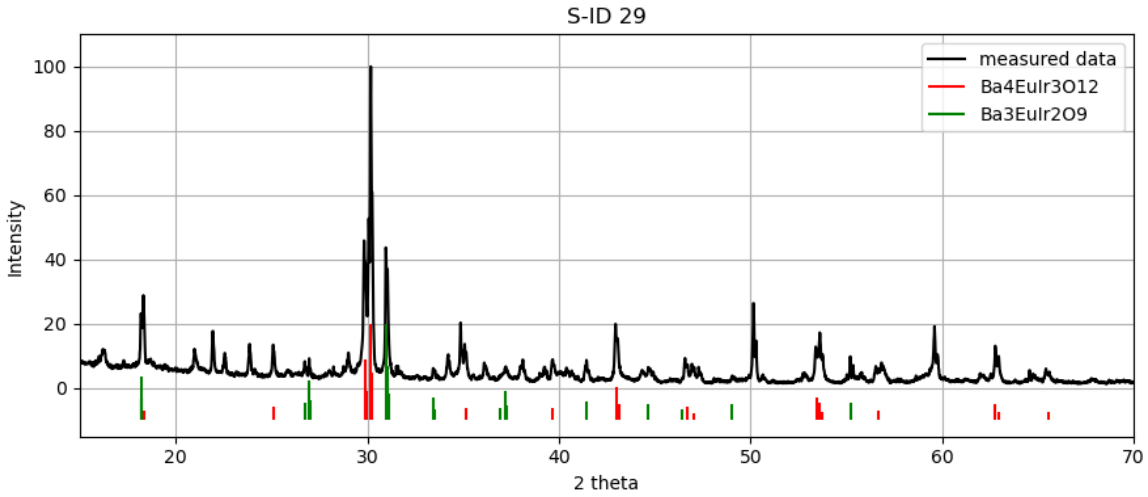
S-ID 29
measured data
Ba4EuIr3O12
Ba3EuIr2O9
Intensity
2 theta

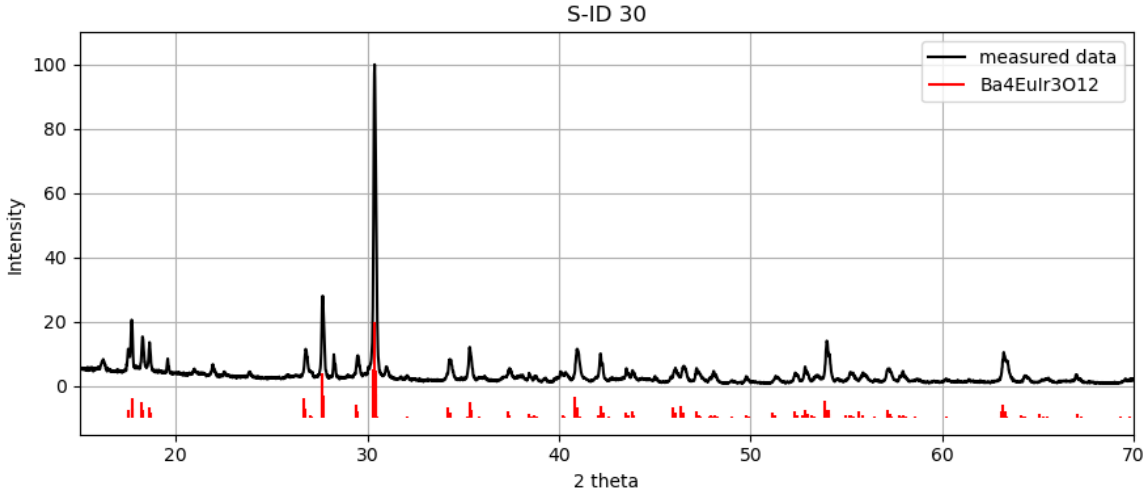
S-ID 30
measured data
Ba4EuIr3O12
Intensity
2 theta

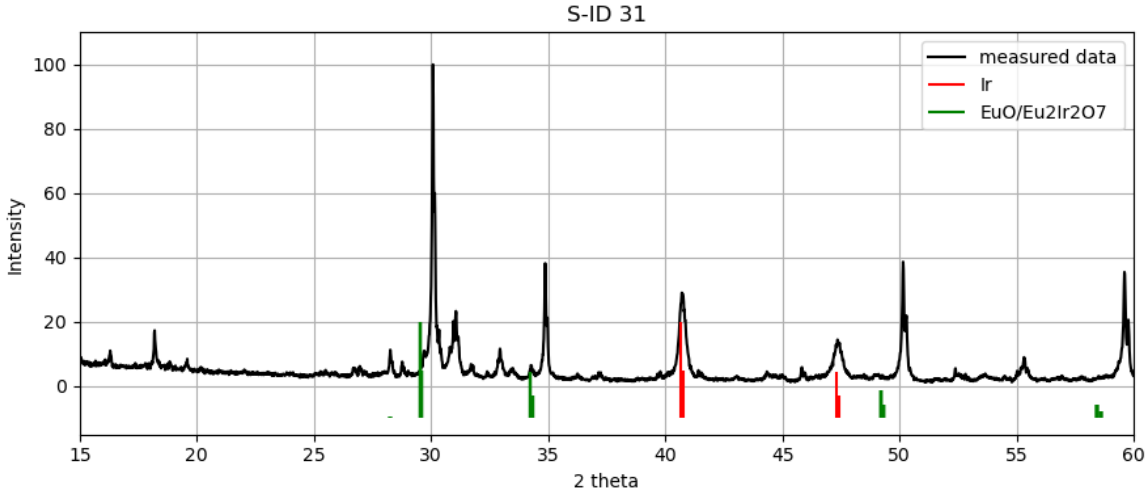
S-ID 31
measured data
Ir
EuO/Eu2Ir2O7
Intensity
2 theta

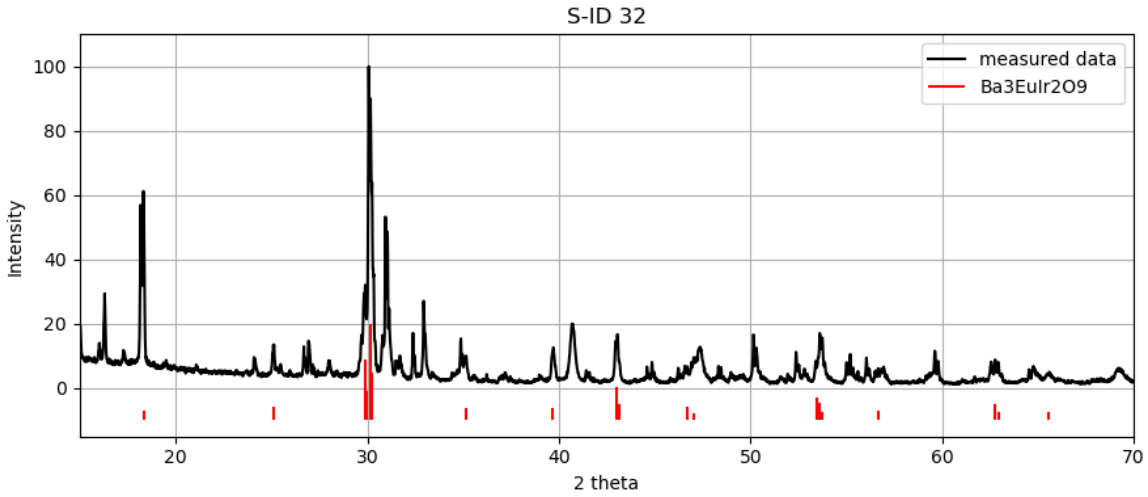
S-ID 32
measured data
Ba3EuIr2O9
Intensity
2 theta

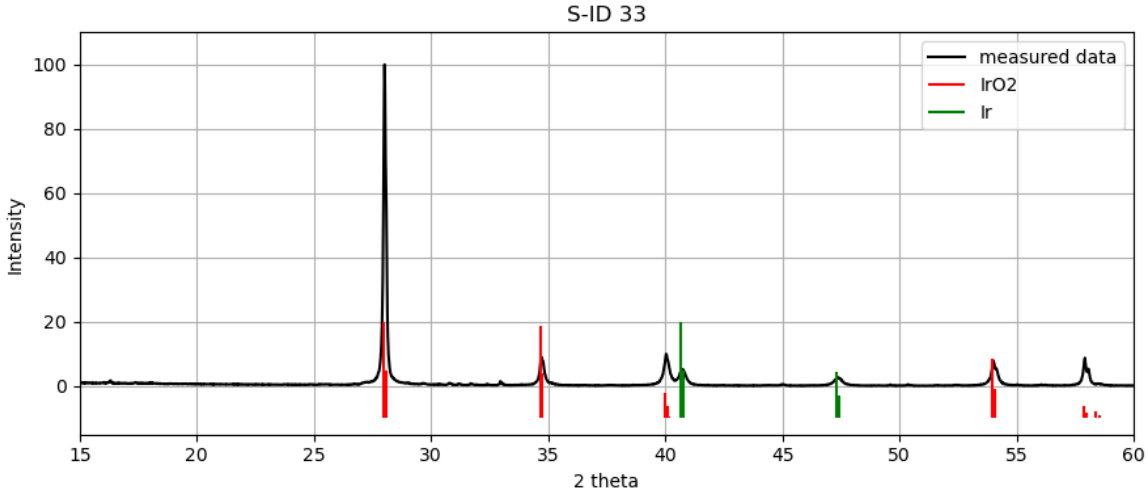
S-ID 33
measured data
IrO2
Ir
Intensity
2 theta

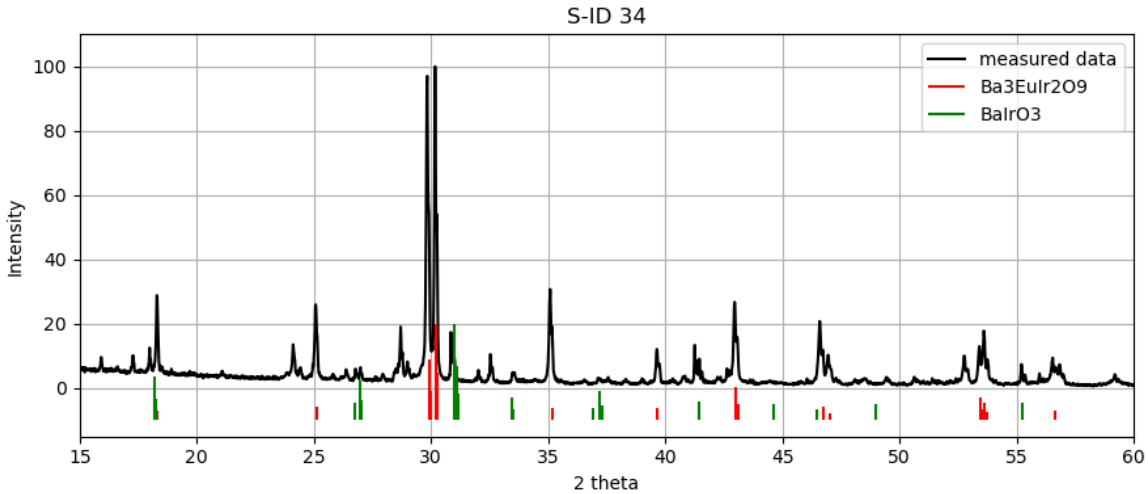
S-ID 34
measured data
Ba3EuIr2O9
BaIrO3
Intensity
2 theta

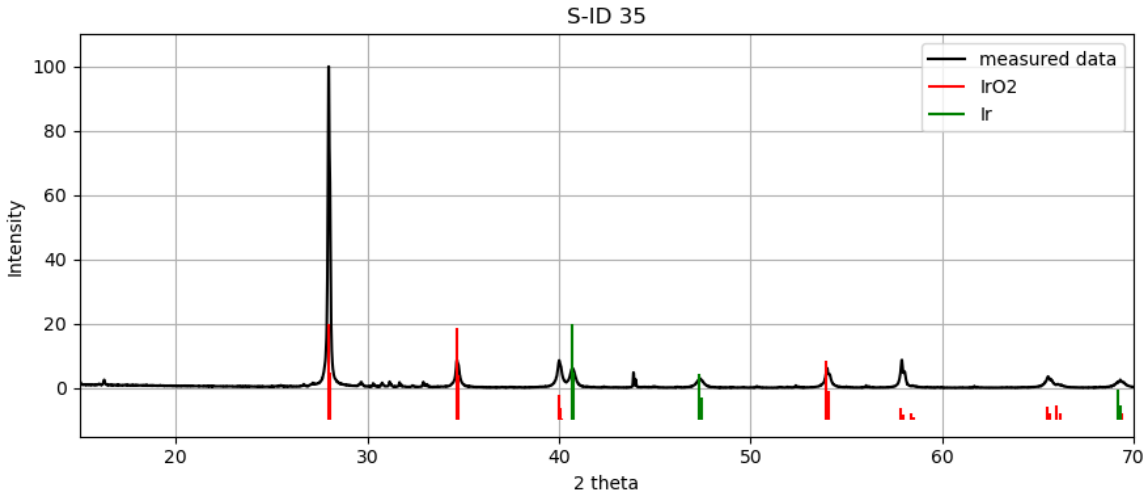
S-ID 35
measured data
IrO2
Ir
Intensity
2 theta

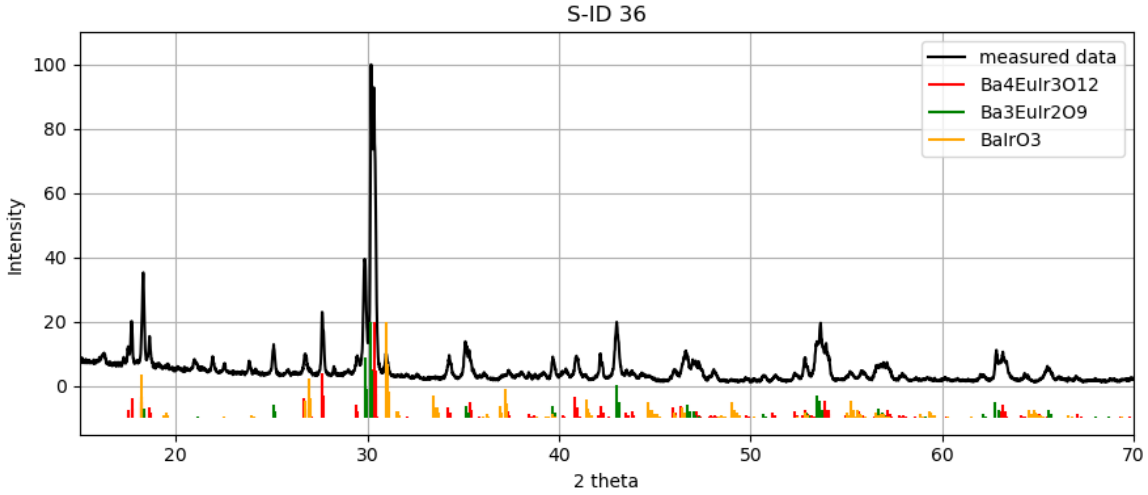
S-ID 36
measured data
Ba4EuIr3O12
Ba3EuIr2O9
BaIrO3
Intensity
2 theta

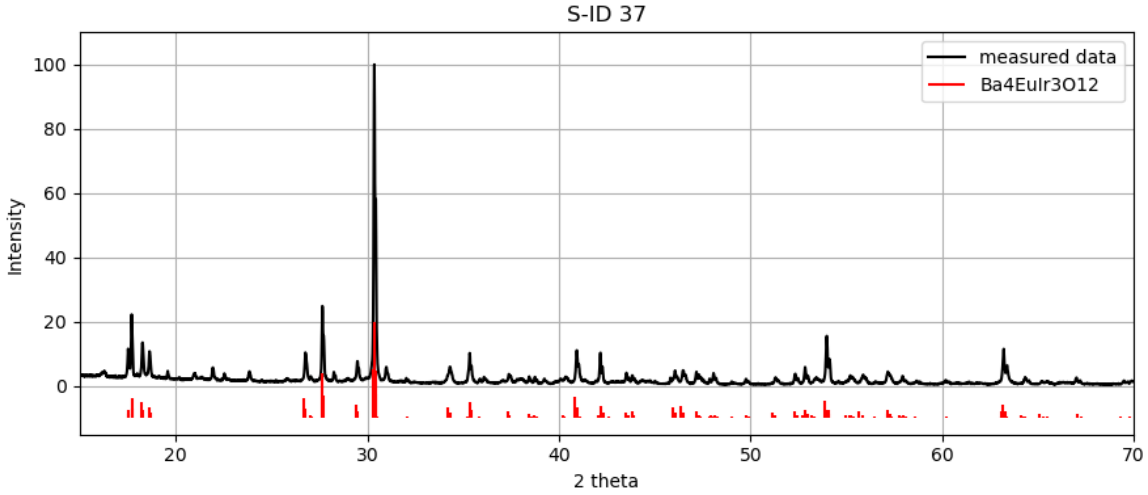
S-ID 37
measured data
Ba4EuIr3O12
Intensity
2 theta

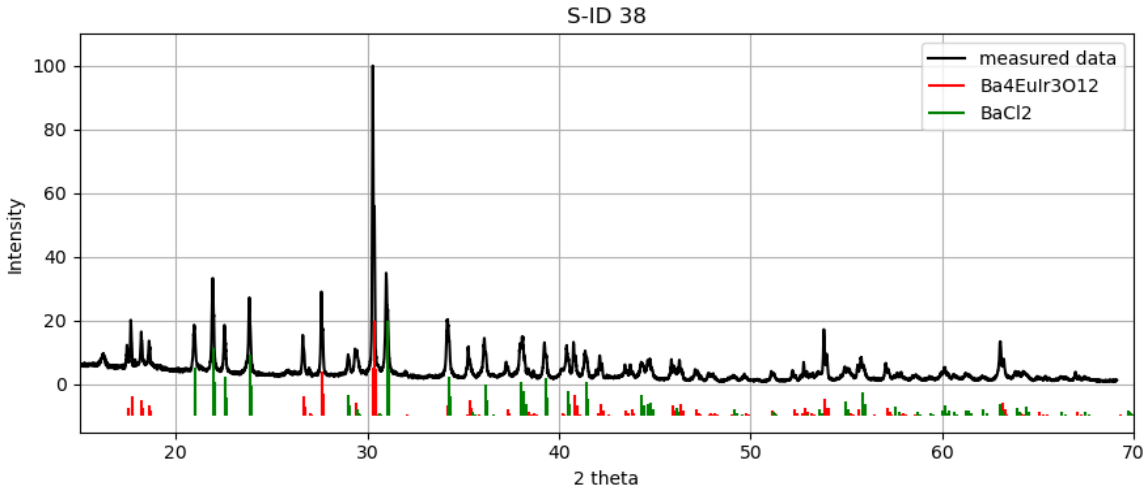
S-ID 38
measured data
Ba4EuIr3O12
BaCl2
Intensity
2 theta
0
20
40
60
80
100
20
30
40
50
60
70

$BaO - CeO_2 - IrO_2$

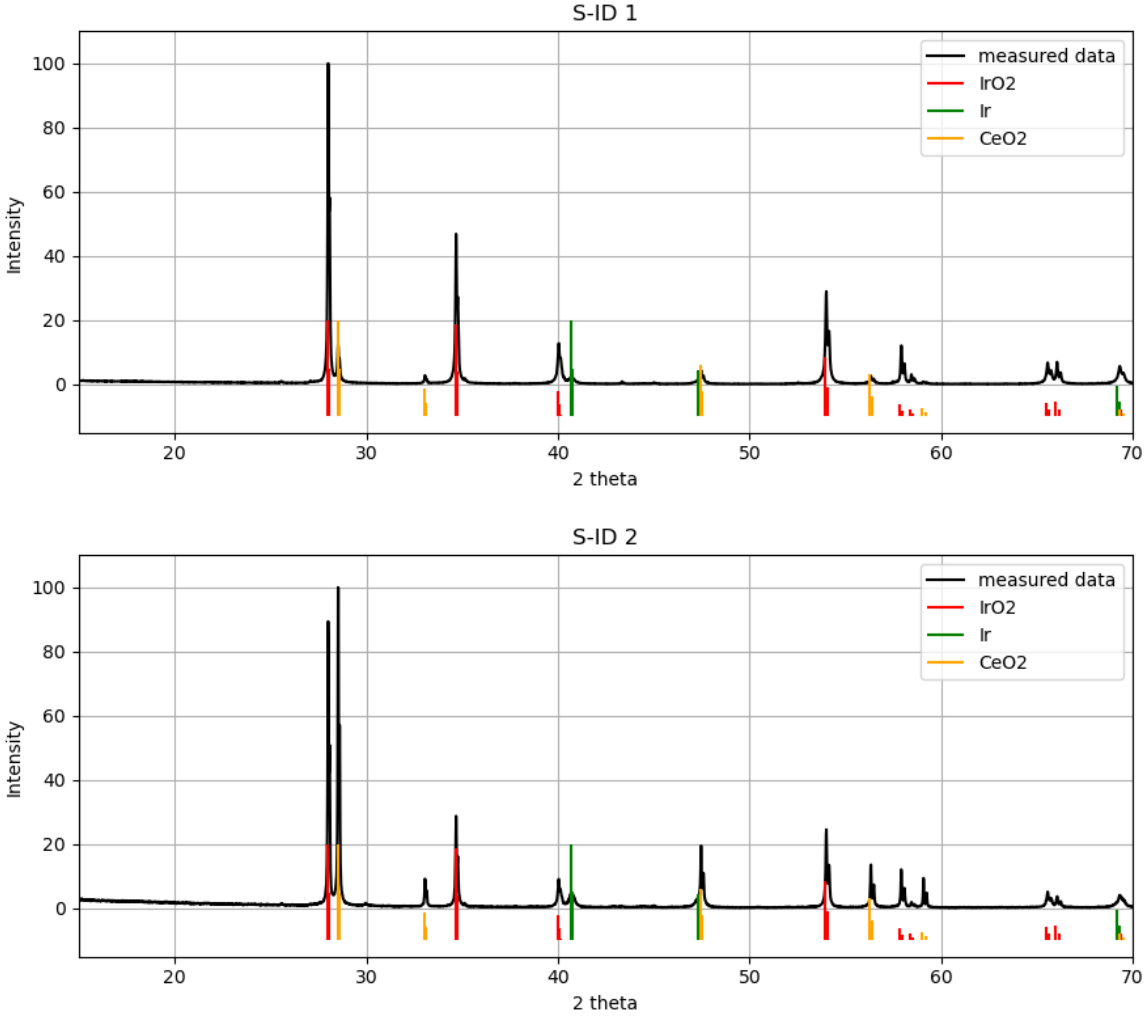

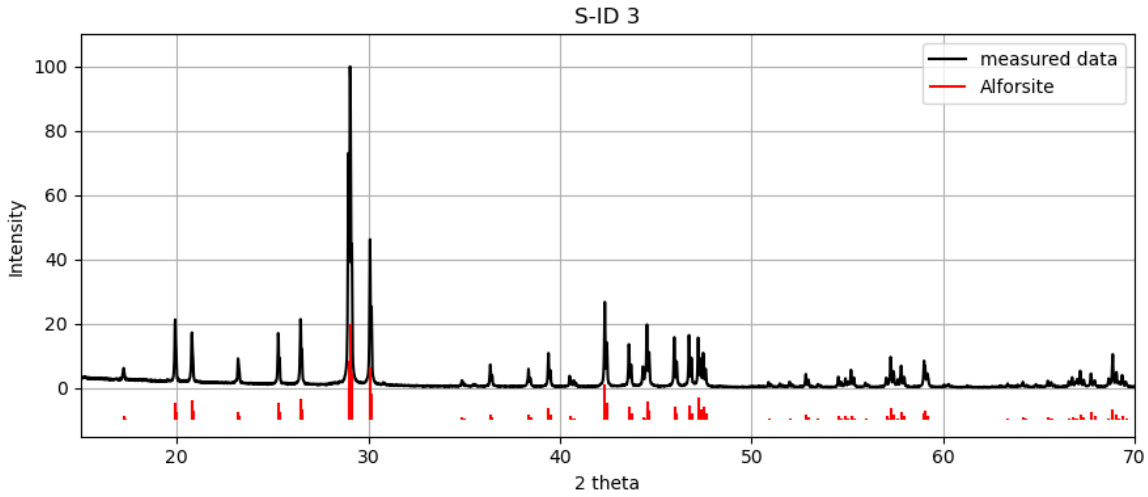
S-ID 3
measured data
Alforsite
Intensity
2 theta

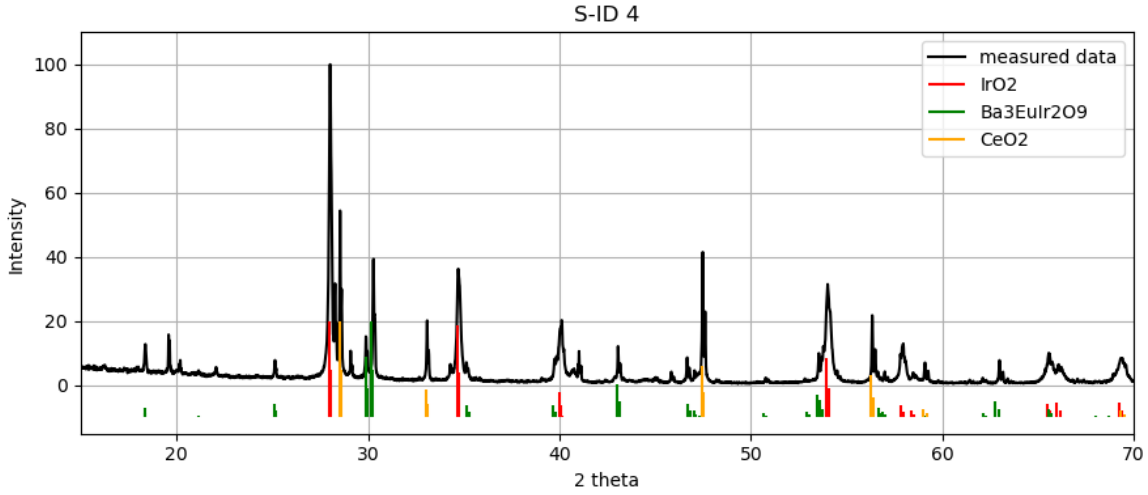
S-ID 4
measured data
IrO2
Ba3EuIr2O9
CeO2
Intensity
2 theta

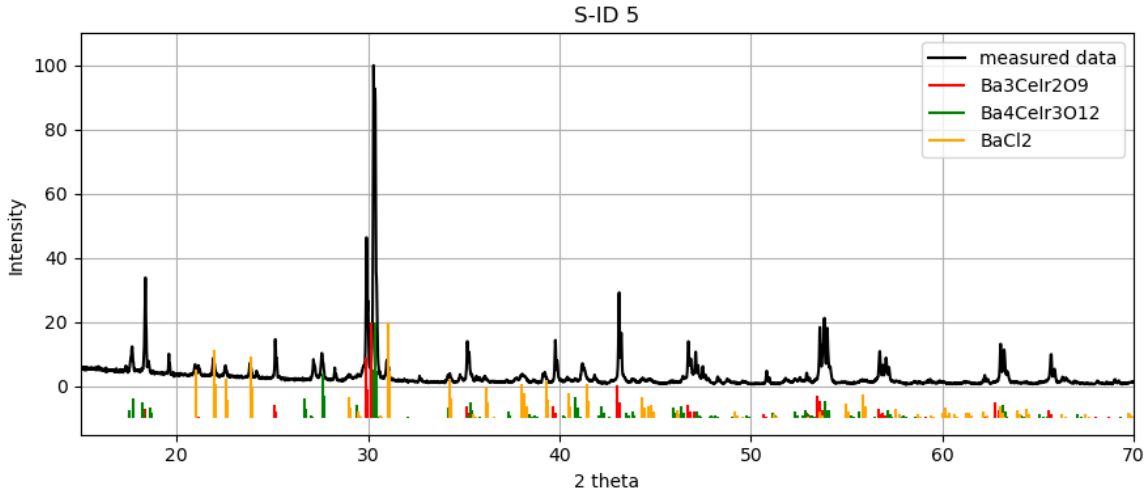
S-ID 5
measured data
Ba3CeIr2O9
Ba4CeIr3O12
BaCl2
Intensity
2 theta

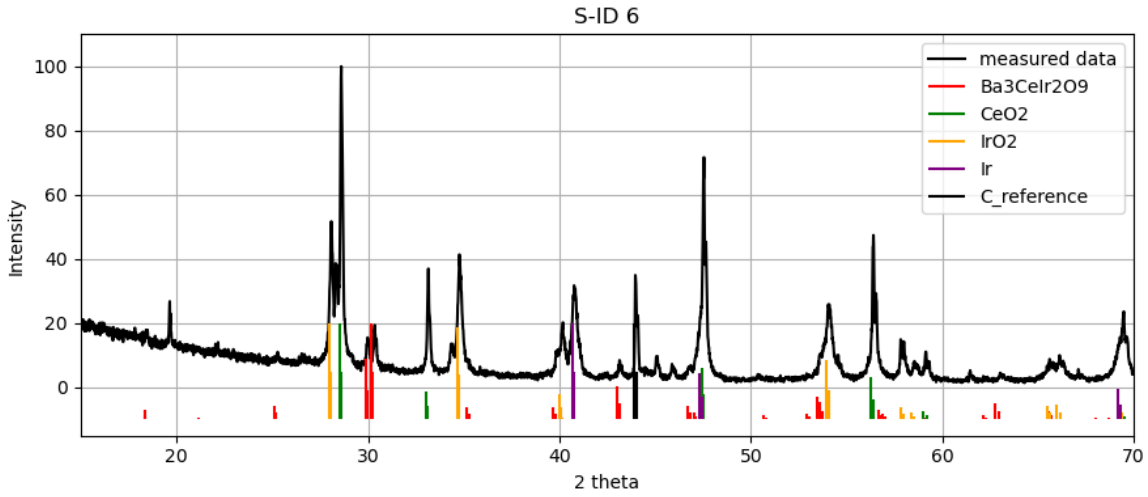
S-ID 6
measured data
Ba3CeIr2O9
CeO2
IrO2
Ir
C_reference
Intensity
2 theta

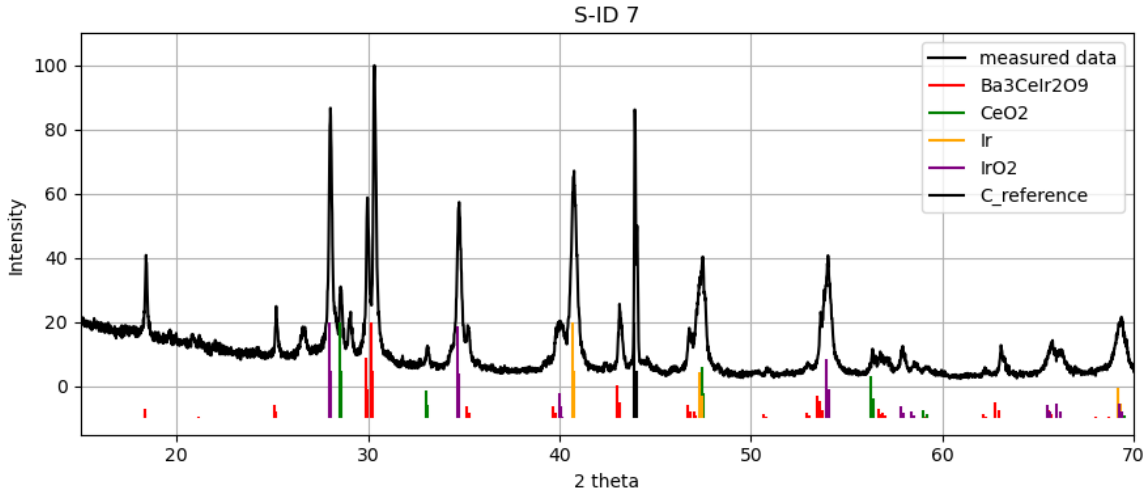
S-ID 7
measured data
Ba3CeIr2O9
CeO2
Ir
IrO2
C_reference
Intensity
2 theta

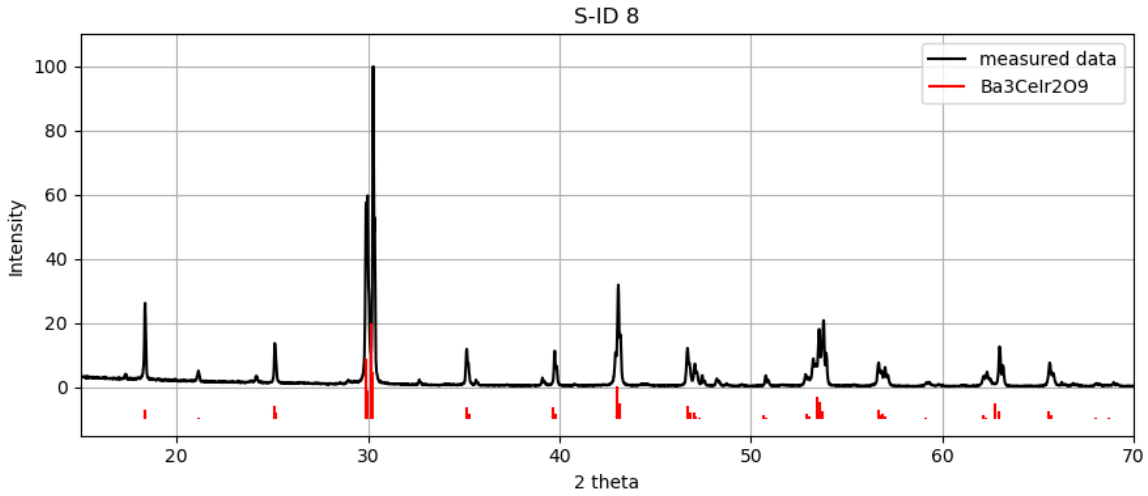
S-ID 8
measured data
Ba3CeIr2O9
Intensity
2 theta

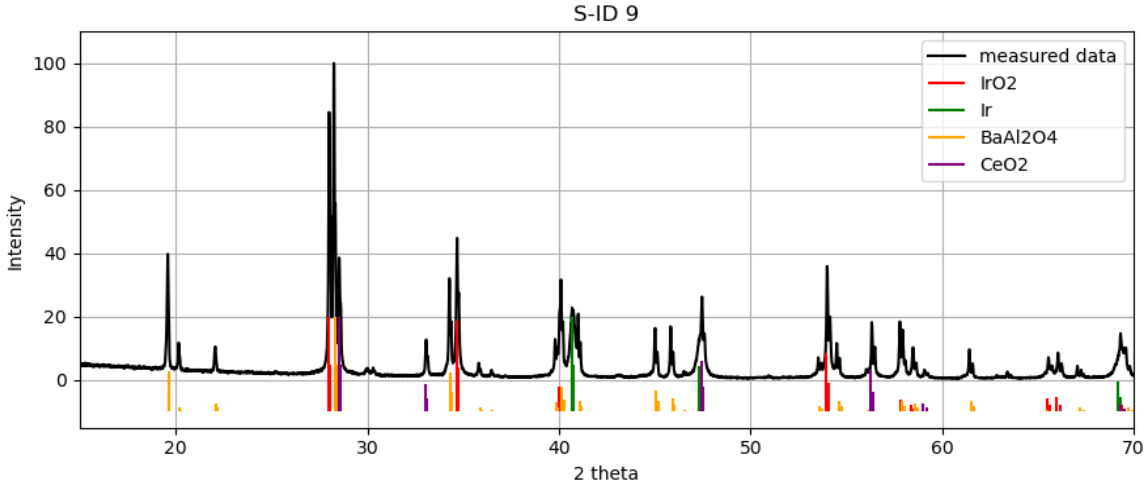
S-ID 9
measured data
IrO2
Ir
BaAl2O4
CeO2
Intensity
2 theta

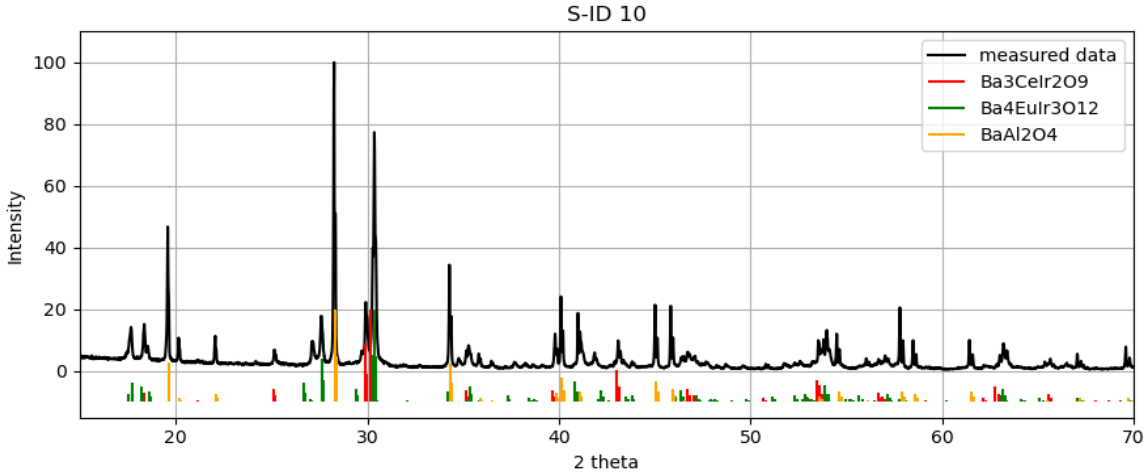
S-ID 10
measured data
Ba3CeIr2O9
Ba4EuIr3O12
BaAl2O4
Intensity
2 theta

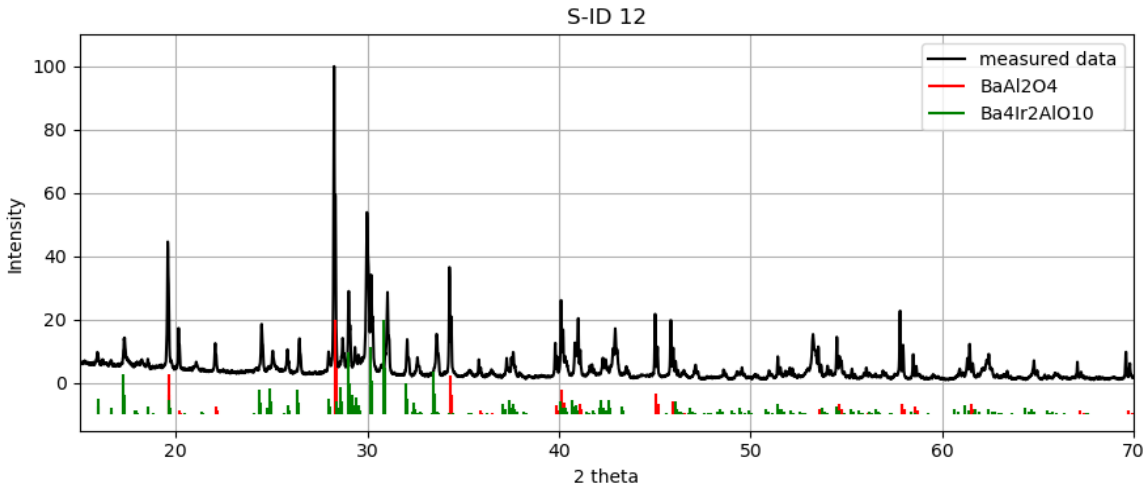
S-ID 12
measured data
BaAl2O4
Ba4Ir2AlO10
Intensity
2 theta

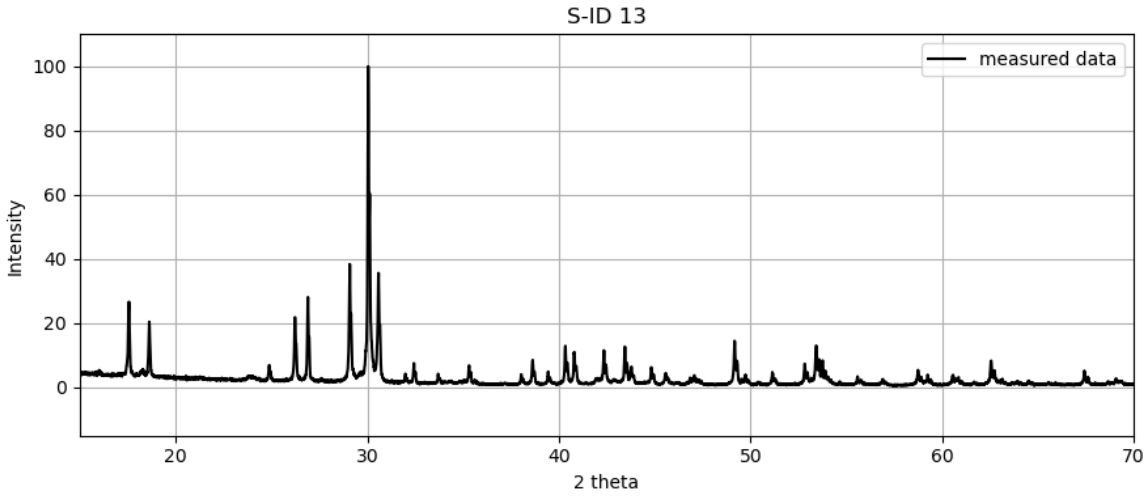
S-ID 13
measured data
Intensity
2 theta

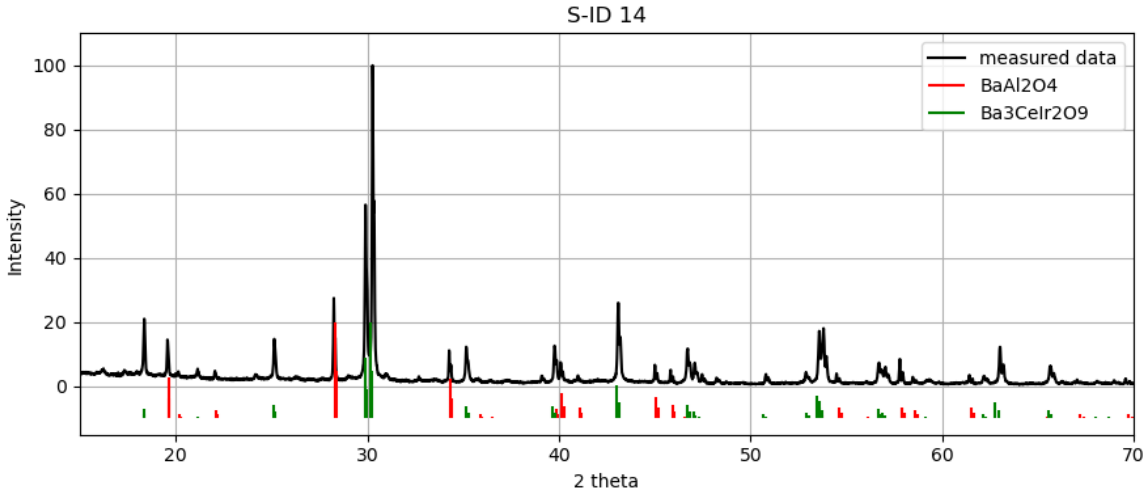
S-ID 14
measured data
BaAl2O4
Ba3CeIr2O9
Intensity
2 theta

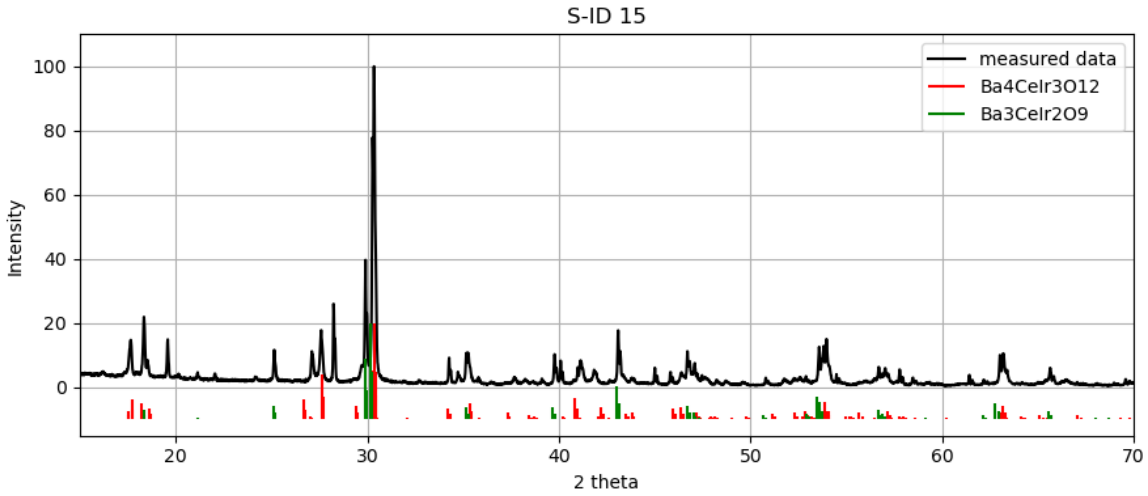
S-ID 15
measured data
Ba4CeIr3O12
Ba3CeIr2O9
Intensity
2 theta

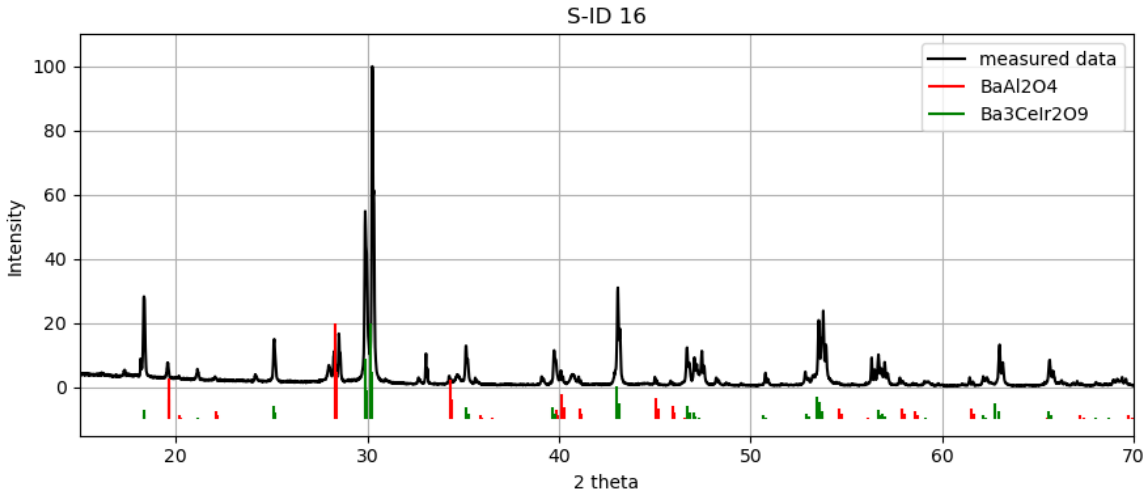
S-ID 16
measured data
BaAl2O4
Ba3CeIr2O9
Intensity
2 theta

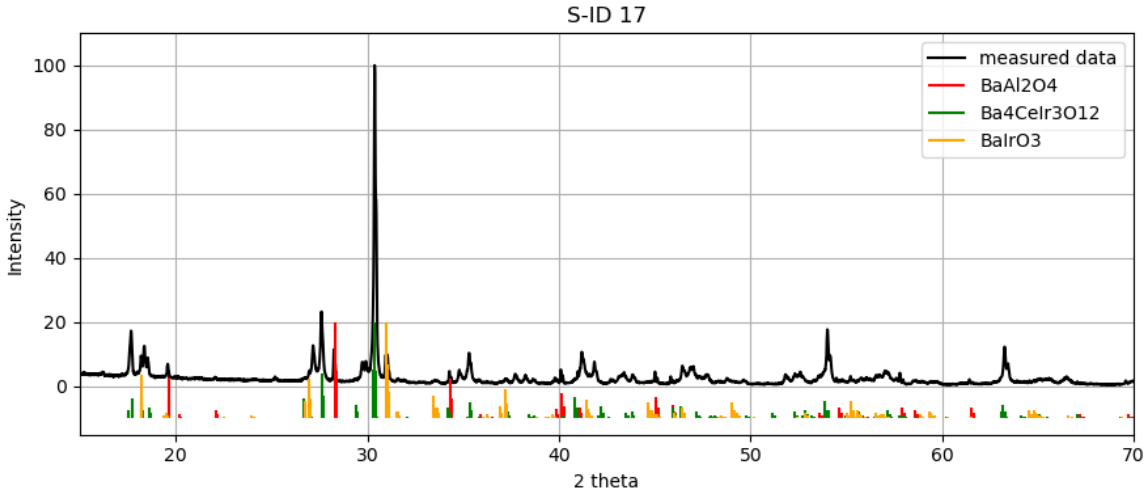
S-ID 17
measured data
BaAl2O4
Ba4CeIr3O12
BaIrO3
Intensity
2 theta

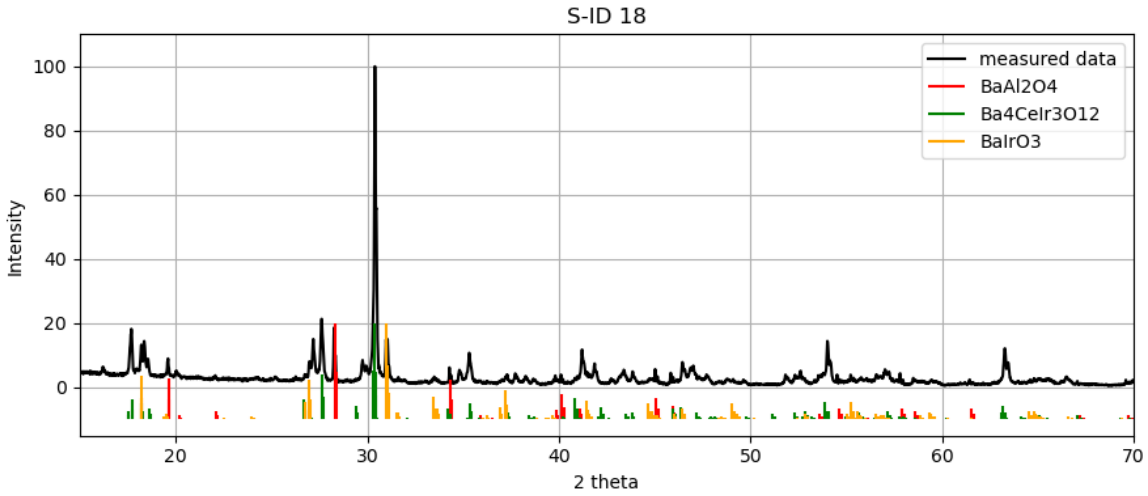
S-ID 18
measured data
BaAl2O4
Ba4CeIr3O12
BaIrO3
Intensity
2 theta

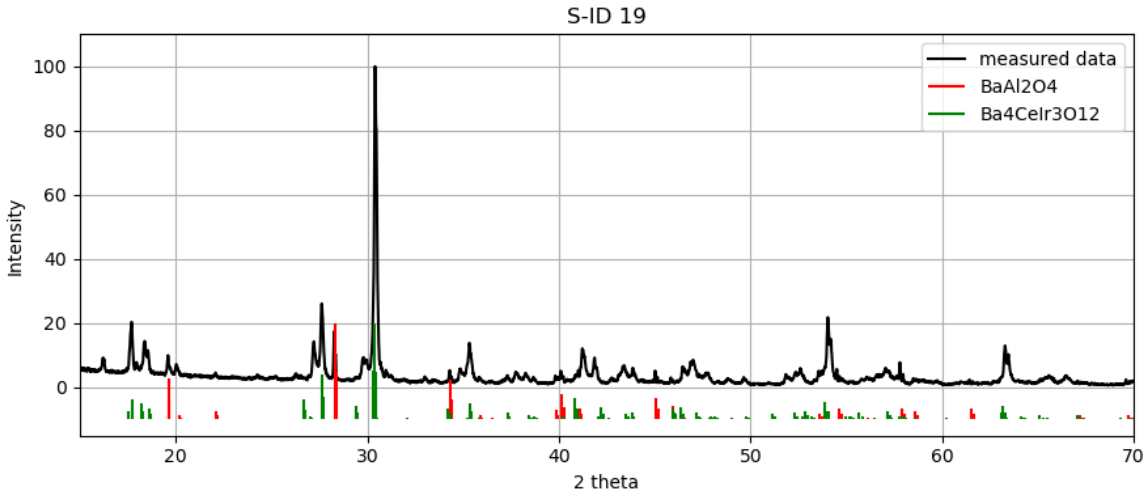
S-ID 19
measured data
BaAl2O4
Ba4CeIr3O12
Intensity
2 theta

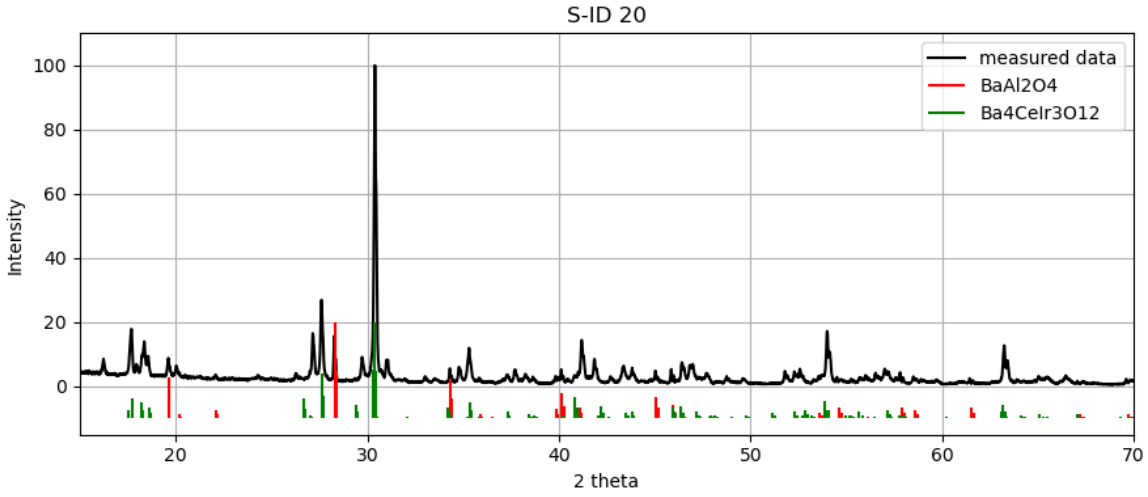
S-ID 20
measured data
BaAl2O4
Ba4CeIr3O12
Intensity
2 theta

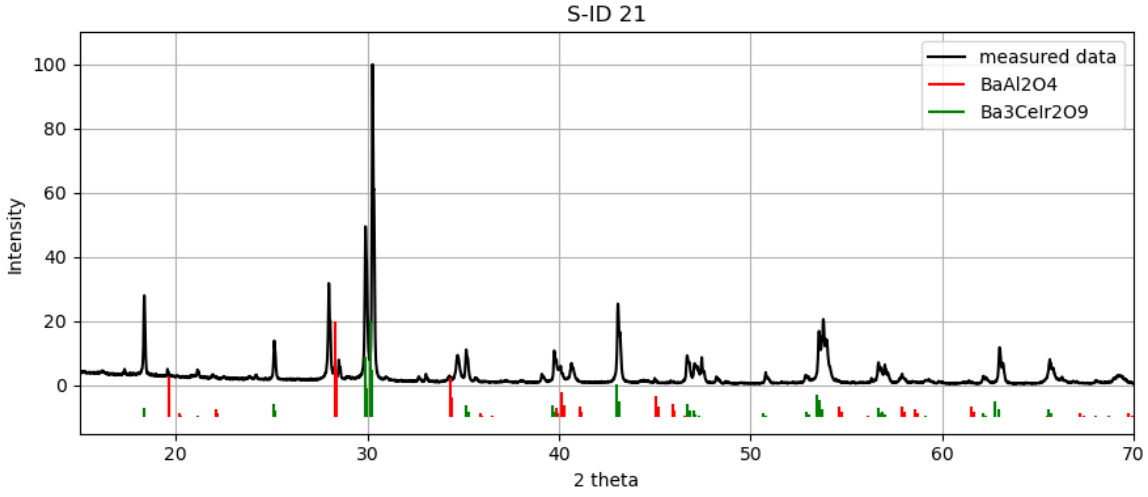
S-ID 21
measured data
BaAl2O4
Ba3CeIr2O9
Intensity
2 theta

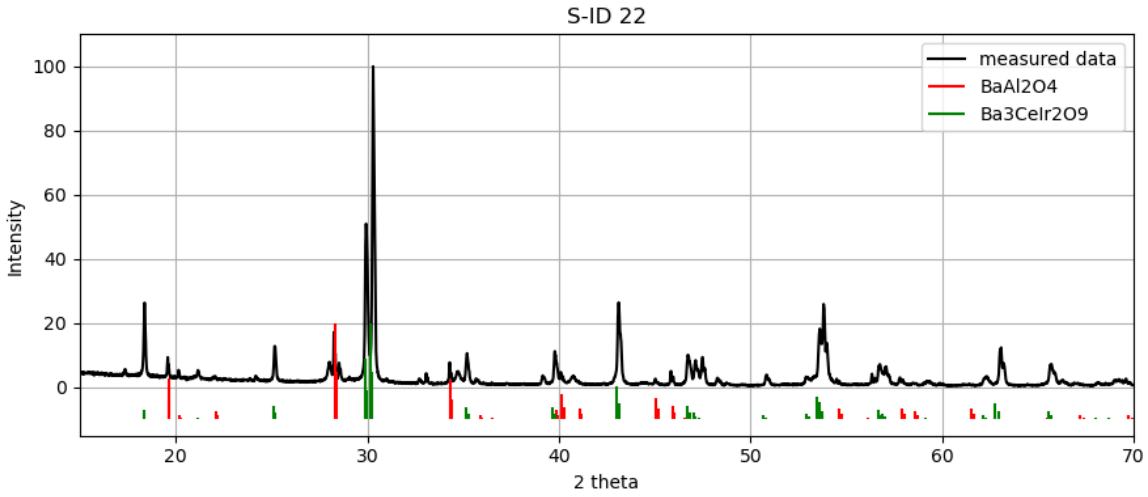
S-ID 22
measured data
BaAl2O4
Ba3CeIr2O9
Intensity
2 theta

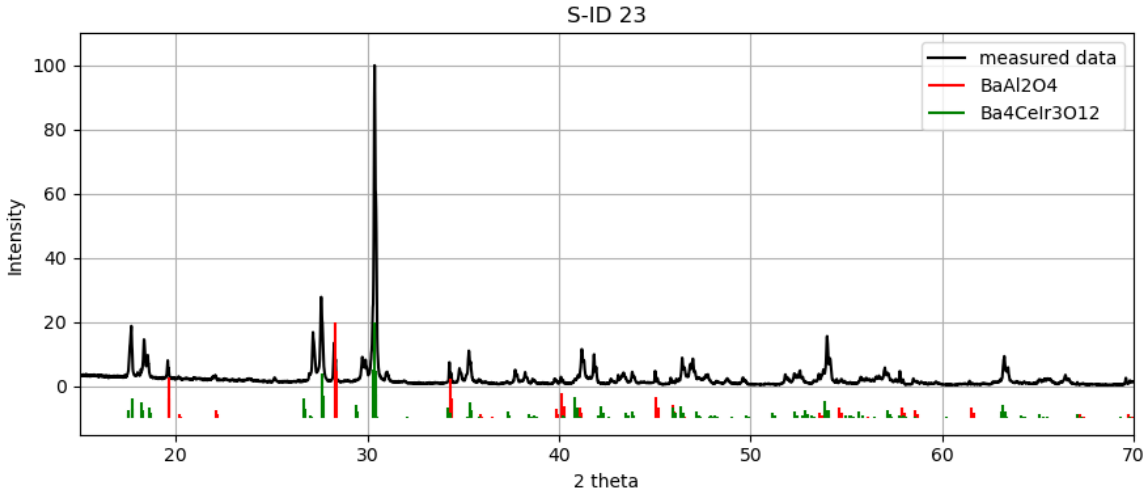
S-ID 23
measured data
BaAl2O4
Ba4CeIr3O12
Intensity
2 theta

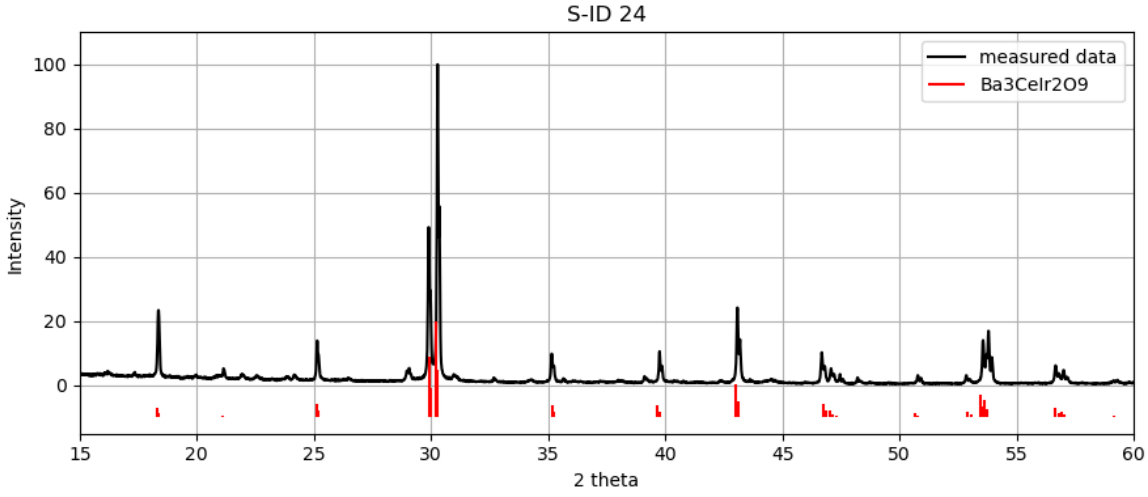
S-ID 24
measured data
Ba3CeIr2O9
Intensity
2 theta

$BaO - Nb_2O_5 - IrO_2$

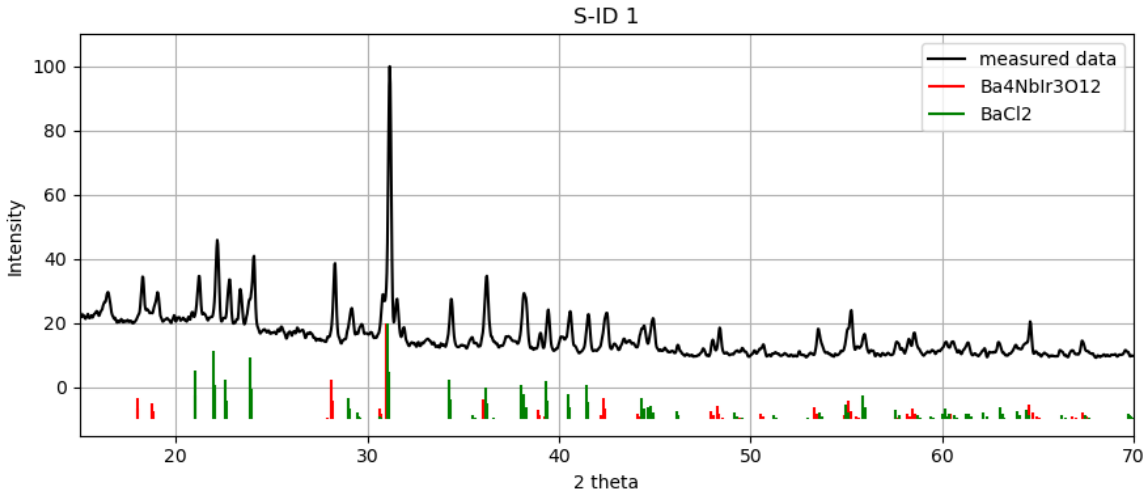

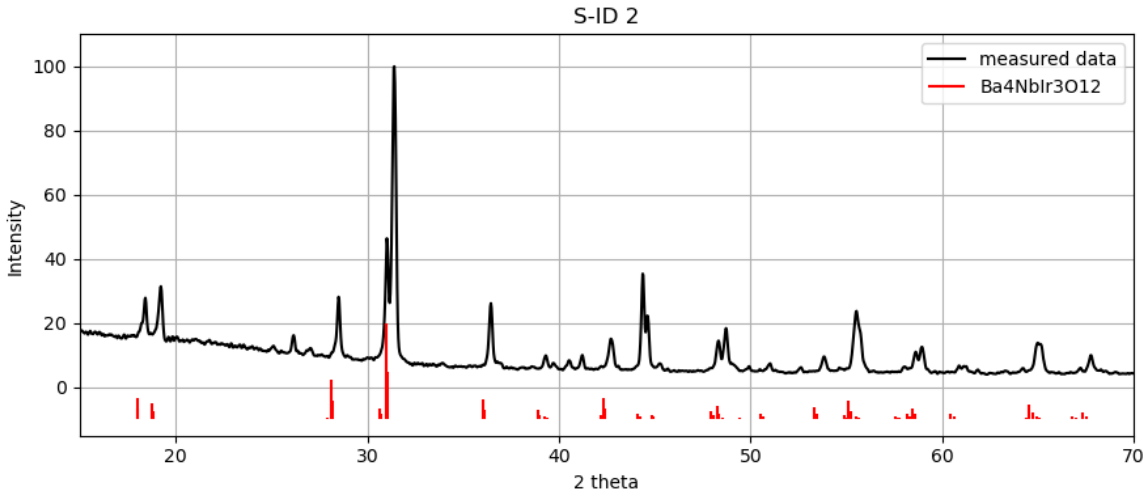

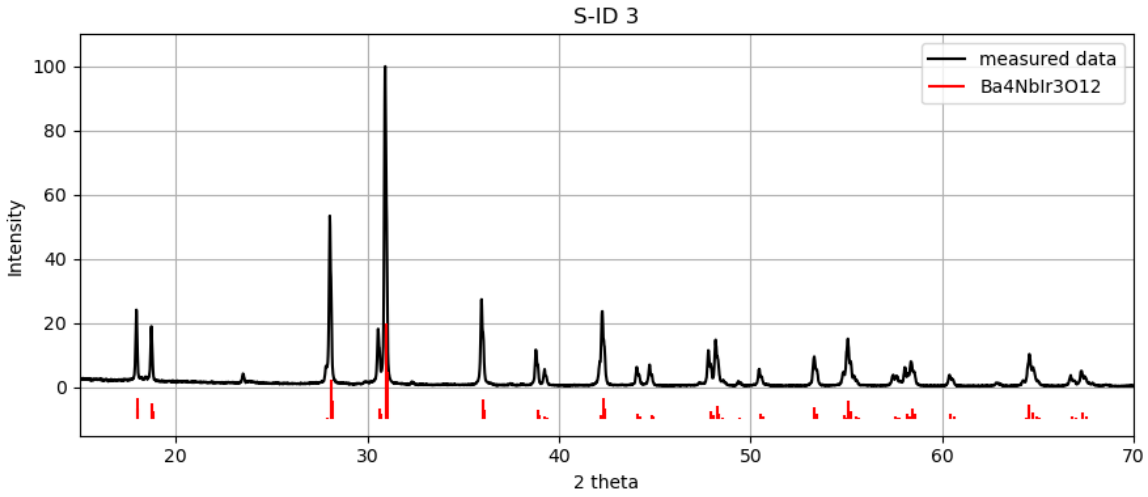
S-ID 3
measured data
Ba4NbIr3O12
Intensity
2 theta

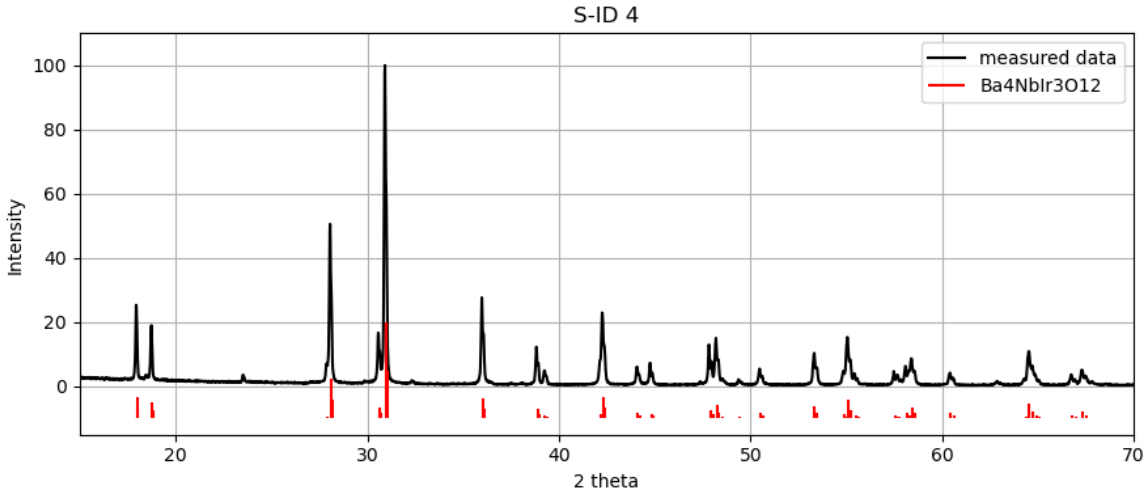
S-ID 4
measured data
Ba4NbIr3O12
Intensity
2 theta

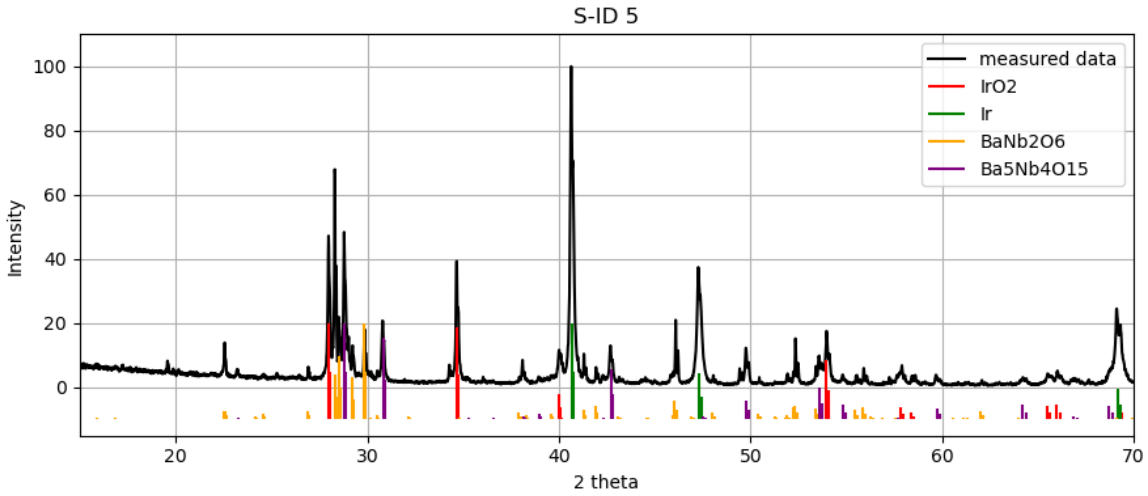
S-ID 5
measured data
IrO2
Ir
BaNb2O6
Ba5Nb4O15
Intensity
2 theta

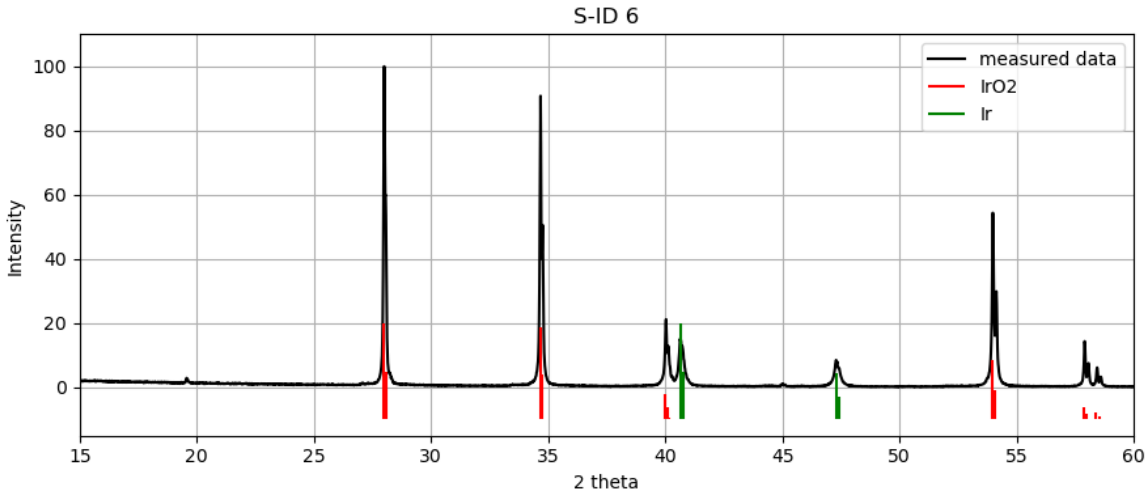
S-ID 6
measured data
IrO2
Ir
Intensity
2 theta

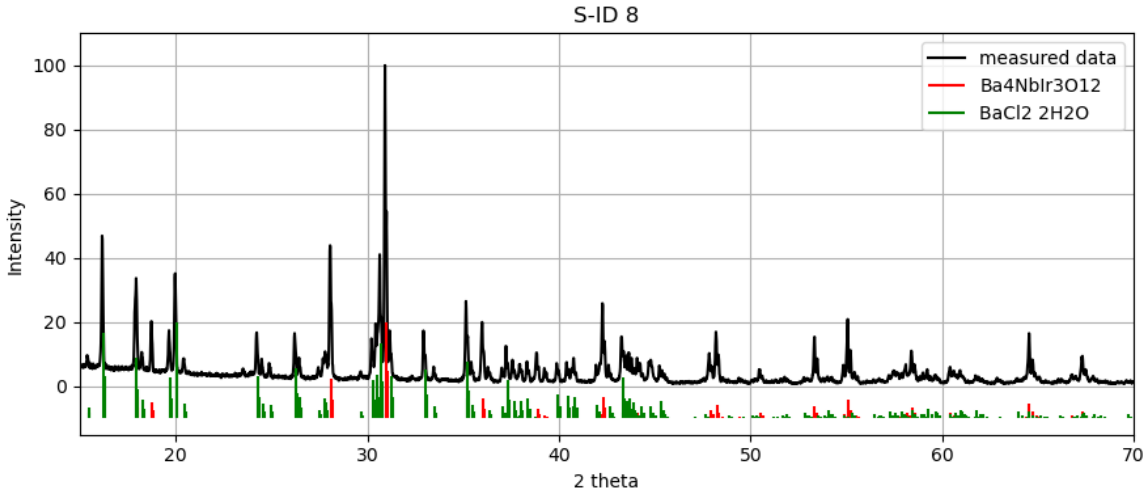
S-ID 8
measured data
Ba4NbIr3O12
BaCl2 2H2O
Intensity
2 theta

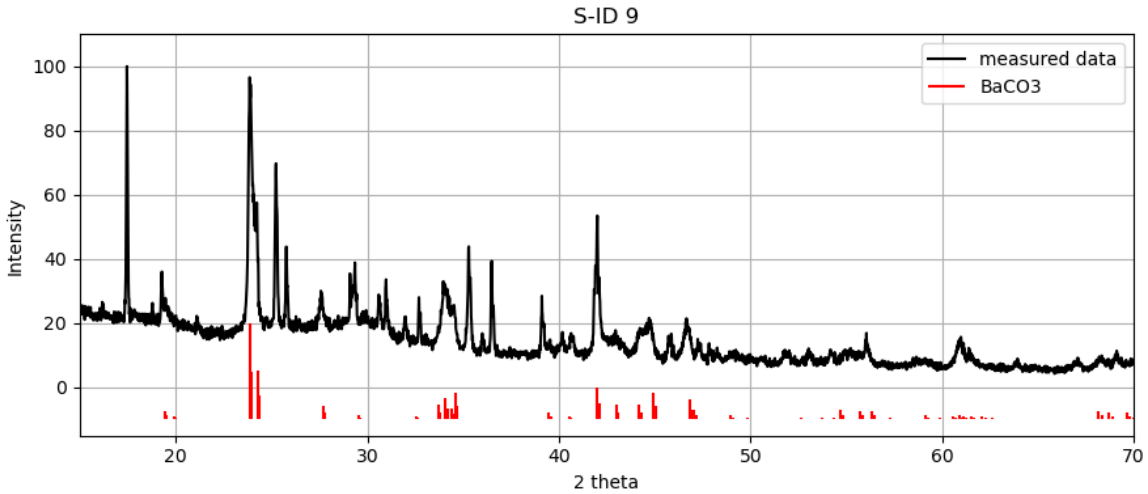
S-ID 9
measured data
BaCO3
Intensity
2 theta

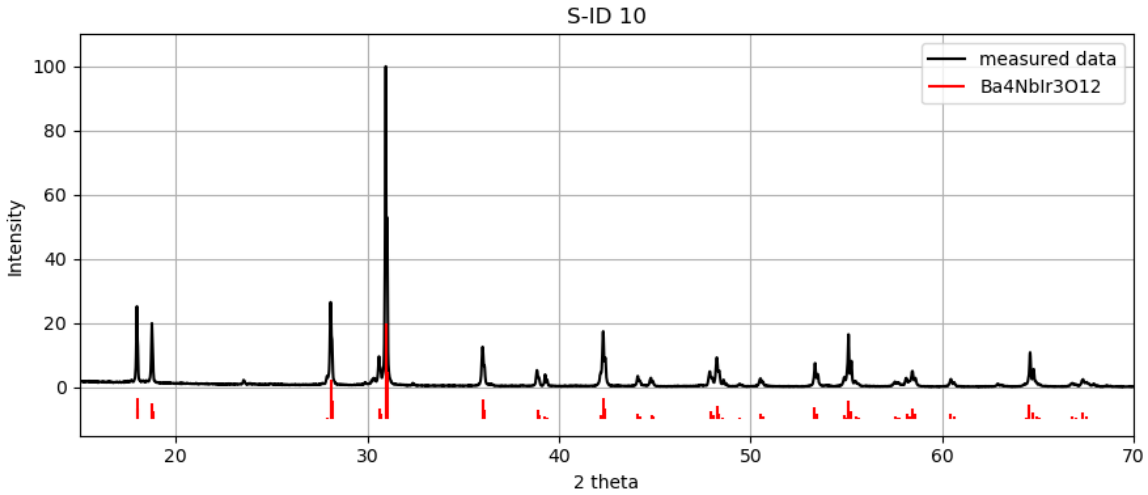
S-ID 10
measured data
Ba4NbIr3O12
Intensity
2 theta

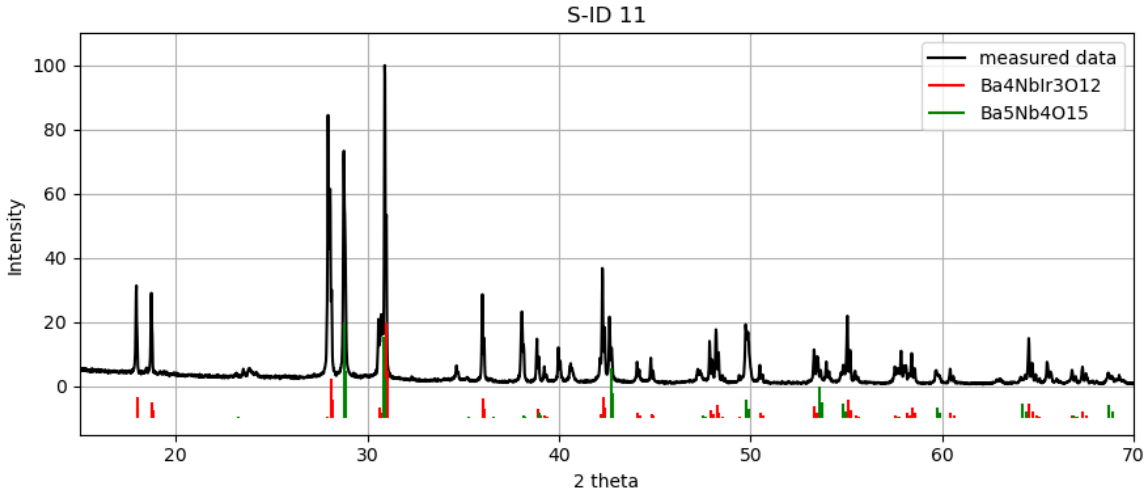
S-ID 11
measured data
Ba4NbIr3O12
Ba5Nb4O15
Intensity
2 theta

$BaO - Ta_2O_5 - IrO_2$

Solid state reaction experiments:

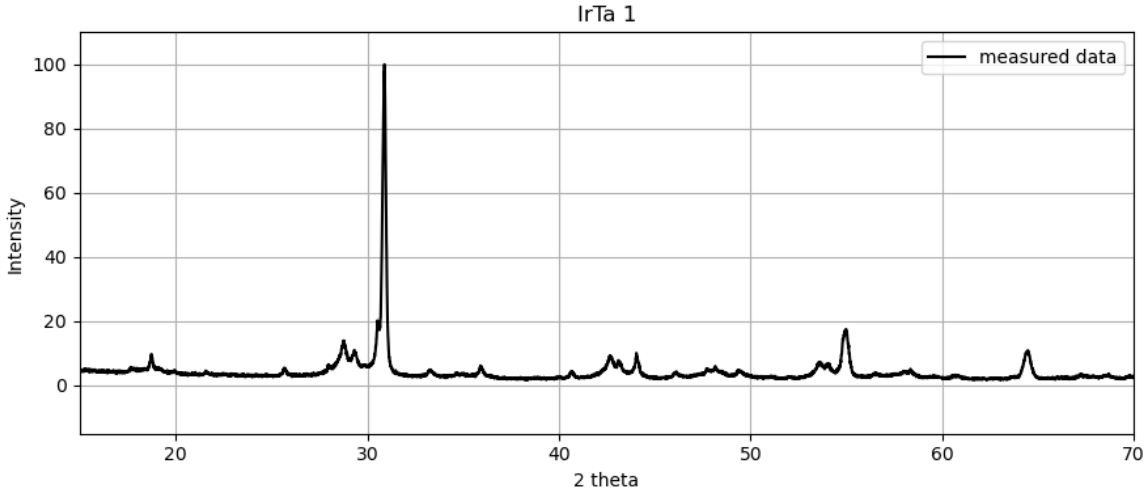

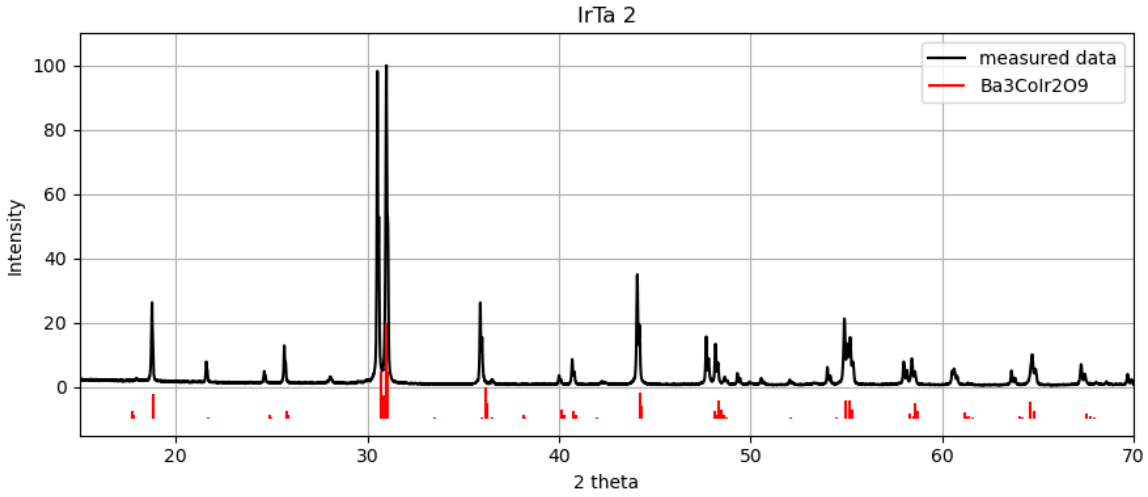

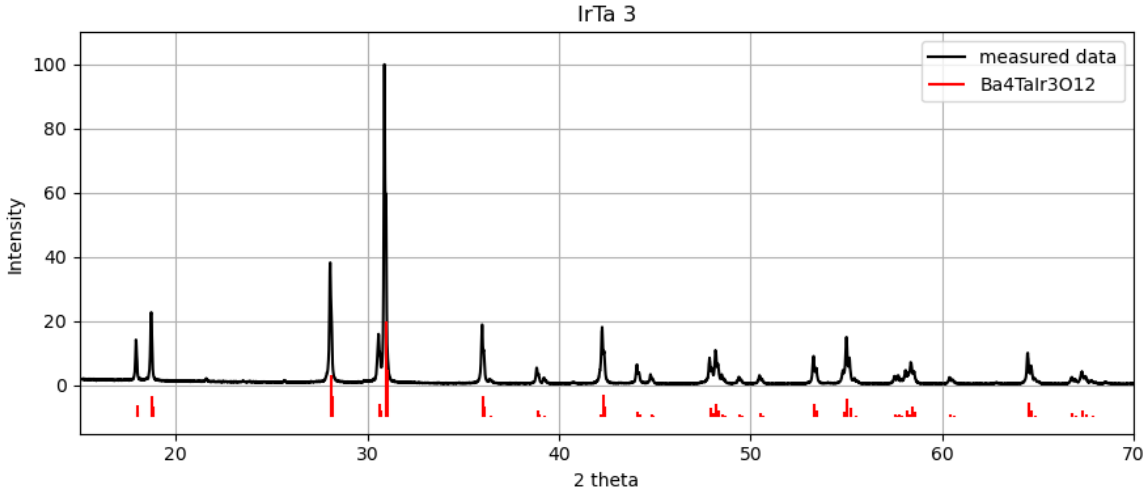

Crystal growth experiments:

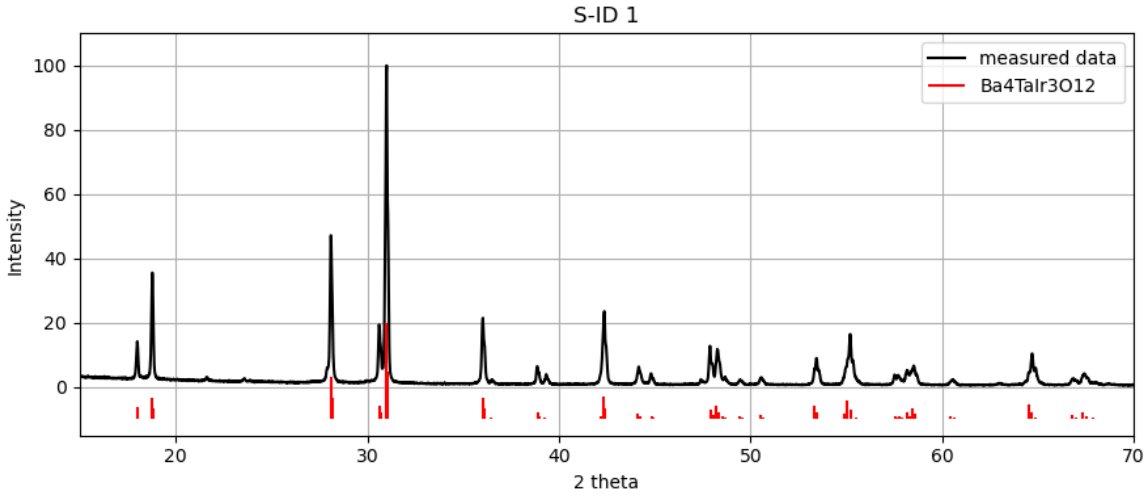

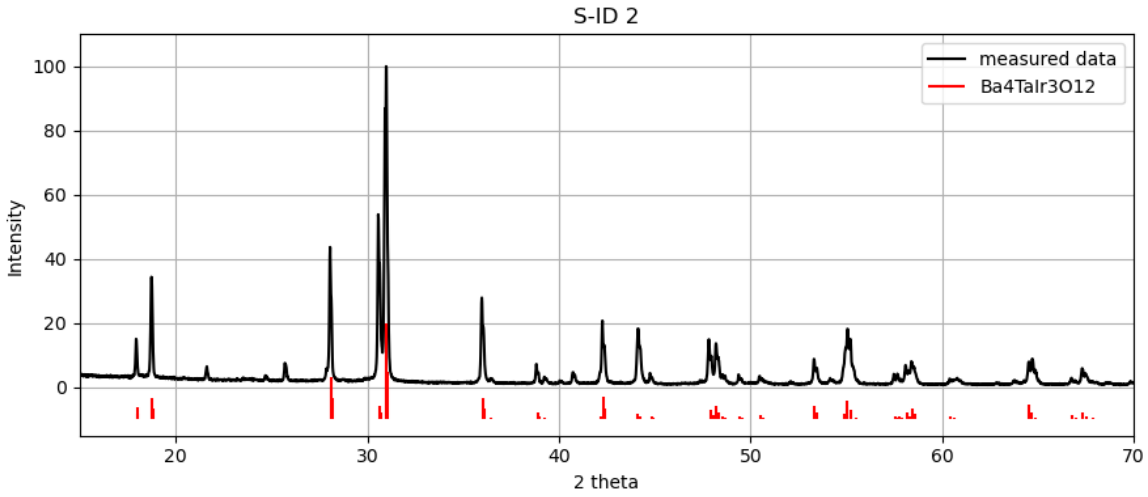
S-ID 2
measured data
Ba4TaIr3O12
Intensity
2 theta

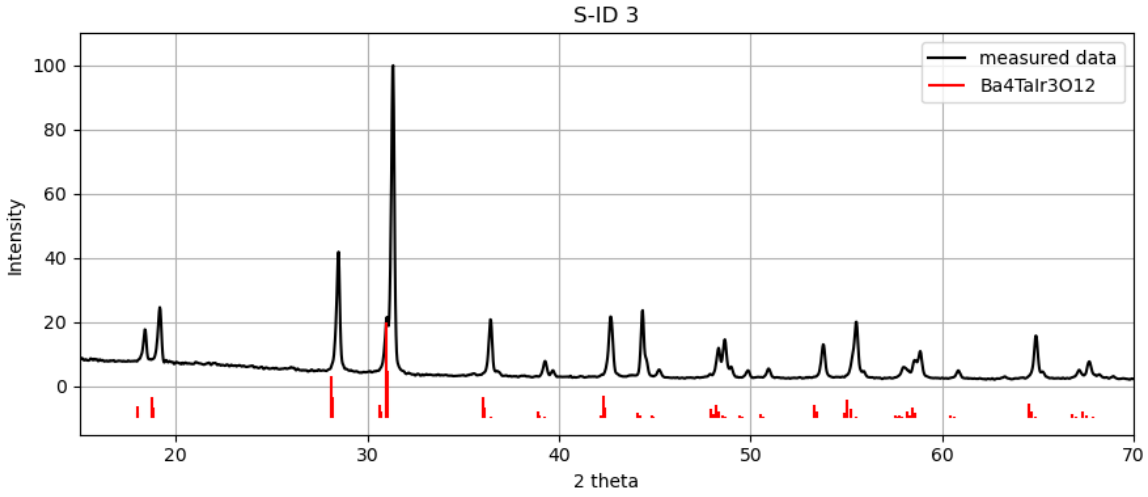
S-ID 3
measured data
Ba4TaIr3O12
Intensity
2 theta

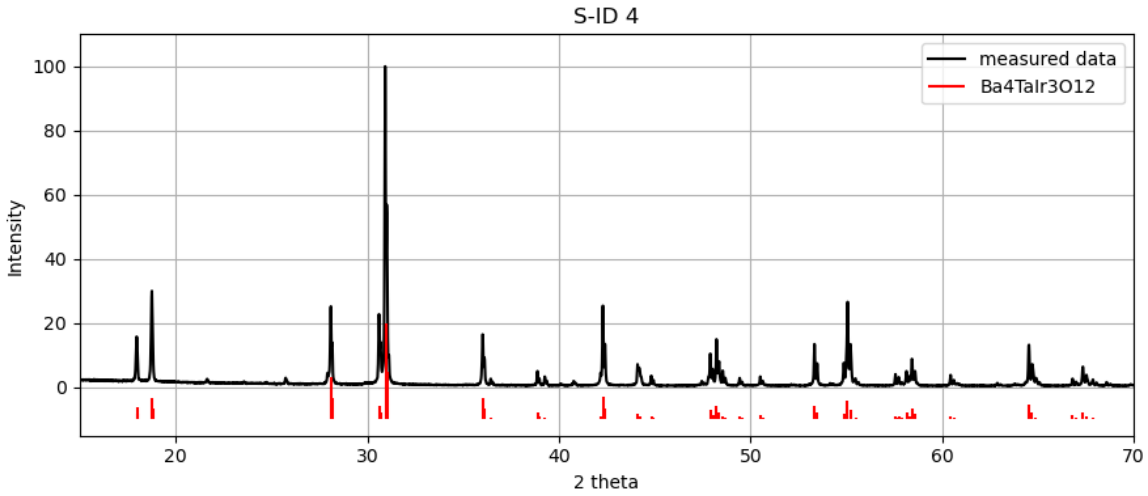
S-ID 4
measured data
Ba4TaIr3O12
Intensity
2 theta

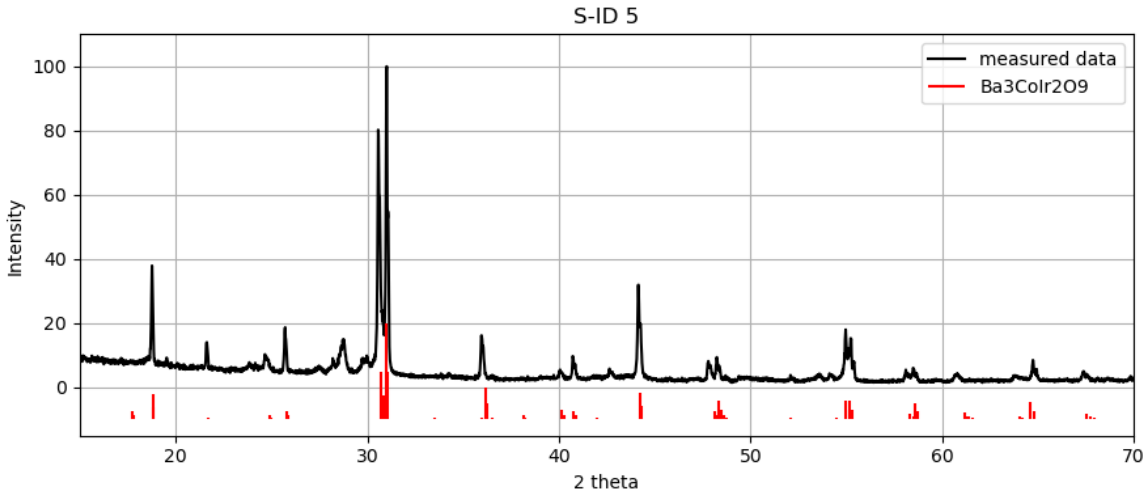
S-ID 5
measured data
Ba3CoIr2O9
Intensity
2 theta
0
20
40
60
80
100
20
30
40
50
60
70

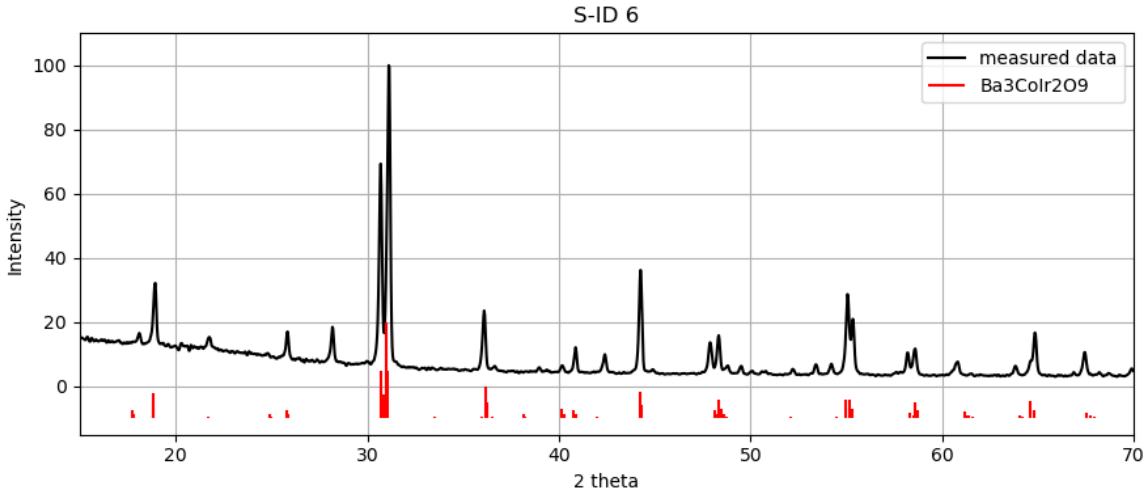
S-ID 6
measured data
Ba3CoIr2O9
Intensity
2 theta
0
20
40
60
80
100
20
30
40
50
60
70

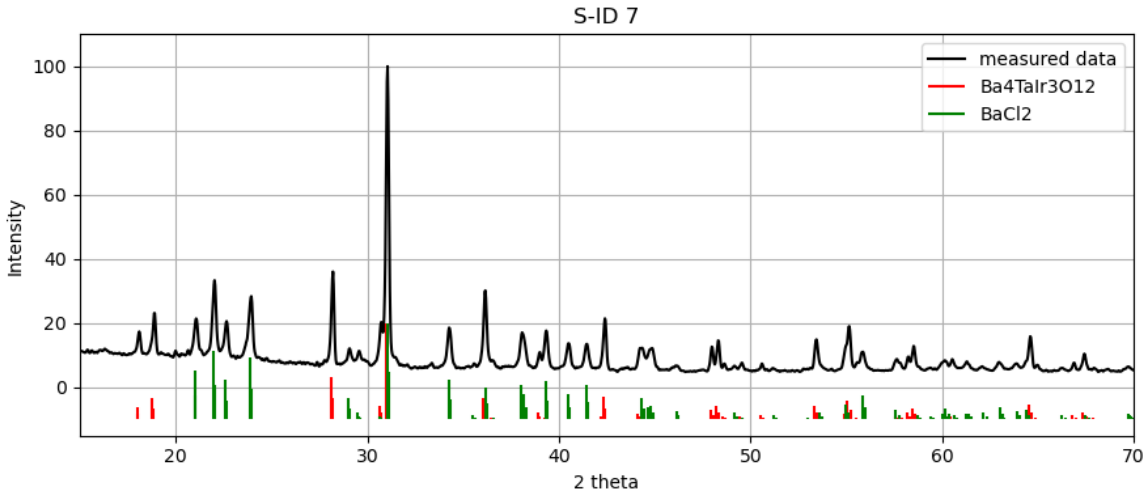
S-ID 7
measured data
Ba4TaIr3O12
BaCl2
Intensity
2 theta
0
20
40
60
80
100
20
30
40
50
60
70

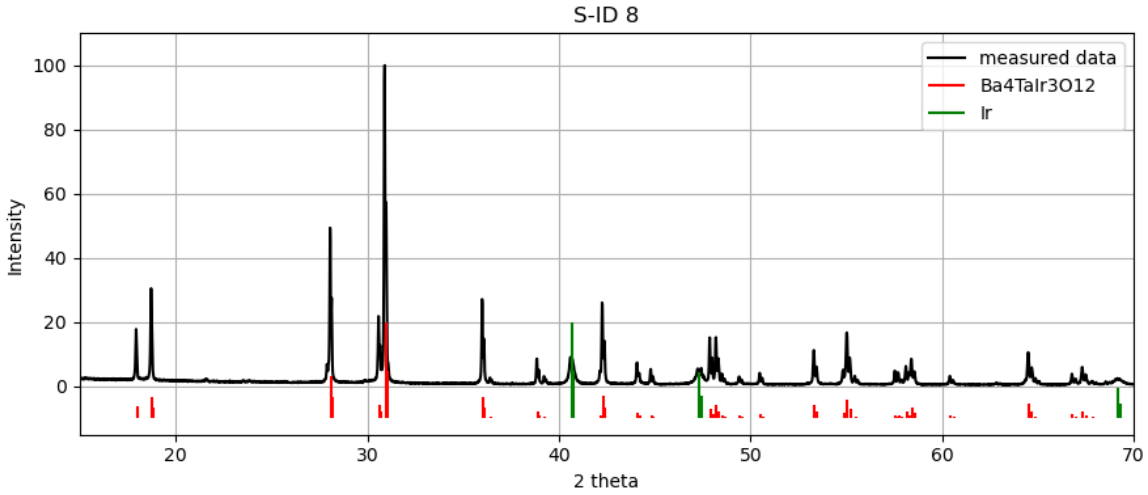
S-ID 8
measured data
Ba4TaIr3O12
Ir
Intensity
2 theta
0
20
40
60
80
100
20
30
40
50
60
70

$BaO - Eu_2O_3 - RuO_2$

Solid state reaction experiments:

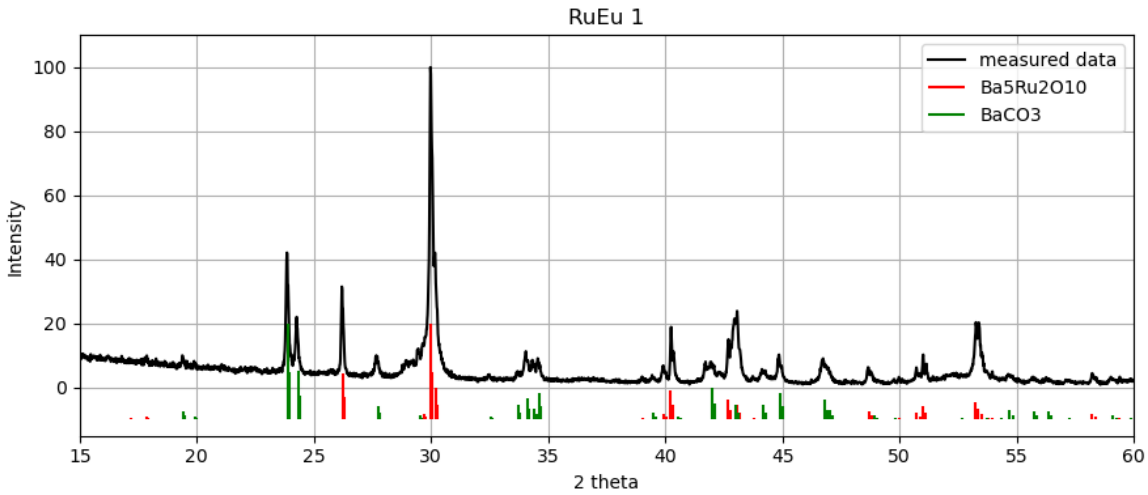

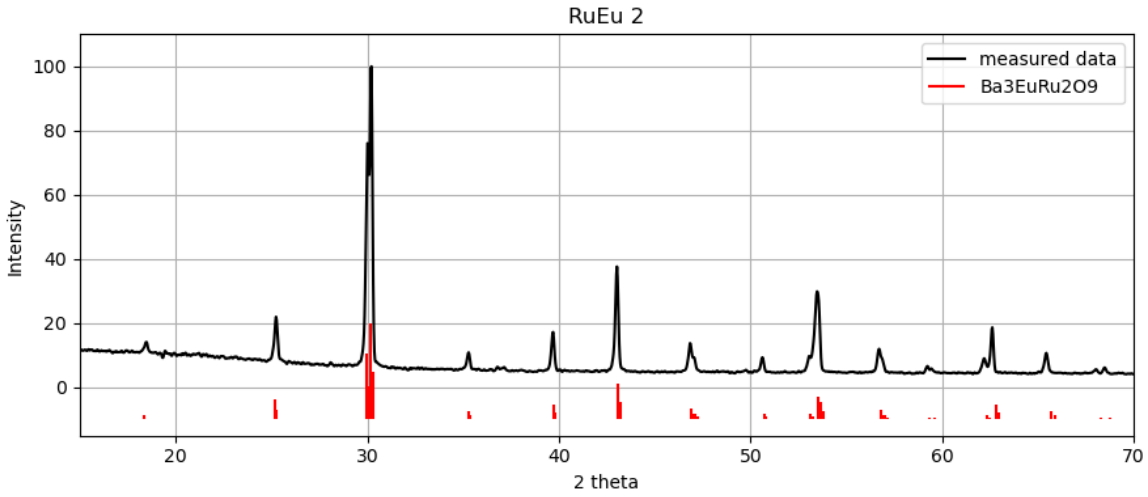

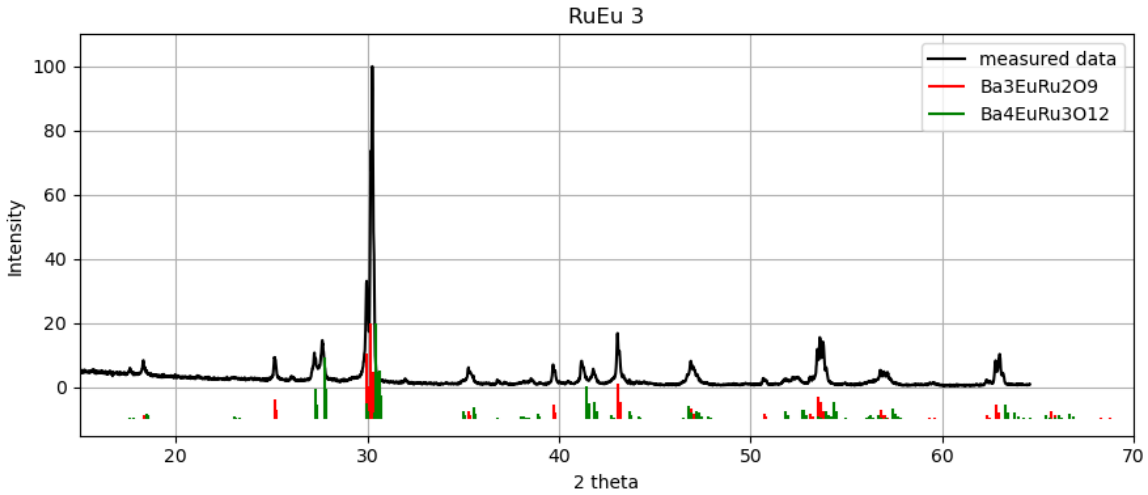
RuEu 3
measured data
Ba3EuRu2O9
Ba4EuRu3O12
Intensity
2 theta
0
20
40
60
80
100
20
30
40
50
60
70

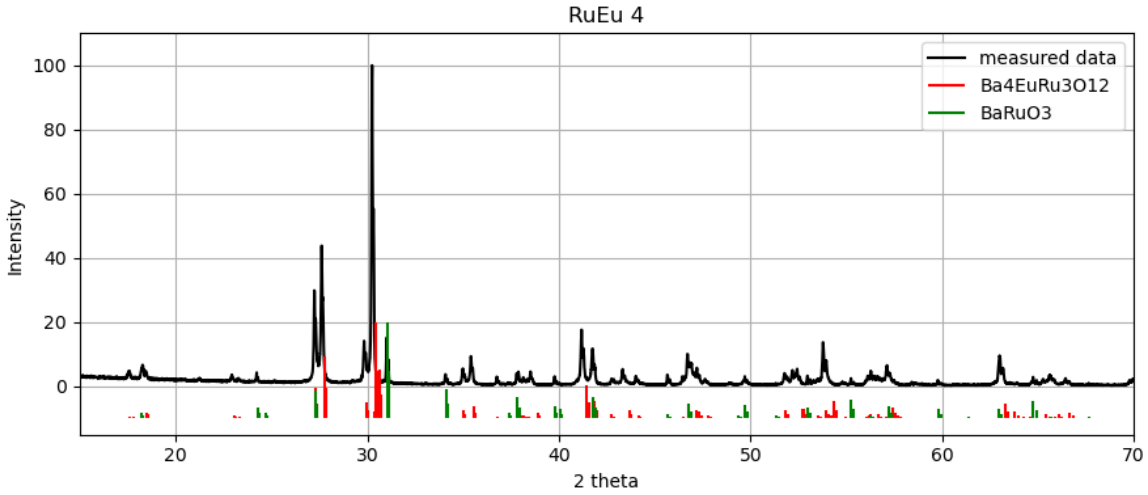
RuEu 4
measured data
Ba4EuRu3O12
BaRuO3
Intensity
2 theta
0
20
40
60
80
100
20
30
40
50
60
70

Crystal growth experiments:

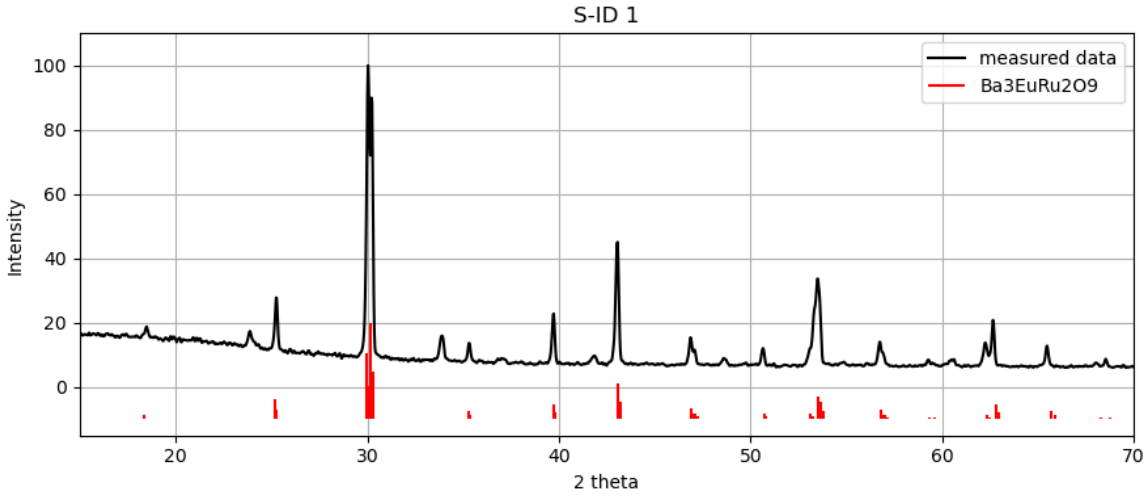

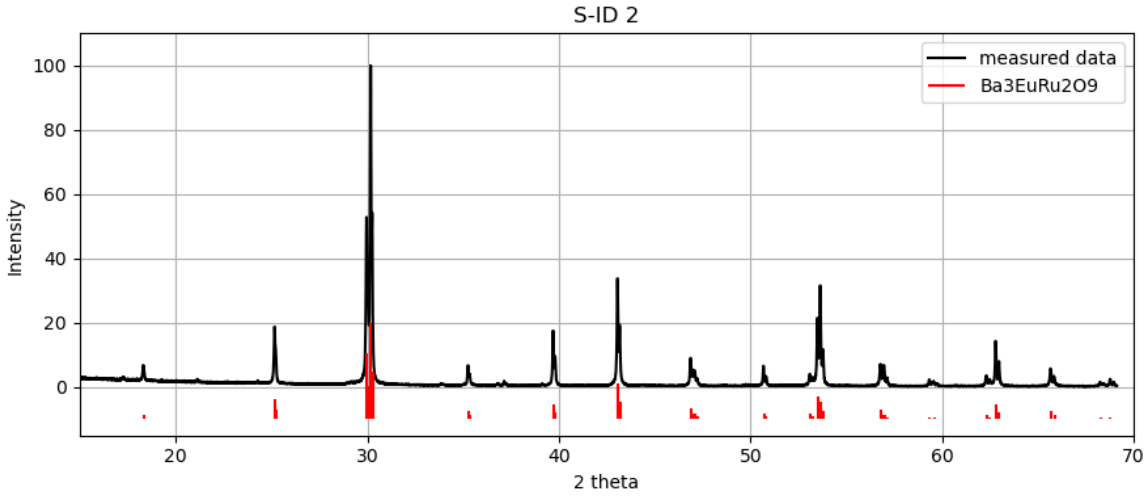

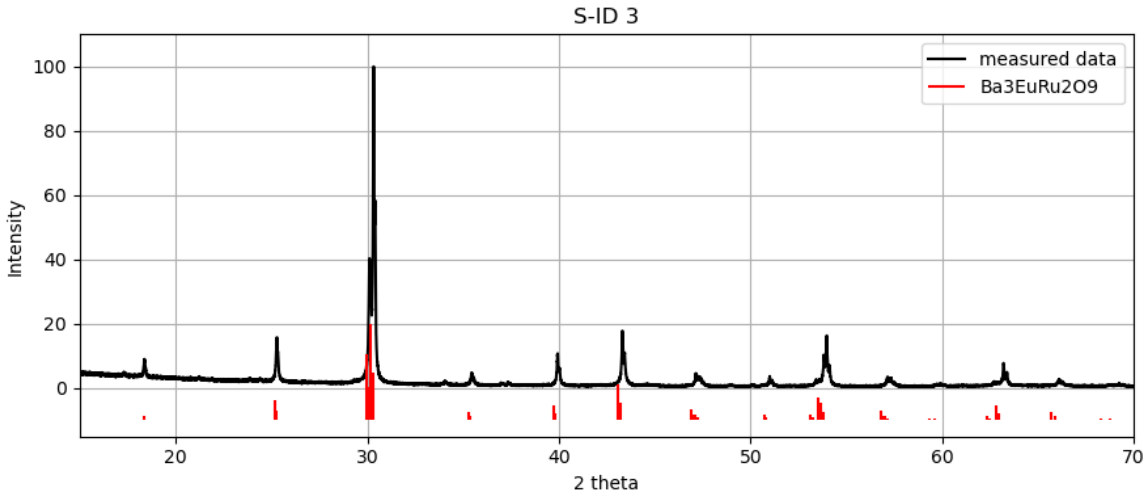
S-ID 3
measured data
Ba3EuRu2O9
Intensity
2 theta

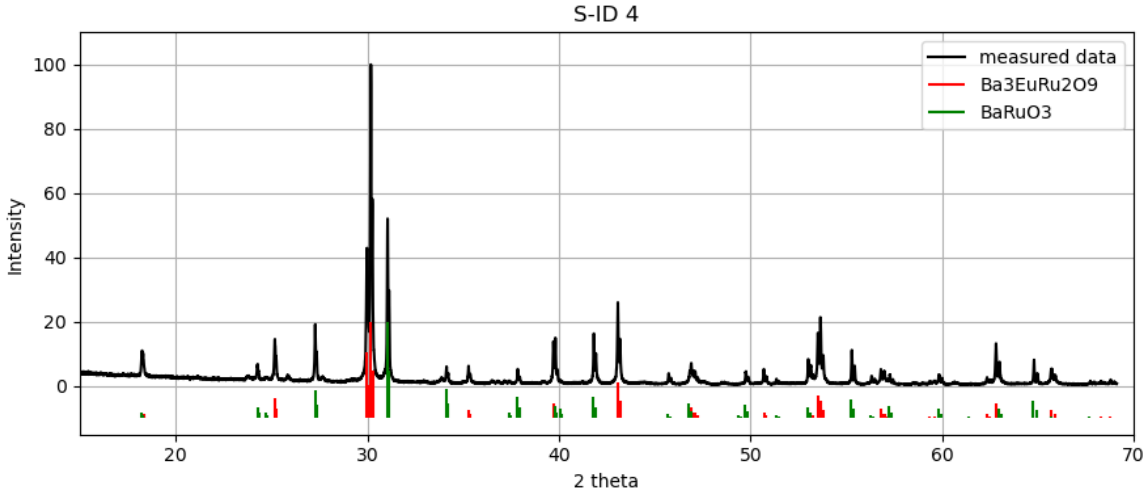
S-ID 4
measured data
Ba3EuRu2O9
BaRuO3
Intensity
2 theta

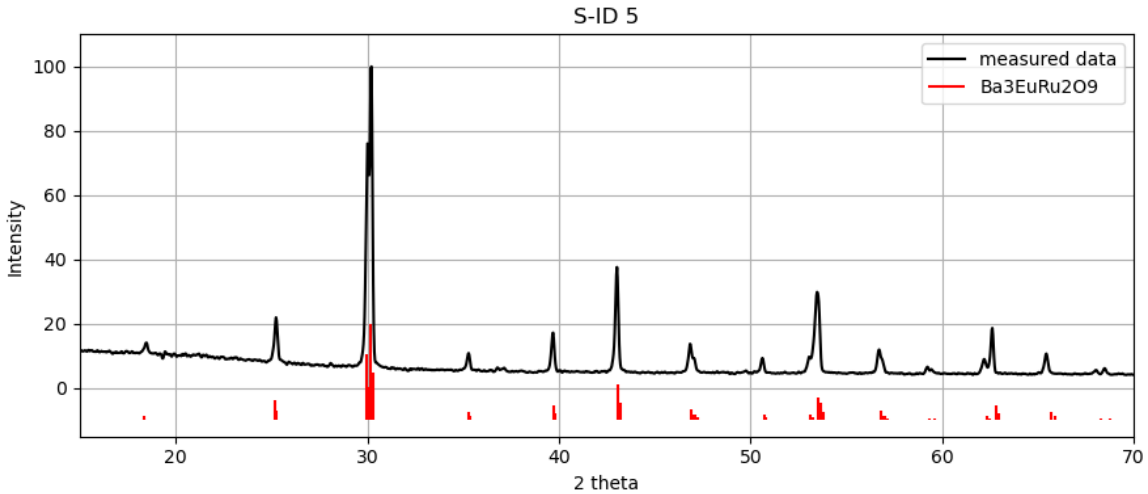
S-ID 5
measured data
Ba3EuRu2O9
Intensity
2 theta

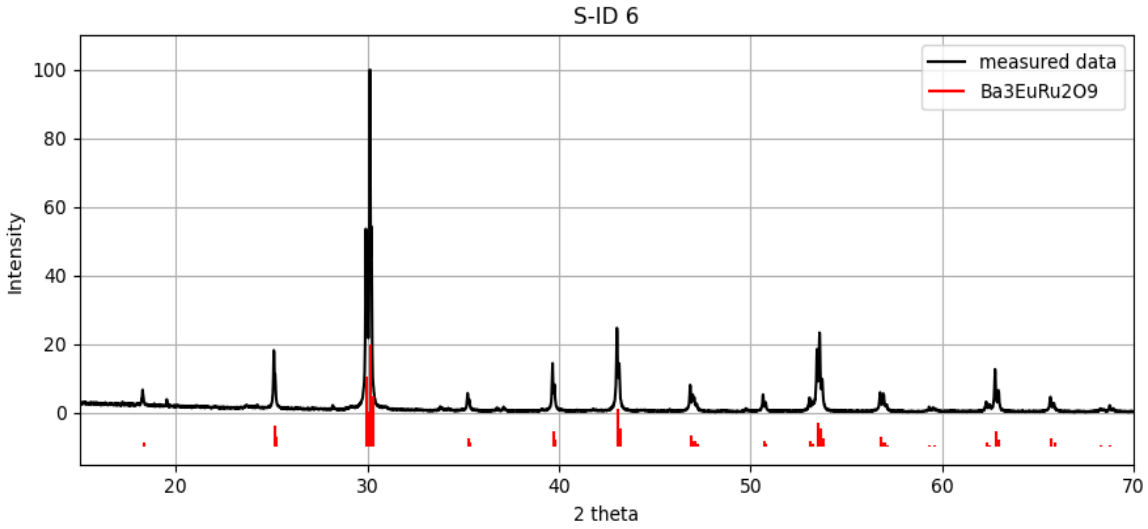

$BaO - CeO_2 - RuO_2$

Solid state experiments:

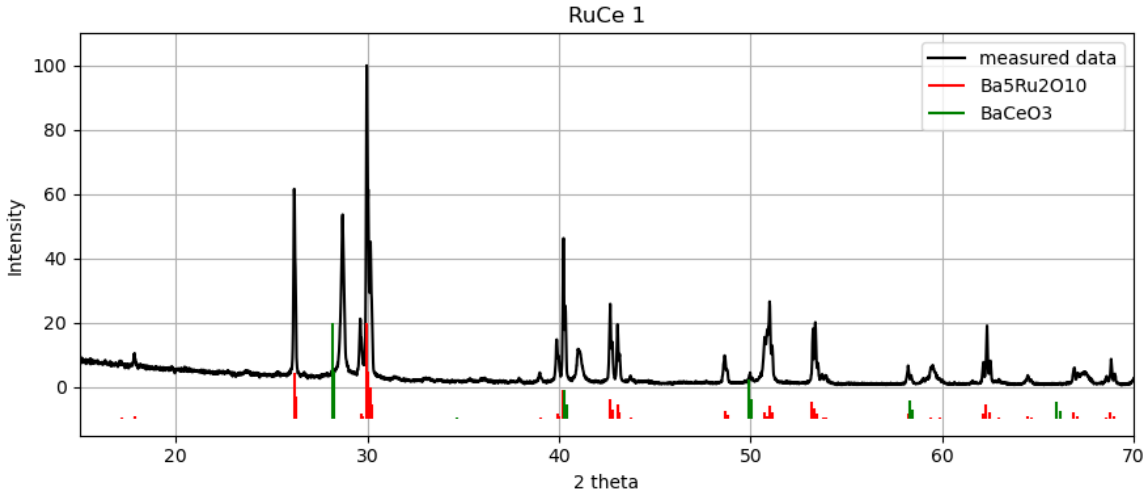

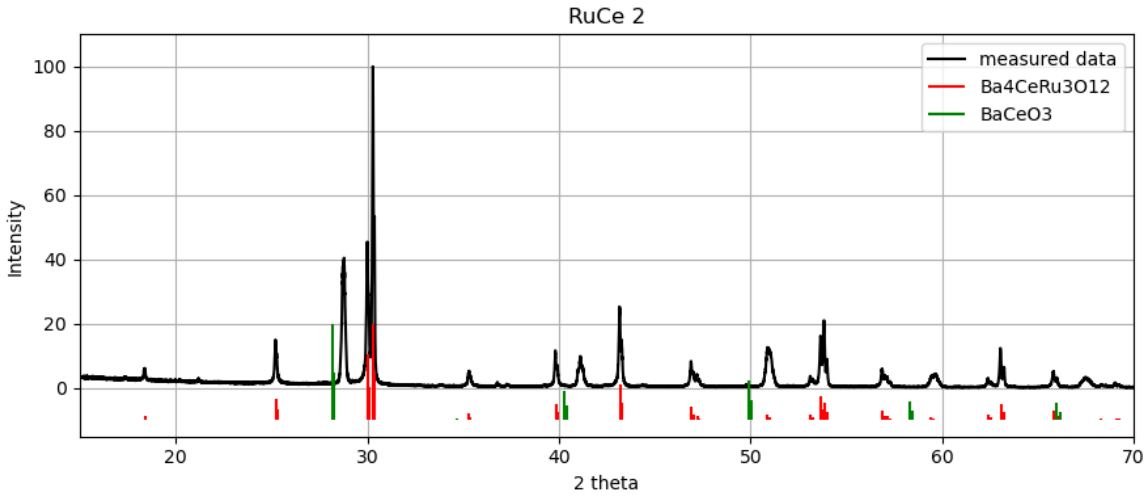
RuCe 2
measured data
Ba4CeRu3O12
BaCeO3
Intensity
2 theta

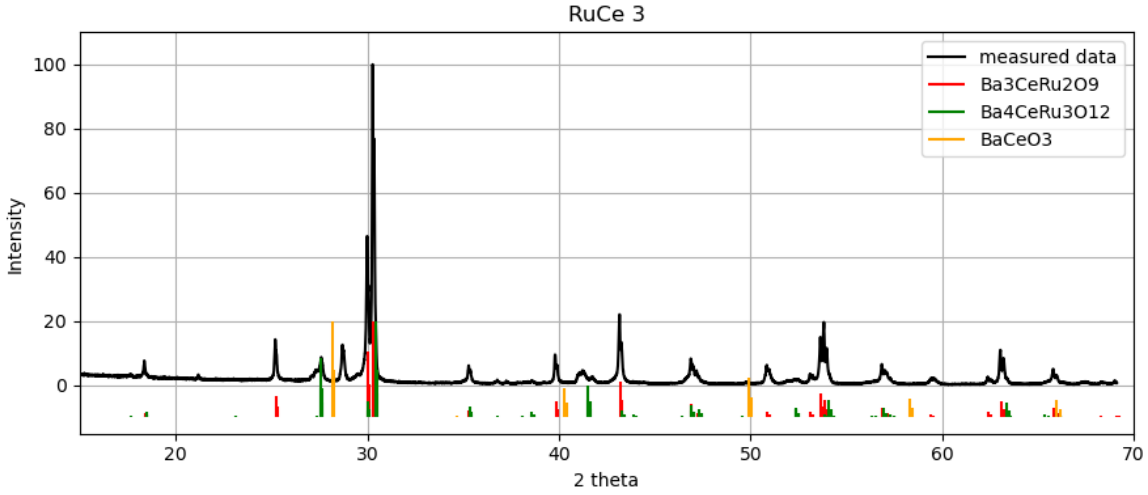
RuCe 3
measured data
Ba3CeRu2O9
Ba4CeRu3O12
BaCeO3
Intensity
2 theta

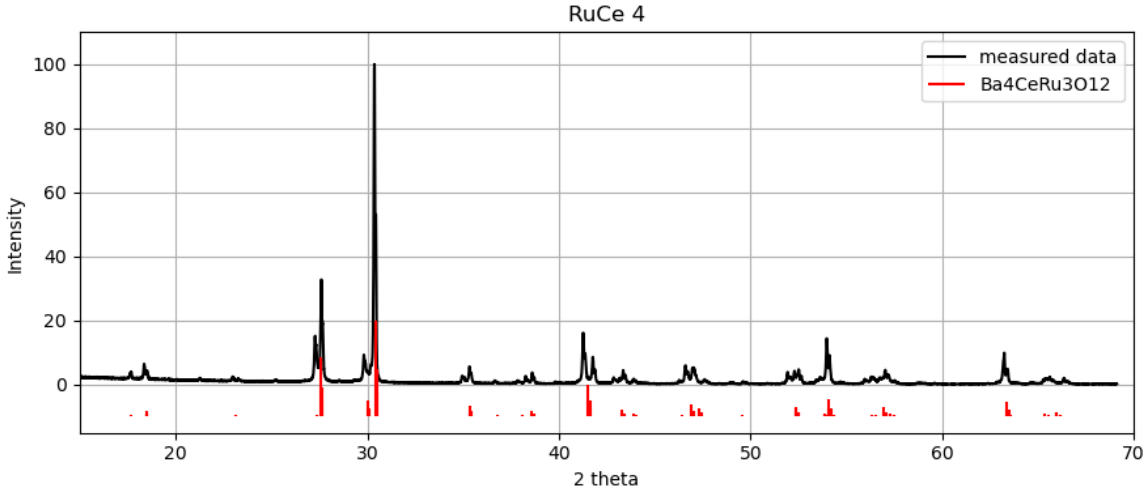
RuCe 4
measured data
Ba4CeRu3O12
Intensity
2 theta

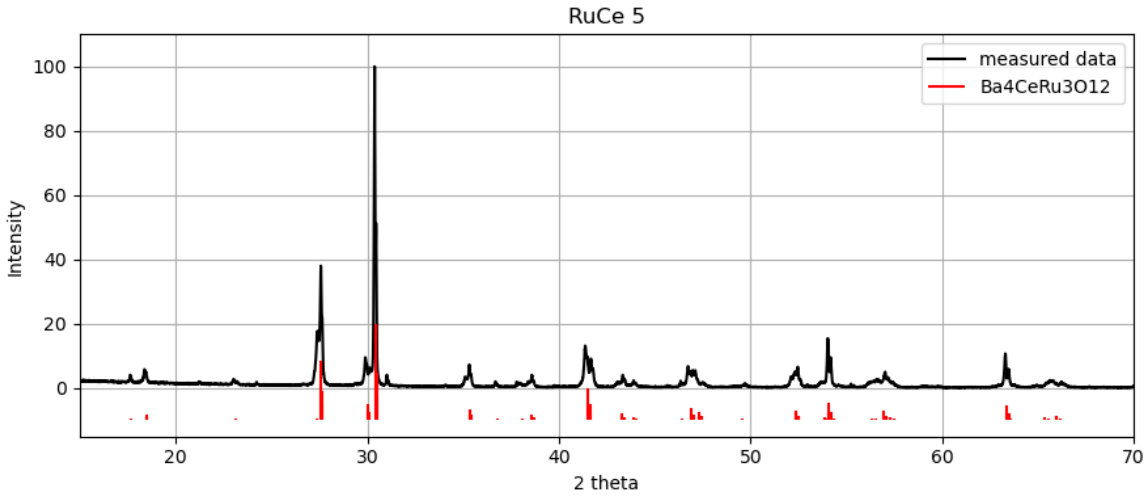

Crytsal growth experiments:

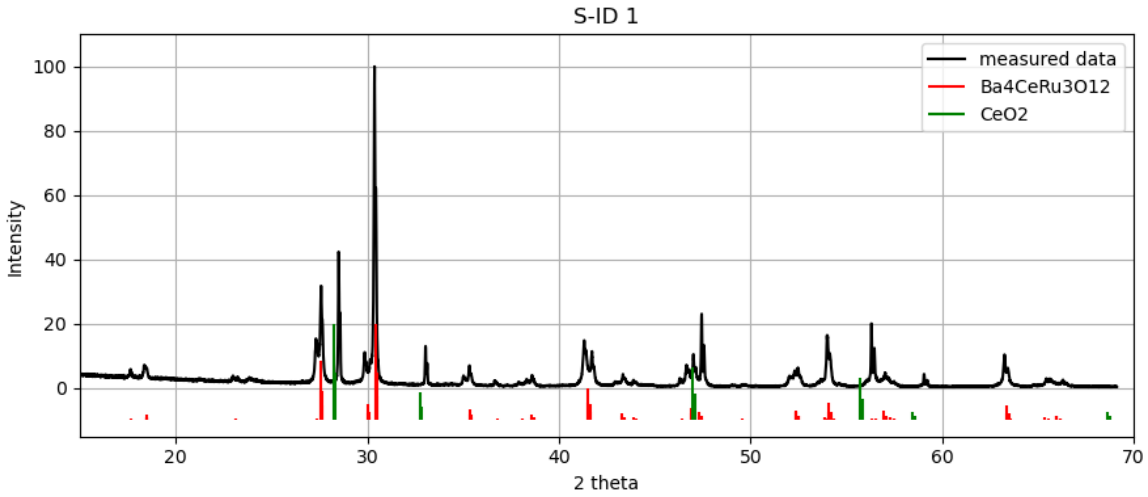

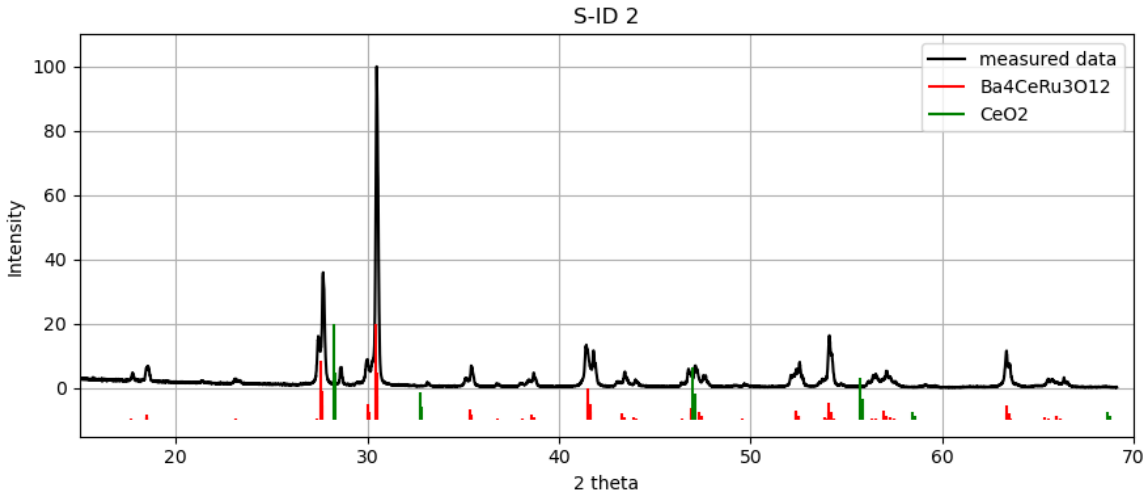
S-ID 2
measured data
Ba4CeRu3O12
CeO2
Intensity
2 theta

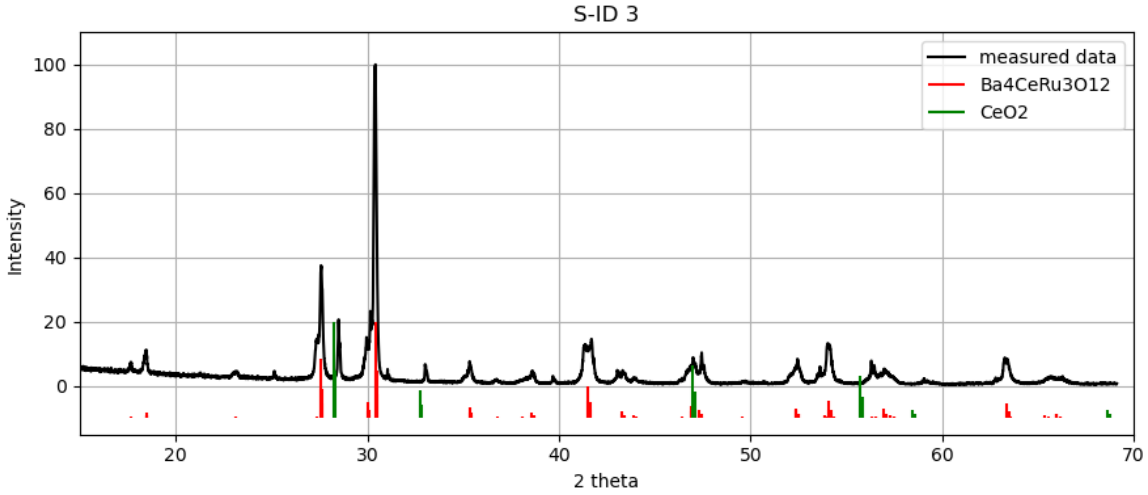
S-ID 3
measured data
Ba4CeRu3O12
CeO2
Intensity
2 theta

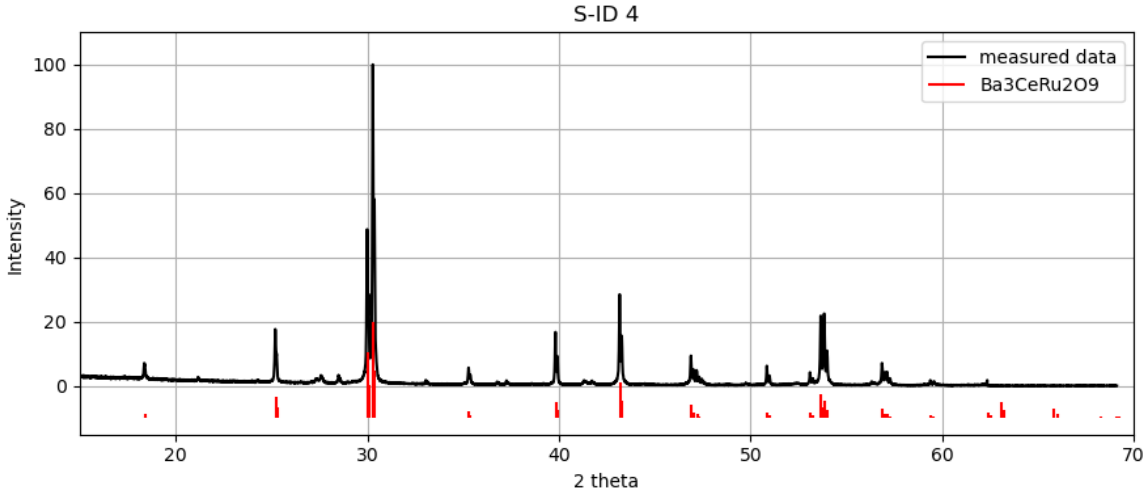
S-ID 4
measured data
Ba3CeRu2O9
Intensity
2 theta

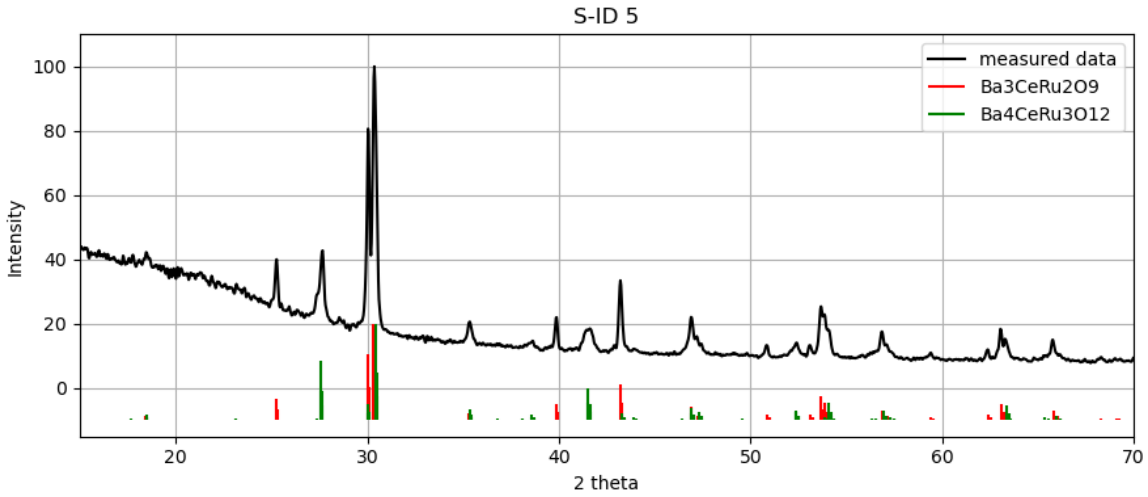
S-ID 5
measured data
Ba3CeRu2O9
Ba4CeRu3O12
Intensity
2 theta

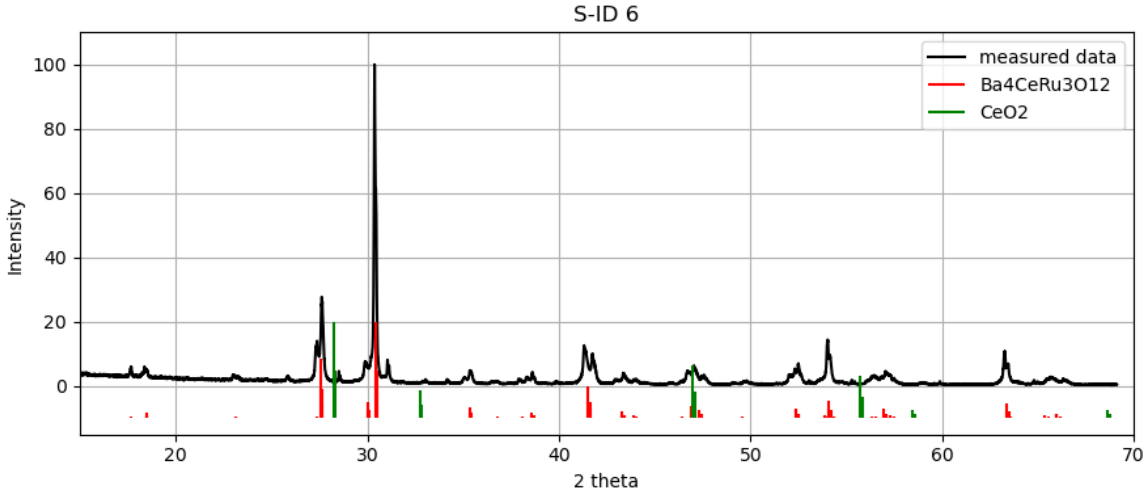
S-ID 6
measured data
Ba4CeRu3O12
CeO2
Intensity
2 theta

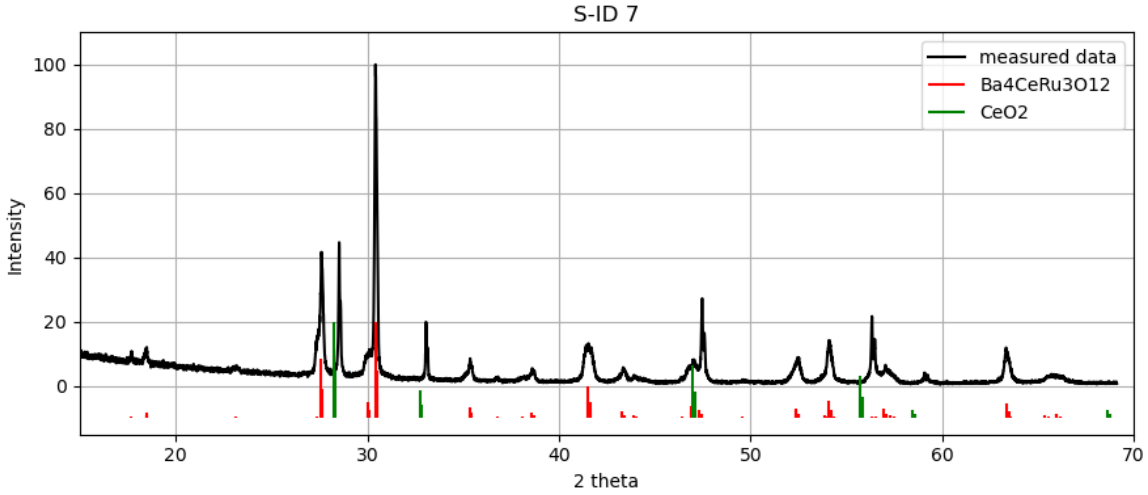
S-ID 7
measured data
Ba4CeRu3O12
CeO2
Intensity
2 theta

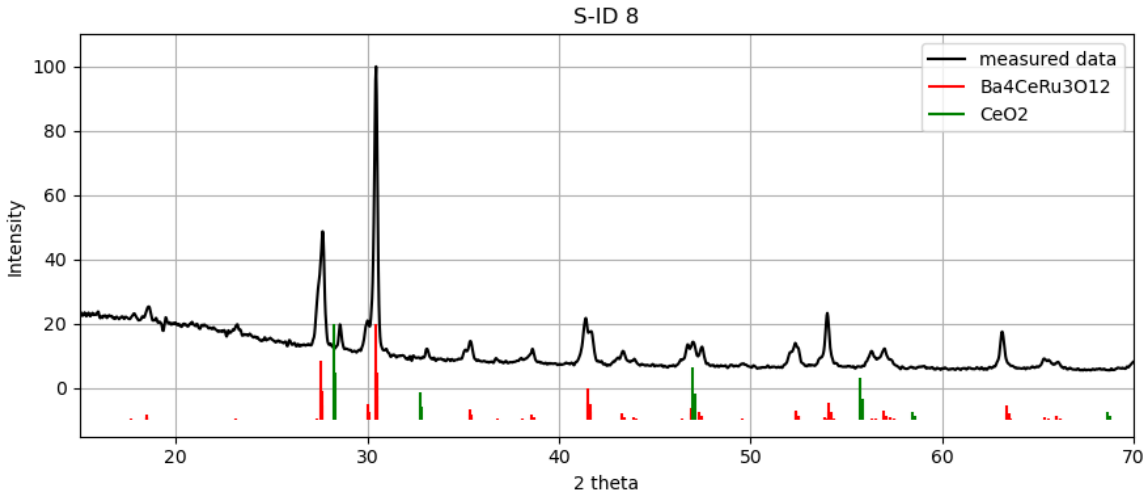
S-ID 8
measured data
Ba4CeRu3O12
CeO2
Intensity
2 theta

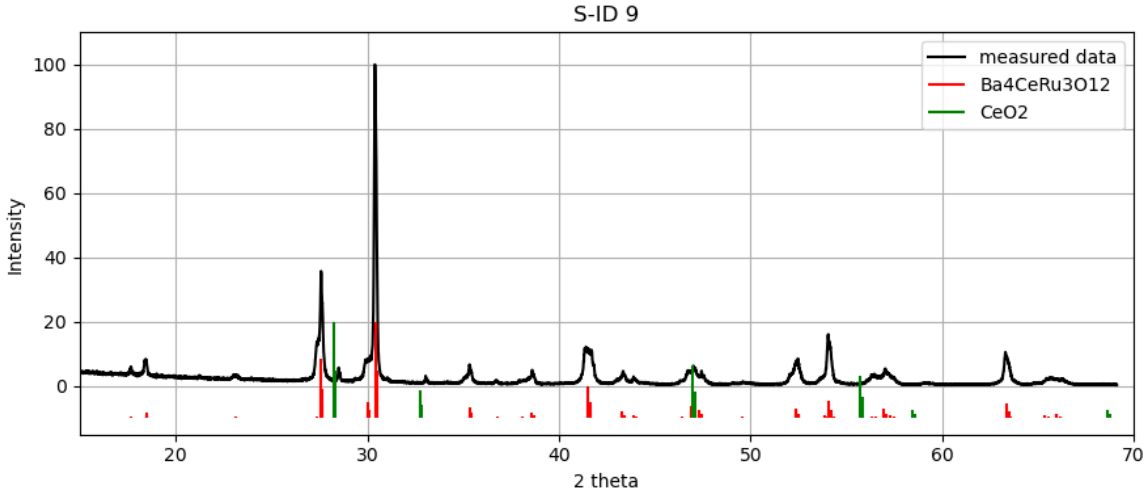
S-ID 9
measured data
Ba4CeRu3O12
CeO2
Intensity
2 theta

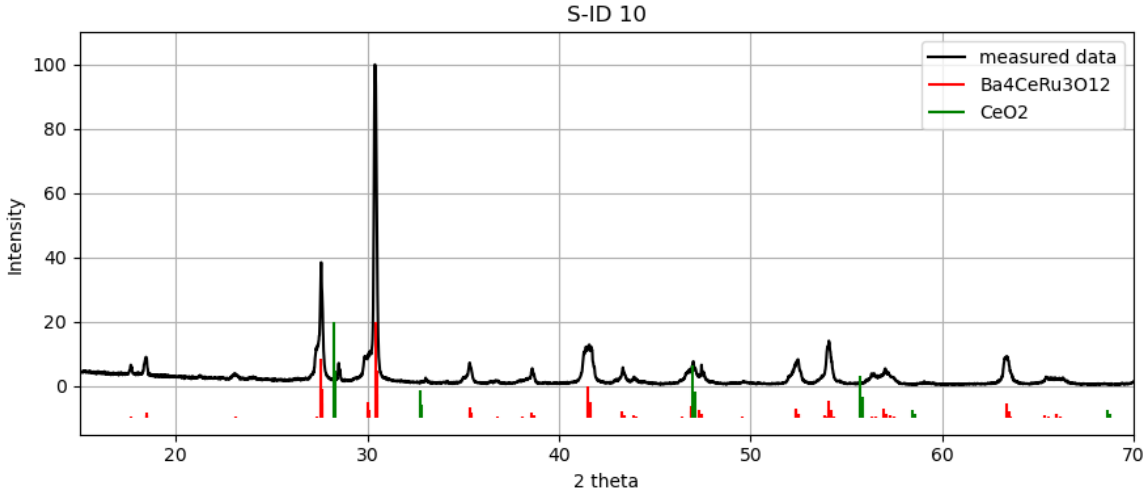
S-ID 10
measured data
Ba4CeRu3O12
CeO2
Intensity
2 theta

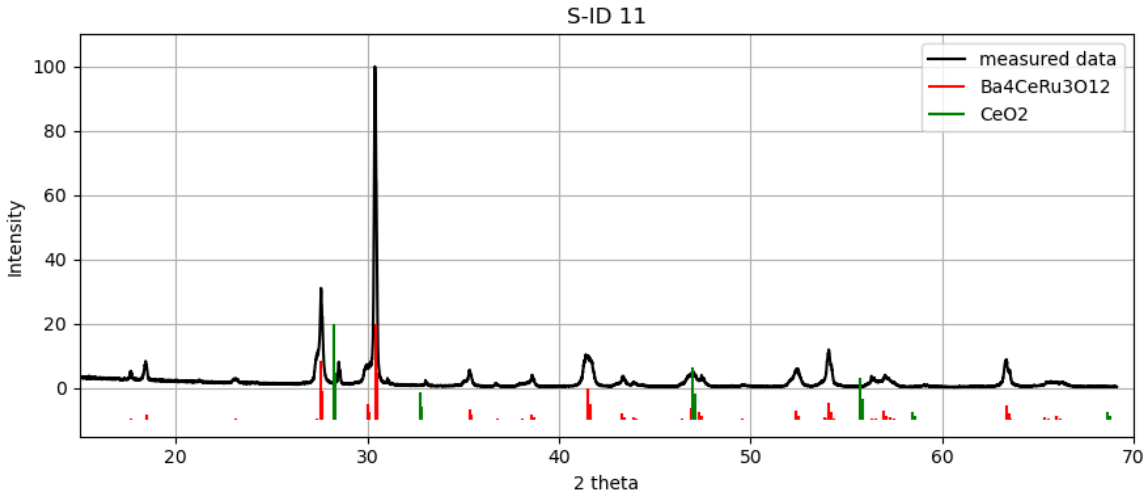
S-ID 11
measured data
Ba4CeRu3O12
CeO2
Intensity
2 theta
0
20
40
60
80
100
20
30
40
50
60
70

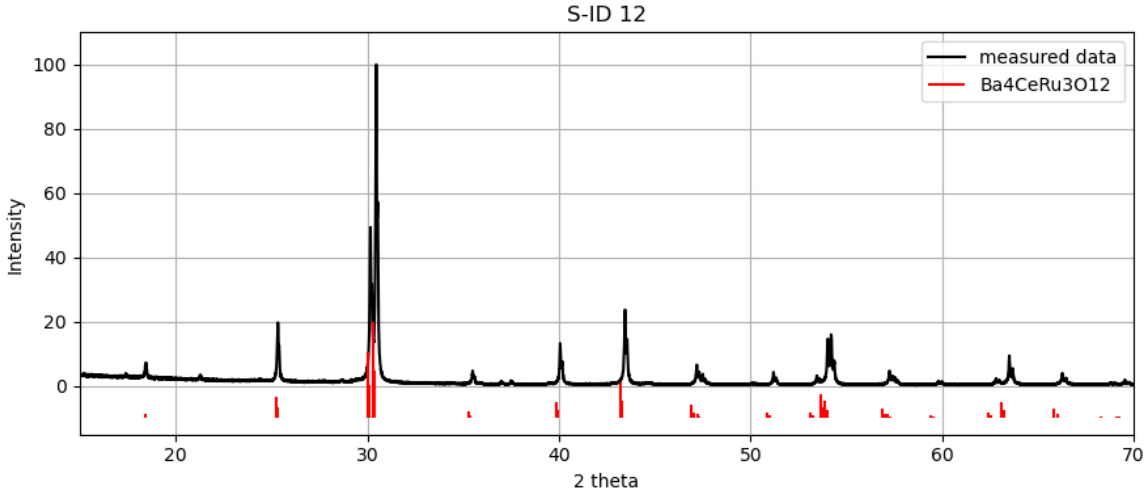
S-ID 12
measured data
Ba4CeRu3O12
Intensity
2 theta
0
20
40
60
80
100
20
30
40
50
60
70

$BaO - Pr_6O_{11} - RuO_2$

Solid state reaction experiments:

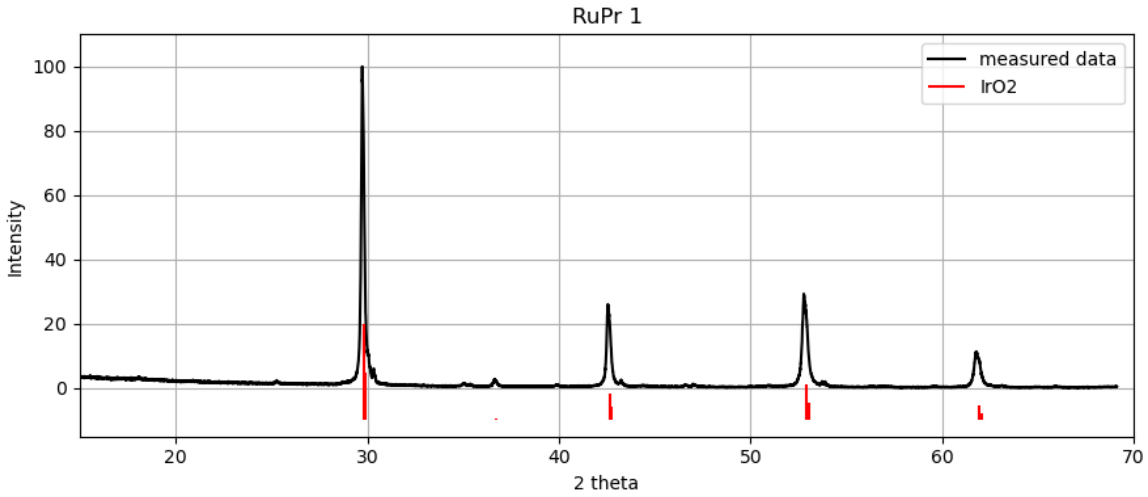

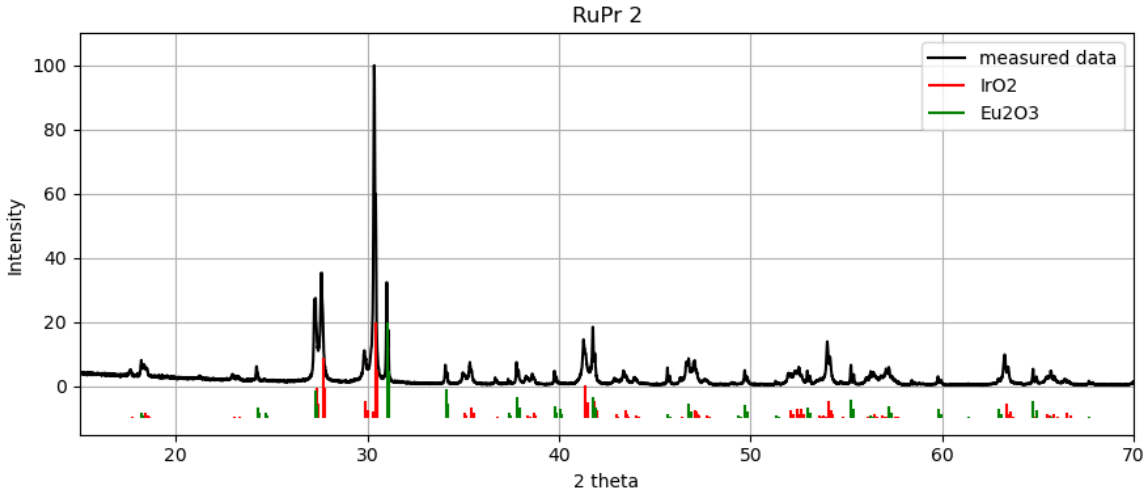

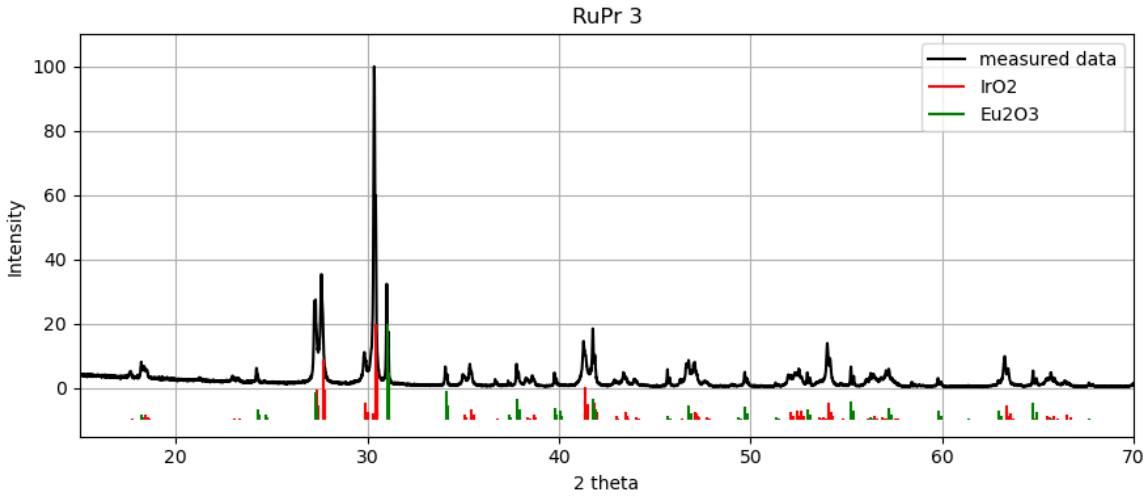

Crystal growth experiments:

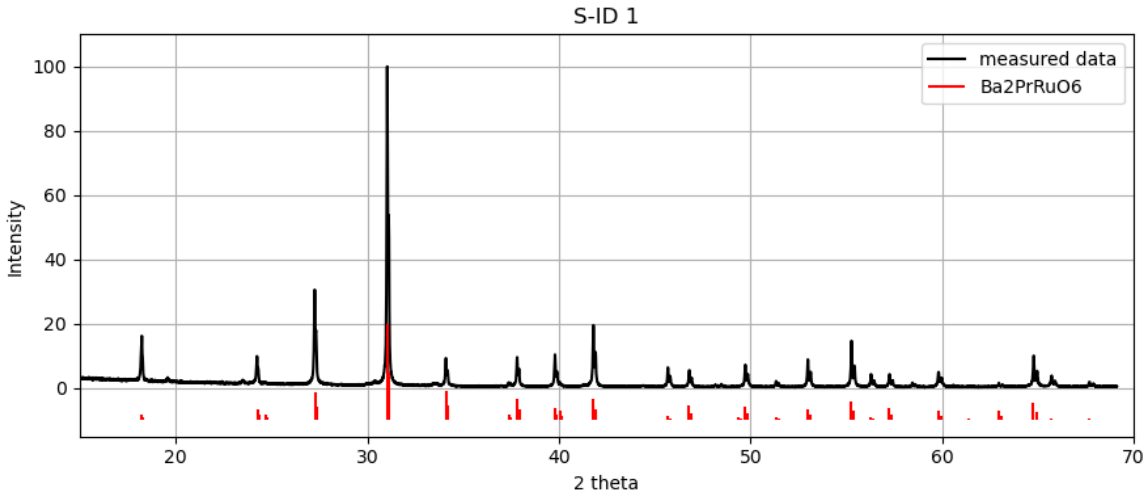

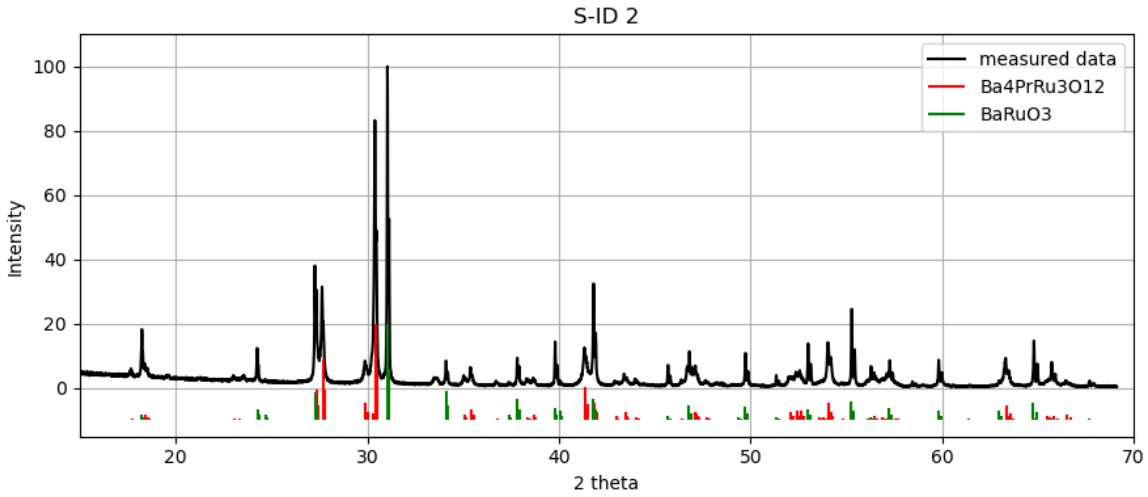
S-ID 2
measured data
Ba4PrRu3O12
BaRuO3
Intensity
2 theta
0
20
40
60
80
100
20
30
40
50
60
70

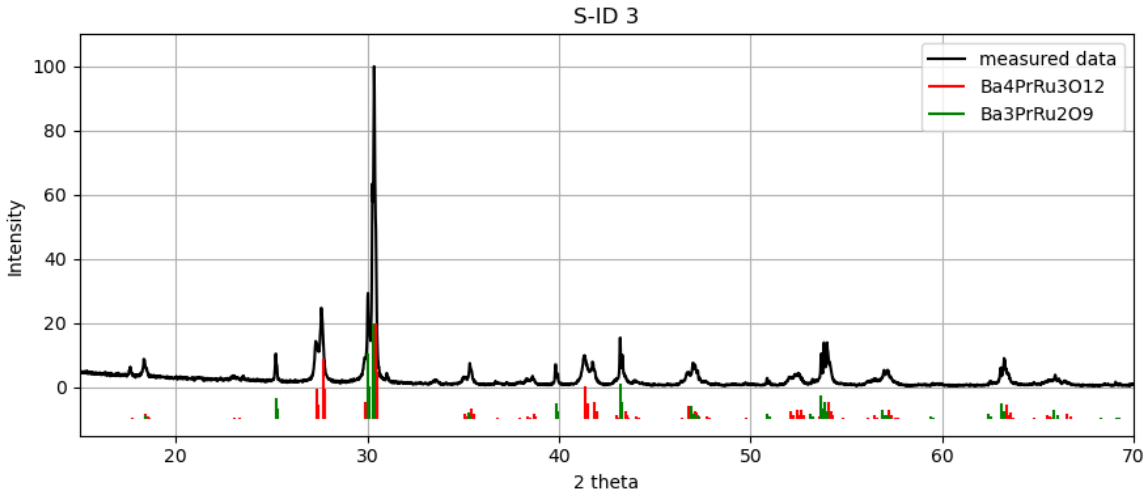
S-ID 3
measured data
Ba4PrRu3O12
Ba3PrRu2O9
Intensity
2 theta
0
20
40
60
80
100
20
30
40
50
60
70

$BaO - Ta_2O_5 - RuO_2$

Solid state reaction experiments:

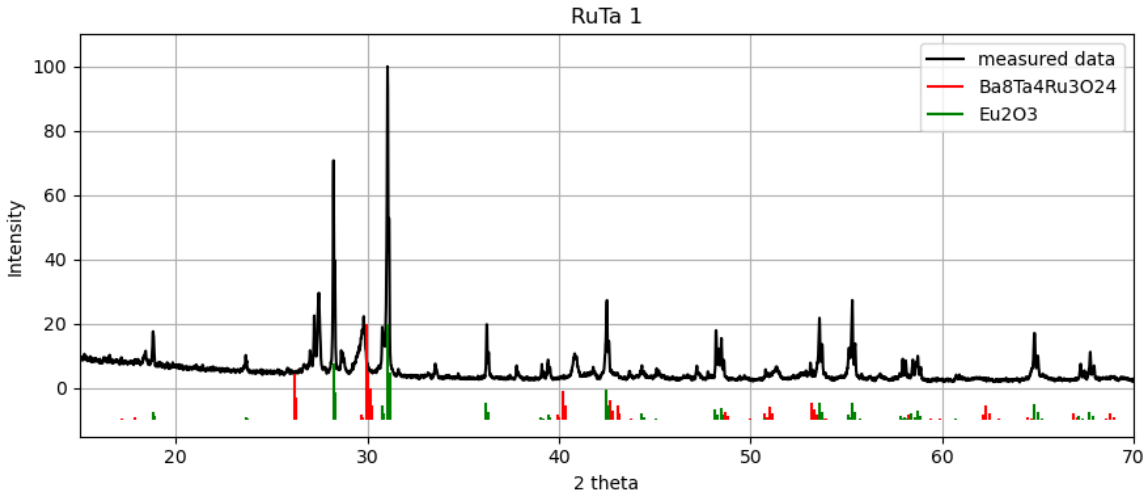

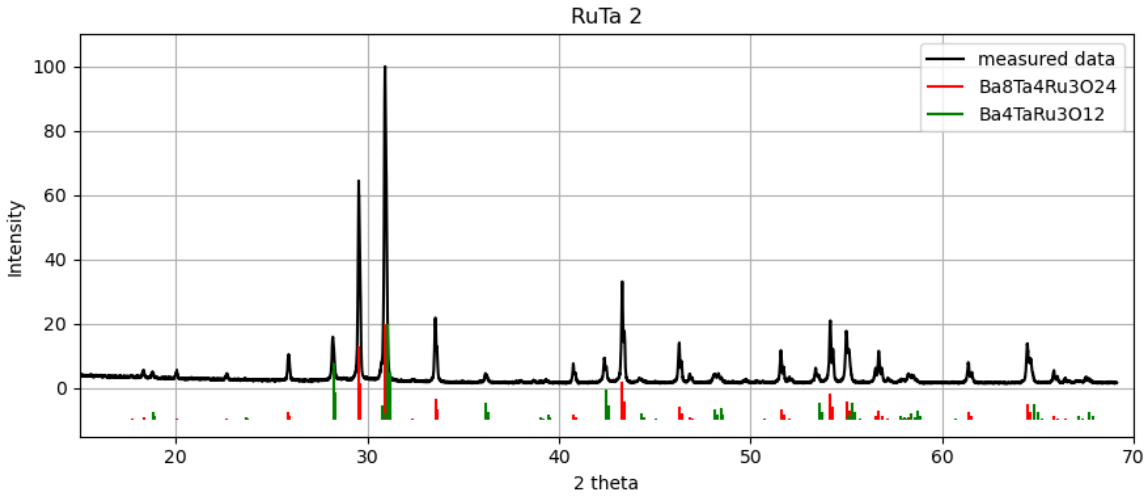

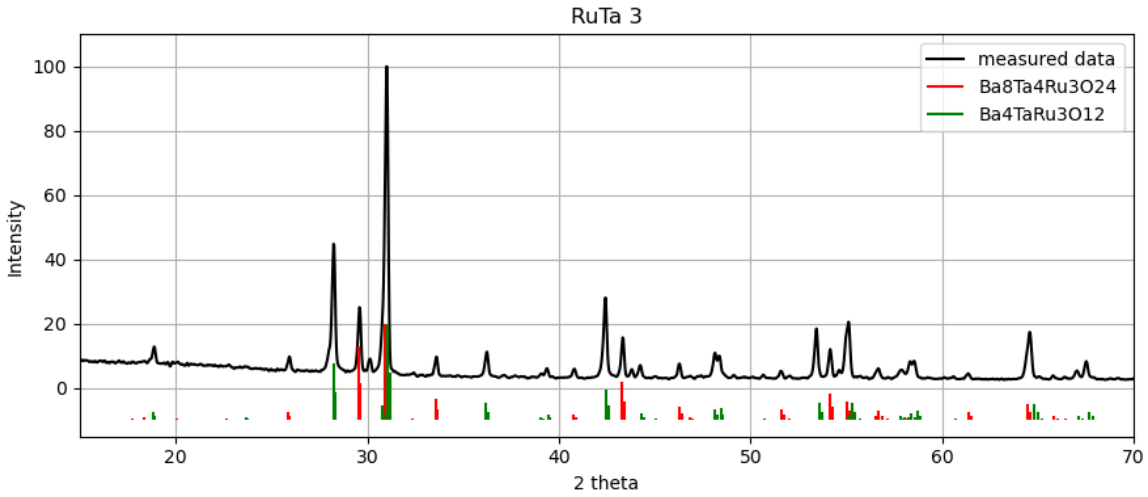
RuTa 3
measured data
Ba8Ta4Ru3O24
Ba4TaRu3O12
Intensity
2 theta

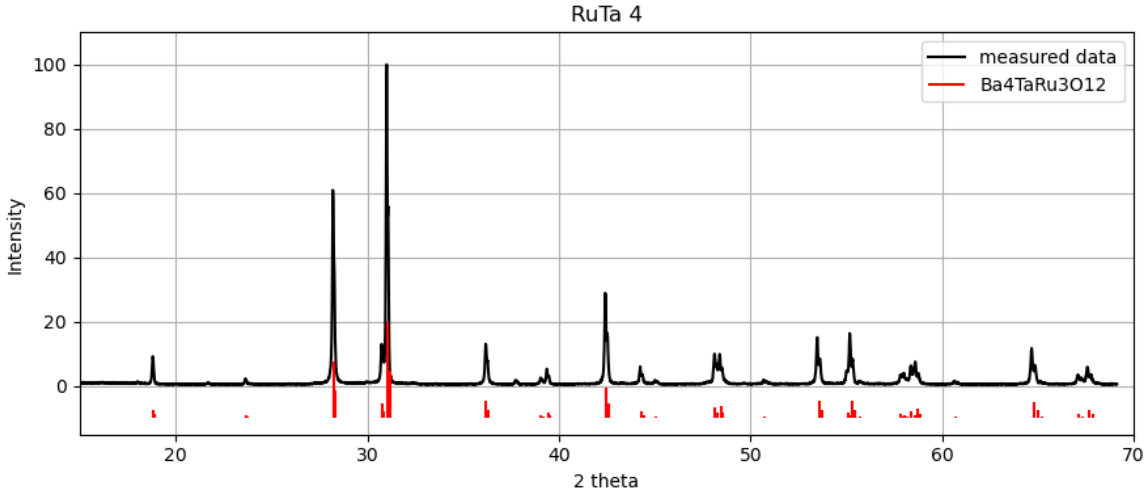
RuTa 4
measured data
Ba4TaRu3O12
Intensity
2 theta

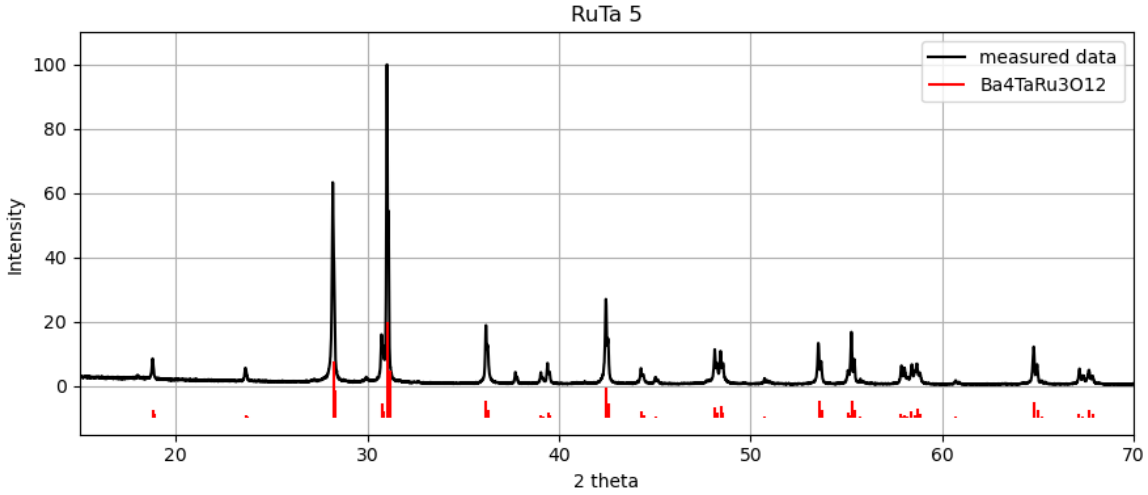
RuTa 5
measured data
Ba4TaRu3O12
Intensity
2 theta

Crystal growth experiments:

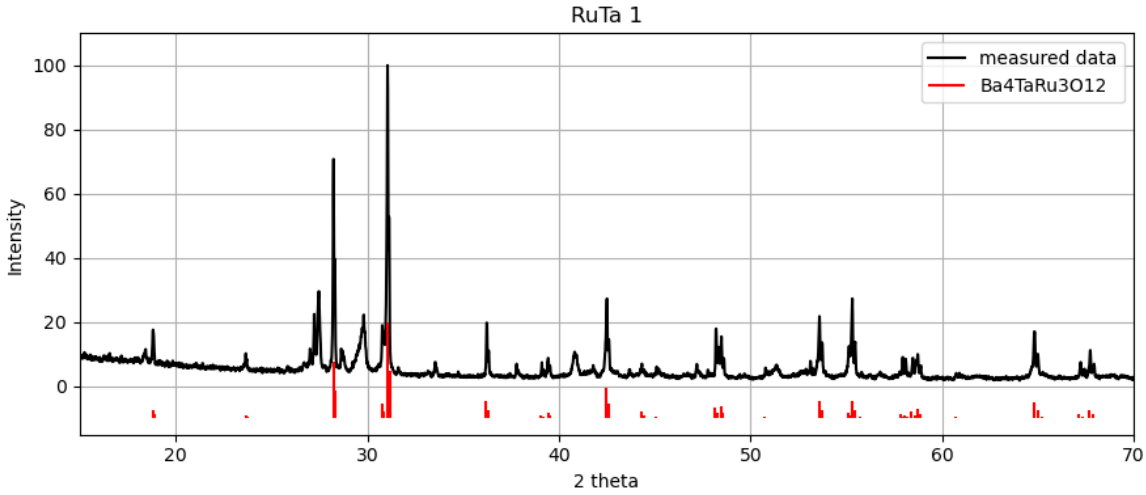

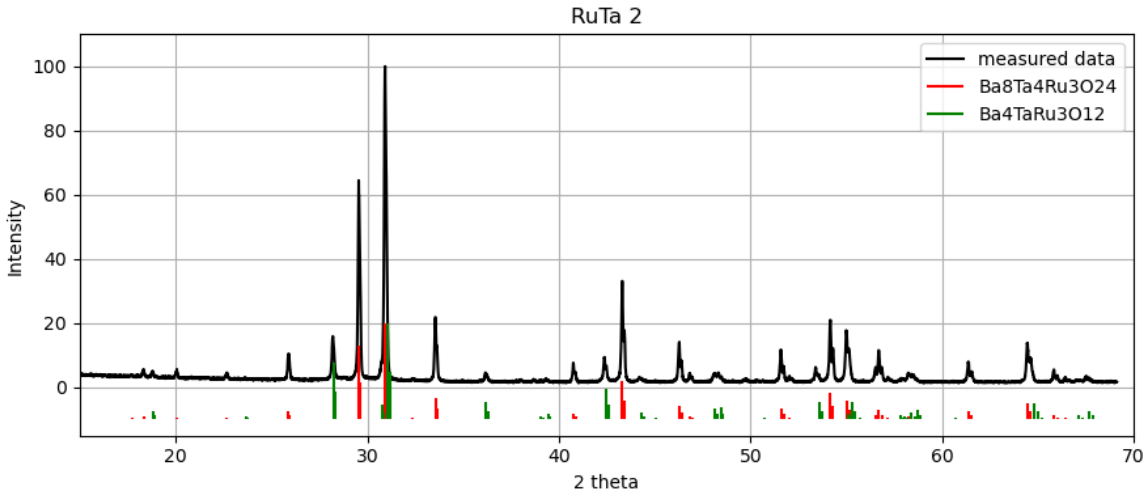

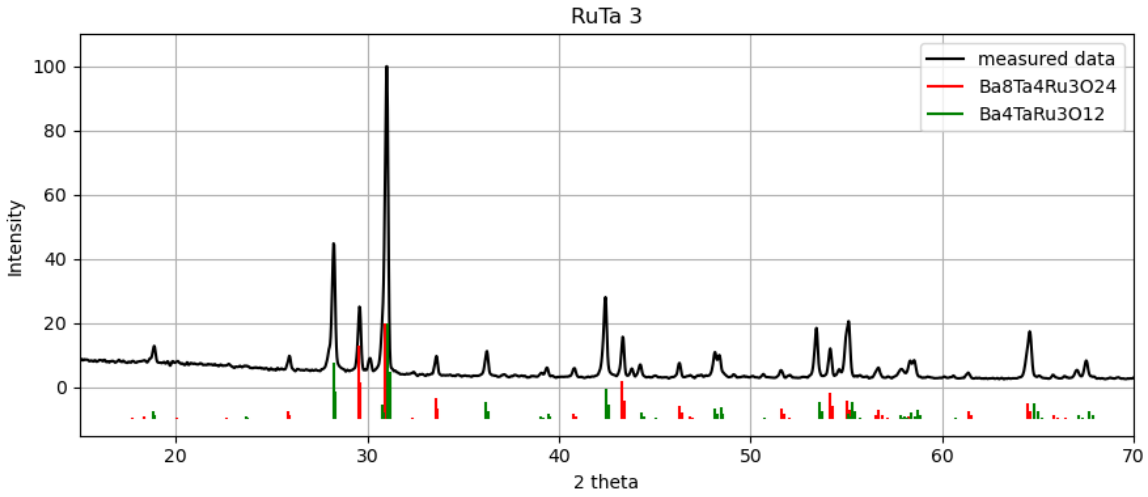
RuTa 3
measured data
Ba8Ta4Ru3O24
Ba4TaRu3O12
Intensity
2 theta

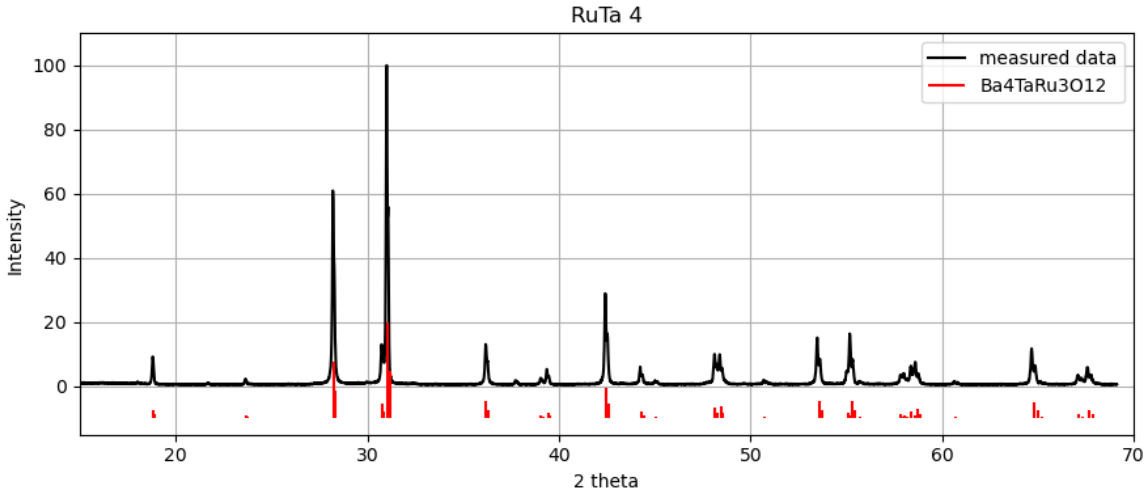
RuTa 4
measured data
Ba4TaRu3O12
Intensity
2 theta

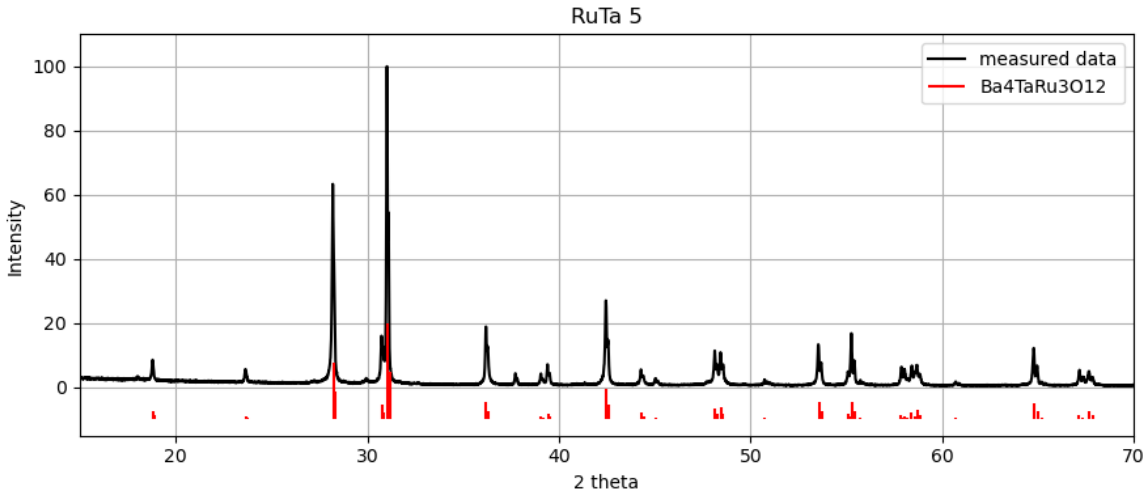
RuTa 5
measured data
Ba4TaRu3O12
Intensity
2 theta

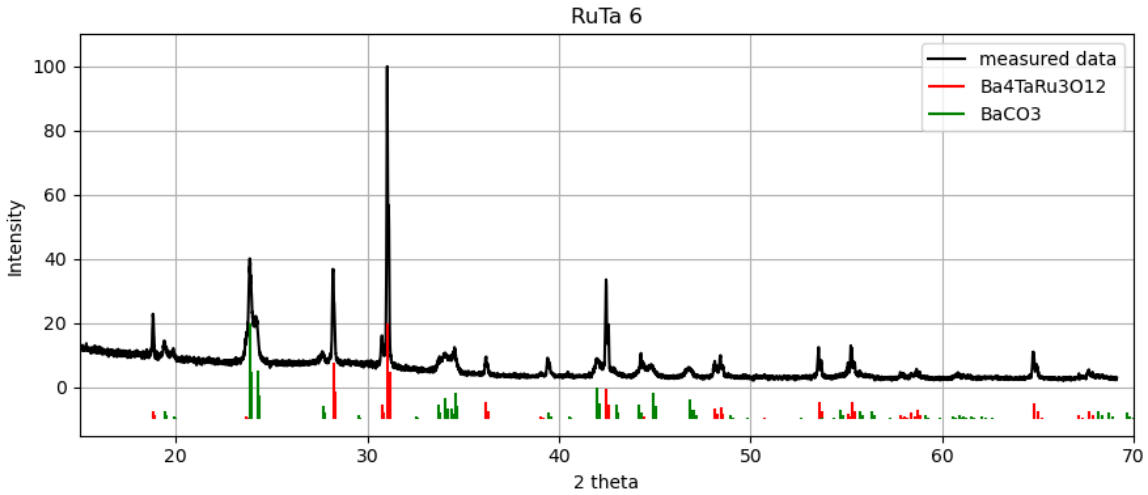
RuTa 6
measured data
Ba4TaRu3O12
BaCO3
Intensity
2 theta

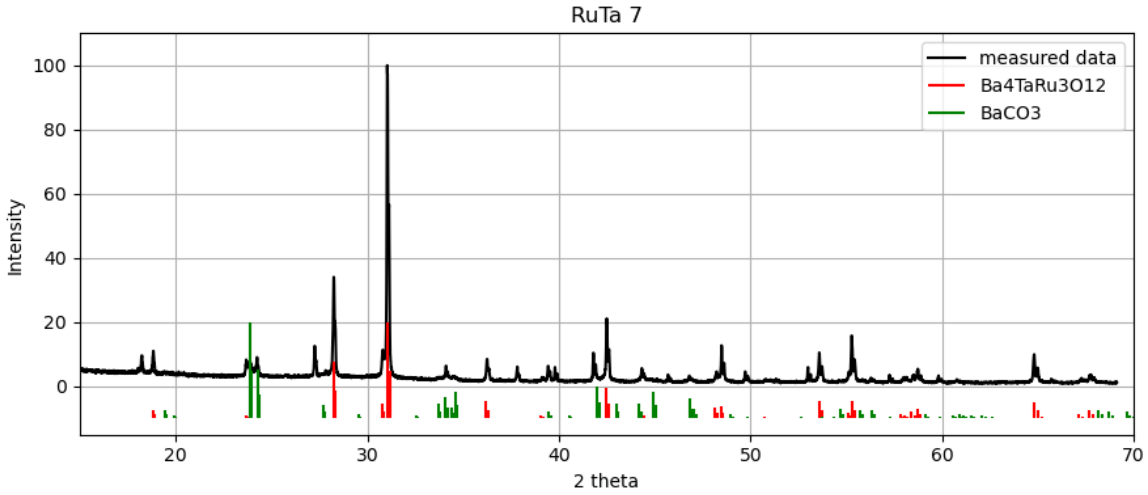
RuTa 7
measured data
Ba4TaRu3O12
BaCO3
Intensity
2 theta

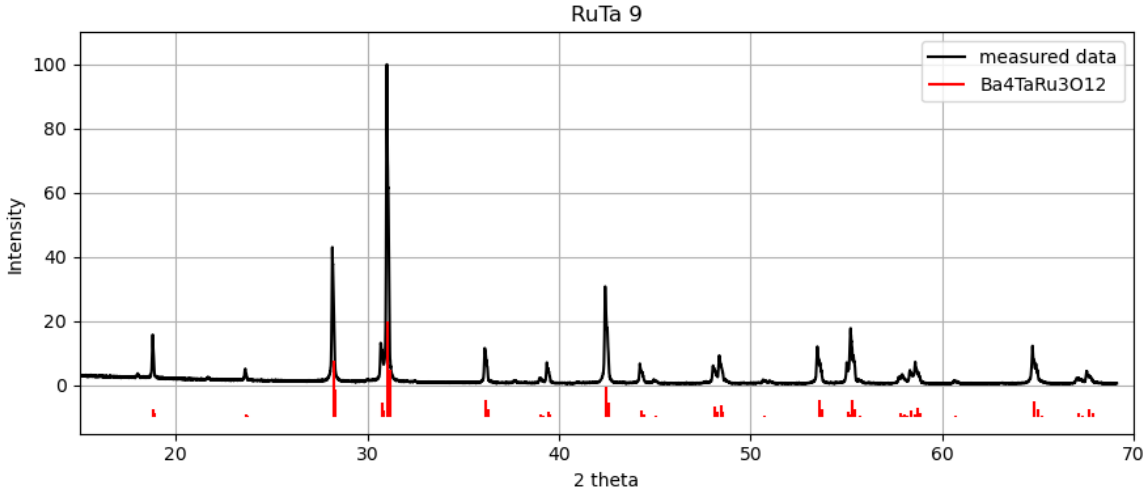
RuTa 9
measured data
Ba4TaRu3O12
Intensity
2 theta

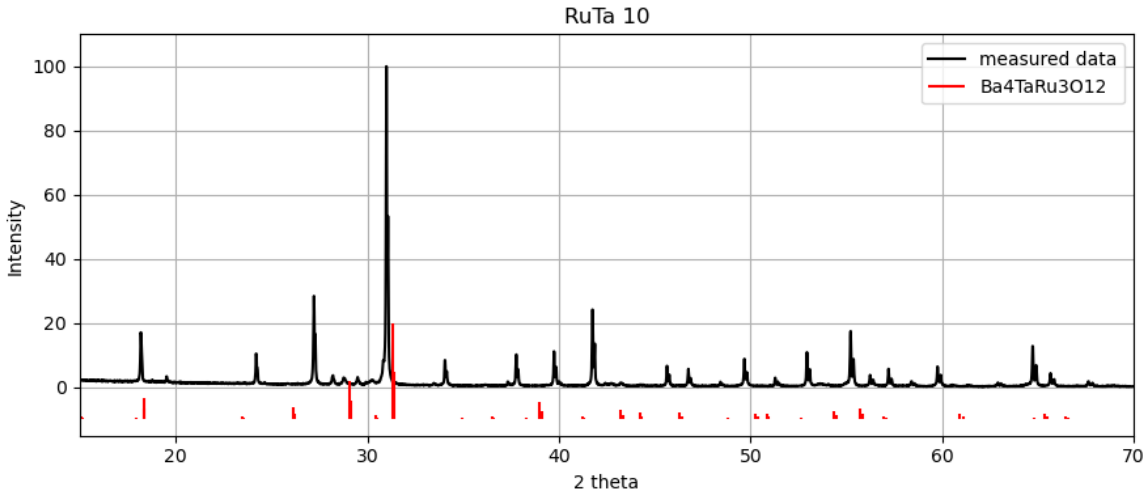
RuTa 10
measured data
Ba4TaRu3O12
Intensity
2 theta
0
20
40
60
80
100
20
30
40
50
60
70

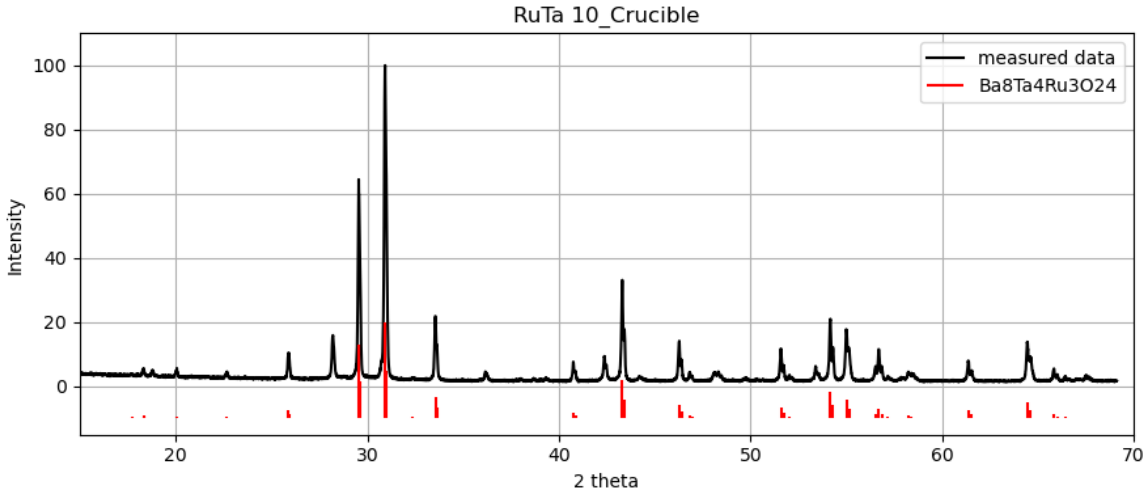
RuTa 10_Crucible
measured data
Ba8Ta4Ru3O24
Intensity
2 theta
0
20
40
60
80
100
20
30
40
50
60
70

$BaO - M_xO_y - RuO_2$
with $M_xO_y = Sc_2O_3, Y_2O_3, Tb_4O_7, Yb_2O_3$ and Lu_2O_3

Solid-State experiments:

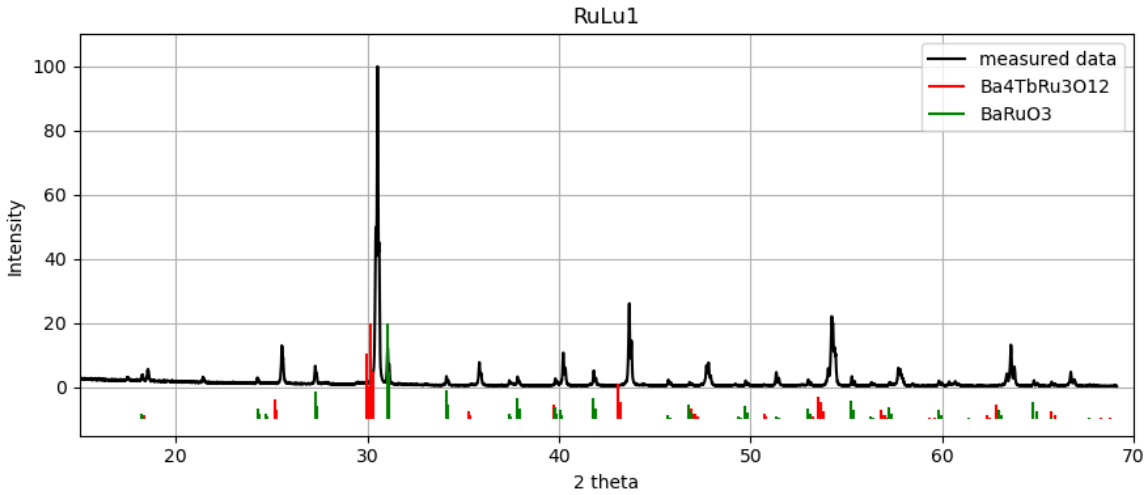

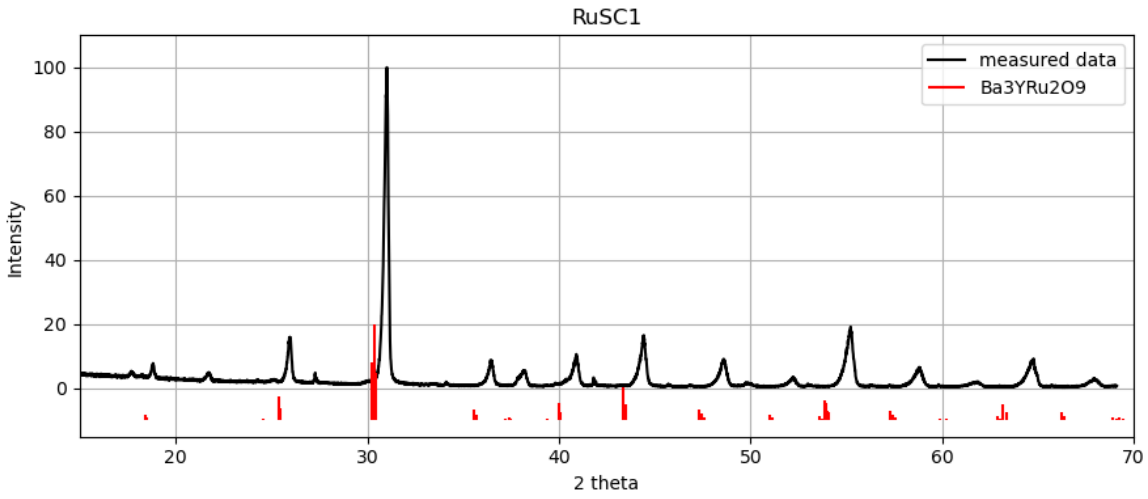

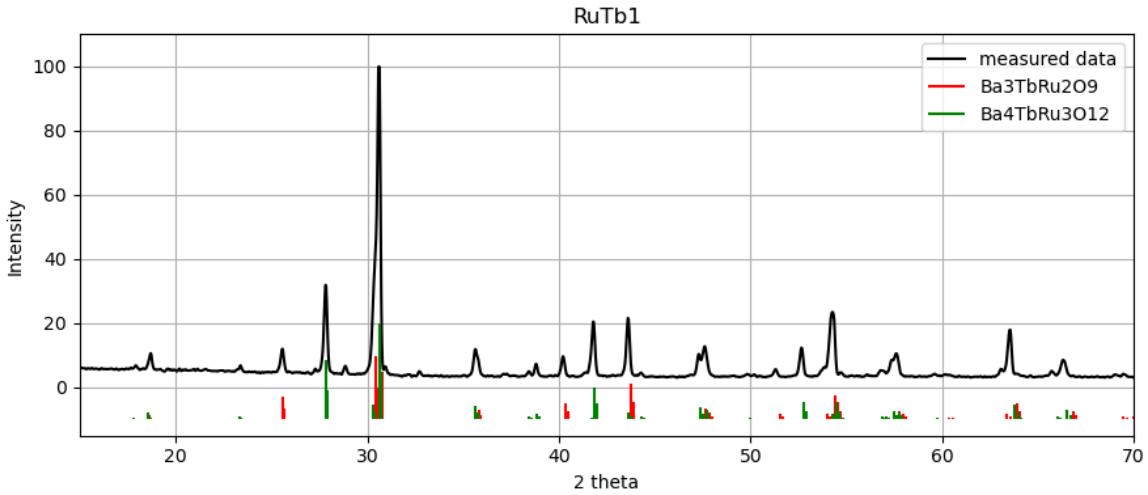
RuTb1
measured data
Ba3TbRu2O9
Ba4TbRu3O12
Intensity
2 theta

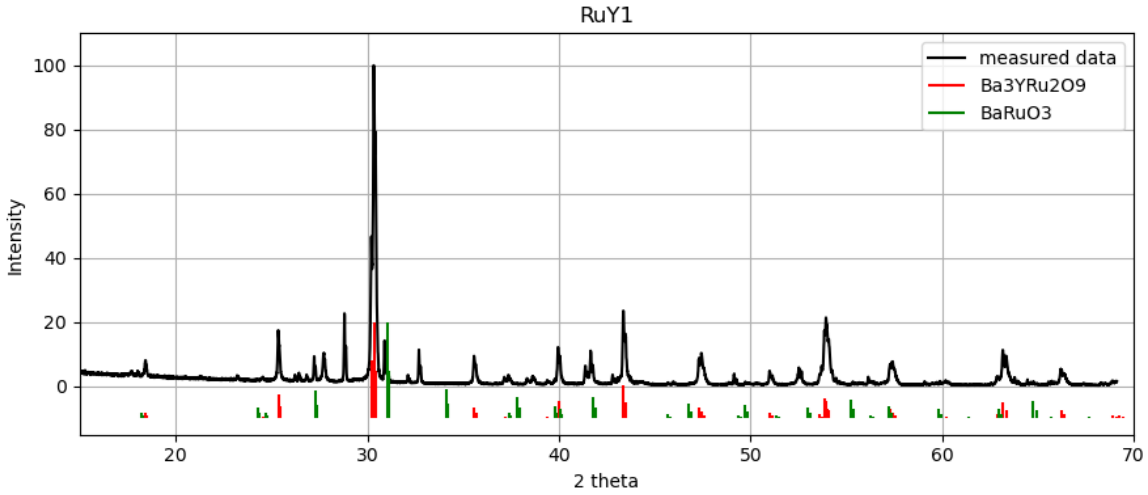
RuY1
measured data
Ba3YRu2O9
BaRuO3
Intensity
2 theta

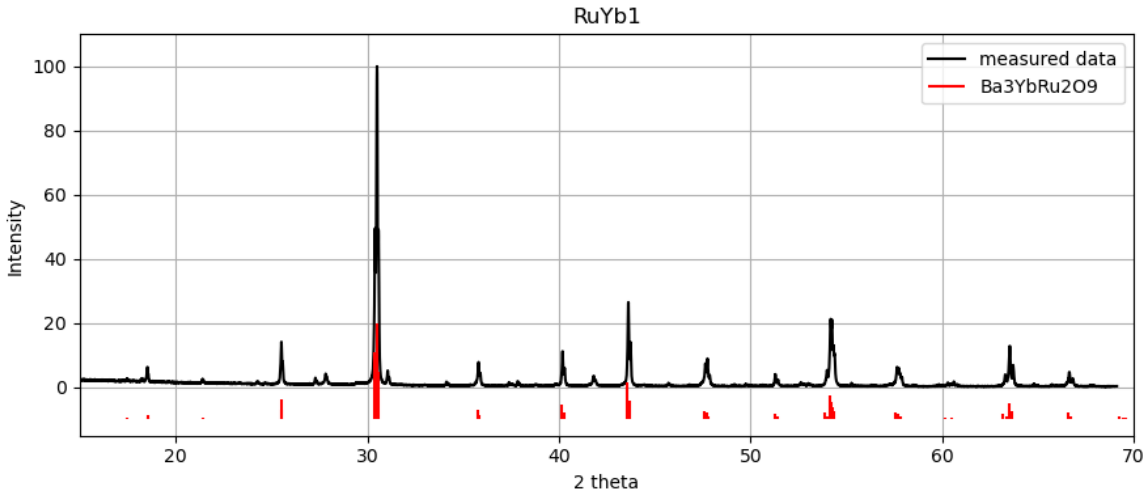
RuYb1
measured data
Ba3YbRu2O9
Intensity
2 theta

Crytsal growth experiments:

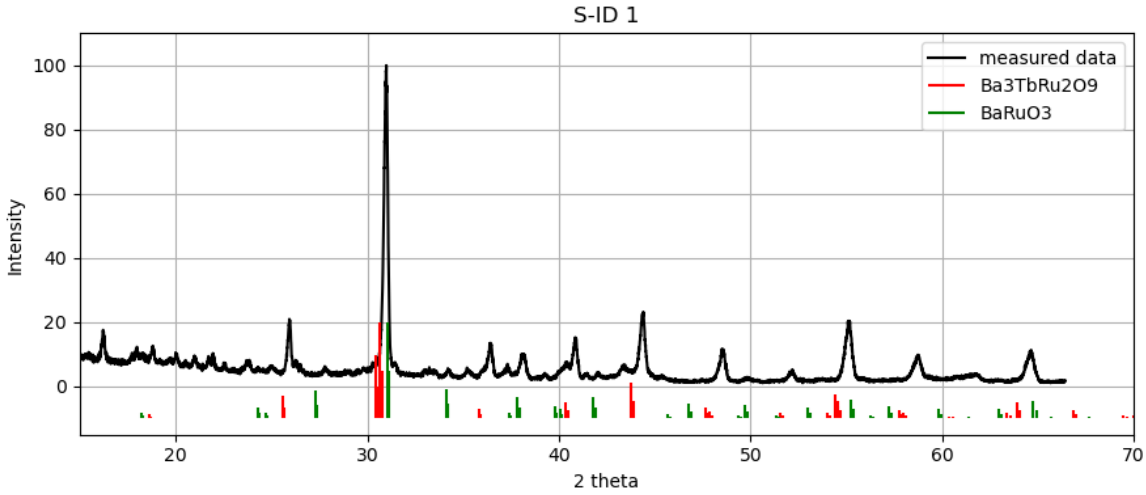

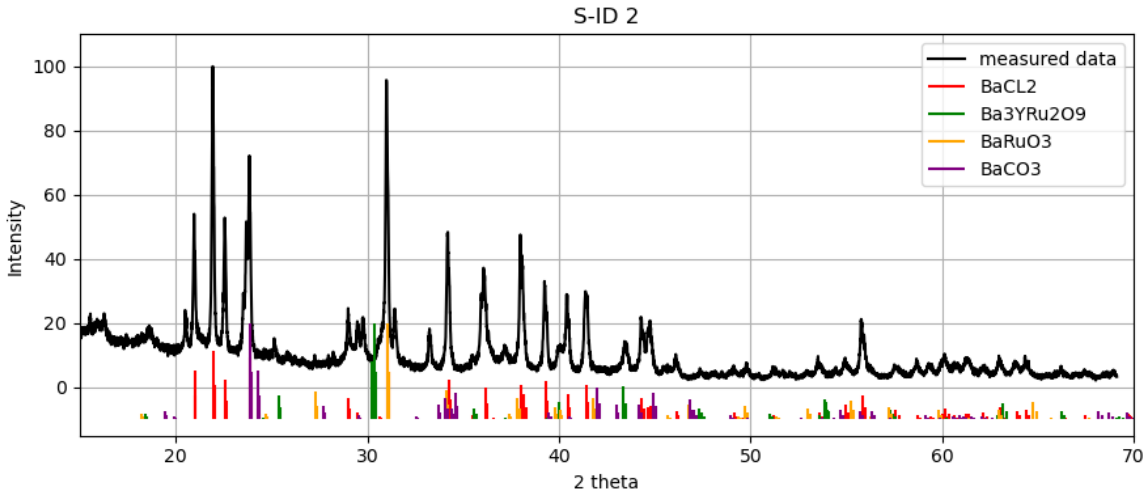

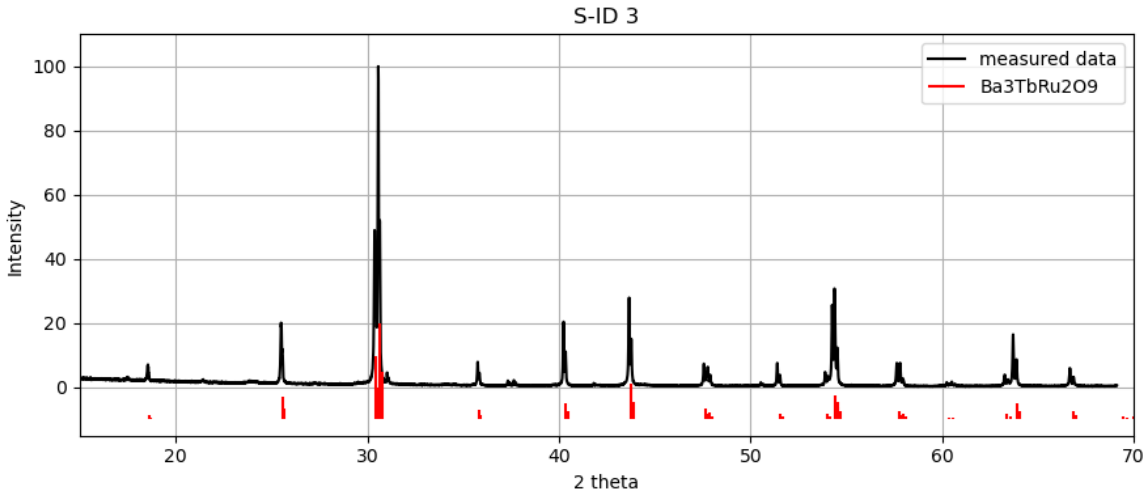
S-ID 3
measured data
Ba3TbRu2O9
Intensity
2 theta

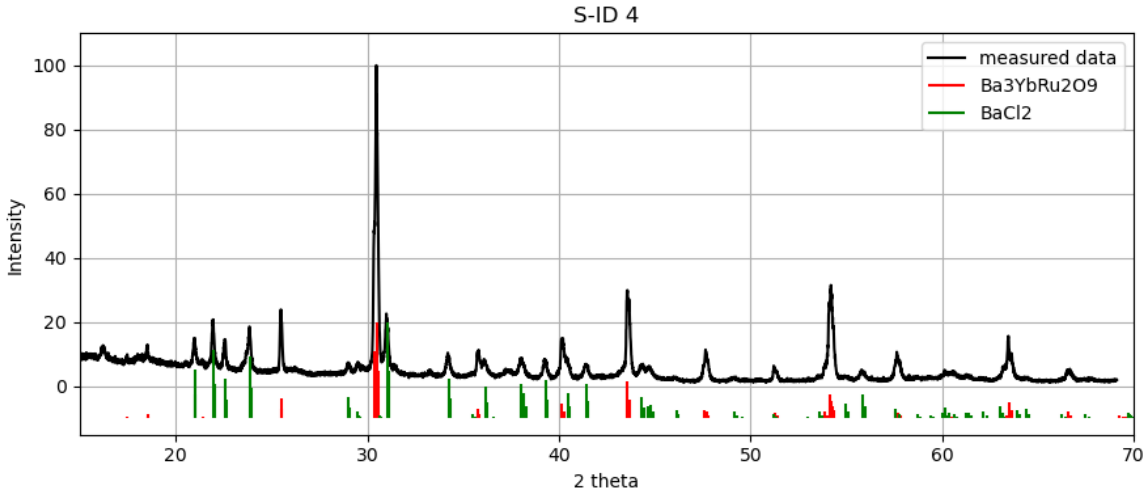
S-ID 4
measured data
Ba3YbRu2O9
BaCl2
Intensity
2 theta

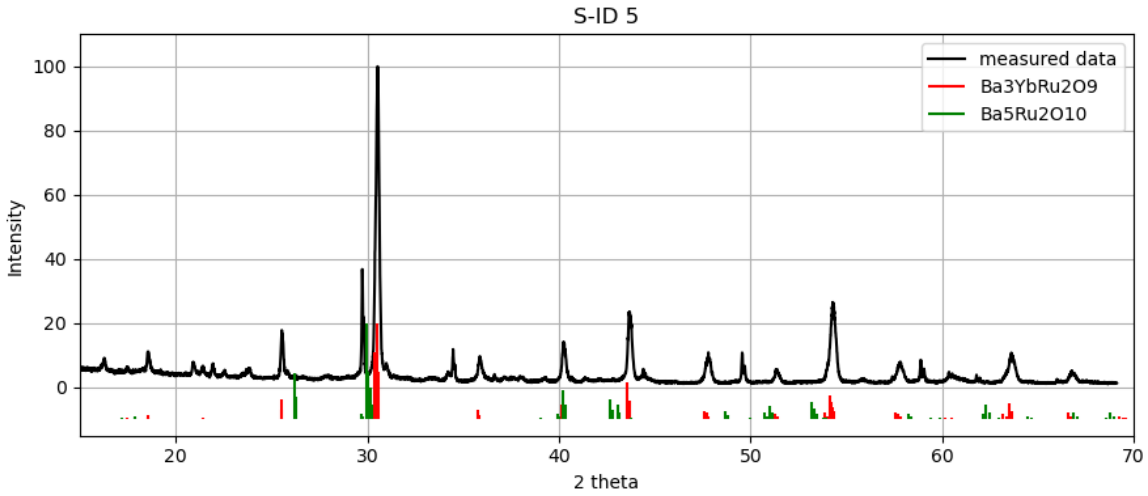
S-ID 5
measured data
Ba3YbRu2O9
Ba5Ru2O10
Intensity
2 theta

Appendix B

This appendix compiles the temperature-dependent powder X-ray diffraction (P-XRD) data described in Sections 6, 7, and 8. For each sample studied, representative measurements at 290 K and 12 K are shown. The respective plots display the experimental data (in black), the corresponding Rietveld fits (in red), and the difference curve (residual) below. This allows a clear assessment of the quality of the structural refinement.

For each dataset, the quality indicators R_{Bragg} and *GOF* are also provided, which quantitatively describe the agreement between experimental and calculated patterns.

The refined parameters include the lattice constants, atomic positions, sample displacement, crystallite size, and preferred orientation if observed. Physically reasonable values were assumed for the isotropic atomic displacement parameters (ADPs): 0.6 $Å^2$ for oxygen atoms and 0.4 $Å^2$ for metal atoms. For low-temperature measurements, the ADPs were set to 0.4 $Å^2$ for oxygen and 0.3 $Å^2$ for metals.

$Ba_3CeRu_2O_9$

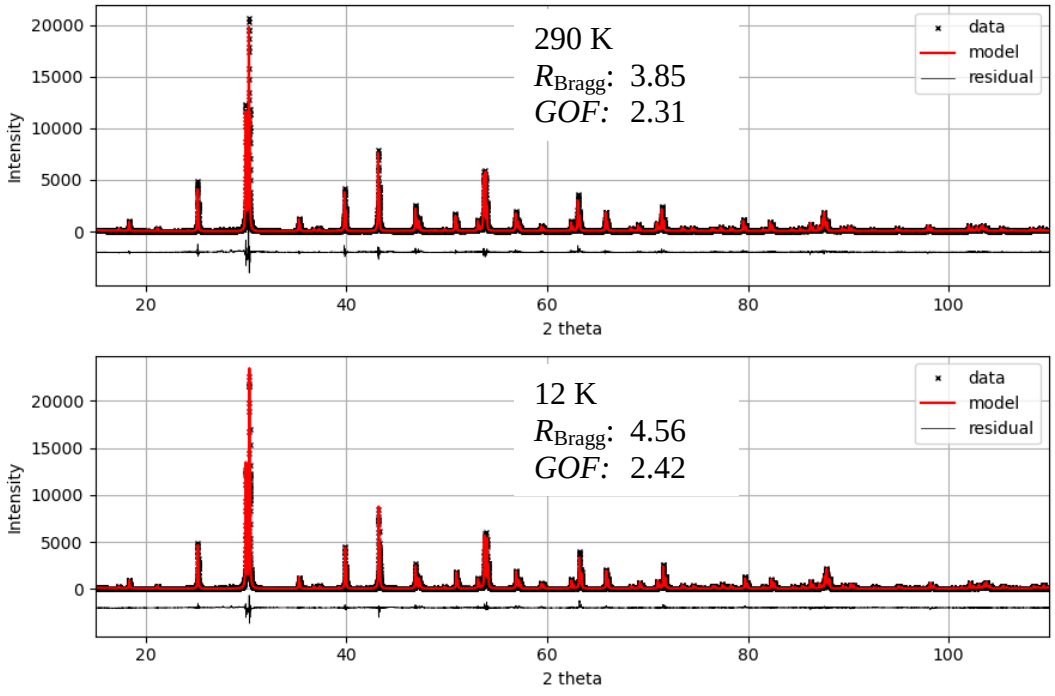

$Ba_4TaRu_3O_{12}$

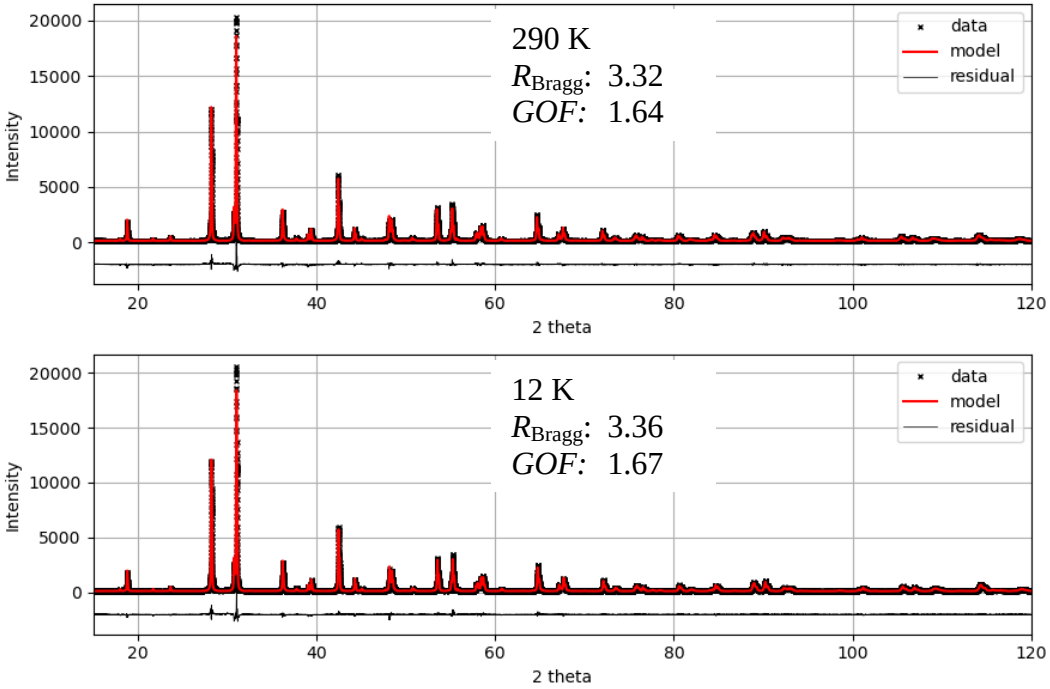

$Ba_4PrRu_3O_{12}$

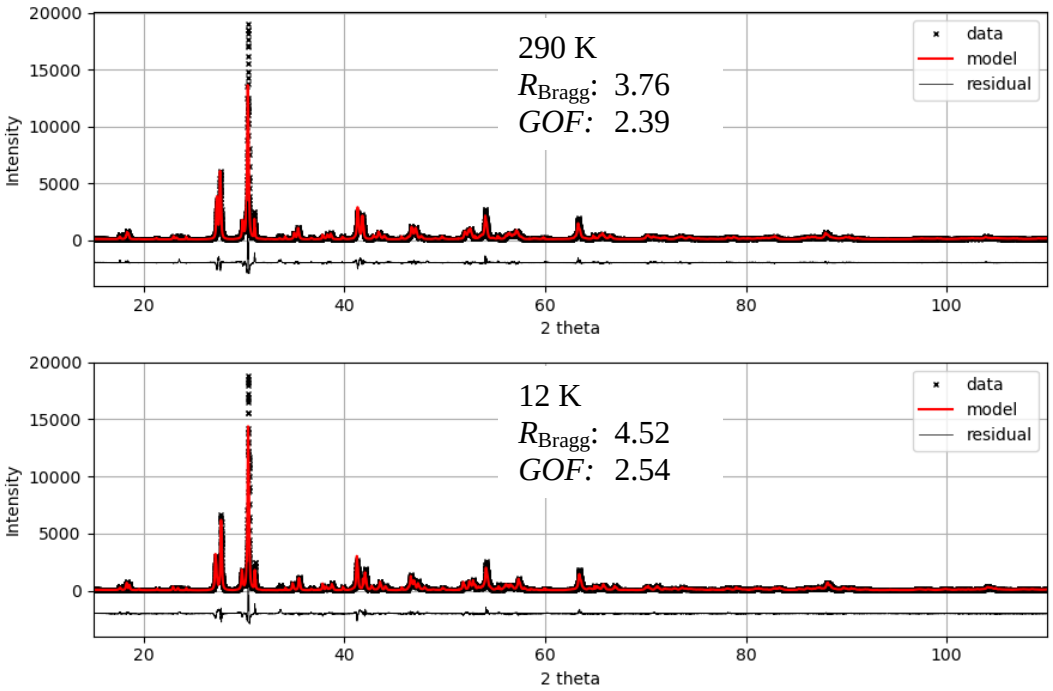

$Ba_4CeRu_3O_{12}$

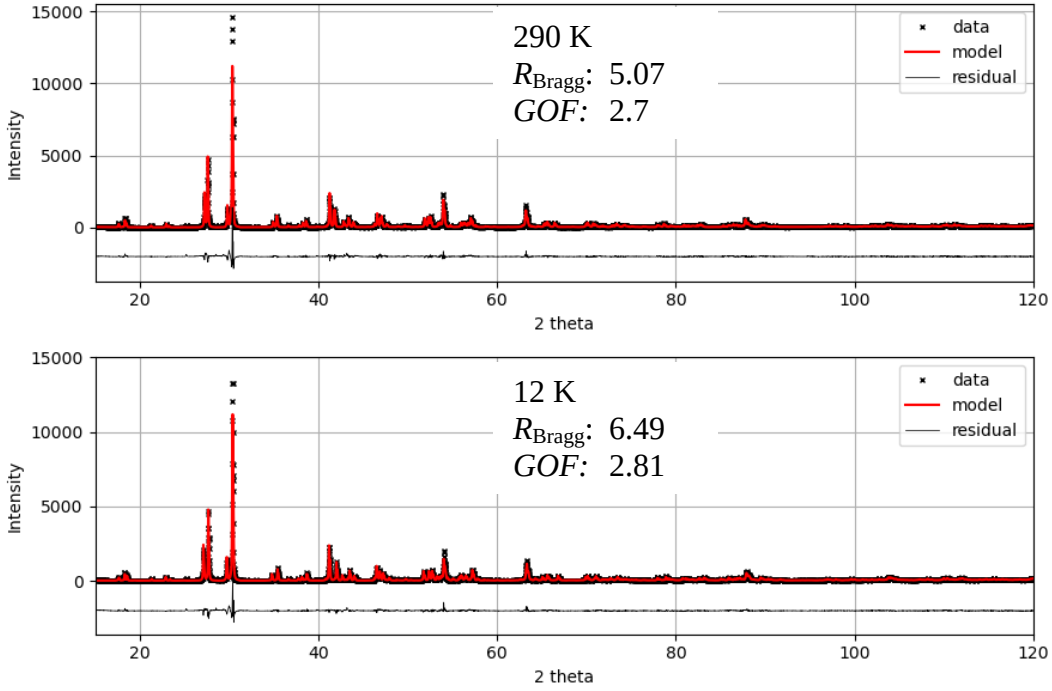

$Ba_4EuIr_3O_{12}$

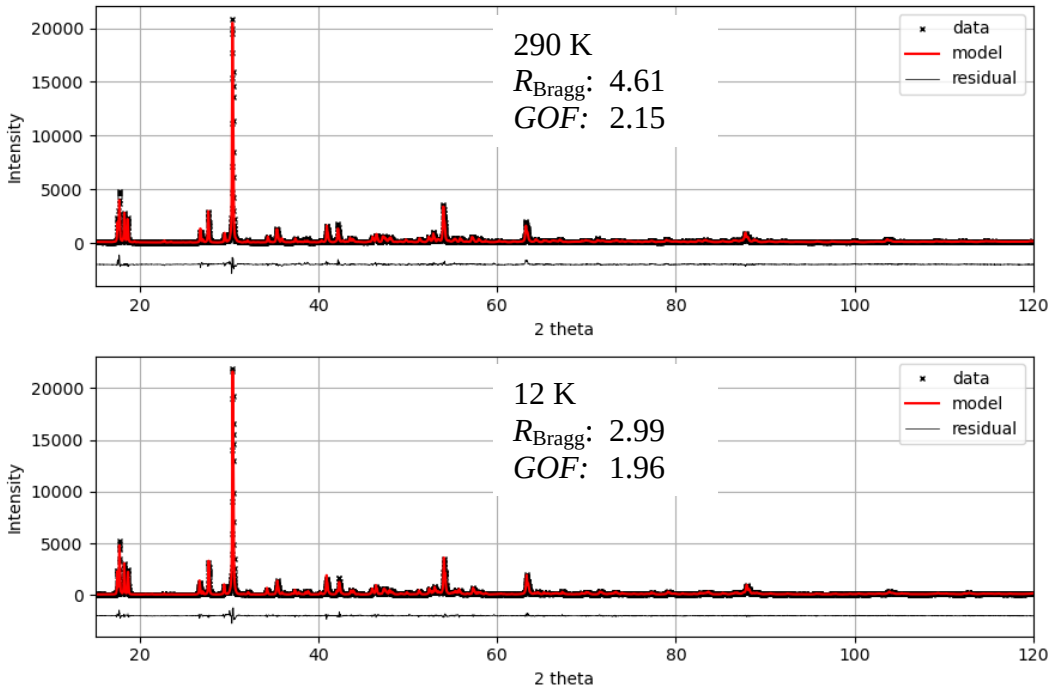

$Ba_4CeIr_3O_{12}$

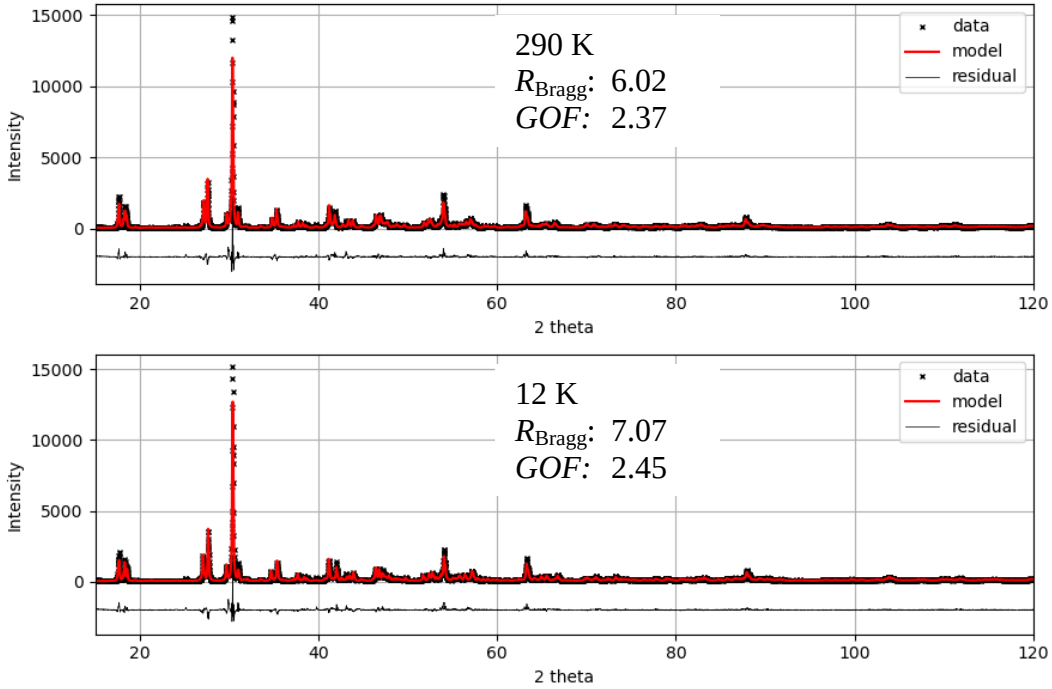

$Ba_4NbIr_3O_{12}$

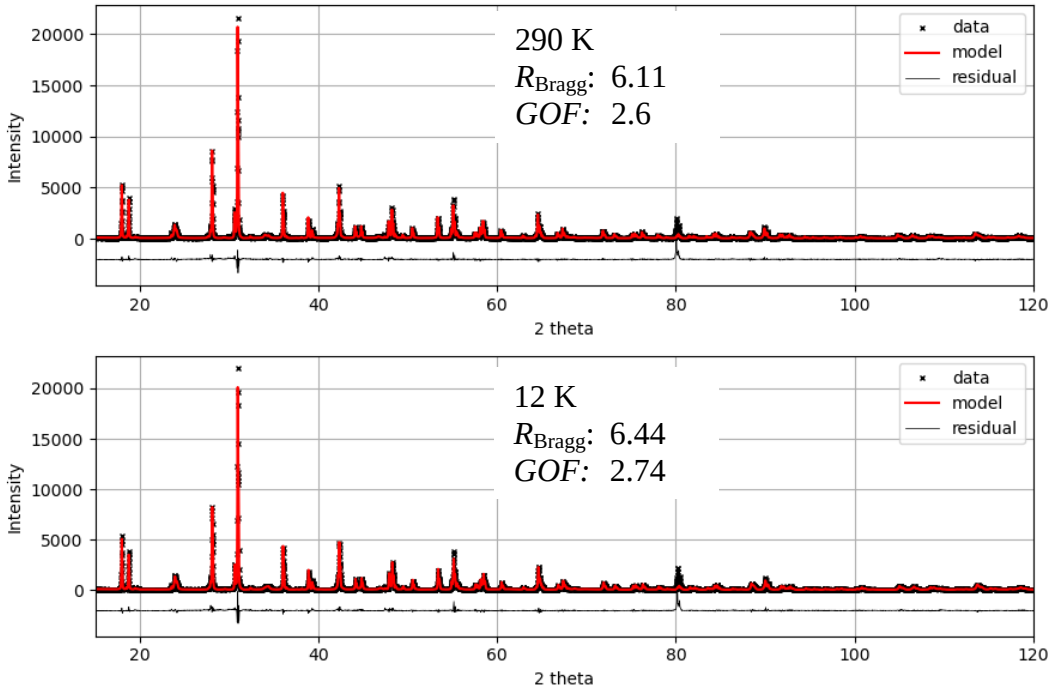

$Ba_4TaIr_3O_{12}$

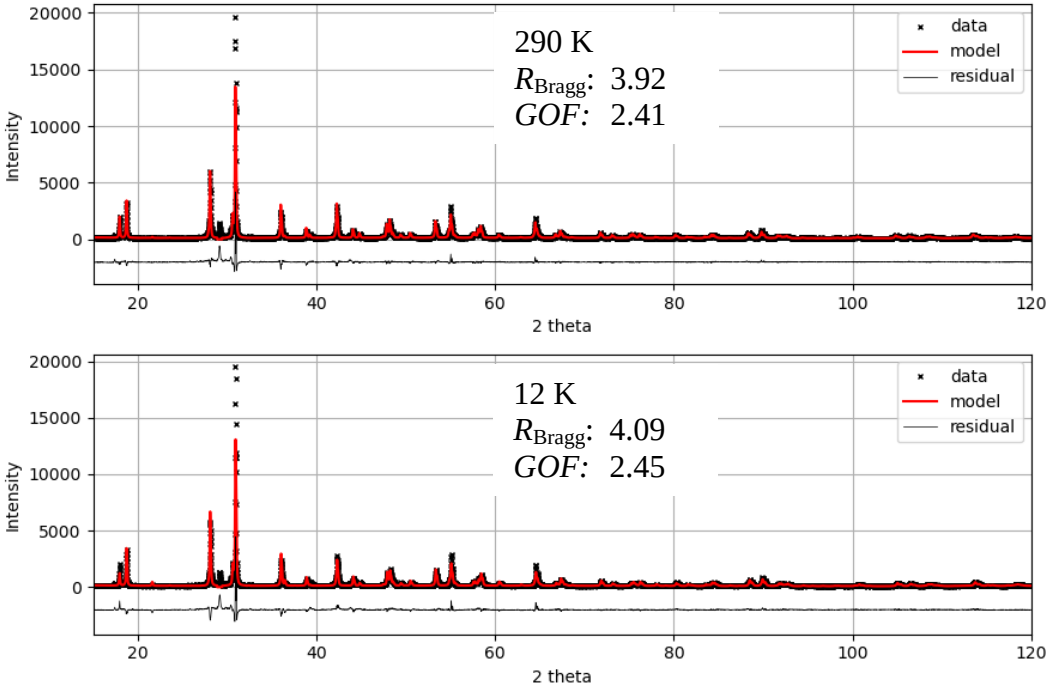

Ni_2InSbO_6:

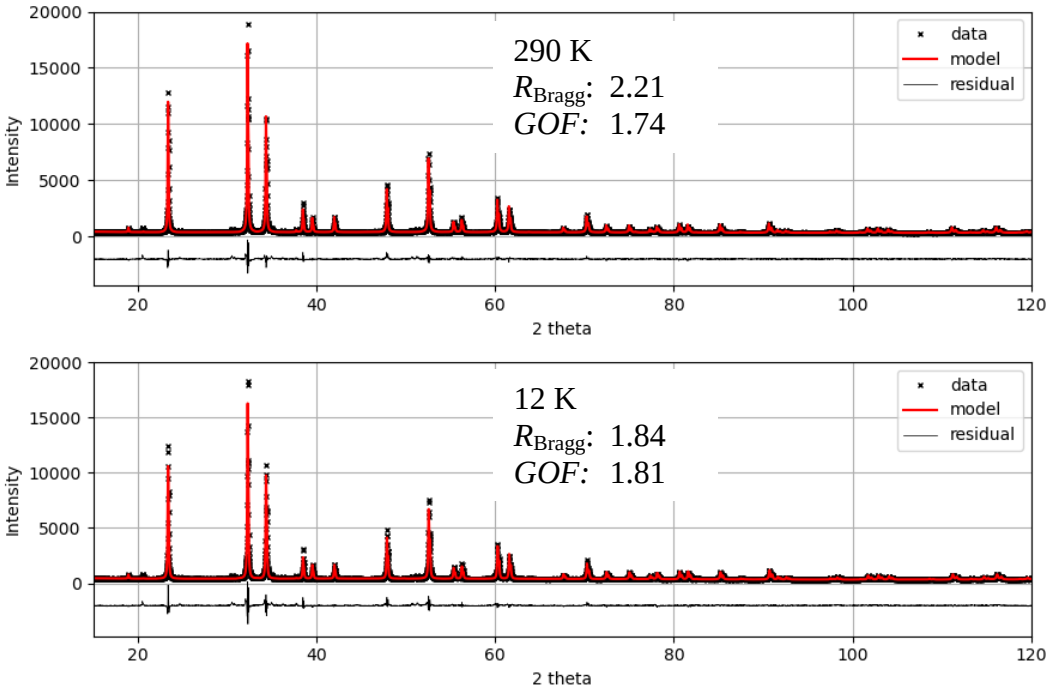

Appendix C

This appendix presents the final crystal structure models obtained from single-crystal X-ray diffraction (SC-XRD) data. The structural refinements were carried out using the crystallographic software Jana2020 as described in detail in Section 6 and 7.
Where the data quality permitted, anisotropic atomic displacement parameters (ADPs) were applied for oxygen atoms to enable the most accurate description of atomic positions and thermal motion within the crystal structure. All heavier atoms were refined anisotropically throughout.

Each table includes the fractional atomic coordinates, site occupancies, and displacement parameters of the respective phase.

$Ba_4TaIr_3O_{12}$: $R\bar{3}m$

Atom	Site	x	y	z	U_{eq}
Ir1	3b	0	0	0.5	0.00416(7)
Ir2	6c	0	0	0.411587(8)	0.00434(5)
Ta1	3a	0	0	0	0.00345(7)
Ba1	6c	0	0	0.285811(16)	0.00719(8)
Ba2	6c	0	0	0.129037(16)	0.00842(9)
O1	18h	0.4908(3)	0.5092(3)	0.12248(12)	0.0077(8)
O2	18h	0.5045(3)	0.4955(3)	0.29406(11)	0.0091(9)

Atom	U11	U22	U33	U12	U13	U23
Ir1	0.00431(8)	0.00431(8)	0.00386(11)	0.00216(4)	0	0
Ir2	0.00447(7)	0.00447(7)	0.00407(9)	0.00224(3)	0	0
Ta1	0.00351(8)	0.00351(8)	0.00332(11)	0.00176(4)	0	0
Ba1	0.00701(10)	0.00701(10)	0.00754(14)	0.00351(5)	0	0
Ba2	0.00767(10)	0.00767(10)	0.00993(17)	0.00384(5)	0	0
O1	0.0092(8)	0.0092(8)	0.0078(10)	0.007(1)	0.0000(4)	0.0000(4)
O2	0.0094(9)	0.0094(9)	0.0115(12)	0.0069(11)	-0.0030(5)	0.0030(5)

$Ba_4TaRu_3O_{12}$: $R\bar{3}m$

Atom	Site	Occ	x	y	z	Ueg
Ru1	3b	1	0	0	0.5	0.00293(10)
Ru2	6c	1	0	0	0.411757 (15)	0.00332(8)
Ta1	3a	0.734(4)	0	0	0	0.00347(8)
Ru3	3a	0.259(4)	0	0	0	0.00347(8)
Ba1	6c	1	0	0	0.128388(14)	0.00769(8)
Ba2	6c	1	0	0	0.286860(13)	0.00581(7)
O1	18h	1	0.4891(3)	0.5109(3)	0.12203(10)	0.0079(6)
O2	18h	1	0.5022(3)	0.4978(3)	0.29433(10)	0.0087(6)

Atom	U11	U22	U33	U12	U13	U23
Ru1	0.00248(12)	0.00248(12)	0.00382(18)	0.00124(6)	0	0
Ru2	0.00341(10)	0.00341(10)	0.00315(14)	0.00170(5)	0	0
Ta1	0.00318(10)	0.00318(10)	0.00405(13)	0.00159(5)	0	0
Ru3	0.00318(10)	0.00318(10)	0.00405(13)	0.00159(5)	0	0
Ba1	0.00627(10)	0.00627(10)	0.01054(14)	0.00314(5)	0	0
Ba2	0.00518(9)	0.00518(9)	0.00708(13)	0.00259(5)	0	0
O1	0.0070(6)	0.0070(6)	0.0125(9)	0.0057(7)	0.0005(3)	-0.0005(3)
O2	0.0065(6)	0.0065(6)	0.0144(11)	0.0042(7)	-0.0010(4)	0.0010(4)

$Ba_4CeRu_3O_{12}$: *C*2/*m*

Atom	Site	Occ	x	y	z	Ueg
Ru1_1	2c	1	0	0	-0.5	0.00335(14)
Ru1_2	4i	1	-0.16815(7)	0.5	-0.833516(14)	0.00761(13)
Ru2_1	4i	1	-0.00387(7)	0	-0.414073(14)	0.00453(11)
Ru2_2	4i	1	-0.17041(7)	0.5	-0.747396(14)	0.00437(11)
Ru2_3	4i	1	0.16207(8)	0.5	-1.080268(17)	0.01136(15)
Ce1_1	2a	1	0	0	0	0.00474(9)
Ce1_2	4i	1	-0.16970(6)	0.5	-0.332996(10)	0.00149(7)
Ba1_1	4i	1	0.00111(6)	0	-0.283888(12)	0.00914(10)
Ba1_2	4i	1	-0.16580(6)	0.5	-0.617080(12)	0.00976(10)
Ba1_3	4i	1	0.16763(7)	0.5	-0.950801(13)	0.01534(14)
Ba2_1	4i	1	0.00142(7)	0	-0.130621(13)	0.01420(13)
Ba2_2	4i	1	-0.16624(5)	0.5	-0.463587(11)	0.00784(10)
Ba2_3	4i	1	0.16595(7)	0.5	-0.796944(14)	0.01416(12)
O1_1	4i	1	0.0164(8)	0.5	-0.1287(4)	0.035(3)
O1_2	4i	1	-0.1521(5)	1	-0.46222(15)	-0.0006(8)
O1_3	4i	1	0.1776(5)	1	-0.79068(17)	0.0035(13)
O1_4	8j	1	-0.2448(4)	-0.2646(8)	0.12281(13)	0.0097(10)
O1_5	8j	1	-0.0788(4)	0.2313(7)	-0.54470(10)	0.0058(8)
O1_6	8j	1	-0.4088(4)	0.2347(8)	-0.20934(15)	0.0148(12)
O2_1	4i	1	0.0172(7)	0.5	-0.2938(3)	0.020(2)
O2_2	4i	1	-0.1552(6)	1	-0.62841(16)	0.0048(11)
O2_3	4i	1	0.1815(7)	1	-0.9612(3)	0.0196(18)
O2_4	8j	1	-0.2490(4)	-0.2581(6)	0.28915(14)	0.0091(9)
O2_5	8j	1	-0.0823(4)	0.2371(8)	-0.37907(12)	0.0109(10)
O2_6	8j	1	-0.4140(5)	0.2385(9)	-0.04504(14)	0.0152(13)

Atom	U11	U22	U33	U12	U13	U23
Ru2_1	0.00202(18)	0.00086(19)	0.00388(11)	0	-0.00252(16)	0
Ru2_2	0.0042(2)	0.0072(2)	0.00767(13)	0	-0.0013(2)	0
Ru2_3	0.0154(3)	0.0068(3)	0.01248(17)	0	-0.0089(3)	0
Ce1_1	0.00398(17)	0.0119(2)	0.01437(12)	0	-0.00050(18)	0
Ce1_2	0.00632(18)	0.00663(18)	0.01232(11)	0	0.00442(17)	0
Ba1_1	0.0165(3)	0.0097(2)	0.02011(15)	0	-0.0030(2)	0
Ba1_2	0.0165(3)	0.0105(2)	0.01625(14)	0	0.0017(2)	0

Ba1_3	0.00188(14)	0.0123(2)	0.01221(11)	0	-0.00019(16)	0
Ba2_1	0.0134(2)	0.0065(2)	0.01863(14)	0	-0.0015(2)	0

$Ba_3CeRu_2O_9$ *$P6_3mmc$*

Atom	Site	x	y	z	Ueg
Ru1	3b	1/3	2/3	0.16513(2)	0.00402(6)
Ce1	3a	0	0	0	0.00403(6)
Ba1	6c	0	0	0.25	0.00814(7)
Ba2	6c	1/3	2/3	0.90192(2)	0.00908(6)
O1	18h	0.4872(2)	0.9744(4)	0.25	0.0072(6)
O2	18h	0.17422(17)	0.3484(3)	0.41271(15)	0.0102(5)

Atom	U11	U22	U33	U12	U13	U23
Ru1	0.00387(7)	0.00387(7)	0.00434(10)	0.00193(4)	0	0
Ce1	0.00394(7)	0.00394(7)	0.00421(10)	0.00197(3)	0	0
Ba1	0.00838(8)	0.00838(8)	0.00766(12)	0.00419(4)	0	0
Ba2	0.00729(6)	0.00729(6)	0.01265(11)	0.00365(3)	0	0
O1	0.0106(7)	0.0012(7)	0.0066(8)	0.0006(4)	0	0
O2	0.0106(6)	0.0087(7)	0.0105(7)	0.0044(4)	0.0020(3)	0.0040(6)

$Ba_3EuRu_2O_9$ *$P6_3/mmc$*

Atom	Site	x	y	z	Ueg
Ru1	3b	1/3	2/3	0.16355 (3)	0.00347(8)
Eu1	3a	0	0	0	0.00419(8)
Ba1	6c	0	0	0.25	0.00770(9)
Ba2	6c	1/3	2/3	0.90314(3)	0.00975(8)
O1	18h	0.4855(2)	0.5145(3)	0.25	0.0062(8)
O2	18h	0.1757(2)	0.3513(5)	0.4107(2)	0.0108(6)

Atom	U11	U22	U33	U12	U13	U23
Ru1	0.00369(9)	0.00369(9)	0.00309(12)	0.00184(5)	0	0
Eu1	0.00440(9)	0.00440(9)	0.00373(12)	0.002237	0	0
Ba1	0.00867(11)	0.00867(11)	0.00576(15)	0.00434(6)	0	0
Ba2	0.00753(9)	0.00753(9)	0.01418(15)	0.00376(5)	0	0

$Ba_3EuRu_2O_9$ *$P6_3mc$*

Atom	Site	x	y	z	Ueg
Ru1	2b	1/3	2/3	0.16361(6)	0.00329(12)
Ru1_1	2b	-1/3	-2/3	-0.16363(6)	0.00412(12)
Eu1	2a	0	0	0	0.00429(4)
Ba1	2a	0	0	0.24978(8)	0.00766(5)
Ba2	2b	1/3	2/3	0.90310(4)	0.00752(10)
Ba2_1	2b	-1/3	-2/3	-0.90347(6)	0.01231(13)
O1	6c	0.4871(2)	0.9743(4)	0.2475(3)	0.0068(3)
O2	6c	0.1819(2)	0.3639(5)	0.4124(2)	0.0033(4)
O2_1	6c	-0.1708(3)	-0.3417(6)	-0.4065(3)	0.0150(8)

Atom	U11	U22	U33	U12	U13	U23
Ru1	0.00327(15)	0.00327(15)	0.00335(19)	0.00163(7)	0	0
Ru1_1	0.00454(16)	0.00454(16)	0.00329(19)	0.00227(8)	0	0
Eu1	0.00455(5)	0.00455(5)	0.00377(7)	0.00228(3)	0	0
Ba1	0.00857(6)	0.00857(6)	0.00583(9)	0.00583(9)	0	0
Ba2	0.00559(12)	0.00559(12)	0.01137(19)	0.00279(6)	0	0
Ba2_1	0.00978(15)	0.00978(15)	0.0174(2)	0.00489(8)	0	0

$Ba_3TbRu_2O_9$ *$P6_3/mmc$*

Atom	Site	x	y	z	Ueg
Ru1	3b	1/3	2/3	0.16374(3)	0.0022(1)
Tb1	3a	0	0	0	0.00228(9)
Ba1	6c	0	0	0.25	0.00355(11)
Ba2	6c	1/3	2/3	0.90636(3)	0.00377(9)
O1	18h	0.4854(3)	0.9708(7)	0.25	0.0017(6)
O2	18h	0.1713 (3)	0.3425 (5)	0.4150(2)	0.0057(6)

Atom	U11	U22	U33	U12	U13	U23
Ru1	0.00224(12)	0.00224(12)	0.00213(16)	0.00112(6)	0	0
Tb1	0.00219(12)	0.00219(12)	0.00246(15)	0.00110(6)	0	0
Ba1	0.00359(13)	0.00359(13)	0.00347(18)	0.00179(7)	0	0
Ba2	0.00338(11)	0.00338(11)	0.00456(14)	0.00169(6)	0	0

$Ba_3TbRu_2O_9$ *$P6_3mc$*

Atom	Site	x	y	z	Ueg
Ru1	2b	1/3	2/3	0.16310(5)	0.00250(15)
Ru1_1	2b	-1/3	-2/3	-0.16441(6)	0.00253(16)
Tb1	2a	0	0	0.00050(4)	0.00208(5)
Ba1	2a	0	0	0.25027(8)	0.00378(6)
Ba2	2b	1/3	2/3	0.90636(4)	0.00495(11)
Ba2_1	2b	-1/3	-2/3	-0.90638(5)	0.00317(10)
O1	6c	0.4870(2)	0.9740(4)	0.2488(4)	0.0038(3)
O2	6c	0.1643(3)	0.3286(5)	0.4126(3)	0.0077(5)
O2_1	6c	-0.1789(2)	-0.3578(5)	-0.4171(2)	0.0001(3)

Atom	U11	U22	U33	U12	U13	U23
Ru1	0.00333(14)	0.00333(14)	0.0008(3)	0.00167(7)	0	0
Ru1_1	0.00197(14)	0.00197(14)	0.0036(4)	0.00098(7)	0	0
Tb1	0.00212(6)	0.00212(6)	0.00200(8)	0.00106(3)	0	0
Ba1	0.00381(7)	0.00381(7)	0.00371(10)	0.00191(4)	0	0
Ba2	0.00520(11)	0.00520(11)	0.0045(2)	0.00260(6)	0	0
Ba2_1	0.00199(9)	0.00199(9)	0.0055(2)	0.00099(5)	0	0

$Ba_3YRu_2O_9$ *$P6_3/mmc$*

Atom	Site	x	y	z	Ueg
Ru1	3b	1/3	2/3	0.16253(2)	0.00456(6)
Y1	3a	0	0	0	0.00449(9)
Ba1	6c	0	0	0.25	0.00838(7)
Ba2	6c	1/3	2/3	0.90616(2)	0.00986(6)
O1	18h	0.48593(19)	0.9719(4)	0.25	0.0078(5)
O2	18h	0.17460 (16)	0.3492 (3)	0.41196(15)	0.0118(4)

Atom	U11	U22	U33	U12	U13	U23
Ru1	0.00455(7)	0.00455(7)	0.00457(10)	0.00228(4)	0	0
Y1	0.00491(11)	0.00491(11)	0.00367(16)	0.00245(6)	0	0
Ba1	0.00900(9)	0.00900(9)	0.00714(11)	0.00450(4)	0	0
Ba2	0.00819(7)	0.00817(7)	0.01319(11)	0.00410(4)	0	0
O1	0.0117(6)	0.0012(6)	0.0070(7)	0.0006(3)	0	0
O2	0.00123(5)	0.0104(6)	0.0119(6)	0.0052(3)	0.0025(3)	0.0051(5)

$Ba_3YbRu_2O_9$ *$P6_3/mmc$*

Atom	Site	x	y	z	Ueg
Ru1	3b	1/3	2/3	0.16374(3)	0.0022(1)
Yb1	3a	0	0	0	0.00228(9)
Ba1	6c	0	0	0.25	0.00355(11)
Ba2	6c	1/3	2/3	0.90636(3)	0.00377(9)
O1	18h	0.4854(3)	0.9708(7)	0.25	0.0017(6)
O2	18h	0.1713 (3)	0.3425 (5)	0.4150(2)	0.0057(6)

Atom	U11	U22	U33	U12	U13	U23
Ru1	0.00224(12)	0.00224(12)	0.00213(16)	0.00112(6)	0	0
Yb1	0.00219(12)	0.00219(12)	0.00246(15)	0.00110(6)	0	0
Ba1	0.00359(13)	0.00359(13)	0.00347(18)	0.00179(7)	0	0
Ba2	0.00338(11)	0.00338(11)	0.00456(14)	0.00169(6)	0	0
O1	0.0020(7)	-0.0001(8)	0.0026(9)	-0.0001(4)	0	0
O2	0.0052(7)	0.0058(9)	0.0063(8)	0.0029(5)	0.0006(3)	0.0012(6)

Appendix D

The following list shows the thermodynamic data of all species considered in the calculations of the CVT reaction attempts during the mathematical computations. All data were taken from Binnewiese et al. [85]

Species	**$\Delta_F H$ [kJ/mol]**	**S° [J/mol*K]**	**C_P [J/mol*K]**			
			A	**B**	**C**	**D**
Cl_2 (g)	0	223.1	36.61	1.08	-0.27	
Cl_2In_2 (g)	-232	362.6	97.4			
Cl_2Ni (g)	-70.2	298.2	68.29	-0.97	-0.66	
Cl_2O (g)	81	271.7	47.91			
Cl_3In (g)	-376.3	341.4	82.63	0.28	-0.54	
Cl_3Sb (g)	-313.1	339.1	82.38	0.7	-0.52	
Cl_5Sb (g)	-388.4	401.8	131-75	0-67	-1.72	
Cl_6In_2 (g)	-888.9	529	182.16	0.44	-0.81	
ClIn (g)	-71.6	248.3	16.13			
ClSb (g)	-10.7	247	35.5			
In (g)	246.4	173.8	22.69	2.36	-0.24	
In (s)	0	57.8	10.96	39.85	-0.35	
In_2O (g)	-65.7	298.3	49.8			
In_2O_3 (s)	-925.8	104.2	122.69	8.1	-2.2	
$InCl_2$ (g)	-222.087	312	34.125			
$InCl_2$ (s)	-362.7	122.2	58.58	50.21		
$InCl_3$ (s)	-537.2	141	78.66	55.65		
InSb (s)	-30.5	87.1	44.77	15.06		
Ni (g)	430	182.2	26.77	-2.04	-0.29	0.18
Ni (s)	0	29.9	19.36	22.46		0.02
NiCl (g)	179.912	251.405	15.34			
NiO (g)	309.6	241.4	39.82	1.54	-0.57	
NiO (s)	-239.7	38	-6.32	131.24	1.02	
NiSb (s)	-83.68	78.241	29.701			
O_2 (g)	0	205.174	27.298	3.266	0.502	
Sb (g)	265.5	180.3	20.79			

Sb (s)	0	45.5	30.51	-15.5	-0.2	18.02
Sb_2 (g)	231.2	254.9	37.41		-0.1	
Sb_2O_3 (s)	-720	110.5	79.968	71.694		
Sb_2O_5 (s)	-993.7	124.9	141.33	-3.73	-2.01	
Sb_4 (g)	206.5	350.1	83.09	0.01	-0.21	
Sb_4O_6 (g)	-1215.5	441.199	162.756			
$SbCl_3$ (s)	-382.2	184.1	40.17	225.94		
SbO (g)	-103.5	238.346	11.8			
SbO_2 (s)	-113.5	15.2	11.3	8.1		
SbOCl (s)	-374.05	107.5	54.5			
Ni_2InSbO_6 (s)	-1519.15	190.55	119.37	264.665	1.085	

The figure shows the measured data of the transport weight plotted against time. The red line is the linear fit used to calculate the transport rates. The length of the line corresponds to the fitted data points. a) corresponds to S-ID1, b) to S-ID2, c) to S-ID3, and d) to S-ID4. In (c), it is clearly visible that the transport rate decreases due to a reduced temperature gradient during the experiment.